

2023-05-01

Geological Mapping Of Ferric And Ferrous Irons In The Apache Hills, New Mexico: Applying Landsat 8 (oli), Spectrometry, And Geographic Information System (gis) Methods

Sergio Gerardo Macias
University of Texas at El Paso

Follow this and additional works at: https://scholarworks.utep.edu/open_etd



Part of the [Geographic Information Sciences Commons](#), [Geology Commons](#), and the [Remote Sensing Commons](#)

Recommended Citation

Macias, Sergio Gerardo, "Geological Mapping Of Ferric And Ferrous Irons In The Apache Hills, New Mexico: Applying Landsat 8 (oli), Spectrometry, And Geographic Information System (gis) Methods" (2023). *Open Access Theses & Dissertations*. 3816.
https://scholarworks.utep.edu/open_etd/3816

This is brought to you for free and open access by ScholarWorks@UTEP. It has been accepted for inclusion in Open Access Theses & Dissertations by an authorized administrator of ScholarWorks@UTEP. For more information, please contact lweber@utep.edu.

GEOLOGICAL MAPPING OF FERRIC AND FERROUS IRONS IN THE
APACHE HILLS, NEW MEXICO: APPLYING LANDSAT 8 (OLI),
SPECTROMETRY, AND GEOGRAPHIC INFORMATION
SYSTEM (GIS) METHODS

SERGIO GERARDO MACIAS
Master's Program in Geological Sciences

APPROVED:

Terry L Pavlis, Ph.D. Chair

Philip C. Goodell, Ph.D. Co-Chair

James Kubicki, Ph.D.

Carlos Martinez, Ph.D.

Stephen L. Crites, Jr., Ph.D.
Dean of the Graduate School

Copyright ©

by

Sergio G. Macias

2023

Dedication

This thesis is dedicated to all the responsible participants who made this project's completion possible. Yeshua (Lord and Savior), whose spiritual power, faith, and love are the rock that gives me the strength to complete the thesis project. A supportive family, through challenging, harsh health, economic, and emotional tribulations, project completion was always important to them for me to complete. To Dr. Terry L Pavlis (Master Pavlis), Chair Committee Member, and his infinite advice, patience, wisdom, and academic/emotional support that he provided me during and even after he retired from the University. Honestly and truly a sincerely unique individual. Dr. James Kubicki (Committee Member) genuinely cares and listens to student concerns/issues attentively, which includes valuable advice, which will result in a positive outcome soon. I am very grateful to Dr. Carlos Martinez for guiding me through the ENVI software and reinforcing the confidence necessary to understand remote sensing and complete the thesis project.

GEOLOGICAL MAPPING OF FERRIC AND FERROUS IRONS IN THE
APACHE HILLS, NEW MEXICO: APPLYING LANDSAT 8 (OLI),
SPECTROMETRY, AND GEOGRAPHIC INFORMATION
SYSTEM (GIS) METHODS

by

SERGIO GERARDO MACIAS, B.S.

THESIS

Presented to the Faculty of the Graduate School of
The University of Texas at El Paso
in Partial Fulfillment
of the Requirements
for the Degree of

MASTER OF SCIENCE

The Department of Earth, Environmental and Resource Sciences,
THE UNIVERSITY OF TEXAS AT EL PASO
Spring 2023

Acknowledgments

The Department of Earth, Environmental and Resource Sciences (DEERS) for their continued moral/ethical support, software student licensing (ArcGIS), and financial funding of a geochemical rock sample analysis (Actlabs). To the Spectral Geologist 8 team for granting me a student discount and a limited license agreement allowing me access to the software program to identify specific minerals essential for this thesis. The United States Geological Survey (USGS) website for all the free extracted and imported spatial data to a GIS software platform; without this priceless information, my thesis methodologies would not be possible. Finally, to all the educated and talented authors who published their research papers.

Abstract

Mineral discoveries are typically tangible on surface studies. Previous research describes mineral deposits of ferric and ferrous irons in the lithology, structures, and alluvial fans in the Apache Hills in southwest New Mexico. The research for this thesis combines and models four methods for validating and mapping the presence of Ferric and Ferrous Irons developed in weathered zones above mineral deposits. A beneficial steppingstone before exploration and discovery begins with extensive research.

This study began with data acquisition and reviewing previous research and was essential for the project methods. The study combines four techniques: spectral geology (e.g., remote sensing and spectrometry), geographic information system (e.g., GIS software ArcMap 10.8 and ENVI 5.3), and geochemical data analysis (e.g., previous research and Act Labs trace element results). These methods were combined to create mineral maps for specific locations and represent an exploration method of collecting diverse data at minimum or no cost. This study concludes that satellite geospatial data, laboratory spectroradiometer, and geochemical results should be combined to conclude and validate the presence of ferric and ferrous irons in a research area.

Table of Contents

Acknowledgments.....	v
Abstract.....	vi
Table of Contents.....	vii
List of Tables.....	ix
List of Figures.....	xi
1. Introduction.....	1
2. Regional Geologic Settings: The Southwestern United States.....	4
2.1 Tectonics, Magmatic Flare-Up, Extension, and Structures.....	4
2.2 Stratigraphy.....	15
3. Geology of the Apache Hills.....	20
3.1 Background and Mining History of the Apache Hills, New Mexico.....	35
4. Methods.....	40
4.1 Spectral Geology.....	42
4.1.1 Landsat 8 Operational Land Imager & Instruments (OLI) (Spaceborne).....	44
4.1.2 Spectroradiometer: Geophysical and Environmental Research (GER 3700) (Laboratory)	48
4.1.2.1 The Spectral Geologist 8 (Software).....	51
4.1.2.2 The Spectral Library 2006 (USGS) (Add-On ENVI)	53
4.2 Geographical Information System (GIS): Software Platforms.	54
4.2.1 Arc Map 10.8.....	55
4.2.2 Environment for Visualizing Images (ENVI 5.0)	63

4.3 Geochemical Analyses.....	63
4.3.1 Activation Laboratories Ltd (Actlabs)	65
5. Results.....	66
5.1 Previous, Present Modern Research & Integration Methods.....	67
5.2 Actlabs: Geochemical Trace Element Results Report.....	79
5.3 Metadata Landsat 8 (OLI) (Table-4)	84
5.4 Integrating Remote Sensing Spatial Data & GIS Platform (ArcGIS & ENVI).....	87
5.5 Spectral Wavelength Signatures (USGS-PRISM, GER3700 & TSG 8 Data	106
5.5.1 USGS-PRISM.....	106
5.5.2 The Spectral Geologist 8 (TSG 8) & GER3700 (Spectroradiometer).....	114
6. Discussion.....	131
6.1 Summary of Key Results.....	140
7. Conclusion.....	154
8. Future Works.....	155
References.....	171
Appendix	190
Appendix (1) Research Data Acquisition.....	191
Appendix (2) Processed Data (ArcGIS-Figure Classification Method.....	193
Appendix (3) Actlabs Certificate of Analysis.....	197
Vita.....	198

List of Tables

Table 1: Report from the U.S. Bureau of Mines, 1927-1990 (from McLemore et al., 1996, table 49, p.105)	38
Table 2: Township and Range in the Apache No. 2 mining district, different deposit types modified (from McLemore et al., 1996 table 50 p.107-108)	39
Table 3: Landsat 8 Bands (μm) (from Inhel 2019, Table 2-1, p.10	47
Table 4: Dataset attribute and values, Landsat 8 OLI bands 1-11, for Raster images on ArcMap (https://earthexplorer.usgs.gov).	86
Table 5a: Landsat 8 Operational Land Imager (OLI) Nand Indices names, general and specific formulas Astrids (*) denotes repeated band formula and ratios.....	58
Table 5b: Landsat 8 Operational Land Imager (OLI) Band Indices Specific Formulas and Reference Source (www.indexdatabase.de/db/is.php?sensor_id=168).....	59
Table 6: Chemical analysis of oxide percentages (FeO and Fe ₂ O ₃ in red box) of selected igneous rocks from the Apache #2 mining District modified (from Peterson, 1976, table 3 p.20)	70
Table 7: Actlabs Geochemical Analysis results from ArcGIS table report.....	83
Table 8: USGS Mineral Resource Data System (MRDS) of the mines surrounding the Apache Hills, Hidalgo County, New Mexico.....	193

Table 9: Leonard Resources AH-14 Assay (1975) results of copper. These results are captured in the Figure in section 13 Township 29S Range 15W for visualization and interpretation that would integrate Remote Sensing band indices combination for future interpretations.....148

Table 10: Leonard Resources AH-11 Assay (1974) results of copper. These results are captured in Figure in section 12 Township 29S Range 15W for visualization and interpretation that would integrate Remote Sensing band indices combination for future interpretations.....148

Table 11: Assay data of mines in the Apache No. 2 mining District, Hidalgo County, New Mexico (modified from Peterson 1976, Table 4 p.61). Red lines describe Limonite Chalcopyrite & Gossans in the Summertime, Daisy, and Apache Mine.....161

Table 12: Interactive Data Language (IDL) logical operator algorithms used with Advanced Spaceborne Thermal Emission and Reflection (ASTER) Radiometer data to map hydrothermally altered rocks in the central and southern parts of the Basin and Range province of the United States. Algorithm notations follow the usage of Mars and Rowan (2006). b, band; float, floating point; le, less than or equal to; lt, less than; ge, greater than or equal to; gt, greater than (Mars and Rowen 2006; Mars and Rowen 2013 p.3).....161

List of Figures

Figure 1: Schematic paleogeography of Late Jurassic to Middle Cretaceous rift to foreland basin transition (modified from Lawton et al., 2020) Figure 13, p.2508 red box denotes the time scale.....	6
Figure 2: Regional tectonic setting of the Bisbee and associated Basins of the USA-Mexican region (modified from Dickinson and Lawton, 2001, Figure 1 p. 476) Red box denotes the study area of the Apache Hills-Sierra Rica Mountains, New Mexico. The purple rectangle is the Laramide foreland.....	8
Figure 3: Paleotectonic maps illustrating two different tectonics models for a mid-Cretaceous time. (a) The Chihuahua trough (Red Circle) is a rift basin separated from the retro-arc foreland basin by a rift shoulder and lowlands, adapted from McGookey et al., 1972 (modified from Mack et al., 1987 figure 1, p. 507).....	10
Figure 4: Paleotectonic maps illustrating two different tectonic models for a mid-Cretaceous time. (b.) A retro arc foreland basin (Red Circle) extends across Utah, Colorado, Arizona, and New Mexico. It is complementary to the Sevier thrust belt and an orogenic belt in southeastern California, western Arizona, and Sonora, Mexico. It was adapted from McGookey et al., 1972(modified from Mack et al., 1987 Figure 1, p. 507).....	11
Figure 5: Possible forces at work during Cenozoic Cordilleran tectonic evolution (modified from Coney, 1987, Figure 2, p. 184).....	11

Figure 6: Ash Flow tuffs calderas of Hidalgo County, New Mexico Outline show the approximate location of the inner margins of calderas flow (6) Apache modified (from Edmond G. Deal, W. E. Elston et al., 1978 P 220. The Red box is the ash-flow tuff caldera).....14

Figure 7: Southwest and northeast stratigraphic cross-section of Bisbee Group, Dakota Formation, and Mancos Formation from Little Hatchet Mountains in southwestern New Mexico to San Ysidro in northwestern New Mexico Rift to foreland transition, Bisbee Basin (modified from Machin, 2013; Lawton et al., 2020, Figure 12, p.2507). The black box with arrows denotes the regional strata of the Little Hatchet Mountains adjacent to the Apache Hills, New Mexico.....16

Figure 8: Model of the Bisbee Basin modified (Yellow Highlights) Little Hatchet Mountains (LHM) near the Apache Hills (modified from Lawton et al., 2020, Figure 1, p.2490).....18

Figure 9: Stratigraphic relationships of rocks in the Apache No.2 mining district, Hidalgo County, New Mexico modified (from Peterson, 1976), figure 14, p. 44). Red-line Chapo Formation. Purple box Tertiary Rhyolite Porphyry skarn mineralization.....19

Figure 10: Geology of the Apache Hills, Hidalgo County, New Mexico. The numbers denote the lithological units and their relevant ages. The red box illustrates the geology that is not included by the USGS. This part of the geology is

courtesy of the Servicio Geologico Mexicano

https://www.sgm.gob.mx/Gobmx/en/About_SGM/Geology.html.....22

Figure 11: Numbered Lithologic Contact Boundaries and Ages including Mines (MRDS) courtesy of the USGS database.....23

Figure 12: Ortho-image of the regional area of the Apache Hills, Hidalgo County, New Mexico. Routing Highways NM 9 West and NM 81 South.....24

Figure 13: Hillshade and World terrain layers on ArcGis stacked for a three-dimensional view of the geological physiography structural features in the regional terrain area.....25

Figure 14: Contacts of Pluton Igneous Bodies of Apache Hills and Sierra Rica, Hidalgo County, New Mexico.....26

Figure 15: Legend of the Tertiary Igneous Intrusions of the Apache Hills and Sierra Rica, Hidalgo County, New Mexico, including Hillshade.....27

Figure 16: The Apache Hills with Normal, Reverse, and Thrust Faults represented in red on Google Earth. Below the image is an elevation profile following each fault (yellow arrows). The blue line is the elevation profile line.....28

Figure 17: Map showing structures and faults (Mairland Syncline-Blue line) (Daisy Anticline-Green line) (Red line Apache fault) (Other red lines are faults) in the Apache Hills (Occidental Anticline-Red Arrow) closer to Sierra Rica. (Modified from Strongin, (1957, p.222, plate 1A).....29

Figure 18: Geologic structural elements in Grant County, Vista Anticline (Purple Box), in between the Hatchet Arc and Cedar Arc (Red Box) (modified from Trauger, 1965, Figure 1, p. 186).....30

Figure 19: Apache Hills map showing the Rhyolite flows and fault Northwest of the Luna Mine (modified from Strongin (1957, p. 222 Plate 1A).....33

Figure 20: Regional comparison of igneous sequence and mineralization (modified from Lasky, 1947, p. 38; Strongin, 1957, Table 2, p.83). Red lines indicate weak mineralization, and purple are the latite flows.....34

Figure 21: LC08_L1TP_034038_20140107_20170306_01_T1, Natural Cover Image Landsat 8 image,) (<http://earthexplorer.usgs.gov>)40

Figure 22: Methodology Flow Chart of all methods used for this thesis. For integration and a final interpretation/conclusion on a GIS platform.....41

Figure 23: A comparison graph of L8 spectral bands and wavelength to that of L7 ETM+. Spectral Bands and Wavelengths for Landsat Sensors modified (from Inhel 2019, p. 50).....42

Figure 24: Illustration of Landsat 8 observatory and instruments (from Inhel 2019, Figure 2-1 p. 8).....46

Figure 25: The spectroradiometer used in this thesis is a GER3700 SN 3700-1002 manufactured by Geophysical and Environmental Research Corporation.48

Figure 26: Manufacturer specifications of the GER3700 Spectro-radiometer at the DEERS building in Dr. Hurtado’s Geophysics lab room 30149

Figure 27: Type 3 measurements were performed to measure the FOV. The illuminating source is a tungsten halogen lamps Type 3a Configuration setup (Type 3a, yellow) of the GER 3700 at the DEERS building in Dr. Hurtado’s Geophysics lab room 301(modified from Schaepman and Dangel, 2000 Figure 1, p.3757)...49

Figure 28: An image containing a geographical user interface created using the USGS Earth Explorer website. The red polygon shape shows the desired user-selected region; the grey area is the dataset results contained in the USGS database for Landsat 8 (OLI)for the study area of the Apache Hills-Sierra Rica, New Mexico. The search results render various data sets. The data set (red arrow) used is LC08_L1TP_034038_20140107_20170306_01_T1 (Figure 21).....69

Figure 29: Location description (Township and Range underlined in red) of the chemical analysis (Table 6) of the igneous rocks from the Apache #2 mining District modified (from Peterson, 1976, table 3 p.20).....71

Figure 30: Apache Hills (Hillshade) consisting of an overlaid Section, Township 28S and 29S, and Range 14W grid blocks (Red blocks) (purple block 34 and red block 33 speculated section of sample 8) as described by Peterson (1976) followed with the local (MRDS) mines in the area. No Remote sensing data is provided in this illustration.....72

Figure 31: Section, Township, and Range integrating Remote sensing results for Ferric and Ferrous Irons to complement a formal visualization of Peterson’s (1976) geochemical results of iron mineral data location.....73

Figure 32: Sections 20, 30, 31, and 33 from Township and Range T 28 S, R 14 W. (Peterson (1976) Table 3 p.20) geochemical analysis locations that are georeferenced on ArcGIS for reference, visualization, identification, and validation of the presence of Ferric and Ferrous Irons by integrating remote sensing band ratio data results of the mapped minerals.....74

Figure 33: Sections 5 and 8 from Township and Range T 29 S, R 14 W. (Peterson (1976) Table 3 p.20) geochemical analysis locations that are georeferenced on ArcGIS for reference visualization, identification and validation of the presence of Ferric and Ferrous Irons by integrating remote sensing band ratio data results of the mapped minerals. Sections 33 and 34 from Township and Range T 28 S, R 14 W location is speculated based on the information given by Peterson (1976). The section location results for sample eight are missing, but the Township and Range and the mine name is given (Chapo Mine). The remote sensing data results, however, are accurate.....75

Figure 34: Legend of concentration results of Ferric (Magenta), Ferrous (Red and Brown), and Gossan (Dark Red) in a Hillshade background.....76

Figure 35: Section, Township and Range and Accumulation of Watershed Flow Direction with the integration of Remote sensing results for Ferric and Ferrous Irons to compliment a formal visualization of Peterson’s (1976) geochemical results of iron mineral data location.....77

Figure 36: Legend of concentration results of Ferric (Magenta), Ferrous (Red and Brown), and Gossan (Dark Red) in a Hillshade background.....78

Figure 37: Actlab geochemical trace element analysis results in the report of the samples collected from the Apache Hills. Highlighted in yellow are the Fe percentages for each example collected.....81

Figure 38: Actlabs geochemical mine sample results overlaid on a GIS platform.82

Figure 39: Actlab geochemical result georeferenced on an ArcGIS platform at the Apache Hills.....83

Figure 40a: Remote sensing band ratio results integrated on an ArcMap 10.8 GIS platform for Simple Iron Ratio (RED/BLUE) Classified (4) Natural Breaks (Jenks) (B4/B2) Hewson, Rob D., et al. (2001) Table 5b reference index 78.....88

Figure 40b: Simple Iron mineral ratio (SWIR1/RED) Classified (4) Natural Breaks (Jenks) (B4/B2) on a Hillshade background Volesky, J.C. et al., (2003). Table 5b reference index 78.....89

Figure 40c: Remote sensing band ratio results integrated on an ArcMap 10.8 GIS platform for Ferric Iron Fe³⁺, (RED/GREEN) Classified (3) Natural Breaks (Jenks) (B4/B3) Rowan, L.C.; Mars, J.C (2003)-Table 5a reference index 20....193

Figure 40d: Remote sensing band ratio results integrated on an ArcMap 10.8 GIS platform for Ferric Iron Fe³⁺, (RED/GREEN) Classified (3) Natural Breaks (Jenks) (B4/B3) Rowan, L.C.; Mars, J.C (2003)-Table 5b reference index 20.....90

Figure 41: Legend: Ferric Iron, Fe³⁺ (RED/GREEN) Classified (3) Natural Breaks (Jenks) on a Hillshade background and a World reference overlay. (B4/B3). Concentration values in Magenta. Rowan, L.C.; Mars, J.C (2003). Table 5a reference index 20.....91

Figure 42: Classification method type Natural Breaks (Jenks) Classes 3 including mean-maximum statistics and standard deviation.....193

Figure 43: Remote sensing band ratio results integrated on an ArcMap 10.8 GIS platform for Ferrous Iron Fe²⁺ (SWIR2/NIR) +(Green/Red) Classified (4) Natural Breaks (Jenks) (B7/B5+B3/B4) Rowan, L.C.; Mars, J.C (2003)—table 5a reference index 19.....92

Figure 44: Legend: Ferrous Iron Fe²⁺) on a Hillshade background and a World reference overlay. Concentrated Ferrous Irons values are in Red. Rowan, L.C.; Mars, J.C (2003).....93

Figure 45: Classification method type Natural Breaks (Jenks) Classes 4 including mean-maximum statistics and standard deviation.....194

Figure 46: Remote sensing band ratio results integrated on an ArcMap 10.8 GIS platform for Ferric Oxides (SWIR1/NIR) Classified (32) Quantile (B6/B5) Henrich, V. et al., (2011). Including lithologic contact boundaries. Table 5a reference index 21.....94

Figure 47: Legend: Concentrated Ferric Oxide values in Magenta and white (Henrich, V. et al., (2011)).....95

Figure 48: Classification method type Quantile Classes 32 including mean-maximum statistics and standard deviation.....194

Figure 49: Remote sensing band ratio results integrated on an ArcMap 10.8 GIS platform for Gossan (SWIR1/RED) Classified (3) Natural Breaks (Jenks) (B6/B4)) on a Hillshade background Volesky, J.C. et al., (2003) Table 5a reference index 26. Red circled areas may be of future interest for the possibility of a hidden porphyry Elston, (1976).....96

Figure 50: Gossan (SWIR1/RED) Classified (3) Natural Breaks (Jenks) (B6/B4) in a Hillshade background Volesky, J.C. et al., (2003) Red Circles Area of Future Interest.....97

Figure 51: Classification method type Classified (3) Natural Breaks (Jenks) including mean-maximum statistics and standard deviation.....195

Figure 52: Remote sensing band ratio results integrated on an ArcMap 10.8 GIS platform for Alteration (SWIR1/SWIR2) Classified Natural Breaks (Jenks) (B6/B7) Volesky, J.C. et al., (2003). Table 5a references 3 and 39. Note: Both references are the same band ratios but different reference sources 3 is referenced as an alteration, and 39 is referenced as a Laterite, which is a form of a profound alteration exposed on the surface by a form of erosional weathering and fluvial transport.....98

Figure 53: Classified Natural Breaks (Jenks) (B6/B7) on a Hillshade background Volesky, J.C. et al., (2003). Table 5a references 3 and 39.....99

Figure 54: Classification method type Classified (5) Natural Breaks (Jenks) including mean-maximum statistics and standard deviation.....195

Figure 55a: ENVI 5.3 images of the Apache Hills in RBG Combination showing Iron Oxides Alterations.....100

Figure 55b: ArcGIS image of the Apache Hills in RGB (7,4,2) with contact boundaries for general lithological mapping (Imbroane, 2007).....102

Figure 55c: Created on ENVI 5.3 (Ferric Iron-Orange) and added to ArcGIS as a shapefile.....103

Figure 55d: Created on ENVI 5.3 (Ferrous Iron-Red) and added to ArcGIS as a shapefile.....103

Figure 55e: Created on ENVI 5.3 (Hydroxyls) and added to ArcGIS as a shapefile.....103

Figure 55f: Gossan (SWIR1/RED) 1 Classified Classes 5 (Band 6/Band 4) Volesky, J.C.; Stern, R.J.et al., (2003).....103

Figure 55g: ArcGIS image of the Apache Hills in RGB (7,4,2) with contact boundaries for general lithological mapping (Imbroane, 2007). A compilation of several band ratios (Figures 55c, 55d, 55e, and 55f) and Actlab analysis results for copper are included.....104

Figure 55h: Legend describes all the band combinations (Figure 55g) lithology, faults, MRDS mine data, and Actlab analysis results for copper.....105

Figure 55i: Classification RGB (7,4,2) Composite Stretch Type Histogram Equalize).....196

Figure 55j: Histogram Equalize for RGB Composite bands 7,4,2. The statistics minimum is -5.06, and the maximum of 2.99, with a standard deviation of 5.30.196

Figure 56: USGS spectral Library 2006a digital data (PRISM) add-on for ENVI 4.8 software. Spectrometer type: Beckman™ 5270 measures spectra in the library covering the spectral range 0.2 to 3 μm (Kokaly, R.F., 2011).....107

Figure 57: Wavelength spectral signature record (9271) of Hematite courtesy of the USGS Spectral Library 2006. For wavelength comparison and validation purposes, the data results from GER 3700 and The Spectral Geologist 8.....108

Figure 58: Wavelength spectral signature record (8296) of Goethite courtesy of the USGS Spectral Library 2006. For wavelength comparison and validation purposes, the data results from GER 3700 and Spectral Geologist 8.....108

Figure 59: Wavelength spectral signature record (8296) closeup of image (0.5-0.9um)of Goethite courtesy of the USGS Spectral Library 2006. For wavelength and validation comparison purposes to the data results from the GER 3700 and The Spectral Geologist 8.....109

Figure-60: Wavelength spectral signature record (11210) of Jarosite courtesy of the USGS Spectral Library 2006a. For wavelength comparison and validation purposes, the data results from GER 3700 and Spectral Geologist 8. Jarosite is not a result of the Spectral Geologist 8 from the samples collected but shares a similar absorption feature of 0.925 (µm) as Goethite and should be recognized. The spectral wavelength signature, however, differentiates from that of Goethite. ...109

Figure 61: Wavelength spectral signature record (12886) of Limonite courtesy of the USGS Spectral Library 2006a. For wavelength comparison and validation purposes, the data results from GER 3700 and Spectral Geologist 8.....110

Figure 62: Wavelength spectral signature records of (9271) Hematite, (8296) Goethite, (12886), Limonite, and Jarosite (11210) courtesy of the USGS Spectral Library 2006a. For wavelength comparison and validation purposes, too, the data results from GER 3700 and Spectral Geologist 8.....111

Figure 63: Laboratory spectra of Limonite, Jarosite, Hematite, and Goethite.

Limonite, Hematite, and Goethite have strong Fe³⁺ absorption features at 0.97–0.83 and 0.48-micrometer. Jarosite has Fe-O-H absorption features at 0.94 and 2.27 micrometers. Red arrows and labels identify and point to absorption features of Limonite FeO·nH₂O Iron (III) Oxide-Hydroxides 0.5-0.975 (μm) (Fe³⁺) Purple Arrows, Jarosite KFe₃(SO₄)₂(OH)₆ Ferric Iron (Fe-III) (0.475 (μm) Fe³⁺), 0.925-2.275 (μm) (Fe O-H) Gold Arrow, Hematite Fe₂O₃-Iron (III) Oxide 0.525-0.875 (μm) (Fe³⁺), Blue Arrow, Goethite FeO (OH) Hydroxide 0.5-0.925 (μm) (Fe³⁺) Green Arrow The generic formula is frequently written as FeO (OH)·nH₂O.

However, the ratio of oxide to hydroxide compositions can vary quite widely (modified from R.A. Ayuso (2010) and Mars and Rowan (2006)).....192

Figure 64: Wavelength spectral signature of Magnetite. Field reconnaissance and previous research (Strongin, 1957) indicate the presence of this mineral.....112

Figure 65: Wavelength spectral signature of Chalcopyrite. Field reconnaissance and previous research (Strongin, 1957) indicate the presence of this mineral.....112

Figure 66: Wavelength spectral signature of Pyrite. Field reconnaissance and previous research (Strongin, 1957) indicate the presence of this mineral.....113

Figure 67: Apache Hills Sample 001 (Apache Mine) wavelength and reflectance data input results from the GER 3700 viewed through a combination of SWIR and VNIR from The Spectral Geologist 8 software platform.....116

Figure 68: Apache Hills Sample 001 closeup of the image indicated by the red arrows (Apache Mine) wavelength and reflectance data input results from the GER 3700 viewed through the visible near-infrared (VNIR) spectral feature option of The Spectral Geologist 8 software platform. A smooth line is the wavelength signature for Goethite according to the Spectral Geologist 8 spectral library. The rough line is the wavelength results from the GER3700.....116

Figure 69: Sample 001 candidate results from The Spectral Analyst Astrid (*) indicate a possible spectral signature match according to The Spectral Geologist 8 data library.....117

Figure 70: Apache Hills Sample 002 (Apache Mine) wavelength and reflectance data input results from the GER 3700 viewed through a combination of SWIR and VNIR from The Spectral Geologist 8 software platform.....117

Figure 71: Apache Hills Sample 002 closeup of image (Apache Mine) wavelength and reflectance data input results from the GER 3700 viewed through the visible near-infrared (VNIR) spectral feature option of The Spectral Geologist 8 software platform. A smooth line is the wavelength signature for Goethite according to the Spectral Geologist 8 spectral library. The rough line is the wavelength results from the GER3700.....118

Figure 72: Sample 002 candidate results from The Spectral Analyst Astrid (*) indicate a possible spectral signature match according to The Spectral Geologist 8 data library.....118

Figure 73: Apache Hills Sample 003 (unknown Mine-Adjacent to Chapo Mine) wavelength and reflectance data input closeup results from the GER 3700 viewed through visible near-infrared (VNIR) spectral feature option of The Spectral Geologist 8 software platform. A smooth line is the wavelength signature for Goethite according to the Spectral Geologist 8 spectral library. The rough line is the wavelength results from the GER3700.....119

Figure 74: Sample 003 candidate results from The Spectral Analyst feature denotes an Astrid (*) indicating a possible spectral signature match according to The Spectral Geologist 8 data library.....119

Figure 75: Apache Hills Sample 004 (Chapo Mine) wavelength and reflectance data input results from the GER 3700 viewed through a combination of SWIR and VNIR from The Spectral Geologist 8. software platform.....120

Figure 76: Apache Hills Sample 004 (Chapo Mine) wavelength and reflectance data input closeup results from the GER 3700 viewed through the visible near-infrared (VNIR) spectral feature option of The Spectral Geologist 8 software platform. A smooth line is the wavelength signature for Goethite according to the

Spectral Geologist 8 spectral library. The rough line is the wavelength results from the GER3700.....120

Figure 77: Sample 004 candidate results from The Spectral Analyst feature denotes an Astrid (*) indicating a possible spectral signature match according to The Spectral Geologist 8 data library.....121

Figure 78: Apache Hills Sample 005 (Mairland Mine) wavelength and reflectance data input results from the GER 3700 viewed through a combination of SWIR and VNIR from The Spectral Geologist 8 software platform.....121

Figure 79: Apache Hills Sample 005 (Mairland Mine) wavelength and reflectance data input closeup results from the GER 3700 viewed through the visible near-infrared (VNIR) spectral feature option of The Spectral Geologist 8 software platform. A smooth line is the wavelength signature for Hematite according to the Spectral Geologist 8 spectral library. The rough line is the wavelength results from the GER3700.....122

Figure 80: Sample 005 candidate results from The Spectral Analyst feature denotes an Astrid (*) indicating a possible spectral signature match according to The Spectral Geologist 8 data library.....122

Figure 81: Apache Hills Sample 006 (Last Chance Mine) wavelength and reflectance data input results from the GER 3700 viewed through a combination of SWIR and VNIR from The Spectral Geologist 8 software platform.....123

Figure 82: Apache Hills Sample 006 (Last Chance Mine) wavelength and reflectance data input close-up results from the GER 3700 viewed through the visible near-infrared (VNIR) spectral feature option of The Spectral Geologist 8 software platform. A smooth line is the wavelength signature for Hematite according to the Spectral Geologist 8 spectral library. The rough line is the wavelength results from the GER3700.....123

Figure 83: Sample 006 candidate results from The Spectral Analyst feature denotes an Astrid (*) indicating a possible spectral signature match according to The Spectral Geologist 8 data library.....124

Figure 84: Apache Hills Sample 007 (Last Chance Mine) wavelength and reflectance data input results from the GER 3700 viewed through a combination of SWIR and VNIR from The Spectral Geologist 8 software platform.....124

Figure 85: Apache Hills Sample 007 (Last Chance Mine) wavelength and reflectance data input close-up results from the GER 3700 viewed through the visible near-infrared (VNIR) spectral feature option of The Spectral Geologist 8 software platform. A smooth line is the wavelength signature for Hematite according to the Spectral Geologist 8 spectral library. The rough line is the wavelength results from the GER3700.....125

Figure 86: Sample 007 candidate results from The Spectral Analyst feature denotes an Astrid (*) indicating a possible spectral signature match according to The Spectral Geologist 8 data library.....125

Figure 87: Apache Hills Sample 008 (Last Chance Mine) wavelength and reflectance data input results from the GER 3700 viewed through a combination of SWIR and VNIR from The Spectral Geologist 8 software platform.....126

Figure 88: Apache Hills Sample 008 (Last Chance Mine) wavelength and reflectance data input close-up results from the GER 3700 viewed through the visible near-infrared (VNIR) spectral feature option of The Spectral Geologist 8 software platform. A smooth line is the wavelength signature for Goethite according to the Spectral Geologist 8 spectral library. The rough line is the wavelength results from the GER3700.....126

Figure 89: Sample 008 candidate results from The Spectral Analyst feature denotes an Astrid (*) indicating a possible spectral signature match according to The Spectral Geologist 8 data library.....127

Figure 90: Apache Hills Sample 009 (Quartz Mine) wavelength and reflectance data input results from the GER 3700 viewed through a combination of SWIR and VNIR from The Spectral Geologist 8 software platform.....127

Figure 91: Apache Hills Sample 009 (Quartz Mine) wavelength and reflectance data input close-up results from the GER 3700 viewed through the visible near-

infrared (VNIR) spectral feature option of The Spectral Geologist 8 software platform. A smooth line is the wavelength signature for Hematite according to the Spectral Geologist 8 spectral library. The rough line is the wavelength results from the GER3700.....128

Figure 92: Sample 009 candidate results from The Spectral Analyst feature denotes an Astrid (*) indicating a possible spectral signature match according to The Spectral Geologist 8 data library.....129

Figure 93: Apache Hills Sample 0010 (Occidental Mine) wavelength and reflectance data input results from the GER 3700 viewed through a combination of SWIR and VNIR from The Spectral Geologist 8 software platform.....129

Figure 94: Apache Hills Sample 0010 (Occidental Mine) wavelength and reflectance data input close-up results from the GER 3700 viewed through the visible near-infrared (VNIR) spectral feature option of The Spectral Geologist 8 software platform. A smooth line is the wavelength signature for Hematite according to the Spectral Geologist 8 spectral library. The rough line is the wavelength results from the GER3700.....129

Figure 95: Sample 0010 candidate results from The Spectral Analyst feature denotes an Astrid (*) indicating a possible spectral signature match according to The Spectral Geologist 8 data library.....130

Figure 96: Schematic view of a sulphide vein. With a clear outlook of the oxidation zone, consisting of the gossan, the leached zone, and the oxidized zone. The reducing zone consists of the enrichment zone and the area of primary mineralization. (Modified from Asmus 2013

(<http://en.archaeometallurgie.de/gossan-iron-cap/>).....142

Figure 96a: Relationship of Laramide porphyry bodies to Cretaceous and basal mid-Tertiary andesites modified (From Elston, 1970, Figure 4, p. 152).....143

Figure 97: Major Tectonic provinces of southwestern New Mexico highlighted in yellow is a possible hidden Laramide porphyry body modified (From Elston, 1970 Figure 1, p. 148).....144

Figure 98: Ferrous Iron 3+ (RED/GREEN) Band 4/Band 3) Classified (5) Rowen, L.C.; Mars J.C (2003) Table reference index 20. Including the Copper assay result samples from *Leonard Resources AH-14 Assay Township 29S and Range 15W in sections 12 and 13(Red Box) (1974-1975) georeferenced on a GIS platform from Peterson (1976) for future exploration.....145

Figure 99: Township 29S and Range 15W Sections 12 and 13 visualize the section area through ArcGIS Peterson describes as an area of favorable exploration of the host rock. Two methods are integrated into this figure, Remote Sensing Ferrous Iron 3+ Band ration (RED/GREEN) and the red boxes showing the Geochemical assay results from the copper values determined by the legend (Figure 100).....146

Figure 100: Legend results from Figure 98 depicting Ferrous Iron 3+ Band ration (RED/GREEN) and the Geochemical Assay Results from Leonard Resources (1975). Sourced from Peterson (1976 with the Township and Range added on an ArcGIS platform).....146

Figure 101: Actlabs Ltd. Certificate of Analysis November 14, 2018.....197

Figure 102: Gossan (Band 6/ Band 4) Section 33 &36 Township 29S, and Range 14W, including mines with copper values in Hillshade.....149

Figure 102a: Gossans (SWIR1/RED) and Copper values from Leonard Resources (1972-1975) reported by Peterson (1976).....150

Figure 102b: Copper values reported by Geochemical Survey (1968), Superior Oil (1966), Peterson (1976), and Actlabs (2018).....151

Figure 103: Township 28S and Range 14W Sections 30,33 and 36 illustrating the presence of Gossan (Dark Red) as described by Peterson (1976) Table 11152

Figure 104: Township 29S and Range 14W Sections 12 and 13 illustrating the presence of Gossan (Dark Red) and a magnetic anomaly as described by Peterson (1976) Table 11.153

Figure 104a: Mines (black dots) with copper values and faults covering the Apache Hills and Sierra Rica.....160

Figure 105: Mines (black dots) with Phyllic Alteration Mars and Rowen algorithm (2006).....161

Figure 106: Mines (black dots), copper values, and Argillic Alterations Mars and Rowen (2006). Figure 107: Mines (black dots), copper values, and Propylitic Alterations Mars and Rowen (2006).....162

Figure 107: Mines (black dots), copper values, and Propylitic Alterations Mars and Rowen (2006).....163

Figure 108: Mines (black dots), copper values, and Hydrothermal-Silica-rich rock Alterations Mars and Rowen (2006).....164

Figure 109: Mines (black dots), copper values, and Propylitic Alterations Carbonate rich rocks and Epidote-Chloride Mars and Rowen (2006).....165

Figure 110: Mines (black dots), copper values, and a Mosaic Composite Landsat 8 (OLI) and ASTER from Mars and Rowen Algorithm (2006).....166

Figure 111: Mines (black dots), copper values, and ASTER date from Rockwell (2017).....167

Figure 112: Mines (black dots) and Copper values a Mosaic alteration composite of ASTER & Landsat 8 (OLI) Data. Including the North American Magnetic Anomaly High Pass 500 km.....168

Figure 113: Vertical variations in trace elements in a porphyry Cu system. c.) Schematic changes in hydrothermal alteration assemblages and trace elements through a porphyry Cu system viewed as a series of map views through a vertical system. Figure 1, p. 12.....169

Figure 114: Trace element distribution and threshold footprints in a porphyry copper alteration system. Combination sample results from Actlabs and Peterson (1976).....170

1. Introduction

The research for this thesis aims to combine and model four methods for mapping ferric and ferrous iron oxides in the Apache Hills Sierra Rica, Hidalgo County, New Mexico. Mineral discoveries typically have surface manifestations. The classic example is iron-stained weathering manifestations (gossans) developed on iron-rich sulfide deposits used for centuries by prospectors, but many other manifestations are known. Gossans are characterized by using iron oxide mineralogy and spectral reflectance as a possible aid to mineral exploration using remote sensing data (Accame et al., 1983). Remote sensing applications by capturing airborne digital images and spectral analysis contributed several dimensions to modern exploration (Swapan et al., 2018).

Remote sensing methods are the science, technology, and art of acquiring information about objects from a distance and taking us well beyond the limits of human capabilities (Aranoff, 2005). Spectral analysis, such as remote sensing and Spectroradiometer methods, remains innovative. Different image processing techniques, such as color composites, band rationing, filtering, supervised classification, and unsupervised classification, are typically used to delineate favorable areas for further exploration (Pour et al., 2008).

Identifying surface mineralogical composition using remote sensing presents an opportunity for exploration geologists seeking potential ore-bearing hydrothermal systems (Huntington,1996). Previous research describes mineral deposits of ferric and ferrous iron oxides in the lithology, structures, and alluvial fans in the Apache Hills in southwest New Mexico. In addition, a current geochemical analysis in the research area highlights the presence of ferrous and ferric iron oxides that represent weathering of iron-bearing sulfide minerals like pyrite and chalcopyrite.

A beneficial steppingstone before exploration and Discovery begins with extensive research. To begin an exploration project, data acquisition and reviewing previous research information are essential for the project methods. This might be followed by four techniques that require mineral investment: spectral geology (e.g., remote sensing and spectrometry), geographic information system (e.g., GIS software ArcMap 10.8 and ENVI 5.3), and geochemical data analysis (e.g., previous research, assay reports, and Act Lab trace element results). Geologists can combine these methods and create mineral maps for specific arid locations when collecting diverse data at minimum or no cost.

A spectroradiometer (e.g., GER 3700) identifies the surface wavelength and reflectance in a laboratory environment from the field samples provided. The results from the examples are then input into software for mineral identification. The Spectral Geologist 8 software (TSG-8) and the USGS Spectral Library 2007 ENVI [add-on] carry a consortium of stored spectra. The spectral signatures from the resulting wavelengths are researched within the software/add-on libraries to confirm the presence of iron oxide minerals from the locations where the samples are extracted. The spectral signatures for Goethite and limonite (e.g., ferric and ferrous irons) are especially relevant for this study. Some of the best quantitative mineralogic descriptions of porphyry copper rocks are from the formation of Goethite and Jarosite during the weathering process of sulfide-bearing felsic rocks of the Goethite, Hematite, and Jarosite in the leached capping rock. (Locke,1926; Tunell,1980; Blahd, 1983). This study reviews remote sensing geospatial raster data image results on a GIS platform applied to the Apache Hills area of southwestern New Mexico, USA. Raster images are generated using unique band ratios and combinations to expose and isolate iron oxide minerals over an extensive land surface area. Minerals that Strongin (1957) reports are present in the area and essentially concur with the previous geochemical research assay results from Peterson (1976). Satellite geospatial data, laboratory spectroradiometer, and geochemical results conclude and validate the presence of ferric and ferrous iron

oxides in the research area. These minerals are precursors that characterize and identify the existence of a porphyry system.

2. Regional Geologic Settings: The Southwestern United States

The tectonics of southwest North America is widely recognized as the product of convergence between western North America and a mosaic of oceanic plates that started in the late Triassic time following the assembly of Pangea. The Cretaceous tectonism in the Southwestern United States and northwestern Mexico is typically interpreted as the product of eastward subduction of the Farallon plate beneath North America (Dickinson, 1981), but the collision of oceanic arcs also played a role in the polarity of those subduction systems (s) debated (Busby et al., 2023).

2.1 Regional Tectonics, Magmatic Flare-Up, Extensions, and Structures

The tectonic history of the US-Mexico border region is less constrained than areas to the north in the western U.S... Nonetheless, evidence indicates a complex Cretaceous history of extension and contraction (Hamilton et al., 1982). The extensional phase of basin development was coeval with Late Jurassic–Early Cretaceous retro-arc shortening that formed Central Nevada and Sevier thrust belts north of Las Vegas, Nevada (DeCelles, 2004; Yonkee and Weil, 2015; Giallorenzo et al., 2018; Lawton et al., 2020).

The proximity of a westward migrating arc (Fitz-Díaz et al., 2018) that provided sediment to Jurassic and early Cretaceous back-arc basins is considered the primary basin-forming process (Fitz-Díaz et al., 2018; Lawton et al., 2020). Shortening to the north created the retro-arc Cordilleran foreland basin. A migrating Jurassic magmatic arc swept westward across northern and central Mexico, including the Late Jurassic Bisbee rift basins (Currie, 1998; DeCelles, 2004; Mael et al., 2011; Lawton et al., 2020). In Cenomanian times, the Arperos basin closed in central and southern Mexico (Martini et al., 2014). The marginal basin model predicts (Figure 1) that the closure of the Arperos basin began sometime between mid-Aptian and mid-Albian time. The diachronous closure of the marginal basin and progressive suturing of Guerrero may explain apparent inconsistencies in the timing of the post-rift increased subsidence. Scientists infer that the well-defined, late Albian subsidence event in Sonora resulted from the collision of the Guerrero super terrane with North America (e.g., Martini et al., 2013; Palacios-García and Martini, 2014; Lawton et al., 2020).

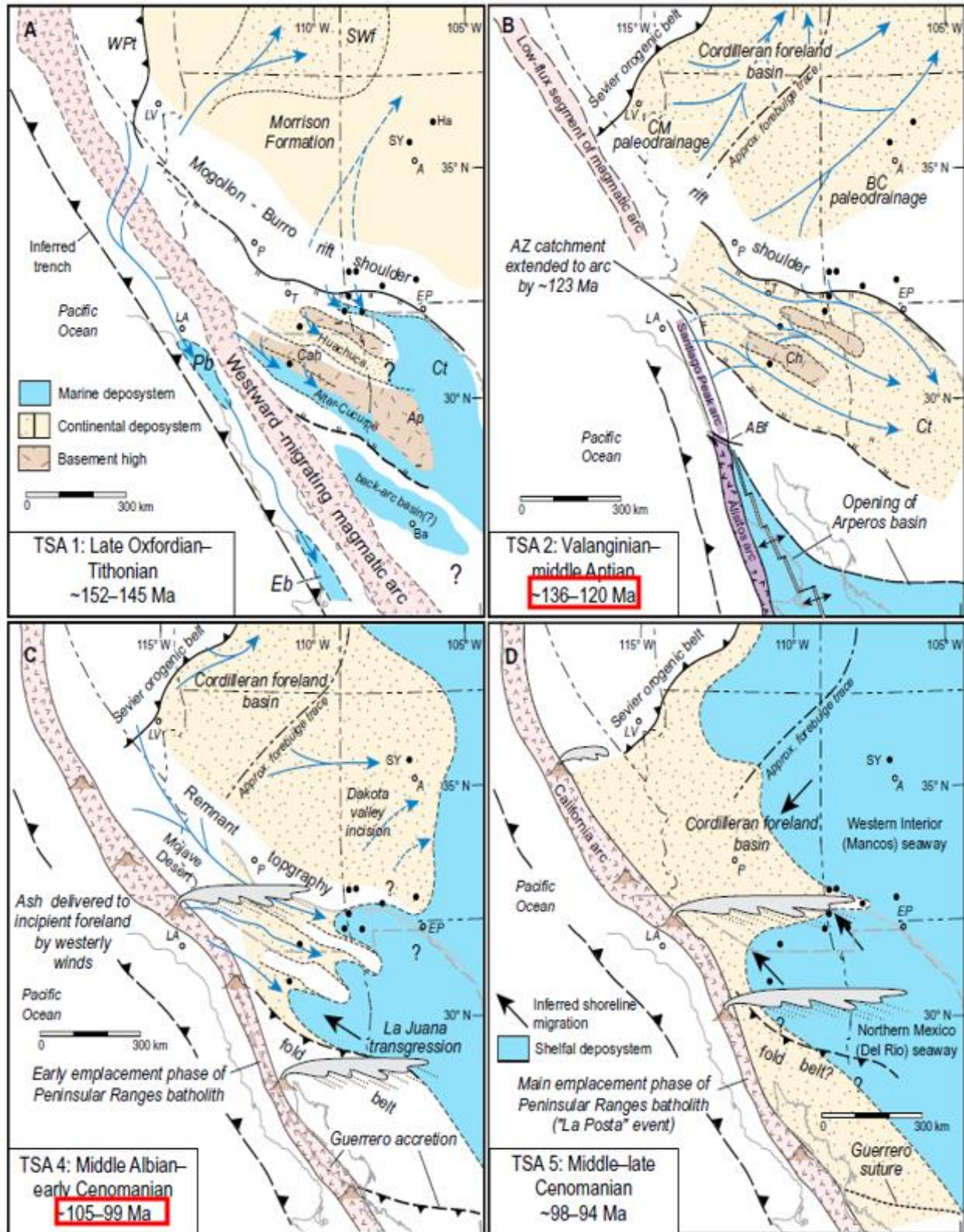


Figure 1: Schematic paleogeography of Late Jurassic to Middle Cretaceous rift to foreland basin transition (modified from Lawton et al., 2020) Figure 13, p.2508 red box denotes the time scale.

The exact time interval marked a magmatic decline in the Sierra Nevada arc of California and a pluton emplacement shift to the batholith's western flank (Ducea, 2001; DeCelles et al., 2009; Nadin et al., 2016; Lawton et al., 2020). The contrasting along-strike magmatic histories of Guerrero and the western United States mirrored the respective, contemporary along-strike transition from Late Jurassic–Early Cretaceous back-arc extension to retro-arc shortening. It presents a mechanism for observed patterns of basin subsidence and sediment sources (Lawton et al., 2020). The sedimentary basin development and provenance relationships of the U.S.–Mexico border region suggest that the basins and arc system evolved with the marginal basin's opening and closing phases. Widespread mid-Cretaceous sedimentation buried the former rift margin in southwestern New Mexico. It accompanied resumed sediment accommodation following a hiatus of at least 20 m.y. in northwestern New Mexico (Lawton et al., 2020).

The stratigraphic section is part of a broad subsiding region that preserved the former basins as separate depocenters with their provenance and sediment routing characteristics (Lawton et al., 2020). The Albian–Cenomanian subsidence event was a long-wavelength phenomenon that resembles modeled dynamic topography resulting from the initial emplacement of a slab subducted into the asthenosphere (Gurnis, 1992; Lawton et al., 2020).

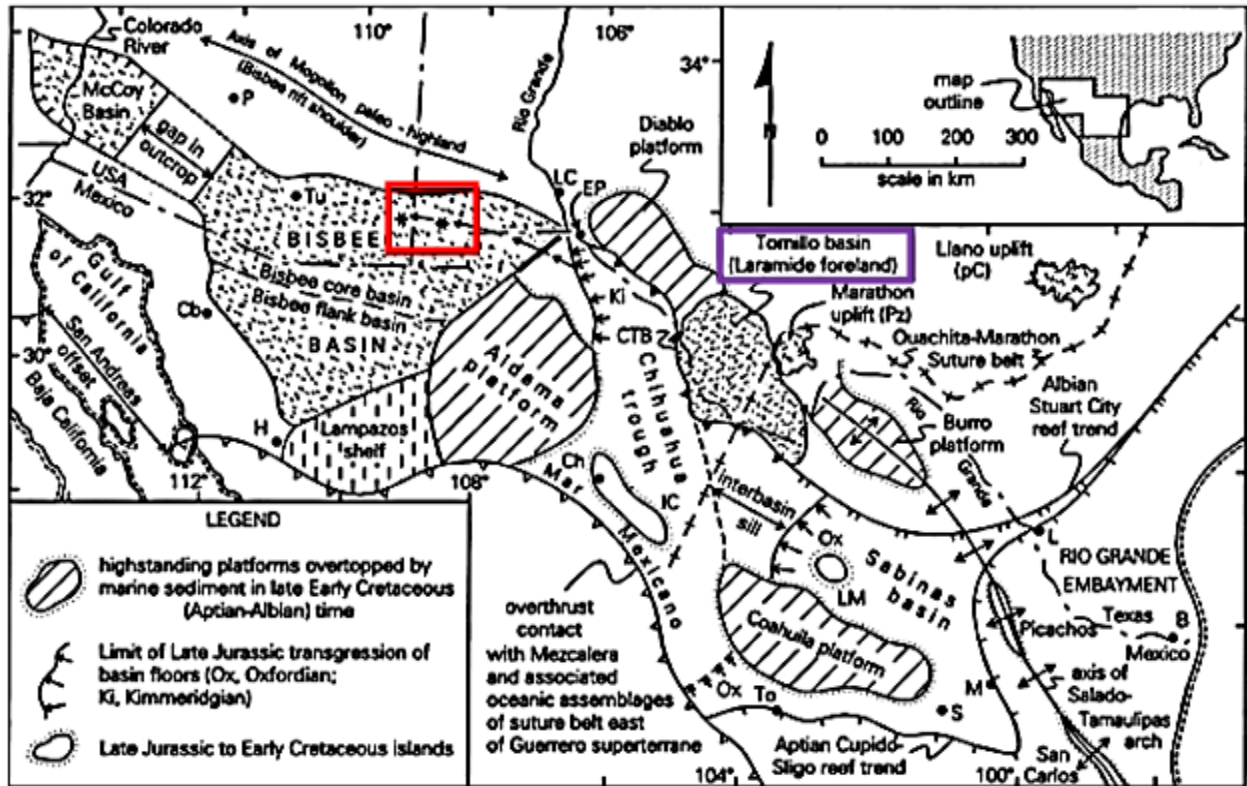


Figure 2: Regional tectonic setting of the Bisbee and associated Basins of the USA-Mexican region (modified from Dickinson and Lawton, 2001, Figure 1 p. 476) Red box denote the study area of the Apache Hills-Sierra Rica Mountains, New Mexico. The purple rectangle is the Laramide foreland.

The inversion of the local basin to form potential tectonic changes by crustal shortening, as recorded by the Bisbee Group clasts in a synorogenic conglomerate, did not occur until Turonian in northern Sonora and Campanian time in southwestern New Mexico. (Gonzalez-Leon et al., 2011; Lawton et al., 2020). In response to subduction, a magmatic arc is formed in western Nevada, western Arizona, eastern California, Baja, California, and Sonora, Mexico (Mack, 1987). Late Jurassic–middle Cretaceous magmatism occurred without apparent interruption along the North American continental margin. (Juárez-Arriaga et al.,

2019; Lawton et al., 2020). During Bisbee Group sedimentation, the Jurassic arc magmatism was succeeded by a bimodal phase of volcanism, transitioning to the tectonics of the Border rift system (Dickinson and Lawton 2001). The Laramide Tornillo basin (Figure 2-purple rectangle) developed in the foreland of the thrust system (Lehman, 1986, 1991; Dickinson and Lawton, 2001). The Lower Cretaceous strata of the Chihuahua trough change facies are eastward and thin rapidly by onlap of a pre-mid-Mesozoic substratum along the flank of the Diablo platform (Gries and Haenggi, 1970; Underwood, 1980; Drewes and Dyer 1993; Dickinson and Lawton, 2001). The Chihuahua trough rift basin is separated from the retro-arc foreland basin to the north by a rift shoulder and lowlands (Figure 4). It complements the Sevier thrust belt and an orogenic belt in southeastern California, western Arizona, and Sonora, Mexico (McGookey et al., 1972). The Sevier thrust belt developed east of the magmatic arc (Armstrong, 1968; Dickinson, 1981). The foreland basin formed east of the Sevier thrust belt and subsided in response to thrust loading and received detrital sediment from the thrust belt McGookey and others, 1972; Dickinson, 1976, 1981; Jordan, 1981; Mack, 1987). The tectonic history is less constrained in southeastern California, western Arizona, and Sonora, Mexico. Dickinson et al. (1986a) suggest that the Chihuahua trough (Figure 3) resulted from either back-arc rifting or was a failed arm of the Gulf of Mexico rift. Middle and Late Cretaceous compressional

deformation overprinted these rift structures along the border region (Hamilton, 1982; Burchfiel and Davis, 1971; Drewes, 1978; Rangin, 1978; Reynolds and others, 1980).

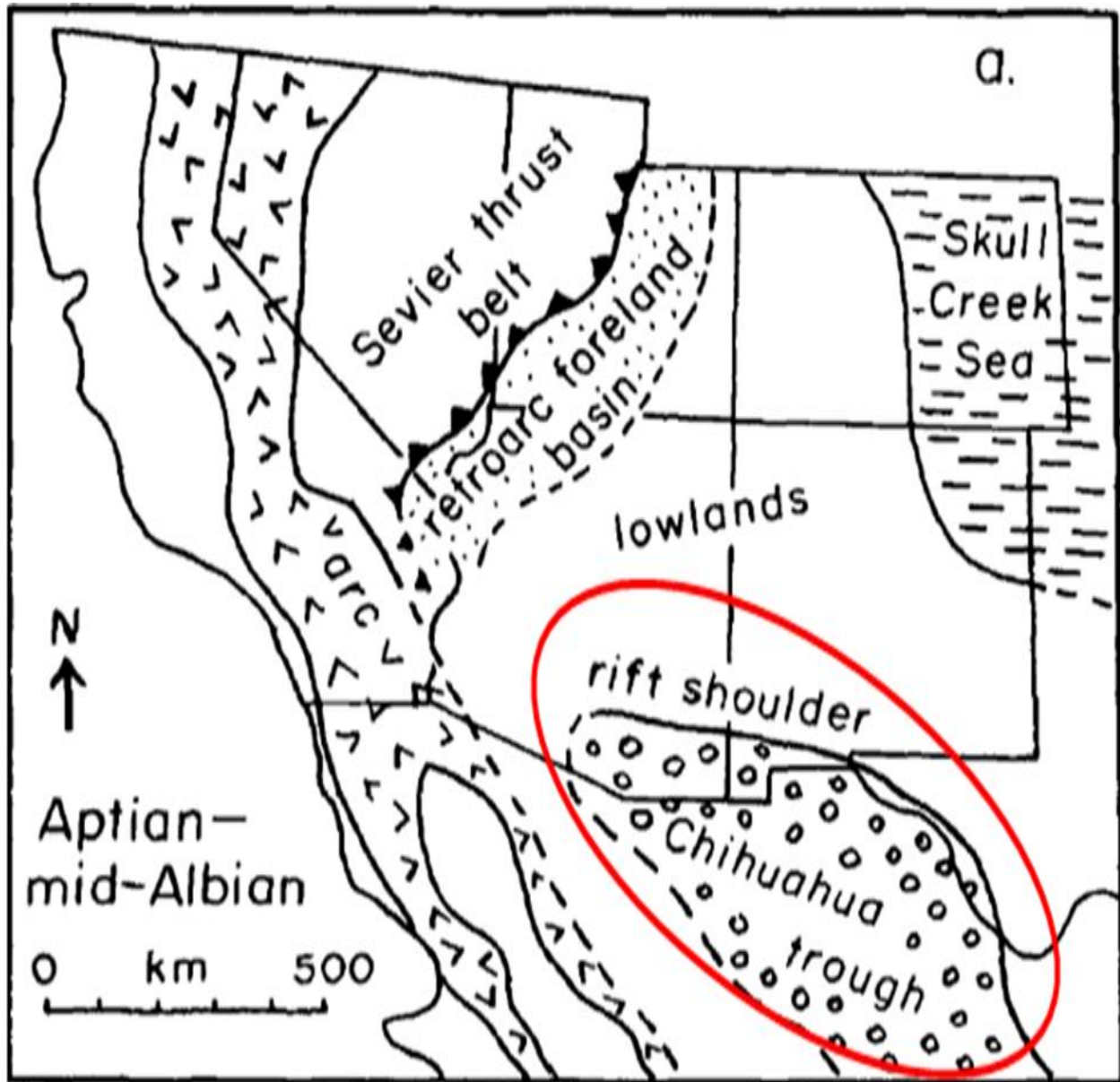


Figure 3: Paleotectonic maps illustrating two different tectonics models for a mid-Cretaceous time. (a) The Chihuahua trough (Red Circle) is a rift basin separated from the retro-arc foreland basin by a rift shoulder and lowlands, adapted from McGookey et al., 1972 (modified from Mack et al., 1987 figure 1, p. 507).

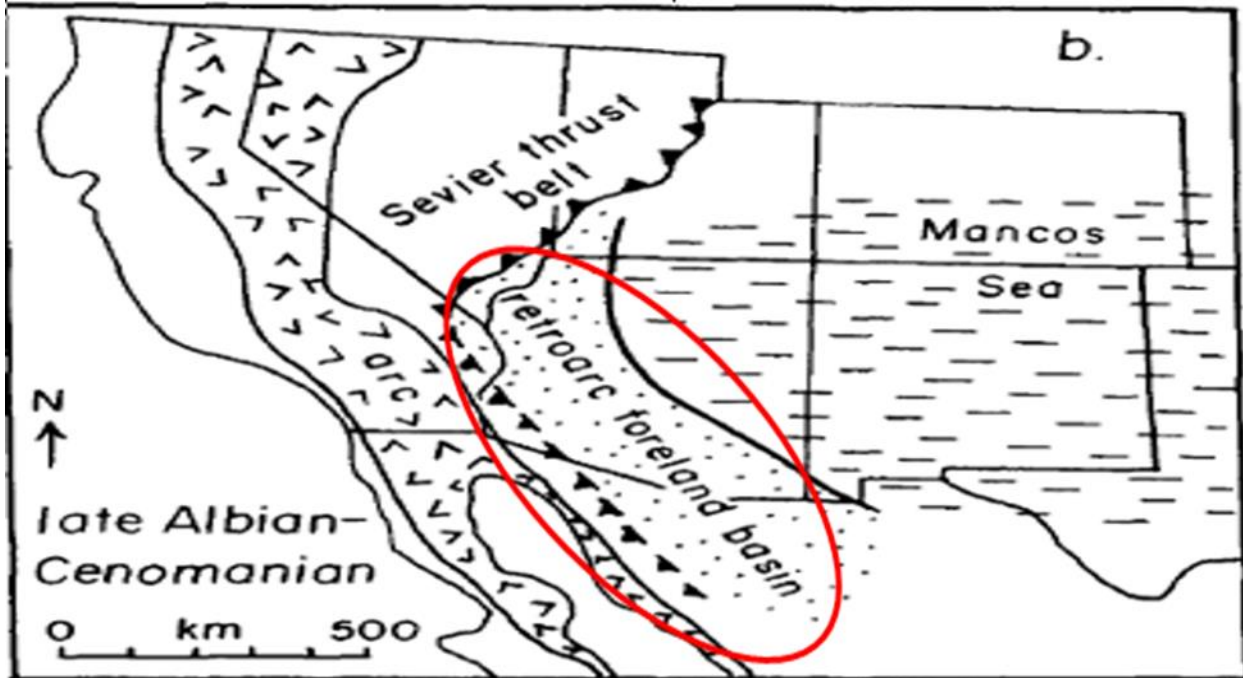


Figure 4: Paleotectonic maps illustrating two different tectonic models for mid-Cretaceous time. (b.) A retro arc foreland basin (Red Circle) extends across Utah, Colorado, Arizona, and New Mexico and it is complementary to the Sevier thrust belt and an orogenic belt in southeastern California, western Arizona, and Sonora, Mexico. It was adapted from McGookey et al., 1972 (modified from Mack et al., 1987 Figure 1, p. 507).

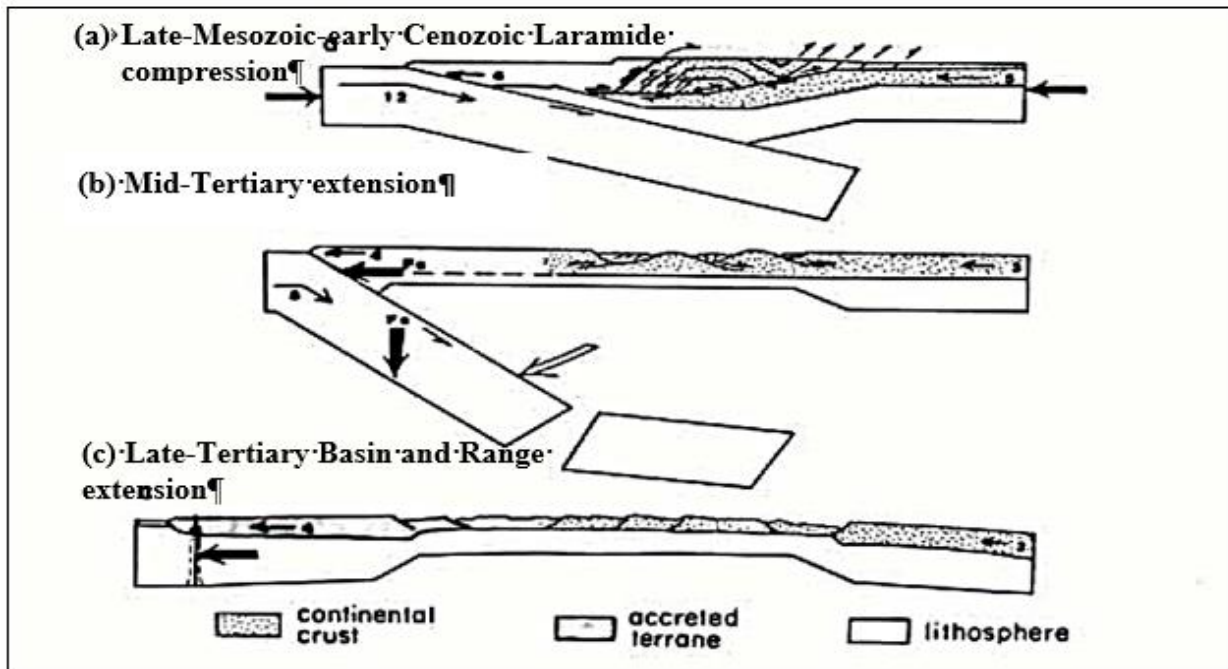


Figure 5: Possible forces at work during Cenozoic Cordilleran tectonic evolution (modified from Coney, 1987, Figure 2, p. 184).

The Basin and Range Province (Figure 5c) developed in the central-western United States and northwestern Mexico through block faulting, strike-slip faulting, and associated relative regional subsidence during the late Cenozoic. During the initial extension in the Neogene, brittle failure of the upper continental crust produces a series of horsts and grabens (Figure 5c). The crust thins to less than average, heat flow is high, and a sparse bimodal basaltic-rhyolitic volcanism has accompanied the extension. The Basin and Range Province remains active from southern California to Idaho and Montana, as well as the Rio Grande rift segment, as evidenced by seismicity and landscape (Coney, 1987). However, the Basin and Range of Arizona and western New Mexico record an older mid-Cenozoic extension that originated under different conditions than the modern, active Basin and Range (Coney, 1987). The timing and tectonic setting of the middle Cenozoic crustal extensions in the North American Cordillera support the concept that an over-thickened crustal welt formed behind or astride the thrust belts produced during Mesozoic (Figure 5a) to early Cenozoic contraction (Coney, 1987). The mid-Cenozoic extension (Figure 5b) in Arizona and southern California is well known for developing sub-horizontal younger over older low-angle normal faults, aka detachment faults of modern terminology (Armstrong 1972). These detachment systems juxtapose un-metamorphosed upper-plate Precambrian to Cenozoic sedimentary and volcanic rocks against lower-plate mylonite-gneiss. The

Cordilleran hinterland's well-known metamorphic core complex extension affected a large area than the younger Basin and Range region, a section covering northern British Columbia through the western United States and southward into Mexico north (Coney, 1987).

A voluminous outburst of caldera-centered ignimbrite eruptions mid-Cenozoic extension (Figure 5b) (Lipman et al.1971; Elston 1976; Coney & Reynolds 1977; Dickinson 1981). Elston (1978) general location of calderas (Figure 6) of Hidalgo County, New Mexico, that were produced during this event. The dashed outlines (Figure 6) show the approximate location of the inner margins of the calderas. A lowering crustal viscosity aided the extension that resulted from an intricate arrangement of volcanism and a decrease in intraplate compressive stress. As plate regimens developed along the Pacific margin during the late Cenozoic, subduction also ceased, as did compressive stress. A developing transform boundary and a massive Cordilleran-wide lithospheric uplift allowed the second phase of the extension to progress across the already thinned and thermally weakened crust to form the Basin and Range Province (Figure 5c) (Coney, 1987).

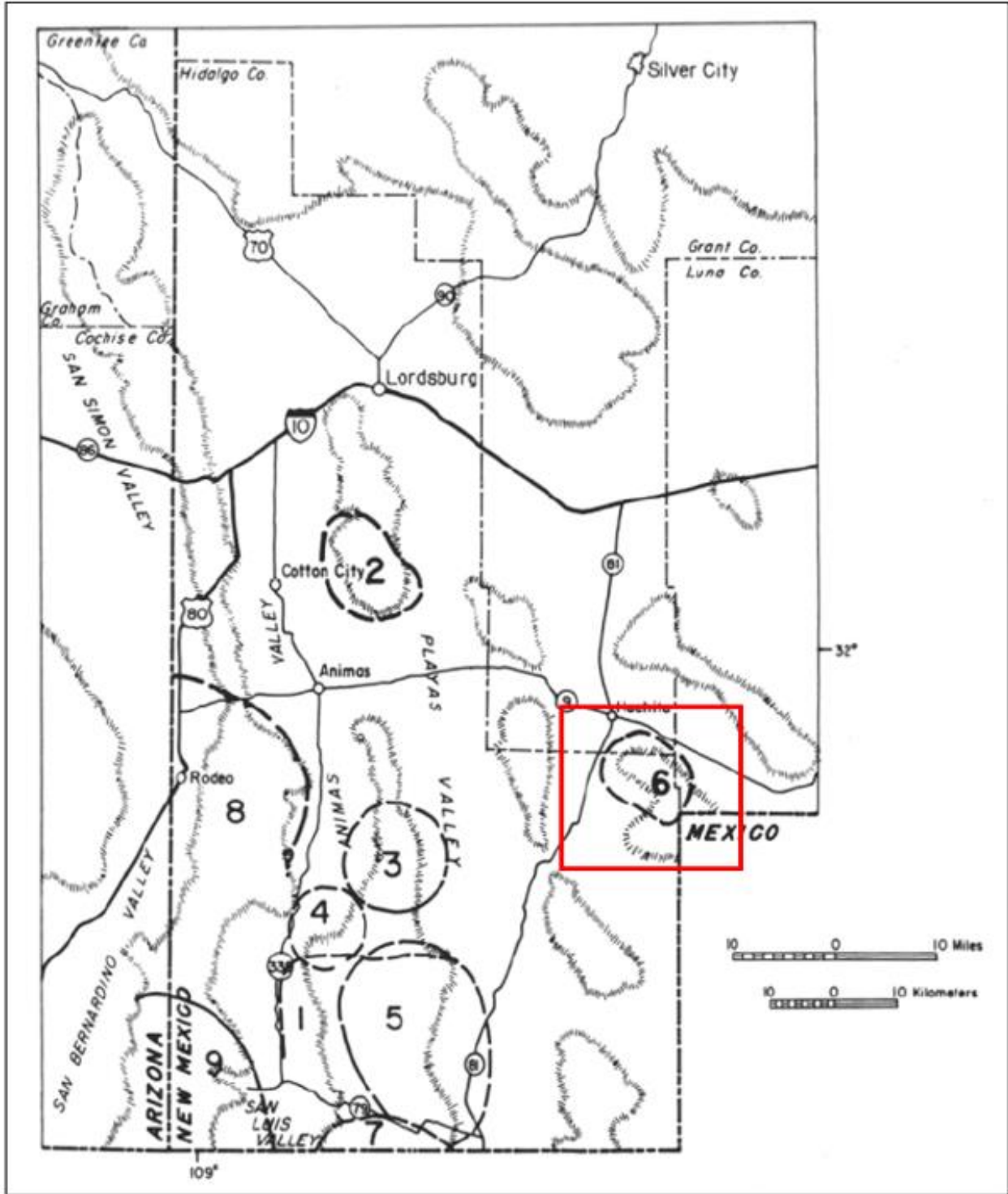


Figure 6: Ash Flow tuffs calderas of Hidalgo County, New Mexico Outline show the approximate location of the inner margins of calderas flow (6) Apache modified (from Edmond G. Deal, W. E. Elston et al., 1978 P 220. The Red box is the ash flow tuff caldera).

2.2 Stratigraphy

Upper Jurassic marine, continental, and mafic volcanogenic strata have been deposited in narrow basins in the study region. These basins are in northern Sonora, southeast Arizona, and southwestern New Mexico. Marine and volcanic strata in the Chiricahua Mountains of southeastern Arizona overlie a thin (40 m) basal conglomerate interpreted as the Glance Conglomerate, establishing a part of the Bisbee Group (Drewes et al., 1995). A stratigraphic convention retained the section and is recognized now as Jurassic (Lawton et al., 2020). The stratigraphy corroborated the previously postulated extensional origin of the Bisbee Group (Lawton et al. 2020). The Bisbee Group nomenclature extends into southwestern New Mexico (Lawton and Harrigan, 1998; Lucas and Estep, 1998b). The Group includes the Upper Jurassic Broken Jug (Figure 7 lower left) Formation and the Lower Cretaceous Hell-to-Finish, U-Bar (Figure 7 left-center), and Mojado Formations (Zeller, 1965, 1970; Lawton, 2004; Lucas and Lawton, 2000; Lucas et al., 2001; Lawton et al., 2020). A well-exposed Jurassic–Lower Cretaceous section overlies Permian carbonate rocks in the Little Hatchet Mountains (Figure 7). To the north of the Little Hatchet, Paleozoic, and Mesozoic strata thin toward the Burro Mountains, where the middle Cretaceous Beartooth Member of the Mojado

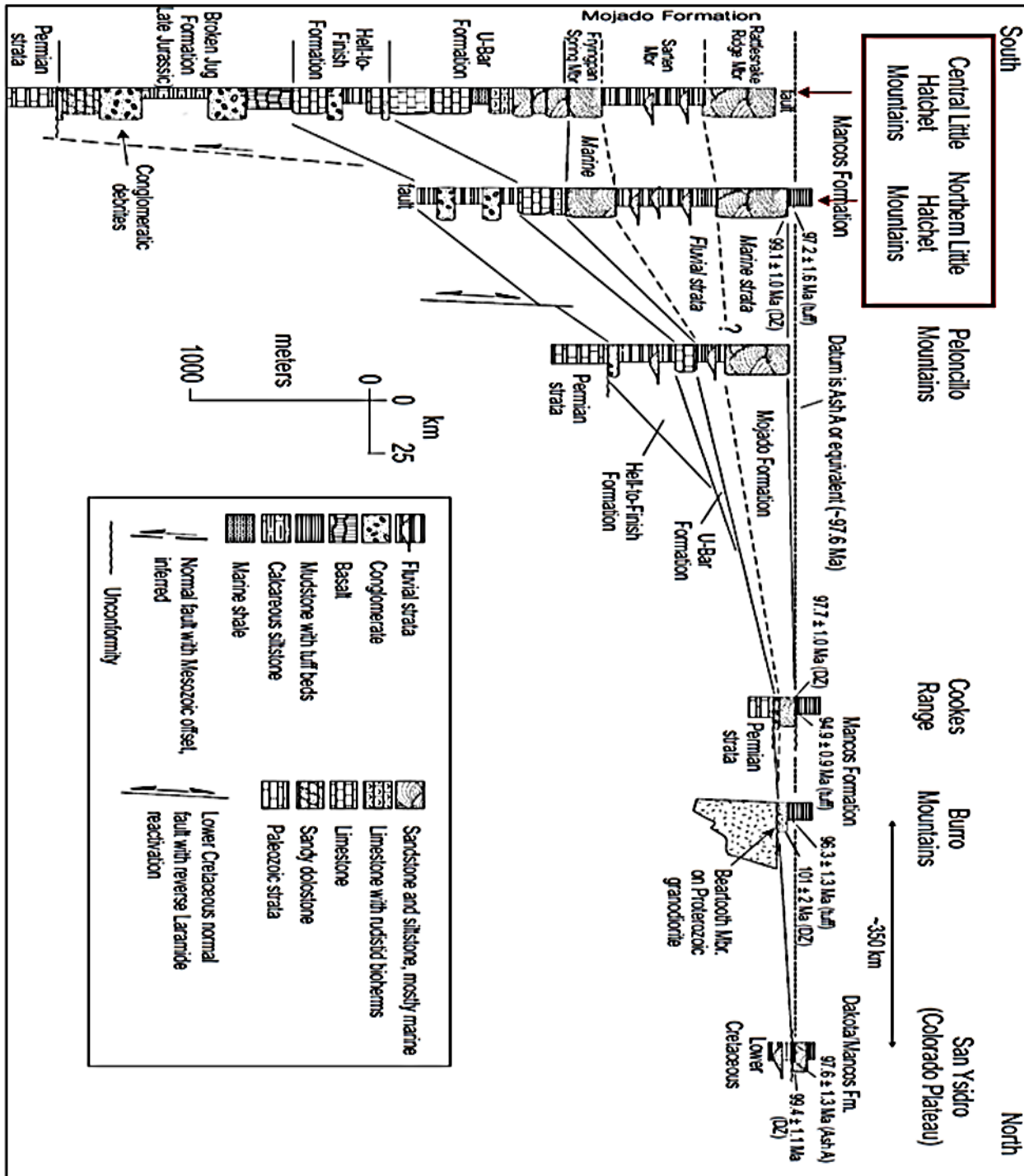


Figure 7: Southwest and northeast stratigraphic cross-section of Bisbee Group, Dakota Formation, and Mancos Formation from Little Hatchet Mountains in southwestern New Mexico to San Ysidro in northwestern New Mexico Rift to foreland transition, Bisbee Basin (modified from Machin, 2013; Lawton et al., 2020, Figure 12, p.2507). The black box with arrows denotes the regional strata of the Little Hatchet Mountains adjacent to the Apache Hills, New Mexico.

Formation directly overlies Mesoproterozoic granitoid and metamorphic rocks (Paige, 1916; Darton, 1917; Lasky, 1936; Chafetz, 1982; Lawton et al., 2020). The thinning of the Paleozoic section was produced by erosional truncation beneath the Jurassic unconformity. Lower Cretaceous strata thin northward by stepwise thinning at syn-depositional normal faults (Bayona and Lawton, 2003; Lawton, 2004; Machin, 2013; Lawton et al., 2020). The Early Cretaceous paleogeographic high in the Burro Mountains is the Burro uplift (Trauger, 1965), which is a southeastward extension of the Mogollon highlands (Figure 8) (Bilodeau, 1986; Lawton et al., 2020). The southeast-trending paleogeographic element, the Burro-Mogollon uplift, is interpreted as a Late Jurassic–Early Cretaceous rift shoulder (Figures 3 & 18) of the Bisbee basin (Figure 8) (Bilodeau, 1982; Dickinson et al., 1986; Mack, 1987a, 1987b; Lawton et al., 2020). The Bisbee Group strata are present on the international border between Chihuahua and New Mexico near El Paso, Texas, where they consist of mudstone and subordinate sandstone intercalated with carbonate strata, which dominate the middle Cretaceous section of the Chihuahua trough (Monreal and Longoria, 2000; Haenggi, 2002; Lucas et al., 2010; Lawton et al., 2020). The Hell-to-Finish Formation (Figure 7) of southwestern New Mexico overlies Jurassic basaltic rocks of the Broken Jug Formation (Figure 7) on a sharp but concordant contact in the central part of the Little Hatchet Mountains. Whereas elsewhere, the Broken Jug overlies Paleozoic

limestone (Lawton and Harrigan, 1998; Gillerman, 1958; Zeller, 1965; Lawton et al., 2020). The Broken Jug Formation comprises red siltstone, thin, upward-fining conglomerate beds, and sandstone with scoured bases. A stratigraphically complete exposure in the central part of the Little Hatchet Mountains is 525 m thick (Lucas and Lawton, 2000; Lawton et al., 2020). The Chapo Formation comprises Paleozoic Limestone (Pzl) to volcanoclastic conglomerates (Figure 9). The Apache Hills map (Figure 18) illustrates the Tertiary Rhyolite flows (Tfr) and fault Northwest of the Luna Mine flow banded rhyolites exposed at the Apache Mine and Christmas mine.

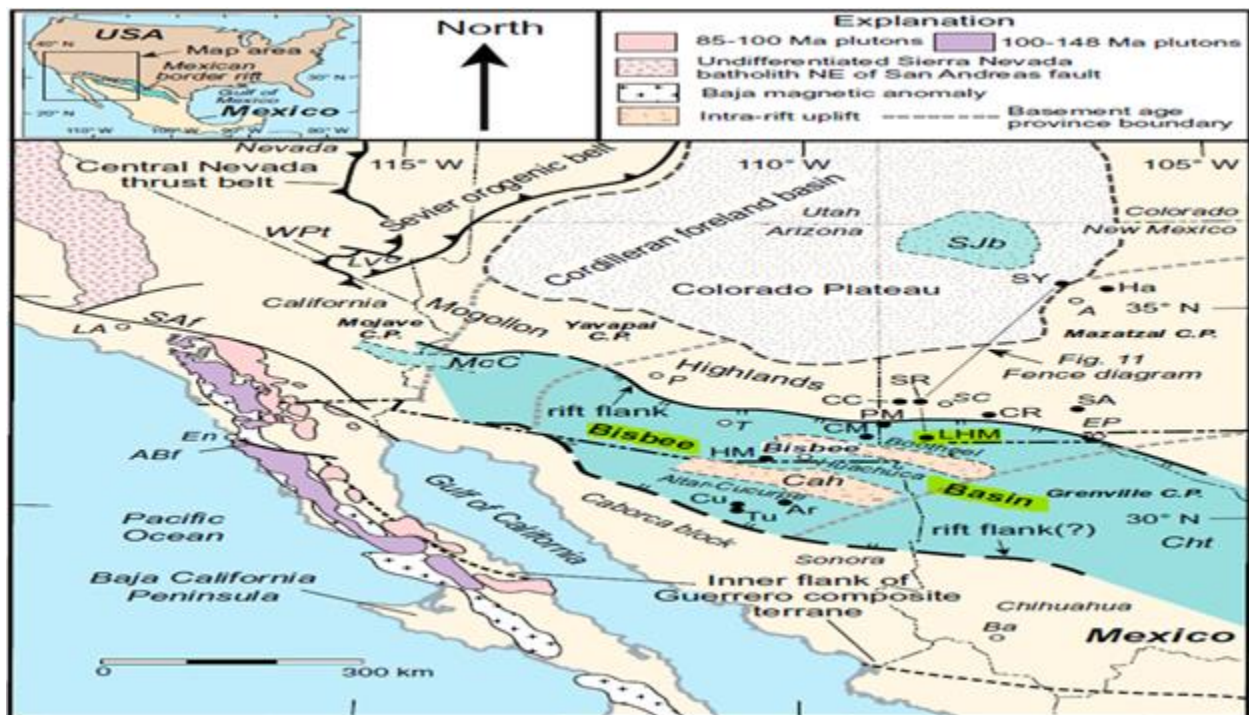


Figure 8: Model of the Bisbee Basin modified (Yellow Highlights) Little Hatchet Mountains (LHM) near the Apache Hills (modified from Lawton et al., 2020, Figure 1, p.2490).

Figure 14. Stratigraphic relationships of rocks in the Apache NO. 2 mining district, Hidalgo County, New Mexico.

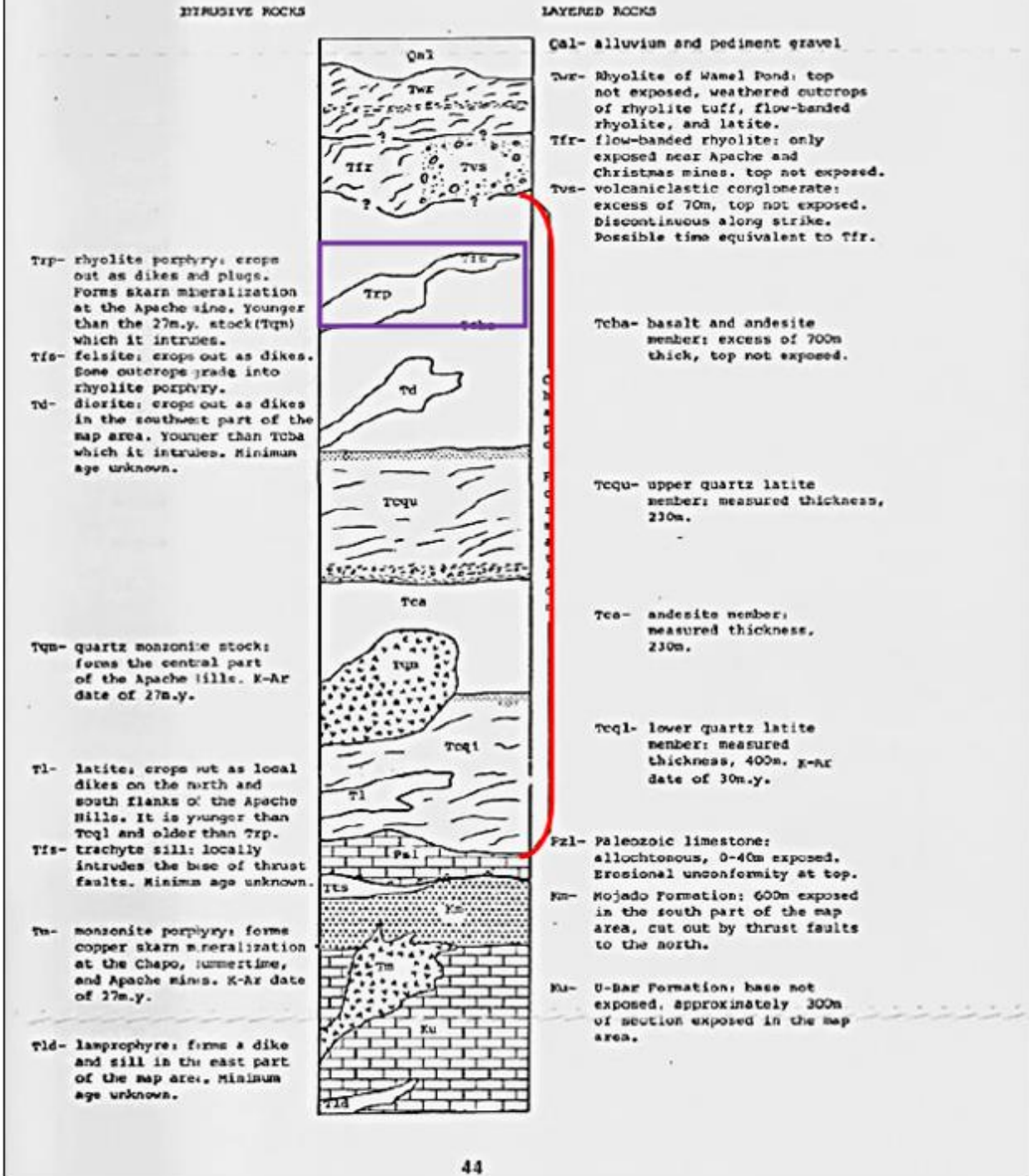


Figure 9: Stratigraphic relationships of rocks in the Apache No.2 mining district, Hidalgo County, New Mexico modified (from Peterson, 1976), figure 14, p. 44). Red-line Chapo Formation. Purple box Tertiary Rhyolite Porphyry skarn mineralization.

3. Geology of the Apache Hills Study Area

The Apache Hills and the Sierra Rica Mountain are separate ranges but similar in stratigraphy and structure (Figure 10-11). The Apache Hills and associated Sierra Rica (Figure 12) form a different complexly faulted block structure (Figure 14-16-17) (Lasky, 1947). Strongin (1957) described the Apache hills as having a composite stock intruding (Figure 14 #25 Red) the Limestone/Sandstone member (Figure 14 #2 below # 25 Apache Peak) of the Howell Ridge Formation and that it is directly responsible for developing a contact metamorphic type deposit. Igneous body intrusions (Figure 14-15) described by Strongin (1957) are a significant feature of the Apache Hills and Sierra Rica visualized through ArcGIS. Two reasonably large intrusive bodies are seen: 1) on the up-thrown block of the Apache fault near Apache Peak and 2) on the down-thrown block fault in Sierra Rica (Figure 14). Dips in the Sierra Rica are southwest, and those in the Apache Hills are mostly northeast, suggesting a faulted dome structure within a larger dome structure (Figure-17-Occidental Anticline structure). Hachita Valley and Warnel Valley are, thus, synclines lying between the Hachet Mountains to the west and the Cedar Mountains to the east, with the Apache Hills and Sierra Rica in the middle (Lasky, 1947). The significant difference between the two is what Strongin (1957) refers to as volcanism which is the intrusive composite that composes most of the Apache Hills complex.

The Apache Hills area has more significant thrusting along the Apache fault (Figure 17), as Strongin (1957) documented. The thrusting is along the Apache Fault and Indian fault from the Apache mine (Figure 9) and further past the Chapo mine (Strongin, 1957). The Sierra Rica represents the southern limb of a significant anticline (Occidental Anticline) (Figure 17 purple line). The axis trends northwest along the foot of Doyle Peak and then west toward the Occidental mines, where the exposed axis is on the surface immediately after border post No. 41 (Figure 17-purple arrows) (Strongin, 1957). Trauger (1965) suggests the axis of the Vista anticline, if projected from the Little Hatchet Mountain across Hachita Valley, would pass along the Apache Hills with the approximate trace of the line of dip reversal running through the Apache Hills and Sierra Rica (Figure 18). The regional area crosses through what is known as the Texas Lineament and the Basin and Range Province (Figure 18).

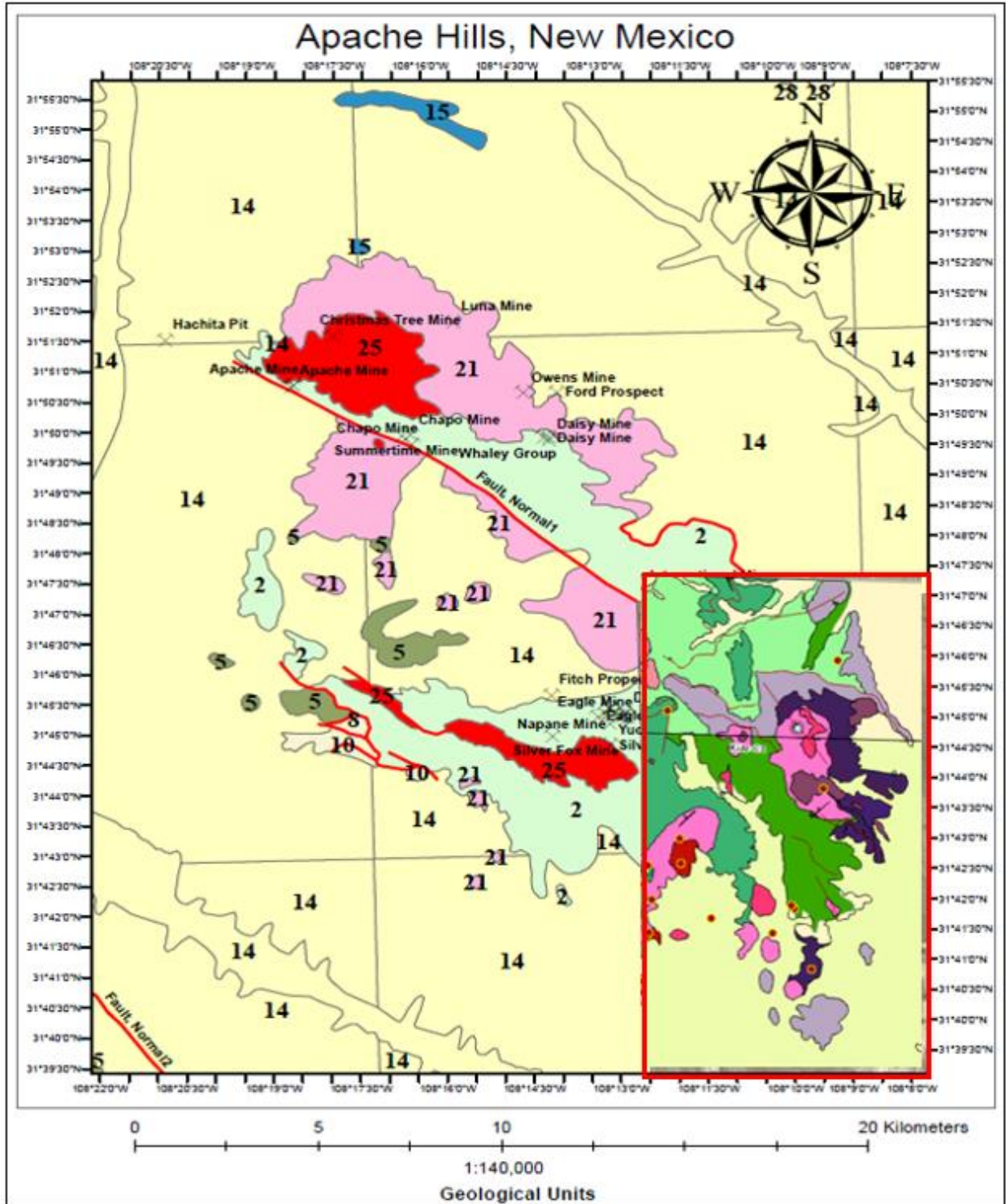


Figure 10: Geology of the Apache Hills, Hidalgo County, New Mexico. The numbers denote the lithological units and their relevant ages. The red box illustrates the geology that is not included by the USGS. This part of the geology is courtesy of the Servicio Geológico Mexicano https://www.sgm.gob.mx/Gobmx/en/About_SGM/Geology.html.

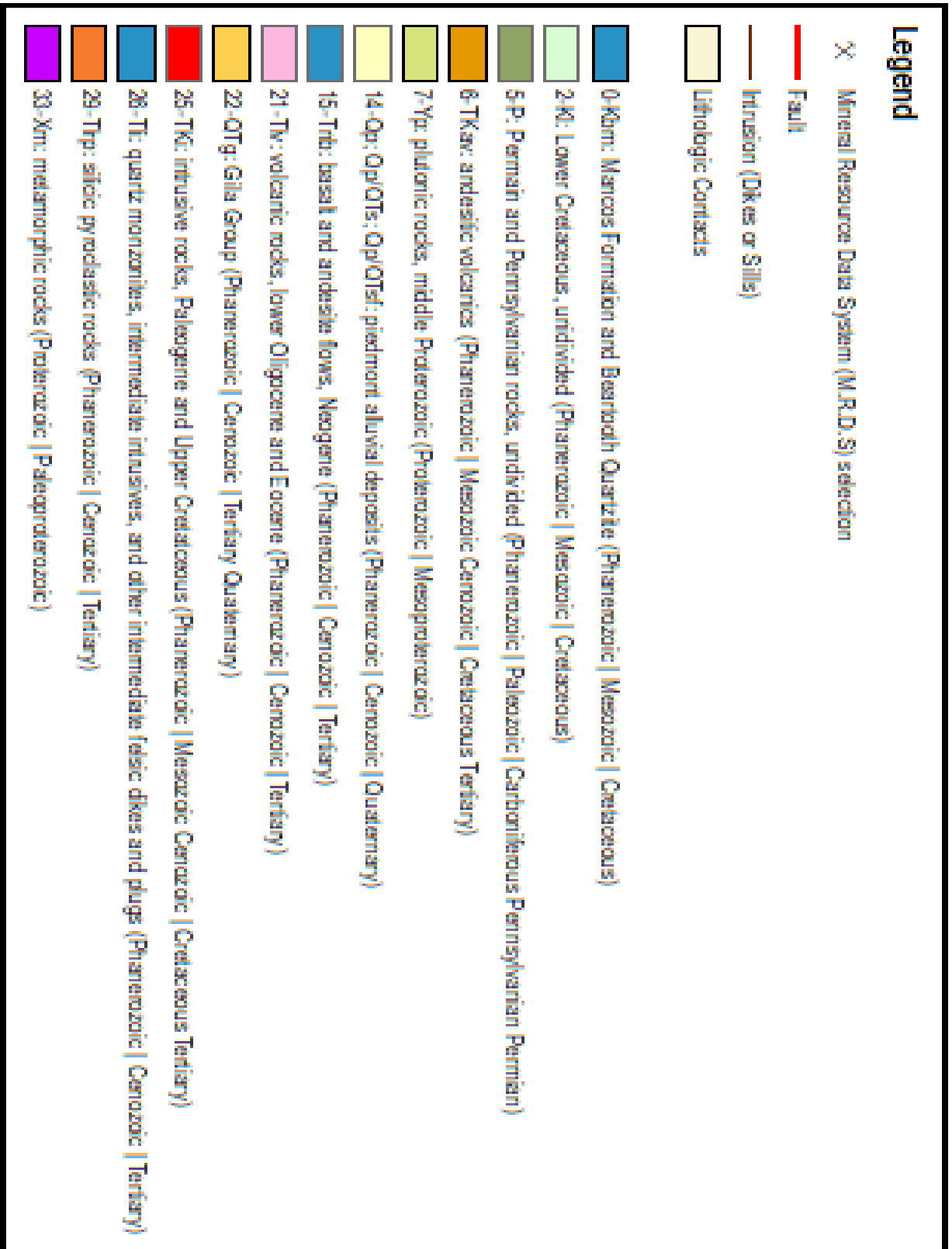


Figure 11: Numbered Lithologic Contact Boundaries and Ages including Mines (MRDS) courtesy of the USGS database.

Apache Hills, Hidalgo County, New Mexico

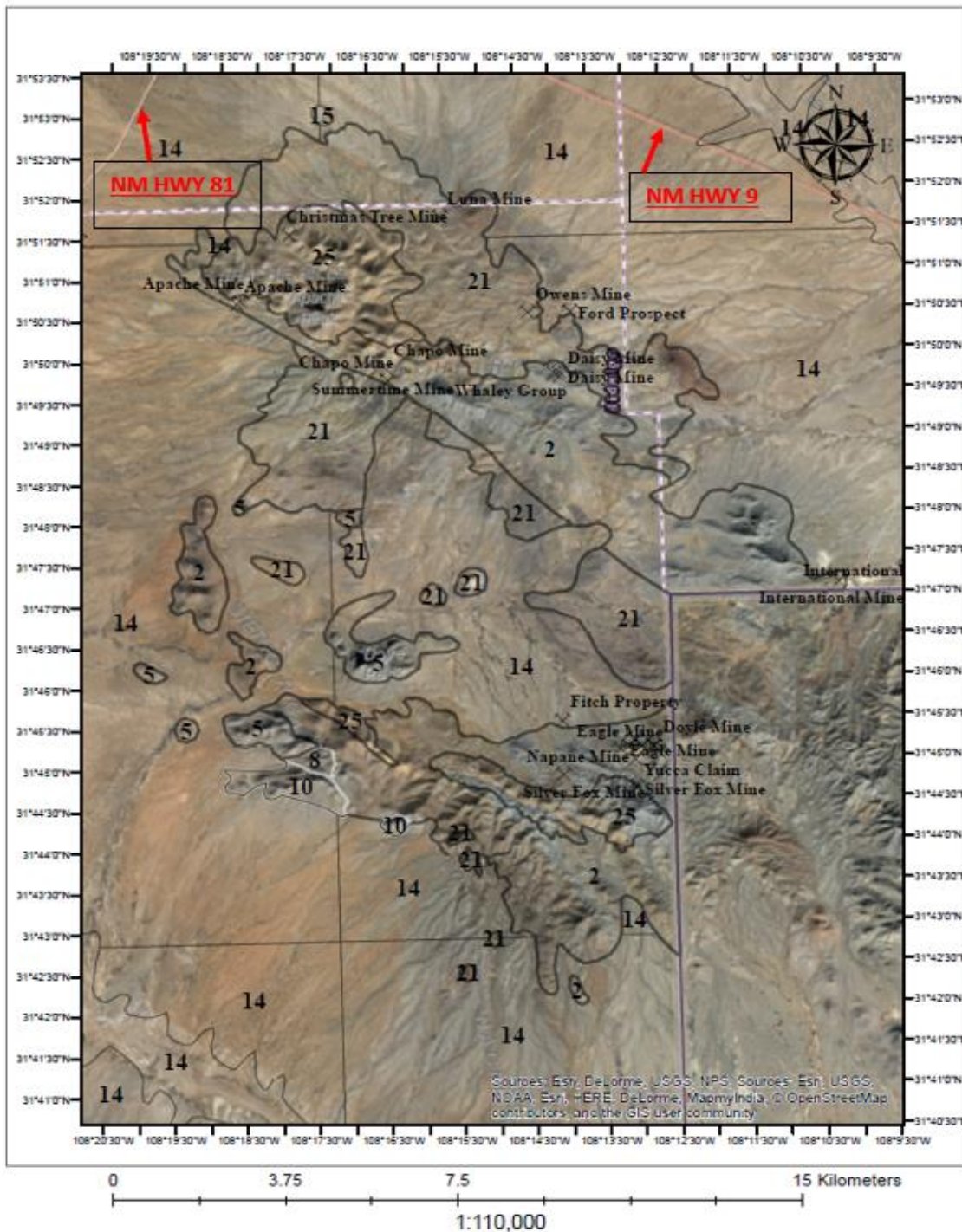


Figure 12: Ortho-image of the regional area of the Apache Hills, Hidalgo County, New Mexico. Routing Highways NM 9 West and NM 81 South.

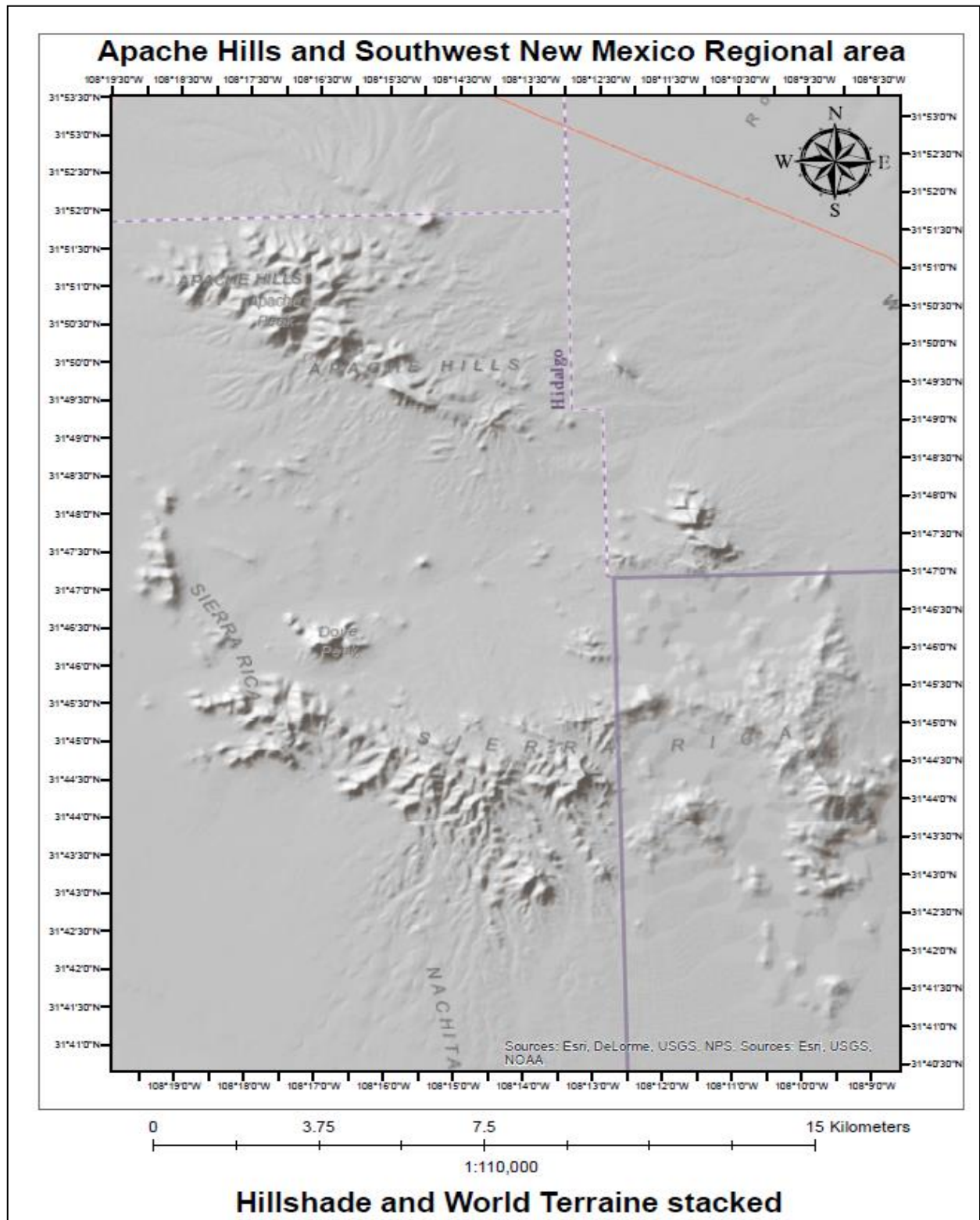
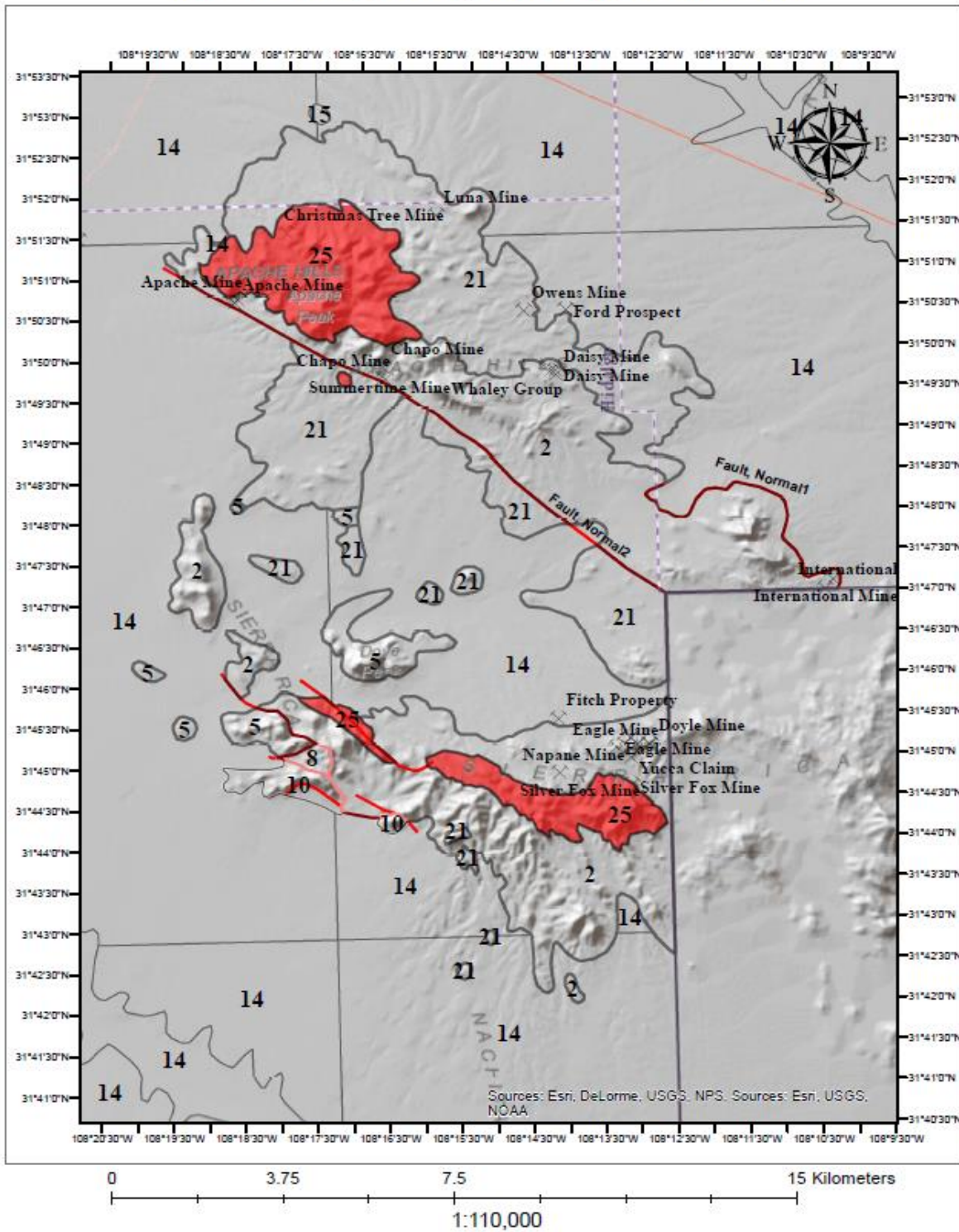


Figure 13: Hillshade and World terrain layers on ArcGis stacked for a three-dimensional view of the geological physiography structural features in the regional terrain area.

Apache Hills, Hidalgo County, New Mexico



**Lithologic Contacts of Pluton Igneous Bodies:
Mid-Tertiary Igneous Intrusions**

Figure 14: Contacts of Pluton Igneous Bodies of Apache Hills and Sierra Rica, Hidalgo County, New Mexico.

Legend

— Fault


— Intrusion (Dikes or Sills)

World Reference Overlay

World Terrain Base

x Mineral Resource Data System (M.R.D.S) selection

Pluton/Igneous Bodies

 Proterozoic-Pluton

 Tertiary-Igneous Intrusion

HillSha_nm_n3_Project3_Cubic1

Value

 - High : 254

Low : 0

Figure 15: Legend of the Tertiary Igneous Intrusions of the Apache Hills and Sierra Rica, Hidalgo County, New Mexico, including Hillshade.

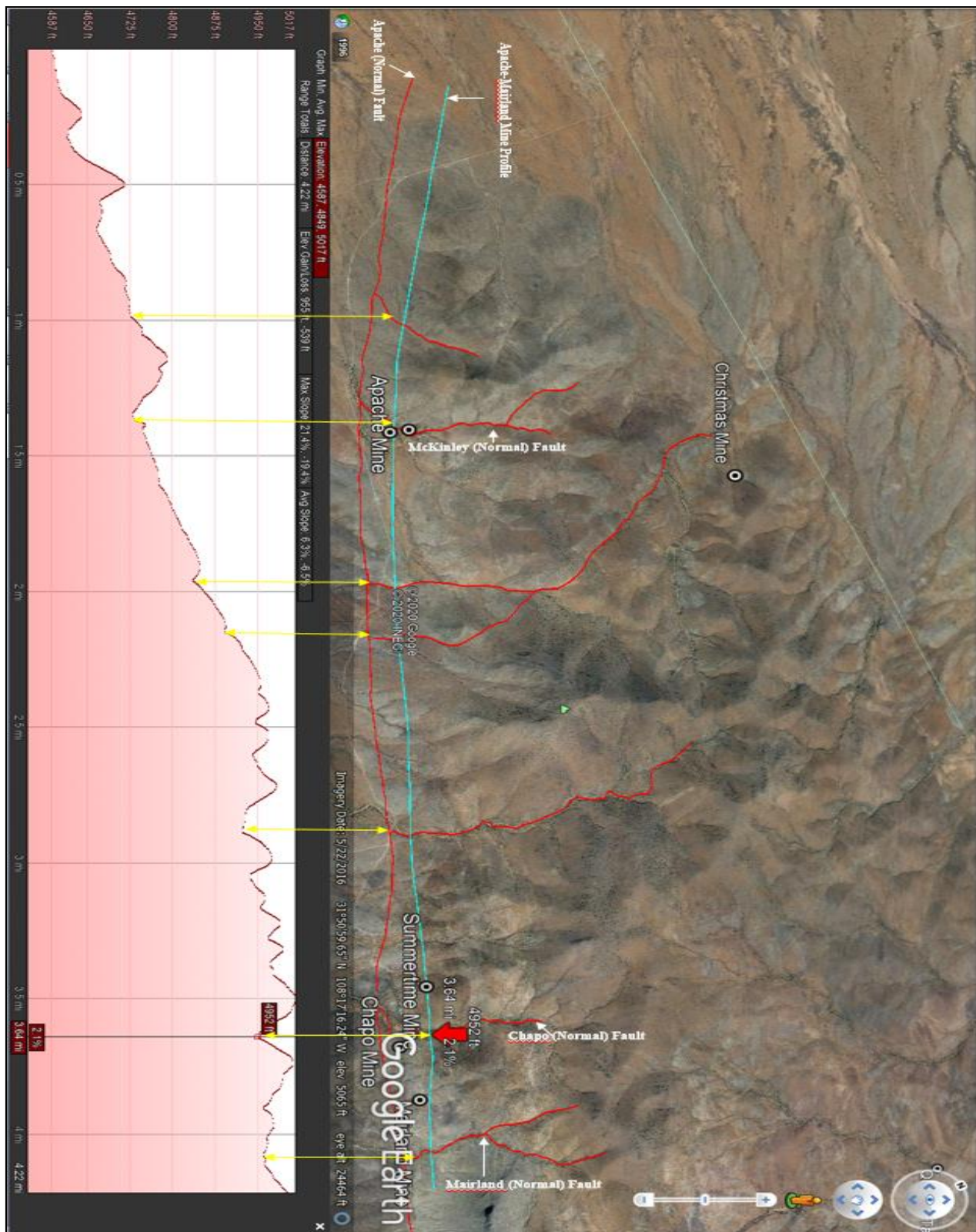


Figure 16: The Apache Hills with Normal, Reverse, and Thrust Faults represented in red on Google Earth. Below the image is an elevation profile following each fault (yellow arrows). The blue line is the elevation profile line.

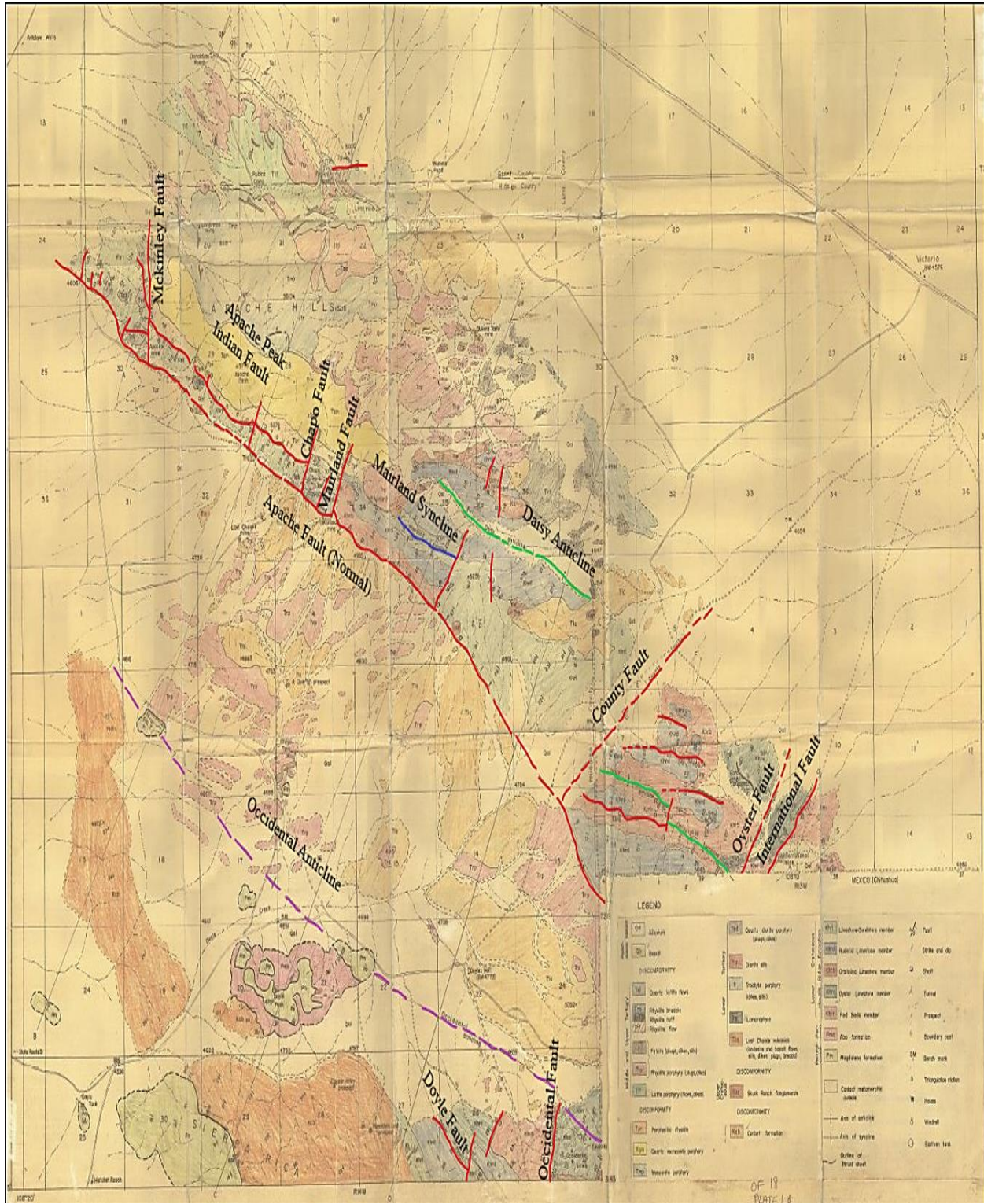


Figure 17: Map showing structures and faults (Mairland Syncline-Blue line) (Daisy Anticline-Green line) (Red line Apache fault) (Other red lines are faults) in the Apache Hills (Occidental Anticline-Red Arrow) closer to Sierra Rica. (Modified from Strongin, (1957, p.222, plate 1A).

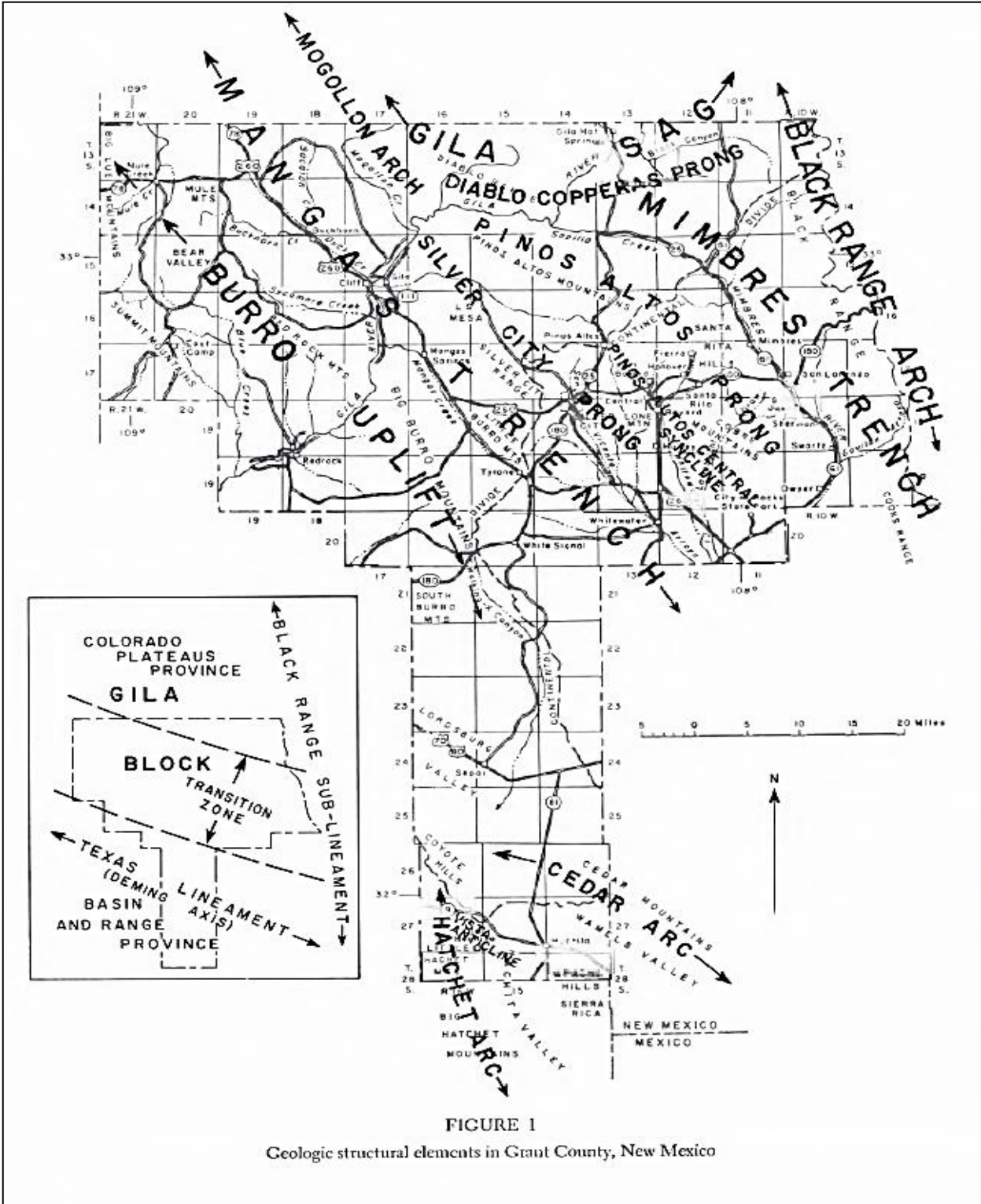


FIGURE 1

Geologic structural elements in Grant County, New Mexico

Figure 18: Geologic structural elements in Grant County, Vista Anticline (Purple Box), in between the Hatchet Arc and Cedar Arc (Red Box) (modified from Trauger, 1965, Figure 1, p. 186).

An anticline and syncline (Figure 17 Blue-Red lines) are exposed north of the Apache fault. These structures suggest that the anticline is a composite structure produced by a succession of structural events. These structural events occurred in a different time-related sequence (Strongin, 1957). The local structural features discussed by Strongin (1957) include high-angle- reverse, thrust, tear, and fissure faults (e.g., McKinley, Chapo, and Mairland Faults, (Figures 16-17) related to the emplacement of the composite stock, followed by vein fissures striking in a west-northwest (earlier) and north-northeast direction. An elevation profile combined with a Google Earth Map of the Apache Hills shows the position of the faults perpendicular to the Apache (Normal) fault as described by Strongin (1957 (Figure 17) (Figure 16, yellow arrows). Strongin (1957) documented three folds in the Apache Hills: the Occidental anticline (red), at the base of Sierra Rica, the Mairland syncline (yellow) and the Daisy (green) anticline north of the Apache fault, and the Indian fault (purple) (Figure 12). The folding of this area marks the local expression of the Laramide Orogeny (Strongin, 1957). The Apache Hills contain two major normal faults (e.g., Apache fault & Indian fault) parallel with the west-northwest extent of the Range (Figure 17). The Indian fault is the fissure along which the stock had risen and subsequently provided a conduit for the rhyolite dikes and is related to other normal faults (Figure 19) like the Mckinley,

Chapo, Mairland, County, International, and others (Figure 17). The faults trend at a high angle to significant regional faults like the Apache (Strongin, 1957).

Strongin (1957) interpreted five significant phases of faulting after the folding but before the stock intrusion in the Neogene (Strongin,1957). North to northeast-trending faults were originally extensional fractures associated with the stock intrusion that formed fissures of this stage. Short transverse faults cutting the mineralized faults reflect a recurrence of faulting toward the close of this vein-forming stage (Strongin, 1957).

Basin and Range extension is also recorded in normal faults forming step-like patterns in the eastern bloc of the Apache Hills (Strongin, 1957). The last phase of faults is northwest of the Luna mine. (Strongin, 1957). Exceptions include the minor ore fissures at the Big Shiner mining area, the Luna mine, the Christmas mine, and the Queens Taste mine, all of which are associated with the intrusive of rhyolite porphyry or related felsite. The bulk of the mining was in the sedimentary rocks cut by sulfide-filled fractures devoid of tactite minerals. Strongin (1957) observed that mineral zoning, though imperfectly developed, is nevertheless noticeable. He suggested from accessible workings that the most intense mineralization is confined to the upper levels in the form of replacement veins, particularly in the calcareous sediments (Figure 20).

Furthermore, the ore zone should not be considered a single body of high-grade material surrounded by lower-grade ore. Instead, Strongin (1957) suggests a wide mineralized area with localized high-grade copper and copper-silver mineralization characterizes the deposits. The type of ore was restricted to the upper levels and occurred as replacement veins in the limestone and rarely shale (Strongin, 1957).

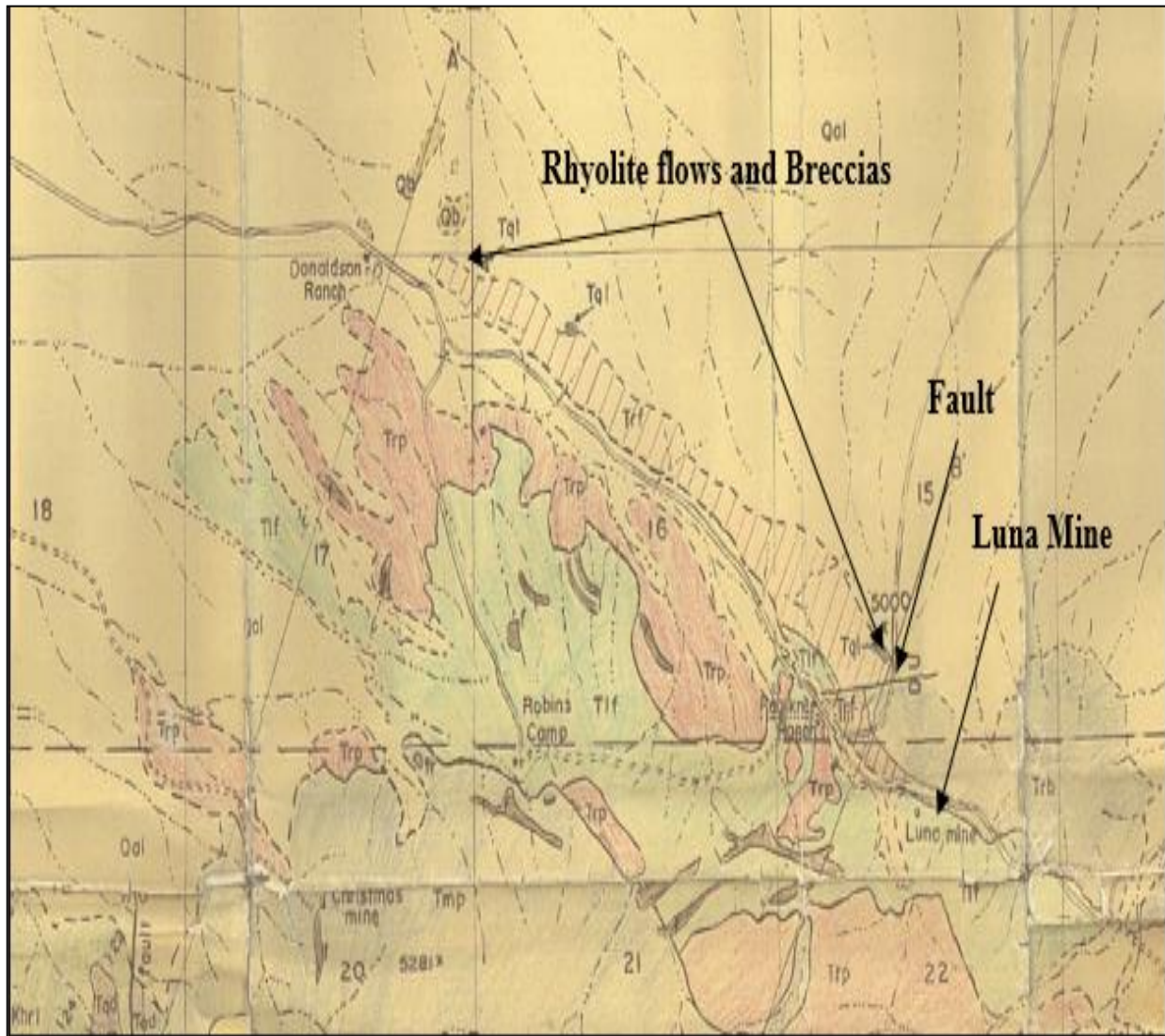


Figure 19: Apache Hills map showing the Rhyolite flows and fault Northwest of the Luna Mine (modified from Strongin (1957, p. 222 Plate 1A).

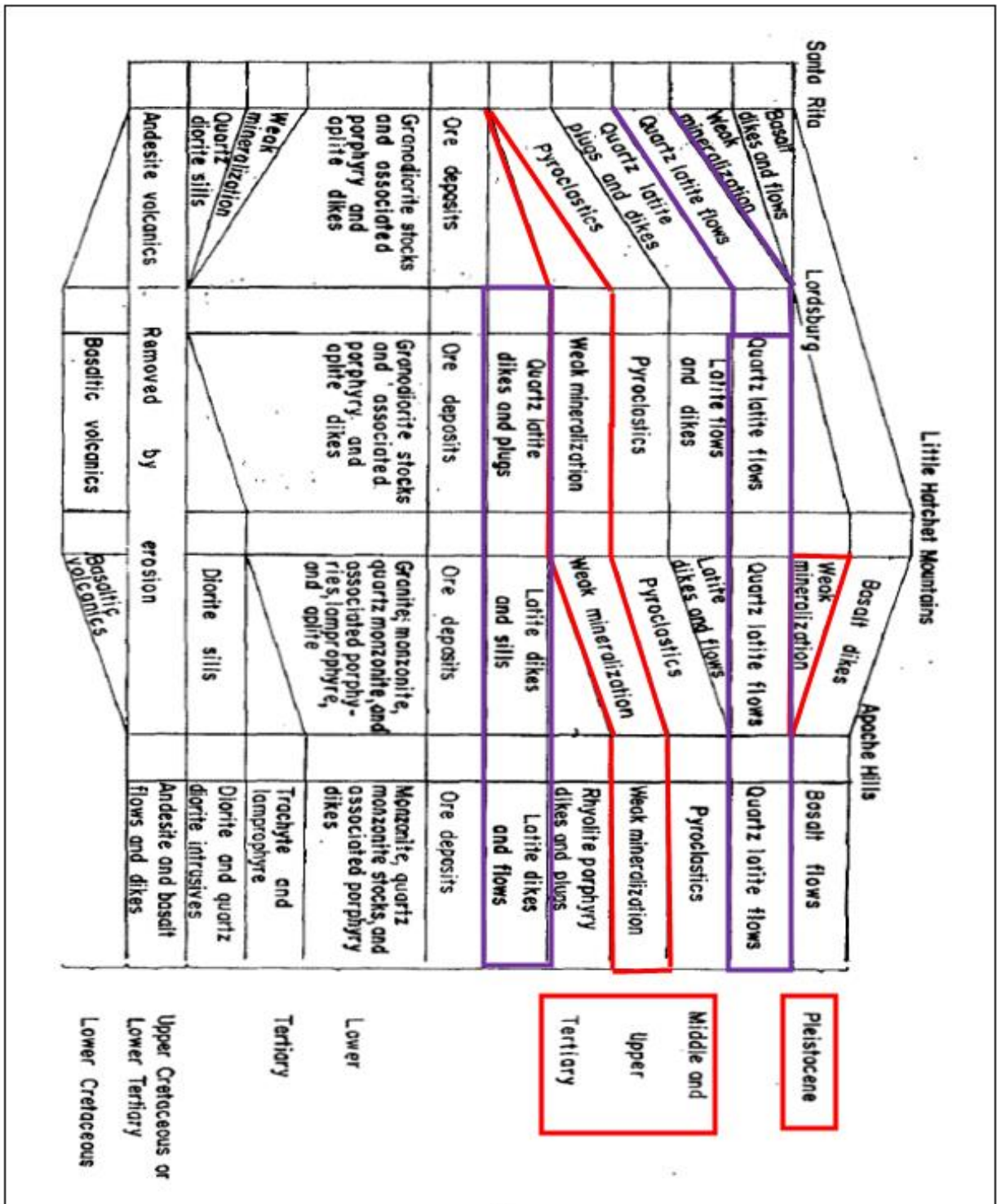


Figure 20: Regional comparison of igneous sequence and mineralization (modified from Lasky, 1947, p. 38; Strongin, 1957, Table 2, p.83). Red lines indicate weak mineralization, and purple are the latite flows.

The mineralization is of an age comparable to that in other local mining districts. It is associated with the intrusion of the mid-Tertiary quartz monzonite and monzonite stocks. Similarly, this is the case in other southwestern U.S. districts and northern Mexico (e.g., Strongin, 1957). The Apache Hills differ from other nearby localities in that it lacks early, pre-stock mineralization as that at the Santa Rita District. Nonetheless, the Apache Hills has weak post-stock mineralization (Figure 20) genetically related to the rhyolite porphyry intrusive. The zone of weakness extends from the rhyolite breccia (Figures 19 & 20) (Strongin, 1957). The dome on the northern fringe of the Apache Hills to the Coyote Hills (Figure 20 Cedar Arc) and the Little Hatchet Mountains' north termination is known as a Basin and Range system. The limestone strata in the Apache Hills strike in a general northerly direction and dip 40° to 70° East (Lindgren et al., 1910; Strongin, 1957).

3.1 Background and Mining History of the Apache Hills, New Mexico.

Prospecting in Hidalgo County began in 1870, with no significant mining until the coming of the Southern Pacific Railroad in 1880 (Elston, 1965). The Apache mine in section 30, T. 28 S., R. 14 W. (Figure 29), accounted for virtually all the Apache No. 2 district production between 1880 and 1929. The area is part of the Arizona & New Mexico west Texas porphyry copper province with all associated mineralization (Elston et al., 1978). Peterson (1976) shows (Figure 9-

purple box) Tertiary Rhyolite porphyry (Trp) erupts out as dikes and plugs forming skarn mineralization. Strongin (1957) says all the ore extracted from the Apache orebody is oxidized. The veins are significantly altered and consist mainly of iron oxide, limonite, or hematite. There are subordinate amounts of copper, gold, and silver in quartz or calcite gangue (Strongin, 1957).

A steady production went on for years in the early 20th century. There have been several theories concerning the origin of this ore. Still, surficial concentration by leaching silver's metallic sulfides and chlorides was the primary origin of the economic deposits leaching out of silver's metallic sulfides and chlorides. The ore has significant manganese and iron (Jones, 1904). The turn of the century estimates of \$107,000 worth of copper, silver, lead, gold, and zinc have been produced from the Apache No. 2 district from 1880 to 1956, including 1.3 million lbs. of Cu and 300,000 lbs. of Pb (Table 1) (McLemore et al.,1996). The chief products of the district are copper ore containing gold and silver. Over the years, some operations produced small quantities of bismuth (Table 2-Apache mine) (Elston,1965). The Apache Hills No. 2 District includes silver, calcite, copper, and gold. Approximately 300 oz. of Gold has been reported and recovered (Table 1) in the Apache mine area. Strongin (1957) described iron oxides such as ferrous FeO Iron (II) oxide and ferric oxide Fe₂O₃ (Hematite) as the most abundant iron oxide in the contact aureole (Strongin,1957).

There are three sections of interest [20,30,33] as presented in Peterson's (1976) geochemical assay report (Table 6) for the occurrence of ferric and ferrous minerals. A geochemical analysis by Peterson (1976) (Table 6) in the research area highlights Ferrous (FeO) and Ferric Oxides Fe₂O₃ within a hydrothermal alteration porphyry deposit (Peterson,1976). The percentages in the assay are significantly high in Ferrous (FeO) and Ferric (Fe₂O₃) iron (Table 6). For example, samples 1, 6, and 7 yielded 8.14, 9.05%, and 8.96 % of FeO. Samples 1, 2, 6, and 8 show high Ferric (Fe₂O₃) percentages of 2.41%, 2.60%, 5.94%, and 3.62%. Unfortunately, according to Peterson (1976), sample 8, in location section (???), is not available (highlighted in red, Figure 28); only the township (28S) and range (14W) information is available. This omission is likely a typo, or the location information is unavailable. I suspect it is section 33, based on the Township and Range information given for the area. The Section, Township, and Range that Peterson (1976) described from the geochemical assay report are sections 20, 30, and 33 (Figure 31). The ferric and ferrous irons are present throughout a large area surrounding and within the intrusive stock of the Apache Hills (Figure 30).

Table 1: Report from the U.S. Bureau of Mines, 1927-1990 (McLemore et al., 1996, Table 49, p. 105).

YEAR	ORE (SHORT TONS)	COPPER (LBS)	GOLD (OZ)	SILVER (OZ)	LEAD (LBS)	ZINC (LBS)	TOTAL VALUE (\$)
1927	4,800	144,000	—	7,200	—	—	—
1939	164	5,600	37	3,636	5,000	—	4,580
1942	30	—	—	—	—	14,300	1,330
1943	332	22,900	3	2,125	57,000	—	8,868
1944	231	400	1	1,236	49,600	—	4,936
1956	50	3,500	—	85	—	—	1,565
TOTAL 1927-1956	5,607	176,400	41	14,282	111,600	14,300	21,279
ESTIMATED TOTAL 1880-1956	—	1,300,000	300	125,000	300,000	20,000	107,000

Three types of deposits occurred in the district (Figure 15): Skarns, 2) Carbonate-hosted Pb-Zn replacement polymetallic vein oxidized skarns, and 3) Carbonate-hosted lead-zin deposits with copper sulfides replacing strata of Cretaceous U-Bar Limestone at the contact with the Quartz Monzonite (McLemore et al.,1996). The deposit extends into the Sierra Rica Mountains of Mexico, where little exploration has been done in the district (McLemore, 1996).

Table 2: Township and Range in the Apache No. 2 mining district, different deposit types modified (from McLemore et.al., 1996 table 50 p.107-108).

MINE NAME (ALIAS)	LOCATION	LATITUDE, LONGITUDE	COMMODITIES	YEARS OF PRODUCTION	DEVELOPMENT	PRODUCTION	TYPE OF DEPOSIT	REFERENCES
Apache (Indian, Squaw Monarch, Copper Crown, Cochise, Navajo, Papoose)	NE30 28S 14W	31° 50' 43", 108° 18' 18"	Cu, Ag, Pb, Zn, Au, Bi, W	1870s - 1956	300, 470 ft shafts, 7500 ft of drifts and crosscuts, opencut, pits	50,000 tons ore since 1870	skarn, carbonate-hosted Pb-Zn	Lindgren et al. (1910), Anderson (1957), Dale and McKinney (1959), Strongin (1957)
Big Shiner	SW33 28S 14W	31° 49' 35", 108° 16' 52"	Cu, Pb, Zn	none	inclined shaft, vertical shaft	none	carbonate-hosted Pb-Zn	Strongin (1957)
Chapo (VE Day, Chappo, Chapel)	NE33 28S 14W	31° 49' 24", 108° 16' 17"	Cu, Pb, Ag, Au	1916 - 1940	180 ft shaft, several prospect pits	40 carloads 4-8% Cu	skarn, carbonate-hosted Pb-Zn	Strongin (1957), Peterson (1976), NMBMMR file data
Christmas (Geiger, Geiger no 2)	20 28S 14W	31° 51' 31", 108° 17' 37"	Cu, Pb, Zn, Mo	none	inclined slope 100 ft long, other shallow workings	some	carbonate-hosted Pb-Zn	Peterson (1976), Strongin (1957)
Daisy	36 28S 14W	31° 49' 46", 108° 13' 55"	Cu, Pb, Zn, Ag, Mo	1860s, 1908	opencuts, shafts no more than 40 ft deep	58,000 Cu-Ag-Au ore	carbonate-hosted Pb-Zn	Peterson (1976), Lindgren et al. (1910), Strongin (1957)
Last Chance	SE32, SW33 28S 14W	31° 49' 20", 108° 17' 04"	Cu, Pb, Zn, Mo	1948, 1949	250 ft shaft, prospect holes	in 1948 - 80 tons Cu-Ag ore	carbonate-hosted Pb-Zn	Peterson (1976), Strongin (1957)
Luna (Lobo nos 1-4, Eaves, Continental)	22 28S 14W	31° 51' 41", 108° 15' 34"	Cu, Pb, Zn, Mo	1930, 1940s	shaft 150 ft deep, 50 ft adit	26 tons ore averaging 15-20% Pb, 16% Zn, 4-5 oz Ag, 1% Cu	carbonate-hosted Pb-Zn	Peterson (1976), Strongin (1957), NMBMMR file data
Mairland	SW34 28S 14W	31° 49' 31", 108° 15' 58"	Cu, Pb	1950	inclined shaft 60 ft deep	1 carload of Pb-Ag ore	carbonate-hosted Pb-Zn	Strongin (1957)
Prospects N30E of Last Chance	SW3 28S 14W	31° 49' 30", 108° 16' 47"	Pb, Zn	none	a few shallow holes	none	carbonate-hosted Pb-Zn	Strongin (1957)
Quartz prospect	NW9 29S 14W	31° 48' 19", 108° 16' 24"	Pb	none	3 prospect pits	none	carbonate-hosted Pb-Zn	Strongin (1957)
MINE NAME (ALIAS)	LOCATION	LATITUDE, LONGITUDE	COMMODITIES	YEARS OF PRODUCTION	DEVELOPMENT	PRODUCTION	TYPE OF DEPOSIT	REFERENCES
Queen's Taste (Lead Queen)	NE26 28S 14W	31° 50' 36", 108° 14' 04"	Cu, Pb, Zn, Mo	1930, 1931, 1937, 1949	prospect pits and shafts	a few tons of Pb-Ag ore	carbonate-hosted Pb-Zn	Peterson (1976), Strongin (1957)
Summertime	SW28 28S 14W	31° 50' 08", 108° 16' 50"	Cu, Pb, Zn, Mo	none	shaft near VE Day shaft	none	carbonate-hosted Pb-Zn	Peterson (1976)
Unknown	S 29S 14W	31° 48' 44", 108° 16' 49"	Cu, Pb	none	7 pits	none	carbonate-hosted Pb-Zn	NMBMMR file data
workings NE of Big Shiner	NW33 28S 14W	31° 49' 48", 108° 16' 41"	Cu, Pb	none	shallow inclined pits	none	carbonate-hosted Pb-Zn	Strongin (1957)

4. Methods

Remote sensing techniques are the science and technology of obtaining information about objects from a distance that takes us well beyond the limits of human capabilities (Aranoff, 2005). Remote sensing has become increasingly sophisticated, and new methodological perspectives continue with this technology (Pour et al., 2008). Different methodologies (Figure 22) and image processing techniques, such as color composites, band rationing, filtering, supervised classification, and unsupervised classification, are typically used to delineate favorable areas for further mineral exploration (Pour et al., 2008). Earth explorer (Figure 21) is the primary search interface accessing the aerial imagery interface for mapping.

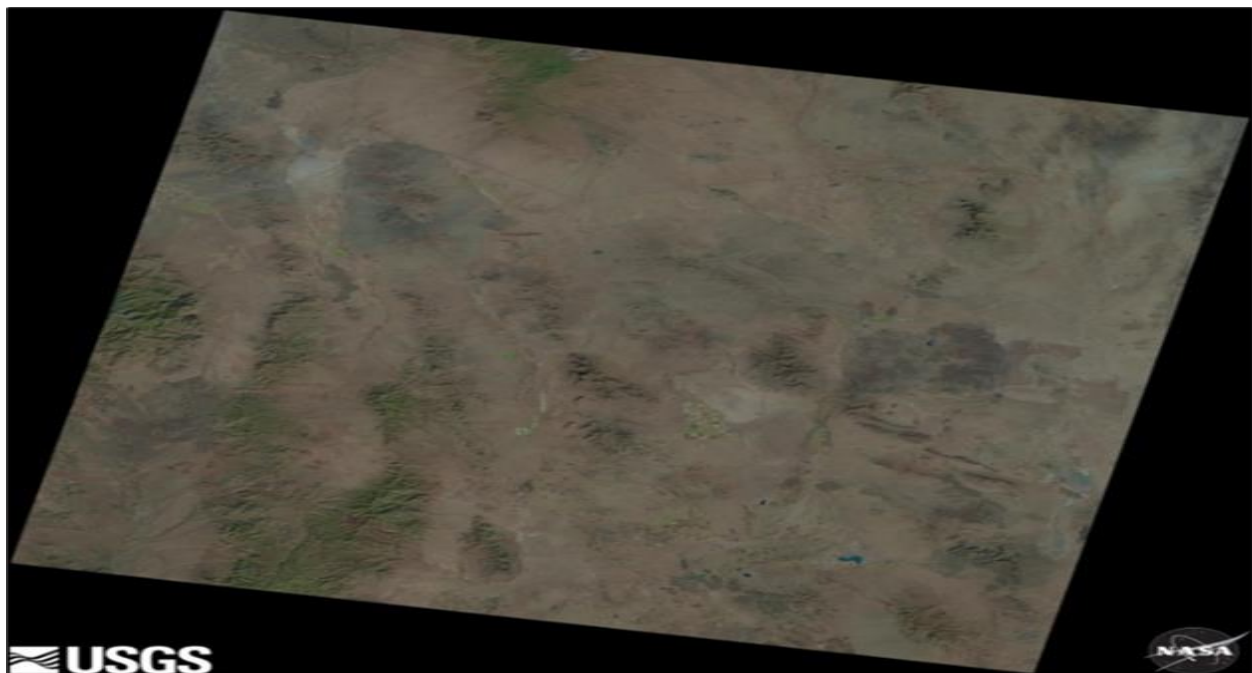


Figure 21: LC08_L1TP_034038_20140107_20170306_01_T1, Natural Cover Image Landsat 8 image,) (<http://earthexplorer.usgs.gov>).

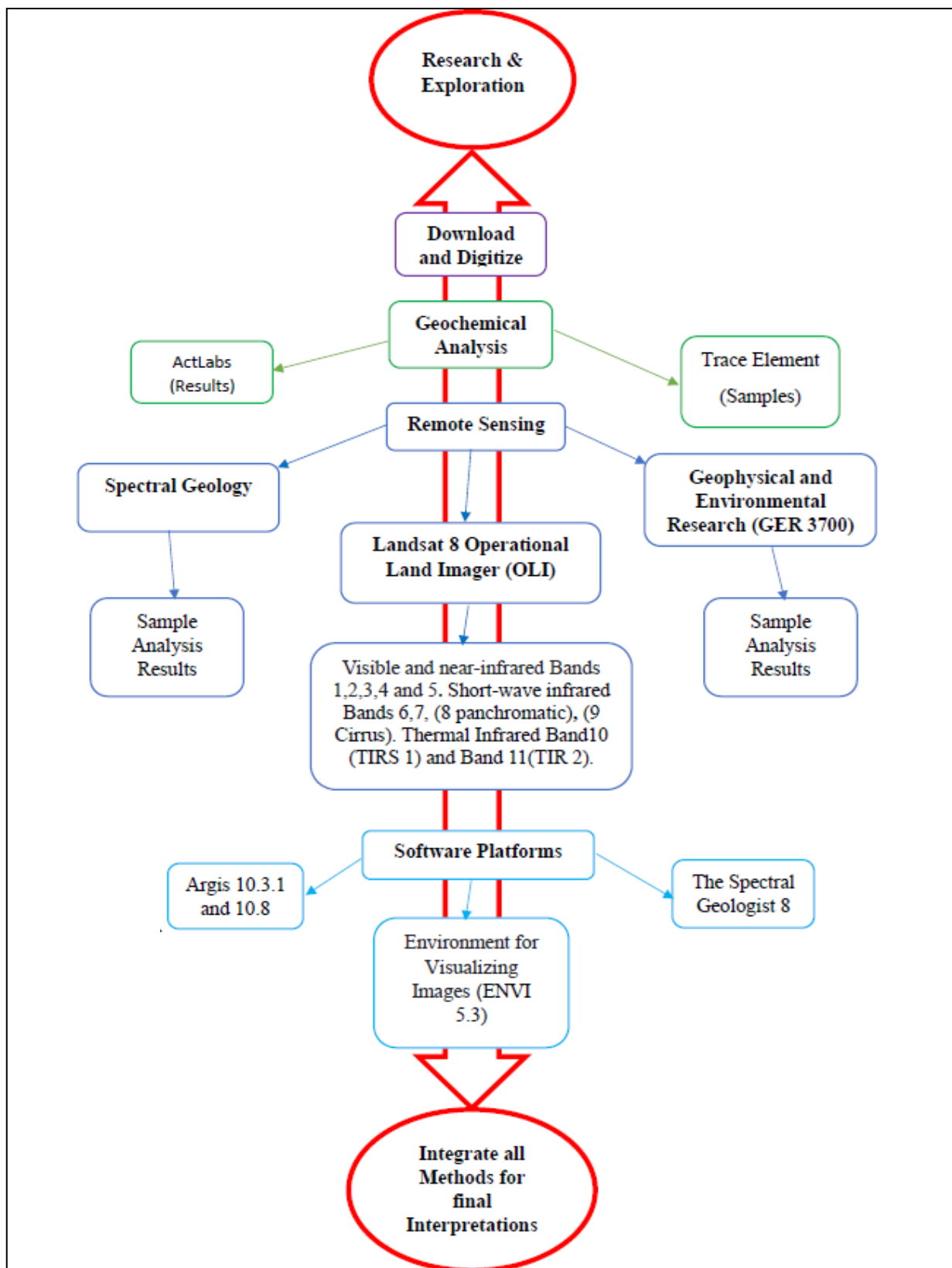


Figure 22: Methodology Flow Chart of all methods used for this thesis. For integration and a final interpreted/conclusion on a GIS platform.

4.1 Spectral Geology

Spectral Geology is a method used for exploration and interpretation, where spectral variation results from different components, the degree of ordering, mixtures, and the size of the grain from various rocks and minerals (Huntington, 1996). This method measures and analyzes sections of the electromagnetic spectrum to recognize spectrally distinct and physically significant features of different rock types and surface materials, mineralogy, and alteration signatures (Geosciences Australia, 2014). The instruments in the remote sensing satellite (Land sat 8 (OLI)) (Figure 24) retrieves global spectral data. Spectral data are

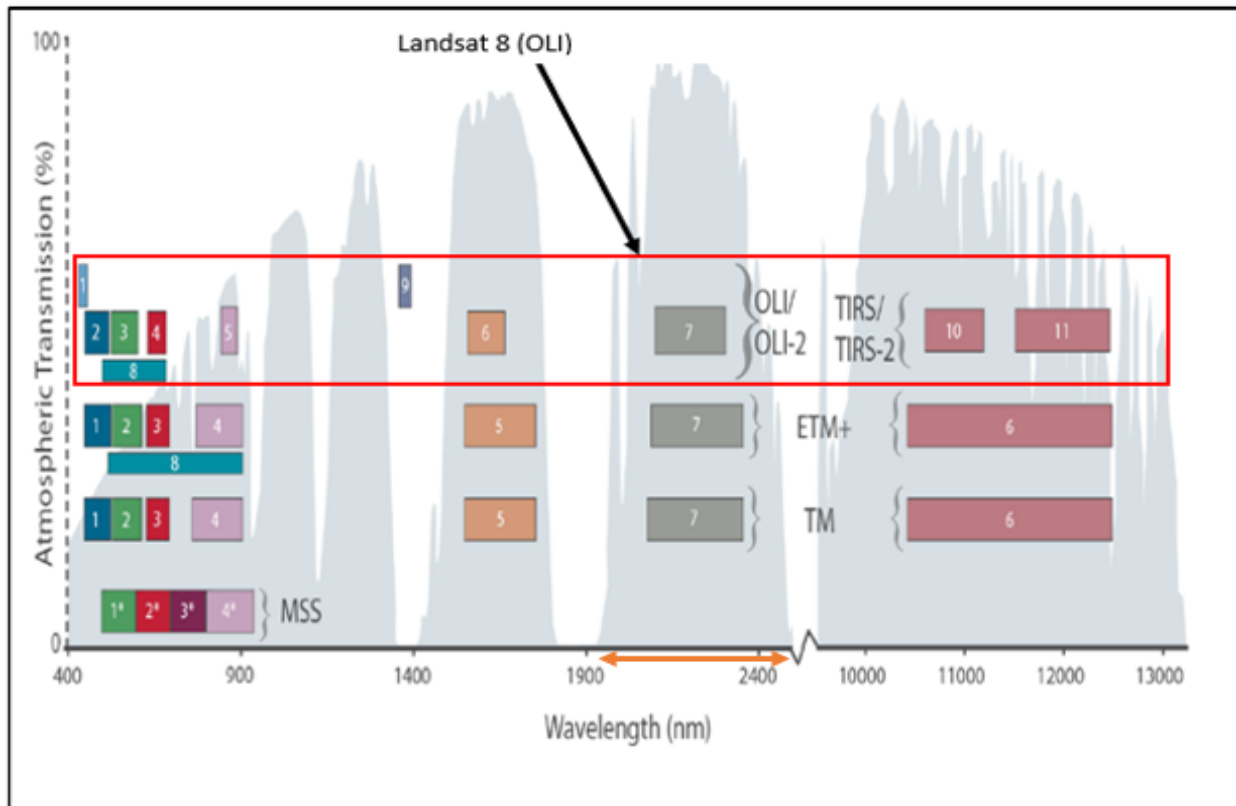


Figure 23: A comparison graph of L8 spectral bands and wavelength to that of L7 ETM+. Spectral Bands and Wavelengths for Landsat Sensors modified (from Inhel 2019, p. 50).

measured using spectral sensors (Figure 23), which register either solar or artificially offered radiation reflected from the surface of materials. Because many materials absorb radiation at precise wavelengths (Figure 23), it is possible to identify them in a spectral curve by their characteristic absorption features (Kruse, 1994). The wavelength ranges most suitable for the discrimination of iron oxides are represented in Table 5a. A spectroradiometer (e.i. GER 3700) is used for the spectral signature wavelength analysis from the Apache Hills samples. The same examples are sent to Actlabs for ICP-MS trace element analysis. The Peterson (1976) geochemical assay results (Table 6) are reviewed and integrated into ArcGIS for iron mineral mapping. The SWIR wavelength area between 2000 and 2500 nanometres (nm) (Figure 23, band seven, orange arrow) is particularly appropriate for mineral plotting. The 2000-2400 nm wavelength region can show many absorptions features characteristic of certain hydroxyl (Figure 55e), carbonate-bearing minerals, and mineral groups distinctive of hydrothermal alteration. (Thomas and Walter, 2002). The use of spectroscopy makes it possible to create accurate maps of surface mineralogy, relative abundances, and mineral assemblages. Mapping techniques can identify individual species of iron minerals, providing detailed information about hydrothermal mineralization and alteration zones (Thomas and Walter, 2002).

Identifying surface mineralogical composition using remote sensing (e.g., Landsat 8 (airborne)) presents an opportunity for exploration geologists seeking refined vectors to potential ore-bearing hydrothermal systems (Huntington, 1996). Samples from the research area are part of a reconnaissance effort to isolate the spectral signatures of the examples collected and validate the presence of ferric and ferrous irons. The GER 3700 spectroradiometer from the Geophysical and Environmental Research Corporation (GER), in conjunction with The Spectral Geologist software 8 (TSG) and the spectral library 2007 (USGS), aids in identifying resembling wavelengths and reflectance.

4.1.1 Landsat 8 Operational Land Imager & Instruments (OLI) (Spaceborne)

The OLI sensor on the Landsat 8 satellite, launched on February 11, 2013, extends the legacy of the Landsat multispectral remote sensing program by adding several significant enhancements that improve spectral mapping capabilities (Rockwell, 2021). Nine ratio-based spectral indices (Table 5b) generated exploit diagnostic absorption feature characteristics from accredited spectral libraries (e.g., spectral library 06a and The Spectral Geologist 8) that highlight Iron Oxide (II) (III) minerals. A new band in the visible (VIS) wavelength region is designed for coastal and aerosol studies. It is ideally suited for more detailed discrimination of iron-bearing mineral species since many iron minerals have diagnostic spectral absorption features (Figure 63) in this wavelength region (Rockwell, 2021).

Landsat 8 satellite contributed to an uninterrupted multispectral record of the Earth's land surfaces since 1972 (Inhel, 2019). Landsat 8's spaceborne data format files, combined with the USGS archival distribution systems, including the metadata (Table 4) and data processing techniques, require information to render usable images in a GIS format (e.g., ArcMap). (Inhel, 2019). Landsat 8 (OLI) (Figure 24) carries a two-sensor payload, the OLI, built by BATC, and the TIRS, made by NASA (GSFC) (Inhel, 2019). Both sensors offer technical advancements over earlier Landsat instruments. The spacecraft is referred to as the L8 Observatory with two integrated sensors. The two sensors' image data (Figure 24) represent nine visible, near-infrared, shortwave infrared bands and two longwave thermal bands (Inhel, 2019). Table 3 shows the Landsat 8 OLI and TIRS bands (μm) 1 through 11, which include the band names, wavelengths, and spatial resolution.

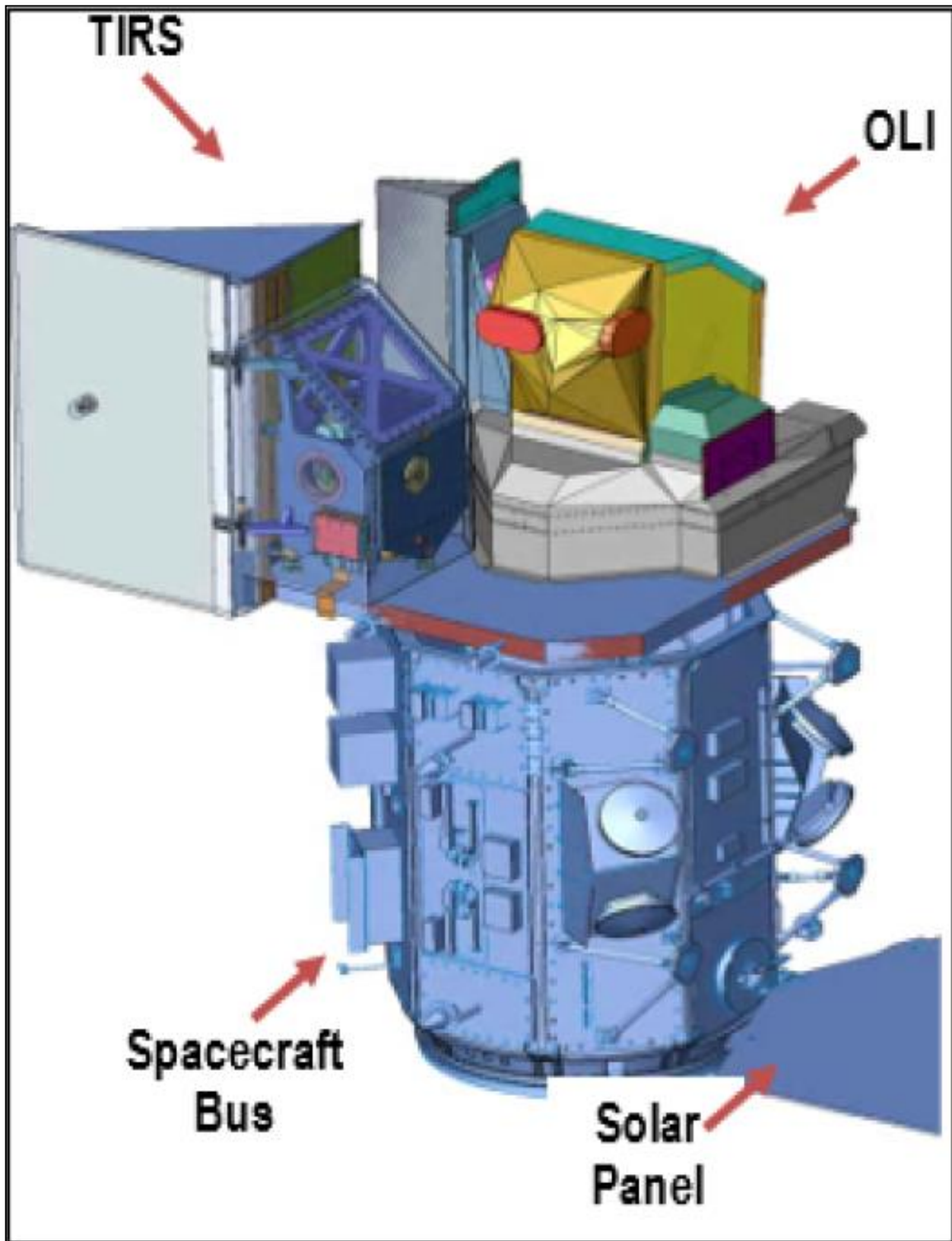


Figure 24: Illustration of Landsat 8 observatory and instruments (from Inhel 2019, Figure 2-1 p. 8).

Table 3: Landsat 8 Bands (μm) (from Inhel 2019, Table 2-1, p.10)

Landsat-8 OLI and <i>TIRS</i> Bands (μm)		
30 m Coastal/Aerosol	0.435 - 0.451	Band 1
30 m Blue	0.452 - 0.512	Band 2
30 m Green	0.533 - 0.590	Band 3
30 m Red	0.636 - 0.673	Band 4
30 m NIR	0.851 - 0.879	Band 5
30 m SWIR-1	1.566 - 1.651	Band 6
<i>100 m TIR-1</i>	<i>10.60 – 11.19</i>	Band 10
<i>100 m TIR-2</i>	<i>11.50 – 12.51</i>	Band 11
30 m SWIR-2	2.107 - 2.294	Band 7
15 m Pan	0.503 - 0.676	Band 8
30 m Cirrus	1.363 - 1.384	Band 9

4.1.2 Geophysical and Environmental Research (GER 3700)

Field-based reference sampling with a non-imaging spectroradiometer has become prevalent for testing field-collected rock samples. Several airborne, spaceborne, and laboratory imaging spectrometers are available for remote sensing (e.g., Landsat 8 OLI and GER 3700) (Schaepman and Dangel, 2000). The laboratory spectroradiometer utilized for sample testing is the GER3700 SN 3700-1002 (Figure 25) manufactured by the Geophysical and Environmental Research



Figure 25: The spectroradiometer used in this thesis is a GER3700 SN 3700-1002 manufactured by Geophysical and Environmental Research Corporation.

GER 3700	
Spectral Range	350 nm to 2500 nm
Channels	704
Linear Arrays	(1) 512 Si (1) 128 PbS (1) 64 PbS
Bandwidth	1.5 nm: 6.5 nm: 9.5 nm:
	350 nm to 1050 nm 1050nm to 1900nm 1900nm to 2500 nm
Scan Time	50 ms and up (selectable)
FOV	3° standard, 10° option 23° option with fiber optic
Head Size	320 mm x 335 mm x 320 mm 12.5" x 13.75" x 4.5"
Weight	6.3 kg, 13.8 lbs.
Battery Type	(1) 12 VDC
Battery Life	4 hours
Digitization	16 bit
Wavelength Repeatability	+0.1 nm
Noise Equivalent Radiance	0.5 s integration time 400 nm: $2.2 \times 10^{-9} \text{ W} \cdot \text{cm}^{-2} \cdot \text{nm}^{-1} \cdot \text{sr}^{-1}$ 700 nm: $1.6 \times 10^{-9} \text{ W} \cdot \text{cm}^{-2} \cdot \text{nm}^{-1} \cdot \text{sr}^{-1}$ 900 nm: $6.2 \times 10^{-9} \text{ W} \cdot \text{cm}^{-2} \cdot \text{nm}^{-1} \cdot \text{sr}^{-1}$ 1500 nm: $1.1 \times 10^{-8} \text{ W} \cdot \text{cm}^{-2} \cdot \text{nm}^{-1} \cdot \text{sr}^{-1}$ 2200 nm: $1.1 \times 10^{-8} \text{ W} \cdot \text{cm}^{-2} \cdot \text{nm}^{-1} \cdot \text{sr}^{-1}$
Maximum Radiance Levels	13 ms integration time 700 nm: $1.5 \times 10^{-4} \text{ W} \cdot \text{cm}^{-2} \cdot \text{nm}^{-1} \cdot \text{sr}^{-1}$
Radiometric Calibration Accuracy (Traceable to NIST)	400nm : ± 5% 700nm : ± 4% 1000nm : ± 5% 2200nm : ± 7%
Dark Current Correction UV-NIR-SWIR	automatic
Spectrum Averaging	selectable
Humidity	10 to 90% RH (non-condensing)
Temperature	-10° to 50°C
Sighting	Laser

Figure 26: Manufacturer specifications of the GER3700 Spectro-radiometer at the DEERS building in Dr. Hurtado's Geophysics lab room 301.

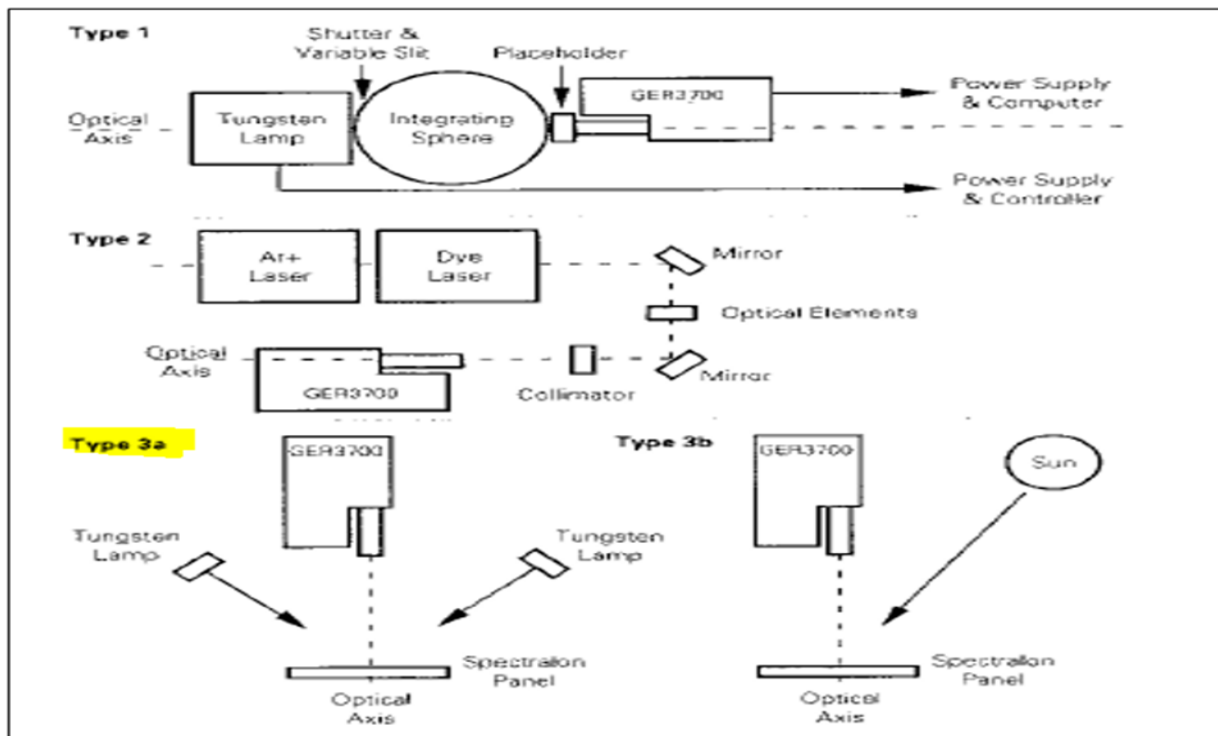


Figure 27: Type 3 measurements were performed to measure the FOV. The illuminating source is a tungsten halogen lamps Type 3a Configuration setup (Type 3a, yellow) of the GER 3700 at the DEERS building in Dr. Hurtado's Geophysics lab room 301(modified from Schaepman and Dangel, 2000 Figure 1, p.3757).

Corporation. The laboratory spectroradiometer provides spectral reference data as wavelength and reflectance results from the mine dump rock samples offered. The spectral signatures from the specimens assist in distinguishing between different spectral images that may constitute mineral or economic importance and distinctively differentiate from surface cover and mineral alterations, particularly in an arid climate with extensive rock exposure. In this case, the collected rock specimens for spectral analysis are initially large rocks. The assessment method for the GER 3700 is a single field of view (FOV) of 3° standards, 10° optional, and 23° option with fiber optic (Figure 26). The spectroradiometer operates in the spectrum's visible, near-infrared, and shortwave-infrared regions. The spectral wavelength range is 350–2500 nm (Figure 26). Three detectors measure the radiance; the first is a silicon (Si) line array with 512 elements. The other two detectors are lead-sulfide (PbS) line arrays with 128 and 64 elements, respectively. (Schaepman and Dangel, 2000). The cut-off wavelength for the (Si) detector can be programmed to be 980–1030 nm; the transition between Pb S1 and Pb S2 is nearly 1900 nm. The resultant setup has 512 bands covering the 400–1000 nm range, 128 bands covering the 1000–1900 nm range, and 64 bands covering the 1900–2500 nm range. In total, 704 spectral band channels are recorded simultaneously (Figure 26) (Staenz et al., 1995). The GER 3700 is adjusted by the National Institute of Standards and Technology (NIST). A spectral panel is a diffuse reflectance

standard calibrated by the NIST (Schaepman and Dangel, 2000). The uncertainties associated with these measurements depend on the sampling strategy (e.g., sampling scheme and sample size) and the ambiguities related to the Spectro radiometric measurements (Schaepman and Dangel, 2000). The rocks are pulverized to fine dust and sieved through a USA Standard 100-micron mesh. Spectral analysis is completed with the sieved samples through the GER 3700. The laboratory configuration of the GER 3700 for the sample analysis is type 3a type (Figure 27). The data results from this spectroradiometer are administered through the Spectral Geologist 8 for further spectral signature mineral identification and administered through the Spectral Geologist 8 for additional spectral signature mineral identification.

4.1.2.1 The Spectral Geologist 8 (Software)

The Spectral Geologist 8 represents the combination of years of research into spectral data analyses in a wide range of mineral exploration and mining environments worldwide and in academia (spectralgeo.com.au/the-spectral-geologist-TSG-software). The program revolutionizes how geological spectral data are processed and analyzed, which means that the spectral data can easily be interpreted in the project context and contributes directly to understanding the alteration in the project area. The software generates value, adding multi-parameter characterization results for infrared-active minerals to support the multi-

disciplinary endeavors of geoscientists across exploration and mining (spectralgeo.com.au/the-spectral-geologist-TSG-software). Spectral Geologist 8 organizes all the spectral data from 10s to 10,000s of file arrangement allowing the data and analysis results from a single project to be stored and analyzed (spectralgeo.com.au/the-spectral-geologist-TSG-software). They are integrating the software platform with other methods to decipher the characteristic wavelength and reflectance signatures of the data provided by the spectroradiometer (GER 3700). The results should reflect the presence of ferric and ferrous irons, as seen through Landsat 8 (OLI). The band ratio index indices and RGB combination are utilized on an ArcMap 10.8 and ENVI 5.3 GIS platform to display the presence and location of these minerals. The results should concur with the geochemical analysis done through Actlabs from the samples collected and the geochemical analysis completed by Strongin (1956) and Peterson (1976) surrounding the Apache Hills concerning the presence of the iron mineral mapped. A comparative study reviews the spectral signature wavelength results from the GER3700, side-by-side with the spectral signatures composed in the Spectral Geologist 8 spectra archive files and the spectral library 2007 (USGS).

4.1.2.2 The Spectral Library 2006 (USGS) (Add-On ENVI 4.8)

The spectra applications of the USGS 2006 library are convolved to the selected spectrometer and imaging spectrometer sampling and band passes and resampled to fixed broadband multispectral sensors. The library collects spectral data measured with laboratory, field, and airborne spectrometers. Spectro-analysis is essential for interpreting spectral (e.g., airborne and laboratory) data gathered in the area, aircraft, or spacecraft. The instrument the USGS utilizes determines the wavelengths of ultraviolet to the far infrared Range from (0.2 to 200 microns [μm]). The file format of the library is the SPECTRUM Processing Routines (SPECPR) data format (Kokaly R.F. et al., 2017). This file format is an [add-on] provided by the USGS website and is integrated into an ENVI software program for spectral signature wavelength visualization. The spectral library 2006 format files (SPECPR) are referenced with the four different spectrometer types used to measure the spectra that depict the wavelength and reflectance spectral signatures of those sought-after minerals (e.g., Ferrous and Ferric) resulting from the GER3700 laboratory analysis. As geochemistry and previous research indicate, a spectral analytical interpretation of the samples submitted would validate the presence of ferrous (III) and ferric (II) minerals. Plotting the propagation of these minerals on a GIS platform with specific software is essential for a clear vector trend and a precise geological mapping of the minerals.

4.2 Geographical Information System (GIS) Software Platform

The geographic information systems (GIS) field started in the 1960s as computers and early quantitative and computational geography concepts emerged. Early GIS work included necessary research by the academic community. GIS allows people to create digital map layers to help solve real-world problems (esri.com/history of GIS). ArcGIS is the leading commercial geospatial software for handling and analyzing geographic data (vector and raster). It provides functionality in raster data storage and management, image processing, image visualization, and image serving over the web (Xu & Gao, 2008; Arunachalam, 2022). ArcGIS supports satellite images by offering geoprocessing tools for basic image processing. The processed image results on ArcGIS render georeferencing raster images, orthorectified images, raster overlay, zonal and hydrology images, generating pan-sharpened images and slope and shaded relief (hill-shade) images from the DEM data (Xu & Gao, 2008; Arunachalam, 2022). ArcGIS lacks advanced image processing and analysis tools for different sensors or camera models offered by other Digital Image processing (DIP) software like ENVI (Xu & Gao, 2008; Arunachalam, 2022). The raster image results using ArcGIS & ENVI software platforms show ferric and ferrous iron mineral alteration surrounding the intrusive igneous rock in the Apache Hills and Sierra Rita region.

The spatial data information is collected for geologic mapping and interpreted for potentially new (Greenfield) or continuous (Brownfield) economic mineral discovery and exploration.

4.2.1 ArcMap 10.8: (Software)

In late 1999, Esri released ArcMap 8.0, replacing ARC/INFO, an earlier command line-based GIS system for manipulating data, and ArcView, a guide-based GIS with limited capabilities. ArcMap software became an alternative mapping and analysis solution (geospatialworld.net). A geographical information system (GIS) software allows for handling and analyzing geographic information by visualizing geographical statistics through layer-building maps like geological mineral mapping. The software makes maps, analyzes data, and shares (geospatialworld.net).

ArcMap incorporates content from Esri's data library, and a user can customize symbols and basement maps to personalize geological maps (geospatialworld.net). Spatial analysis tools available in the ArcMap toolbox (e.g., map algebra, raster calculator) and map styles are accessible as an add-data feature from GIS basement data or GIS online to assist in refining data. The maps created from the compiled digital data and the raster images can then tell a digital data story in relationship with the airborne observable mineralization of the regional area. The raster data downloaded from the USGS website is added to ArcMap, and

the image is further altered. The layer properties symbology in the raster image or shapefile are altered to visualize the bands' combination. The alterations made to understand different perspectives on the resulting images reveal new vectoring patterns from a ground surface that may display geological mineral alterations surrounding the intrusive igneous body. There may be surface features not previously seen or known to interpret further the geology or physiology of an extensive arid regional area. Georeferencing the downloaded raster images and digital data transforms longitude and latitude into points on ArcMap. True color images are the composite result of three visual primary grey images initially appearing when uploaded to ArcMap. Color images are composed of three primary colors (i.e., blue, green, and red). False color images, mainly color infrared images, have specific advantages over actual color. It is easy to recognize different geological units using true-color images. Various combinations of false color band scans highlight many features ranging from mineralogy to moisture changes (Banerjee et al., 2019). The main advantage of true color images is that it is easy to recognize units in areas where the stratigraphy is known and increases the interpreter's ability to identify rock units where the geologic section is unknown (Banerjee et al., 2019). Landsat 8 OLI image capabilities, which utilize some band numbers for rock discrimination of alteration zones based on color intensity

variations, such as RGB Band combinations, eliminate most atmospheric attenuation like haze and backscattering (Banerjee et al., 2019).

Band ratios can reduce the effect of environmental artifacts. Current research suggests that iron-rich minerals or other minerals associated with hydrothermal processes can be delineated using band ratios beneficial for mapping minerals. Several bands have defined various rock-mineral types (Banerjee et al., 2019). Color variations can be seen in different band ratio results, which are the primary keys to identifying a hydrothermally altered zone. The altered zones illustrate typical mineral alterations using band ratios that enhance lithological features. The band indices 4/2 are visible as a combined image composite of iron (II-III) (Figure 40), iron oxide 6/5 (Figure 46), hydroxyl-bearing rock (Figure 55e), and ferrous mineral (B7/B5+B3/B4) (Figure 43). Processing the Landsat 8 (OLI) images generated through remote satellite sensors is often affected by distortions resulting from solar and atmospheric effects and distortion associated with differences in the sensor's calibration. Radiometric calibration is a common term used in remote sensing that refers to converting digital numbers (DNs) recorded by satellite sensors into radiance, reflectance, or brightness temperature at the sensor. Adding raster images from earth explorer to a GIS platform such as ArcMap creates black-and-white raster imagery that has to be modified.

Table 5a: Landsat 8 Operational Land Imager (OLI) Nand Indices names, general and specific formulas Astrid's (*) denotes repeated band formula and ratios.

Landsat 8 Operational Land Imager (OLI) Band Indices			
Numbers	Name	General Formula	Specific Formula
3	Alteration Fe3+	1600:1700 / 2145:2185	*SWIR1/SWIR2
39	Laterite Fe3+	1600:1700 2145:2185	*SWIR1/SWIR2
19	Ferrous Iron, FEO Fe2+(II)	2145:2185 / 760:860 + 520:600 / 630:690	*SWIR2/Near Infrared+Green/Red
22	Ferrous Iron, FEO Fe2+(II)	2145:2185 760:860 + 520:600 630:690	*SWIR2/Near Infrared+Green/Red
21	Ferric Oxides	1600:1700 / 760:860	SWIR1/ Near Infrared (B6/B5)
20	Ferric Iron, Fe3+	630:690 / 520:600	Red/Green (B4/B3)
23	Ferrous Silicates	2145:2185 1600:1700	SWIR2/SWIR1
26	Gossan	1600:1700 / 630:690	SWIR1/Red (B6/B4)
78	Simple Ratio Red/Blue Iron Oxide (II, III)	RED/BLUE (B4/B2)	General Iron Oxide Ratios (II-III) Red/Coastal
<i>Index Data Base (remote sensing indices) www.indexdatabase.de/db/is.php?sensor_id=168 (Astrid's)*repeated band ratios*</i>			

Table 5b: Landsat 8 Operational Land Imager (OLI) Band Indices Specific Formulas and Reference Source (www.indexdatabase.de/db/is.php?sensor_id=168).

Numbers	References
3	Volesky, J.C.; Stern, R.J.; Johnson, P.R (2003)
39	Kalinowski, Aleks; Oliver, Simon (2004)
19	Rowan, L.C.; Mars, J.C (2003)
22	Rowan, L.C.; Mars, J.C (2003)
21	Henrich, V. et al. (2011)
20	Rowan, L.C.; Mars, J.C (2003)
23	Henrich, V. et al. (2011)
26	Volesky, J.C.; Stern, R.J.et al., (2003)
78	Hewson, Rob D. et al. (2001)

DNs are the initial pixel values we see when loading satellite images in geospatial software. Satellite images are not directly measured to actual radiometric measurements it is due to two main reasons: (1) to reduce the size of computer memory required to store the measurements and (2) to provide data with adequate precision (Knudby, 2021; Arunachalam et al., 2022). The atmospheric condition affects the DN values of Landsat data. Radiometric calibration employs algorithms and processes that improve the quality of the Landsat data (Mishra et al., 2014). The Landsat 8 data users handbook provides more information on radiometric characterization.

It provides algorithms to convert DN to a-sensor spectral radiance, top-of-atmosphere (ToA) reflectance, or brightness temperature (Arunachalam et al., 2022). The Conversions of DN's to physical units by radiometric calibration and atmospheric correction applied to bands 1 and 7. Ihlen (2019) describes the Landsat images handled in parts of absolute radiance using 32-bit floating-point calculations. These values convert to 16-bit number values in the finished Level 1 product. They can then be converted to spectral radiance using the radiance scaling factors offered in the metadata file:

$$L\lambda = ML * Q_{cal} + AL$$

Where:

$L\lambda$ = Spectral radiance (W/ (m² * sr * μ m)).

ML = Radiance multiplicative scaling factor for the band (RADIANCE_MULT_BAND_N from the metadata).

AL = Radiance additive scaling factor for the band (RADIANCE_ADD_BAND_N from the metadata) (Ihlen, 2019).

Like the conversion to radiance, the 16-bit integer values in the Level 1 product can also be converted to TOA reflectance.

The following equation is used to convert Level 1 DN values to TOA reflectance (Ihlen, 2019):

$$\rho\lambda' = M_p * Q_{cal} + A_p$$

Where:

ρ_{λ}' = TOA Planetary Spectral Reflectance, without correction for solar angle (Unitless).

M_p = Reflectance multiplicative scaling factor for the band (REFLECTANCE_W_MULT_BAND_N from the metadata) (Ihlen, 2019).

A_p = Reflectance additive scaling factor for the band (REFLECTANCE_ADD_BAND_N from the metadata).

Q_{cal} = Level 1 pixel value in DN.

The ρ_{λ}' is not true TOA Reflectance because it does not contain a correction for the solar elevation angle. This correction factor is left out of the Level 1 scaling at the users' request; some users are content with the scene-center solar elevation angle in the metadata, while others prefer to calculate their own per-pixel solar elevation angle across the entire scene. Once a solar elevation angle is chosen, the conversion to true TOA Reflectance follows (Ihlen, 2019):

$$\rho_{\lambda} = \frac{\rho_{\lambda}'}{\cos(\theta_{SZ})} = \frac{\rho_{\lambda}'}{\sin(\theta_{SE})}$$

Where:

$\rho\lambda$ = TOA planetary reflectance θ_{SE} = Local sun elevation angle; the scene center sun elevation angle in degrees is provided in the metadata θ_{SZ} = Local solar zenith angle; $\theta_{SZ} = 90^\circ - \theta_{SE}$ (Ihlen, 2019).

The ArcMap 10.8 software spatial analysis tool (map algebra) converts bands 1-7 using the calculations presented. The metadata used for the calculations can be observed in Table 4. The raster images continue to be changed through the raster properties and symbology features. Once the raster images were altered, new black/white raster image results were created. The final results will be discussed further.

Other software, such as ENVI 5.3, in conjunction with ArcMap 8.0, collaborate well in analyzing raster imagery. They make for a clear distinction between the localization of the minerals and the band ratio indices created on GIS platforms. Peterson's (1976) assay report (Figure 28) describes the locality of the core samples analyzed as a township and the Range from which they were extracted. This report gives geographical context using ArcMap 10.8 to Peterson's (1976) descriptive area of the same geochemical analysis for accurate visual confirmation of the minerals described.

4.2.2 Environment for Visualizing Images (ENVI): (Software)

ENVI's geospatial software and Esri's ArcGIS platform work well using geospatial data obtained by Landsat 8. With ENVI software, a geologist can generate visual mineral maps. Professional analysts can get accurate information from geospatial imagery created by the software. The software is a widespread industry standard for image processing and analysis. It lets GIS users seamlessly access and analyze imagery to solve critical problems confidently (L3Harris Geospatial Solutions, Inc. 2022). ENVI is used to create geospatial imagery using the band ratio indices to plot potential mineral alteration concentric zone (e.g., Ferrous and Ferric), propagation patterns, and surface mineral alteration transport on multiple GIS platforms. Extending ArcGIS with ENVI analytics, a geologist can derive quantitative, actionable results from remotely sensed data and use the information to make a scientific interpretation based on the available statistics of a given study area. Once converted to an appropriate file type (e.g., raster or shapefile), the ENVI analytical digital data uploads to any ArcGIS environment, and the results can be displayed directly from ArcMap. (L3Harris Geospatial Solutions, Inc. 2022).

4.3 Geochemical Analyses

Determining elemental and isotopic compositions of geological samples is necessary for achieving dynamic, reproducible, and accurate analytical results. It

must be a prerequisite for successful mineral exploration and basic geochemical and geochronological studies (Balaram et al., 2022). Sample preparation is critical in the geochemical analysis and complete sample dissolution for accurate and precise data for geological materials. During a rock analysis, sample digestion involves steps from simple dilution to partial or total digestion, which is essential and is a regulating dynamic for achieving reproducible and accurate analytical results. A geochemical analysis determines the proportion of metallic (Cu, Pb Zn, Au, Ag, etc.) or nonmetallic (Fl, S, P, etc.) elements in a sample. It is commonly referred to as an assay (gov.nl.ca/iet/mines/pro prospector/matty-mitchell/assay-geochemical/). The sample material chemically analyzed included in this research are rocks collected at specific areas known for mines (Figure 37). The assay results are labeled by the location of the mine dump (Figure 36) where the samples were collected. Lab analyses like those done at Activation Laboratories Ltd. (Actlabs) provide single and multi-element analyses through various methods.

For this study, the method selected for the rock analysis is the ICP-MS (Inductively Coupled Plasma Mass) Spectrometer. A technique most applied for these studies and expected results for mineral identification. In this process, rock samples are crushed, powdered, fused, or digested in acid and then analyzed. Whole rock analysis defines a total determination of significant element concentrations typically in rock samples. Elements are expressed as common

oxides of each component (i.e., SiO₂, Al₂O₃, CaO, Fe₂O₃, K₂O, MgO, MnO, Na₂O, P₂O₅, TiO₂). The analyses also include measuring all volatile phases' concentration by loss on ignition (LOI). These volatile phases could include water, sulfur, and carbon dioxide (gov.nl.ca/iet/mines/pro prospector/matty-mitchell/assay-geochemical/). Geochemical analyses provide a cost-effective brownfield exploration method in searching available mine sites for additional deposits. The rock samples from Apache Hills mines were prepped, crushed, meshed to 100 microns, processed, and sent to Activation labs for a geochemical 60+ trace element analysis.

4.3.1 Activation Laboratories Ltd (Actlabs)

Actlabs provided the geochemical analysis results for the ten crushed and meshed samples on the 14th of November, 2018. The ICP-MS package chosen for the geochemical rock analysis id Code: UT-1-0.5g Aqua Regia ICP-MS (Certificate of Analysis/Appendix). The digestion method choice is critical in interpreting the resulting data. However, the geochemical analysis report A18-17520 provides the results (ppm) for dozens of elements within the sample submitted; for this thesis, only the iron (ppm) results are mentioned for the applied methods. The iron results from samples AH-001-AH010 are georeferenced in ArcGIS. But it is not without saying that the remaining results are not significant. On the contrary, the remaining results from the Actlabs geochemical report are equally crucial for the presence of

iron alterations and the existence of a porphyry copper system. The results may reveal prominent information for future work in combination with the remote sensing methods for further interpretations.

5. Results

The scientific results for the thesis are part of an extensive research and multiple scientific methods project that results in mineral mapping alterations of Ferric and Ferrous irons within the local area of the Apache Hills and Sierra Rica. Those techniques include remote sensing from Landsat 8 (OLI), a geochemical analytical report provided by previous Peterson (1976), research from Strongin (1957), the use of a lab spectroradiometer (GER3700), and new trace element ICP-MS analysis results from Actlabs.

All contribute to visualizing the presence of iron mineral alterations on a GIS platform. Several samples collected (AH-001-AH-010) are sent out for a geochemical trace element analysis (Figure 37). The laboratory in-house (GER3700) and out-house (Actlabs) results are applied to the methods, referenced, identified, and validated the presence of concentration and distribution of ferric and ferrous iron minerals. The results are presented in the order shown in the methodology flow chart (Figure 22). All the ArcMap full-scale location figures that integrate the remote sensing spatial data are confined to a 1:110,000 scale size for constant consistency. A grid coordinate system on the map figures ensures a proper

and accurate location and identification of specific mine areas. Previous research assay results from Peterson (1976) from the Apache Hills are offered as a Section, Township, and Range. A Section, Township, and Range grid shapefile is available through the USGS website. When the research results are integrated, it provides excellent graphical context for the presence of ferric and ferrous irons on an ArcGIS platform. Extensive research from previous publications (Strongin, 1957) describes and acknowledges the existence of iron-derived oxides and sulfides. One of the methods presented in this thesis is integrating research (prior or current) into GIS and image analysis software programs. When processed, the areal satellite (Landsat 8 OLI) remote sensing raster spatial data on GIS show different band (1-11) ratios and RGB combinations. The laboratory spectroradiometer (GER3700) results from the same samples analyzed by Actlabs Ltd. identify iron mineral wavelength and reflectance spectral signatures.

5.1 Previous, Present Modern Research & Integration Methods

A previous publication by Strongin (1957) describes iron minerals such as Hematite or Specularite (Fe_2O_3) as the most abundant iron oxide in the contact aureole—Hematite as isolated plates or groups of plates with a brown-to-black color (Strongin, 1957). Chalcopyrite (CuFeS_2) invariably accompanies Andradite-Epidote veins, appearing with other sulfides in veins cutting metamorphosed sediments, particularly at the Apache mine (Strongin, 1957). Pyrite (FeS_2) is

ubiquitous in all sediments. It has probably formed in many cases under purely thermal conditions from the reaction of iron oxide and sulfur initially present and shared in tactite veins. A common mineral associated with tactite zones is Magnetite (Fe_3O_4) (Strongin, 1957).

A geochemical analysis (Oxide %) for 8 samples (Table 6) provided by Peterson (1976) illustrates the presence of FeO and the Fe_2O_3 (Table Red-Rectangle) from selected igneous intrusive rocks collected at the Apache Hills No. 2 mining District. The Landsat 8 (OLI) remote sensing spectral raster images of selected band ratio indices (Table 5a) on a GIS platform provides a visual perspective of the distribution of these minerals. Peterson (1976) provided a detailed geographical description of the location of these minerals (Figure 29). Underlined in red are the local mine areas, the significant rock formations, the monzonite porphyry, and the geologic time, where the minerals are locally distributed. Peterson's (1976) sample (Figure 29), converted to geographic coordinates via GIS and areas Peterson (1976) describes (Figure 30, 32-33), sections 05, 08, 20, 30, 31, 33, and 34 in Township 28S and Range 14W represent an area where remote sensing and spectrometry data also detect the presence of FeO and Fe_2O_3 in the Apache Hills.

Modern methods for integrating previous research involve applying the Earth Explorer (<https://earthexplorer.usgs.gov/>) website to download and assemble public domain spatial data for remote sensing evaluation (Figure 28). The resulting spatial data images were merged in the GIS with analytical data (sections 5.1 & 5.4), creating geographically referenced raster images. Earth Explorer provides the user with several areas of interest by manually drawing out (point-point) a red polygon (square). The results from the red polygon reveal a larger grey square that encompasses the smaller red polygon, and datasets are available for download from the Landsat 8 (OLI) Collection 1 Tier 1 source (Figure 28).



Figure 28: An image containing a geographical user interface created using the USGS Earth Explorer website. The red polygon & black circle shows the desired user-selected region; the grey area is the dataset results contained in the USGS data base for Landsat 8 (OLI) for the study area of the Apache Hills-Sierra Rica, New Mexico. The search results render various data sets. The data set (red arrow) used is LC08_L1TP_034038_20140107_20170306_01_T1 (Figure 21).

Table 6: Chemical analysis of oxide percentages (FeO and Fe₂O₃ in red box) of selected igneous rocks from the Apache #2 mining District modified (from Peterson, 1976, table 3 p.20).

Table 3. Chemical analyses and norms of selected igneous rocks from the Apache No. 2 Mining District, Hidalgo County, New Mexico.

CHEMICAL ANALYSES (OXIDE PERCENTAGES)

	1	2	3	4	5	6	7	8
SiO ₂	61.18	61.52	65.26	65.50	74.63	54.00	62.08	53.91
Al ₂ O ₃	14.20	14.55	14.30	14.35	12.01	14.10	15.00	15.28
FeO	8.14	5.67	7.29	5.70	3.44	9.05	8.96	3.87
Fe ₂ O ₃	2.41	2.60	1.60	2.12	1.12	5.94	0.07	3.64
MgO	1.08	1.34	0.74	0.76	0.35	1.97	0.75	0.94
CaO	2.21	3.50	1.48	1.88	0.23	5.29	3.02	6.29
Na ₂ O	4.50	2.92	4.11	3.11	1.93	4.00	4.90	2.43
K ₂ O	4.26	3.23	4.35	4.22	5.08	2.50	4.07	7.70
TiO ₂	0.58	0.66	0.34	0.43	0.16	1.49	0.26	0.40
MnO	0.08	0.117	0.07	0.09	0.04	0.14	0.11	0.10
SrO	0.03	0.02	0.03	0.02	0.01	0.07	0.07	0.10
P ₂ O ₅	0.20	0.20	0.15	0.15	0.04	0.37	0.13	0.24
H ₂ O ⁺	0.01	1.14	0.11	0.37	0.45	0.02	0.07	0.68
H ₂ O ⁻	0.10	0.24	0.12	0.28	0.14	0.22	0.10	0.49
CO ₂	0.98	2.47	0.50	1.32	0.15	1.30	0.70	3.63
Total	99.96	100.18	100.45	100.30	99.78	100.46	100.29	99.68

1. Chapo Formation andesite (Tca), north of Apache Peak (sec. 20, T 28 S, R 14 W).
2. Chapo Formation andesite (Tca), south of the Apache Fault (sec. 5, T 29S, R 14 W)
3. Quartz Monzonite porphyry (Tqm) from the west flank of Apache Peak (sec. 31, T 28 S, R 14 W)
4. Chapo Formation, lower quartz latite member (Tcql) near middle of stratigraphic section (sec. 8, T 29 S, R 14 W)
5. Chapo Formation, upper quartz latite member (Tcqu), ash flow tuff at base of section (sec. 5, T 29 S, R 14 W)
6. Chapo Formation, basalt and andesite member (Tcba) south of the Apache Fault near middle of stratigraphic section (sec. 33, T 28 S, R 14 W)
7. Monzonite porphyry (Tm) west of the Apache Mine (sec. 30, T 28 S, R 14 W)
8. Monzonite porphyry (Tm) in endoskarn zone with sulfide mineralization at Chapo Mine area (sec., T 28 S, R 14 W)

Figure 29: Location description (Township and Range underlined in red) of the chemical analysis (Table 6) of the igneous rocks from the Apache #2 mining District modified (from Peterson, 1976, table 3 p.20).

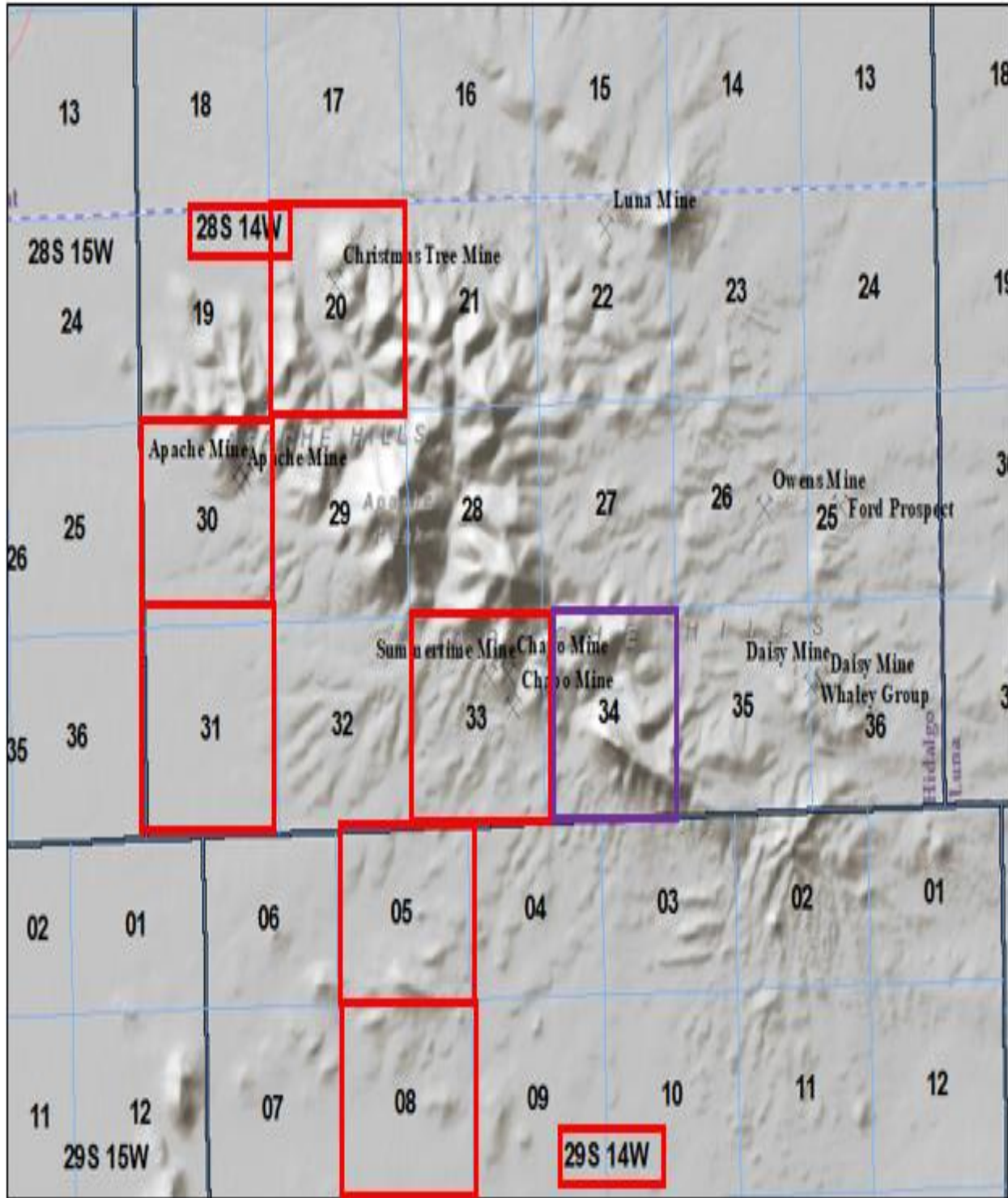
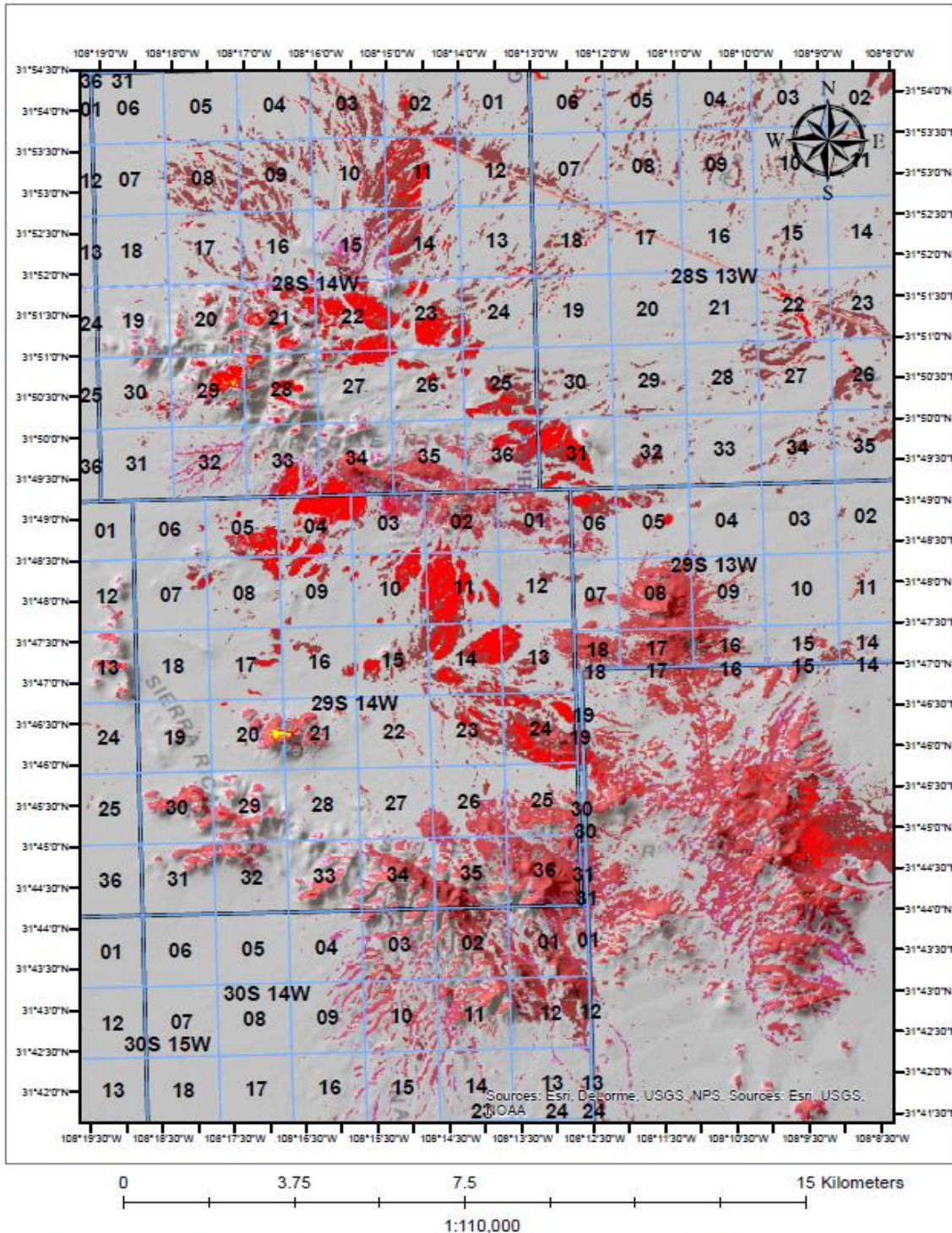


Figure 30: Apache Hills (Hillshade) consisting of an overlaid Section, Township 28S and 29S, and Range 14W grid blocks (Red blocks) (purple block 34 and red block 33 speculated section of sample 8) as described by Peterson (1976) followed with the local (MRDS) mines in the area. No Remote sensing data is provided in this illustration.

Apache Hills, Hidalgo County, New Mexico



Section, Township and Range (Ferric and Ferrous Irons)

Figure 31: Section, Township, and Range integrating Remote sensing results for Ferric and Ferrous Irons to complement a formal visualization of Peterson's (1976) geochemical results of iron mineral data location.

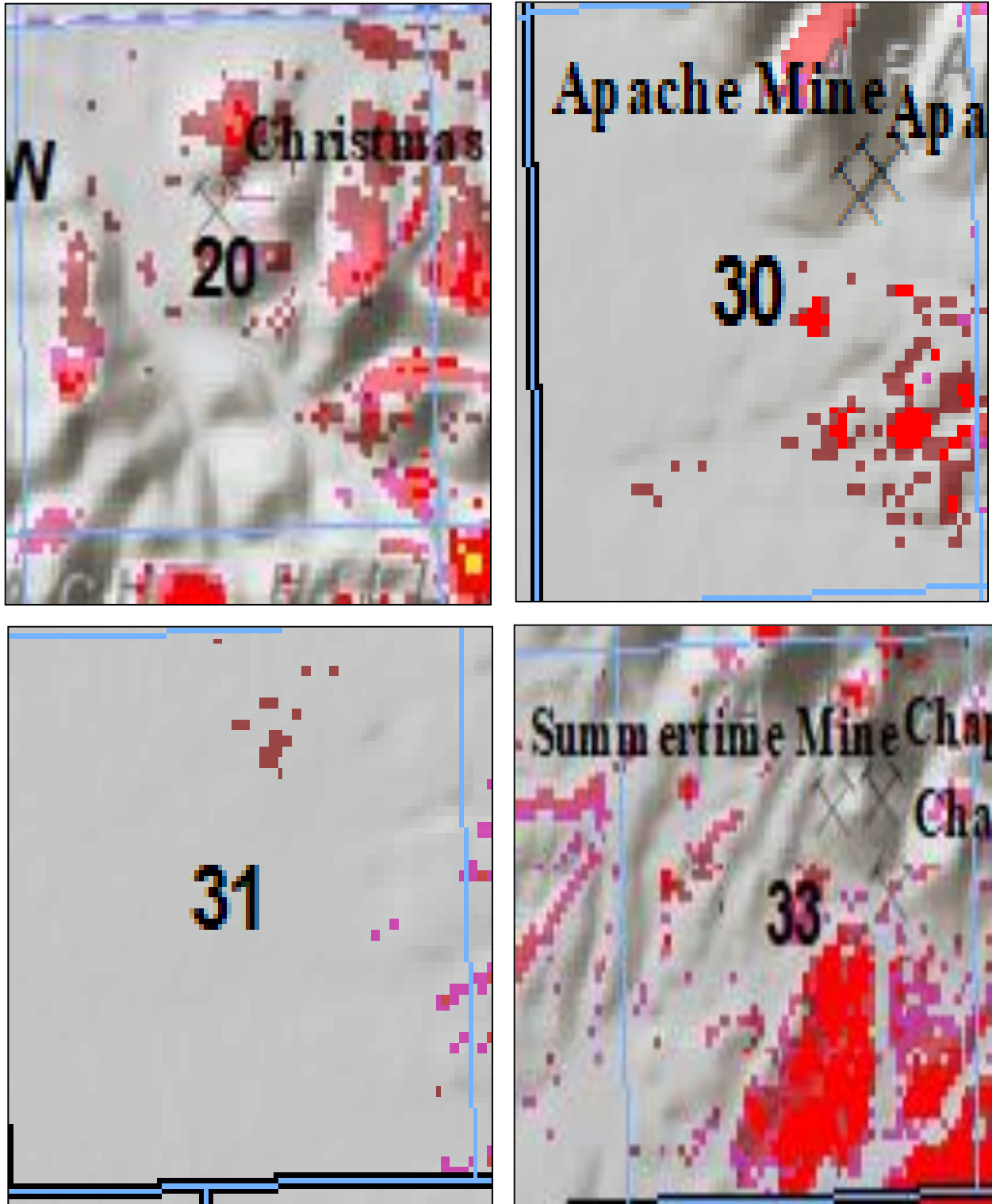


Figure 32: Sections 20, 30, 31, and 33 from Township and Range T 28 S, R 14 W. (Peterson (1976) Table 3 p.20) geochemical analysis locations that are georeferenced on ArcGIS for reference, visualization, identification, and validation of the presence of Ferric and Ferrous Irons by integrating remote sensing band ratio data results of the mapped minerals.

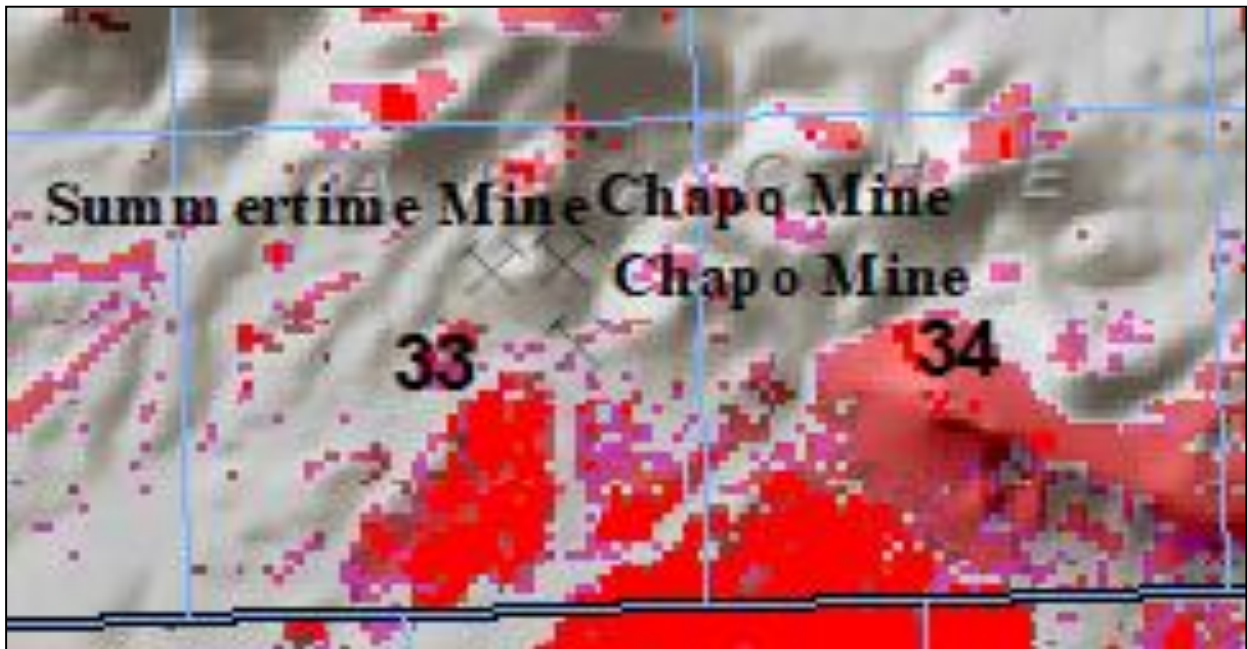
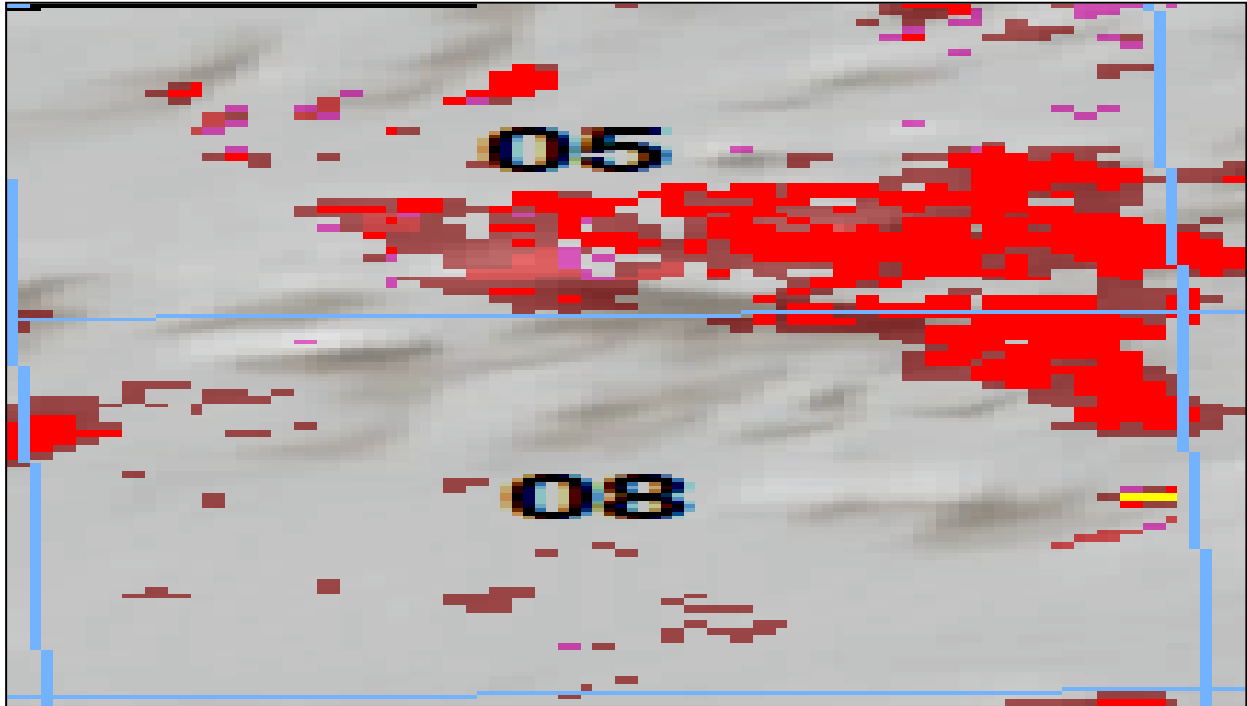


Figure 33: Sections 5 and 8 from Township and Range T 29 S, R 14 W. (Peterson (1976) Table 3 p.20) geochemical analysis locations that are georeferenced on ArcGIS for reference visualization, identification, and validation of the presence of Ferric and Ferrous Irons by integrating remote sensing band ratio data results of the mapped minerals. Sections 33 and 34 from Township and Range T 28 S, R 14 W location is speculated based on the information given by Peterson (1976). The section location results for sample eight are missing, but the Township and Range and the mine name is given (Chapo Mine). The remote sensing data results, however, are accurate.

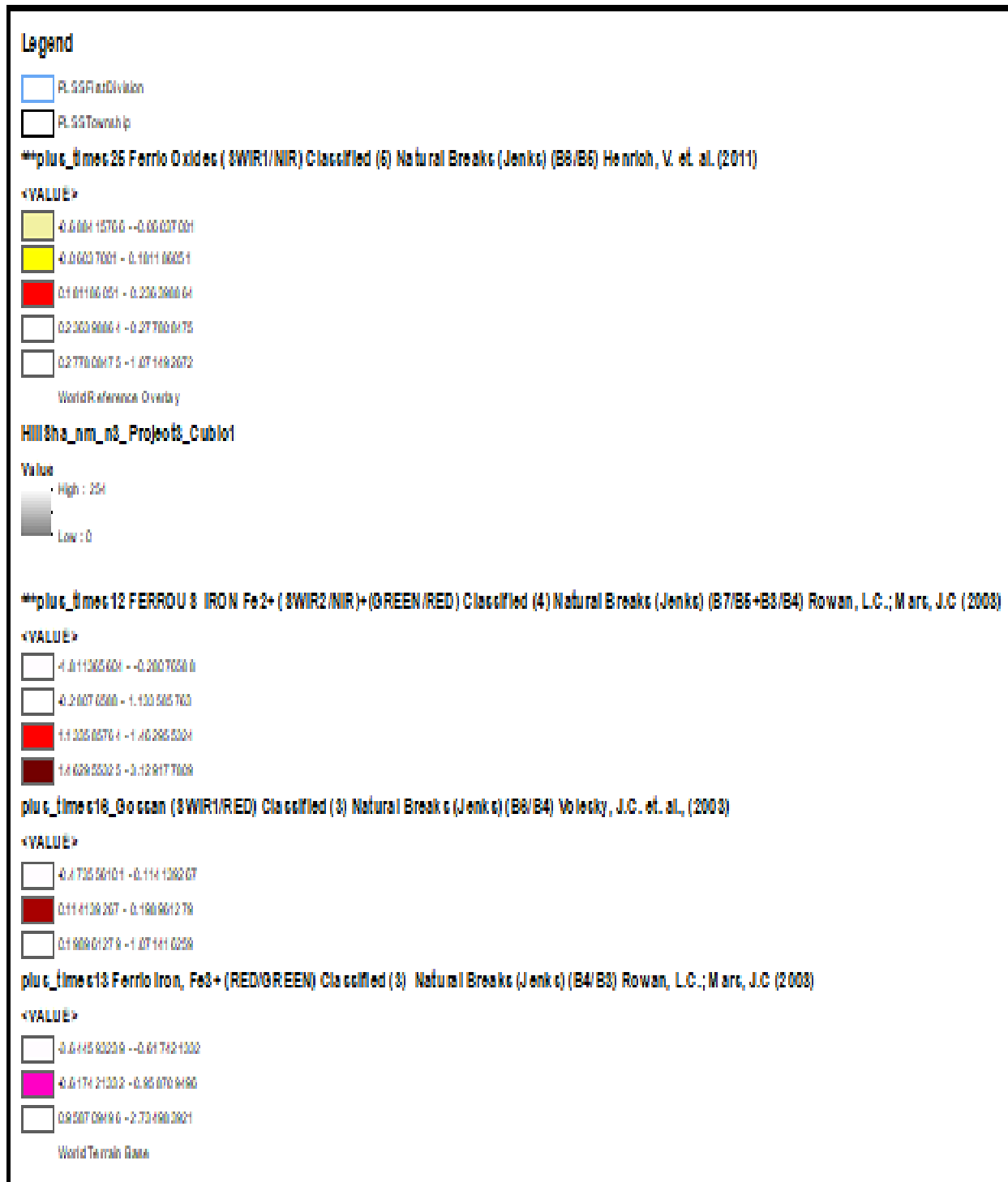
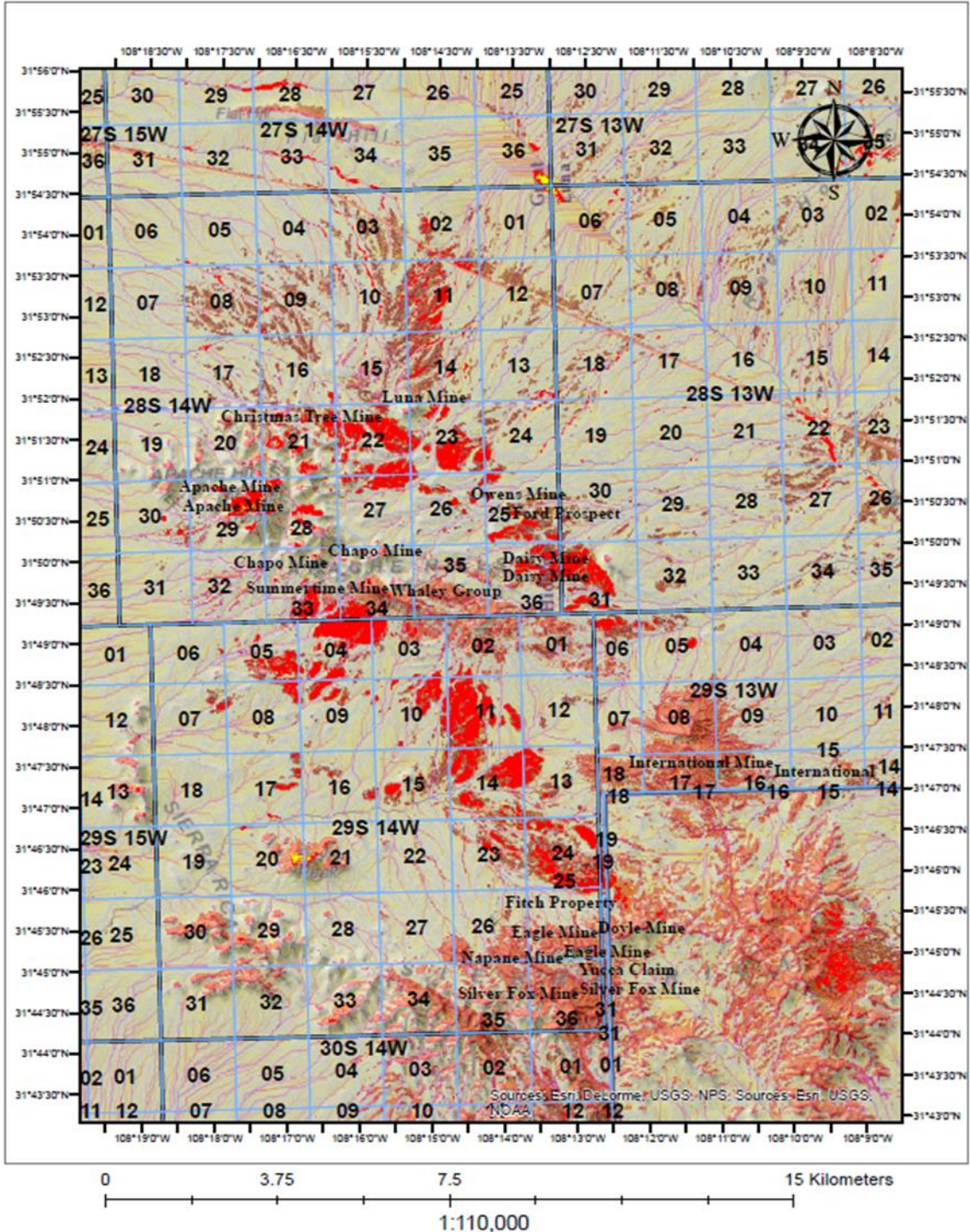


Figure 34: Legend of concentration results of Ferric (Magenta), Ferrous (Red and Brown), and Gossan (Dark Red) in a Hillshade background.

Apache Hills, Hidalgo County, New Mexico



**Section, Township and Range (Ferric and Ferrous Irons)
Accumulation of Sub-Watersheds Flow Direction**

Figure 35: Section, Township and Range and Accumulation of Watershed Flow Direction with the integration of Remote sensing results for ferric and ferrous irons to compliment a formal visualization of Peterson's (1976) geochemical results of iron mineral data location.



Figure 36: Legend of concentration results of Ferric (Magenta), Ferrous (Red and Brown), and Gossan (Dark Red) in a Hillshade background.

The results from figures 35-36 illustrate the Section, Township, and Range accumulation of iron minerals and the watershed flow direction integrating remote sensing spatial data and adding multiple band indices (Figure 36). The ferric and ferrous irons complement a formal visualization of what Peterson (1976) describes as the geochemical results of iron mineral data location (Figure 32-33). The watershed direction flow demonstrates the distribution of iron minerals dispersal by erosion in the Apache Hills and Sierra Rica area. Because of variable deposition, iron mineral concentrations are more abundant in some areas than others.

5.2 Actlabs: Geochemical Trace Element Results Report (Results)

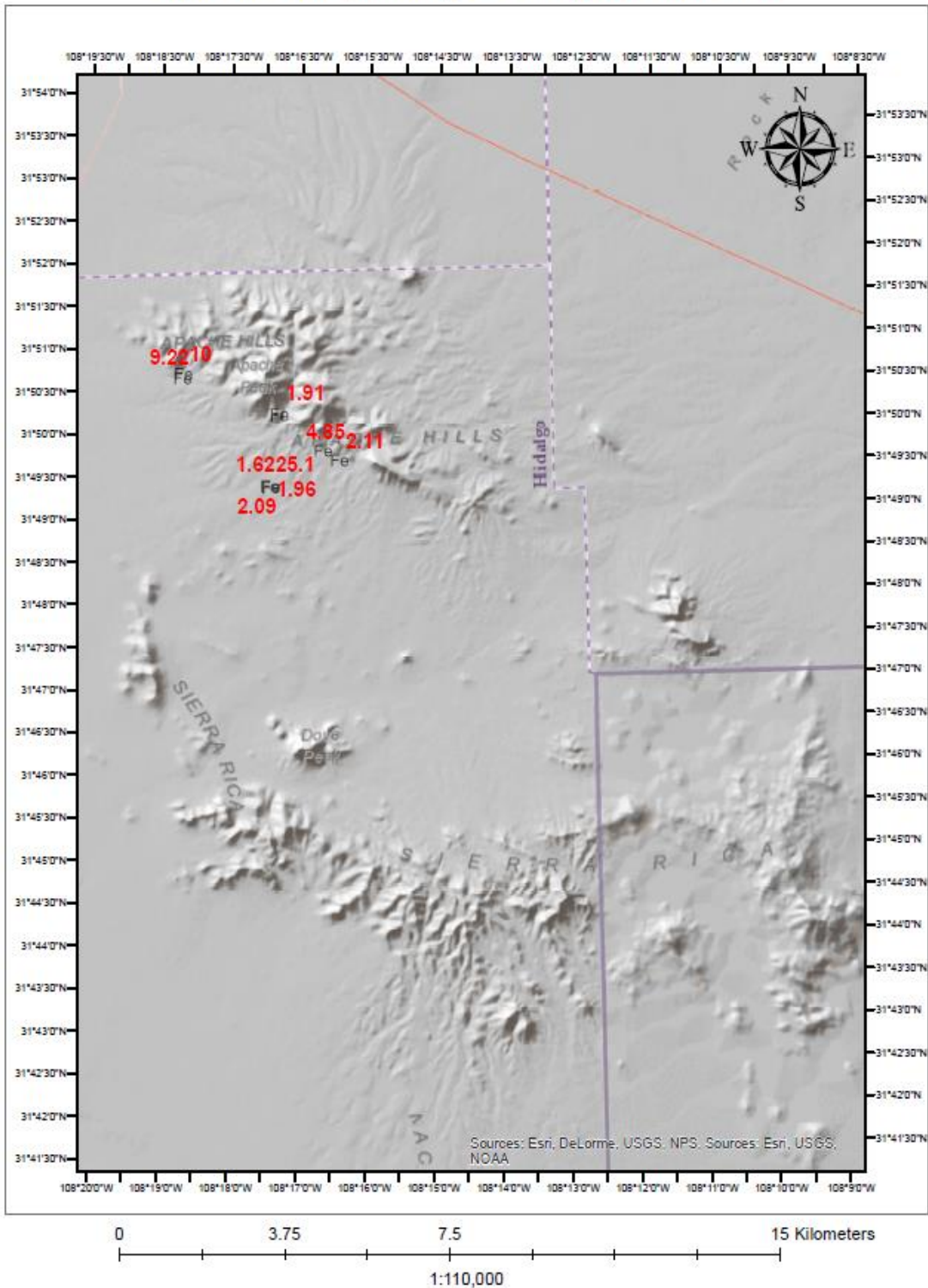
Ten mine dump samples were collected for detailed geochemical analysis. The geochemical analysis results (Table 7) are spatially referenced in ArcGIS, which identifies the samples (AH-001-AH 010), the mines (names), the location (Geo-Coordinates), and the amount of iron present, according to the mine dump samples (Figure 38). The samples (AH-001-AH010) results are shown in ArcGIS with a Hillshade background (Figure 38-39). The results collected from mine dumps are highlighted in red (Figure 38). The sample results from the Apache Hills mine dump are shown on a GIS platform (Figure 38). Iron's geochemical assay result concentration values (Figure 37-highlighted-yellow) are mapped on a GIS platform within the Apache Hills and Sierra Rica alteration zones.

The Fe percentage results (highlighted in yellow Figure 37) in the samples (AH-001-AH-002-and AH-010) were of particular interest to validate the presence of iron in the local area. The sample results from the Apache Hills mine dumps are shown on a GIS platform (Figure 38). Those samples reveal a Fe percentage of 10, 9.22, and 25.1 %. The first two are samples from the Apache mine (AH-001-AH-002 (10, 9.22 %)) and the last from Quartz Prospect (AH-010, 25.1%) (Figure 38). The USGS provides an applicable Mineral Resource Data System (MRDS) (Table 8) that identifies mines, production status, and any extracted mineral resources from the Apache Hills (red boxes). Although Section, Township, and Range are methods used to describe a location in previous research, it is more practical to use a coordinate system, especially when applying data results to a GIS platform. The USGS provides an applicable Mineral Resource Data System (MRDS) (Table 8) that identifies mines, production status, and any extracted mineral resources from the Apache Hills (red boxes).

		Results										Activation Laboratories Ltd.										Report: A18-17520									
Analyte Symbol	Ti	S	P	Li	Be	B	Na	Mg	Al	K	Bi	Ca	Sc	V	Cr	Mn	Fe	Co	Ni	Cu	Zn	Ga	Ge								
Unit Symbol	%	%	%	ppm	ppm	ppm	%	%	%	%	ppm	%	ppm	ppm	ppm	ppm	%	ppm	ppm	ppm	ppm	ppm	ppm								
Lower Limit	0.001	1	0.001	0.1	0.1	1	0.001	0.01	0.01	0.01	0.01	0.02	0.01	1	1	1	0.01	0.1	0.1	0.2	0.1	0.02	0.1								
Method Code	AR-MS	AR-MS	AR-MS	AR-MS	AR-MS	AR-MS	AR-MS	AR-MS	AR-MS	AR-MS	AR-MS	AR-MS	AR-MS	AR-MS	AR-MS	AR-MS	AR-MS	AR-MS	AR-MS	AR-MS	AR-MS	AR-MS	AR-MS								
AH-001	0.131	<1	0.017	9.7	3.8	2	0.023	0.35	2.80	0.08	2.07	17.5	3.2	32	19	>10000	10.0	15.6	5.0	66.2	47.4	14.2	<0.1								
AH-002	0.177	<1	0.029	8.9	0.5	2	0.017	0.43	2.70	0.01	2.21	17.2	5.5	33	33	2100	9.22	2.1	2.3	126	19.0	5.53	<0.1								
AH-003	0.494	<1	0.085	42.7	0.8	3	0.286	1.92	3.18	0.49	0.22	4.58	12.1	106	102	582	1.91	10.3	44.2	19.4	101	9.66	<0.1								
AH-004	0.006	3	0.022	5.4	0.4	<1	0.025	0.90	0.59	0.13	1.09	19.4	1.4	31	3	1330	4.85	29.3	3.9	44.0	99.8	6.10	<0.1								
AH-005	0.022	<1	0.081	5.5	0.7	2	0.056	0.23	0.97	0.38	0.07	1.88	1.7	14	2	1160	2.11	4.0	2.4	56.6	>5000	3.95	<0.1								
AH-006	0.001	<1	0.017	0.8	0.1	1	0.031	0.03	0.52	0.32	5.89	0.13	0.1	3	2	66	0.89	0.9	1.3	55.5	18.1	1.35	<0.1								
AH-007	<0.001	<1	0.019	14.5	2.1	2	0.031	0.68	2.02	0.54	0.25	0.77	1.5	11	6	1050	2.09	2.6	4.6	6.3	70.8	6.31	<0.1								
AH-008	0.001	<1	0.108	5.8	0.9	2	0.038	0.23	1.57	0.56	13.5	0.78	0.6	4	3	1460	1.96	5.6	1.0	63.3	77.1	3.15	<0.1								
AH-009	0.003	<1	0.063	11.0	1.2	1	0.055	0.54	1.67	0.55	61.3	5.80	1.4	22	6	1230	1.62	7.0	18.0	98.1	420	4.71	<0.1								
AH-010	0.006	<1	0.280	5.8	0.4	5	0.108	0.10	0.59	0.11	0.11	10.6	1.0	17	9	1840	25.1	1.3	4.3	46.2	>5000	4.72	<0.1								

Figure 37: Actlab geochemical trace element analysis results in the report of the samples collected from the Apache Hills. Highlighted in yellow are the Fe percentages for each example collected.

Apache Hills, Hidalgo County, New Mexico



ActLabs Ltd. Geochemical (Fe) Results

Figure 38: Actlabs geochemical mine sample results overlaid on a GIS platform.

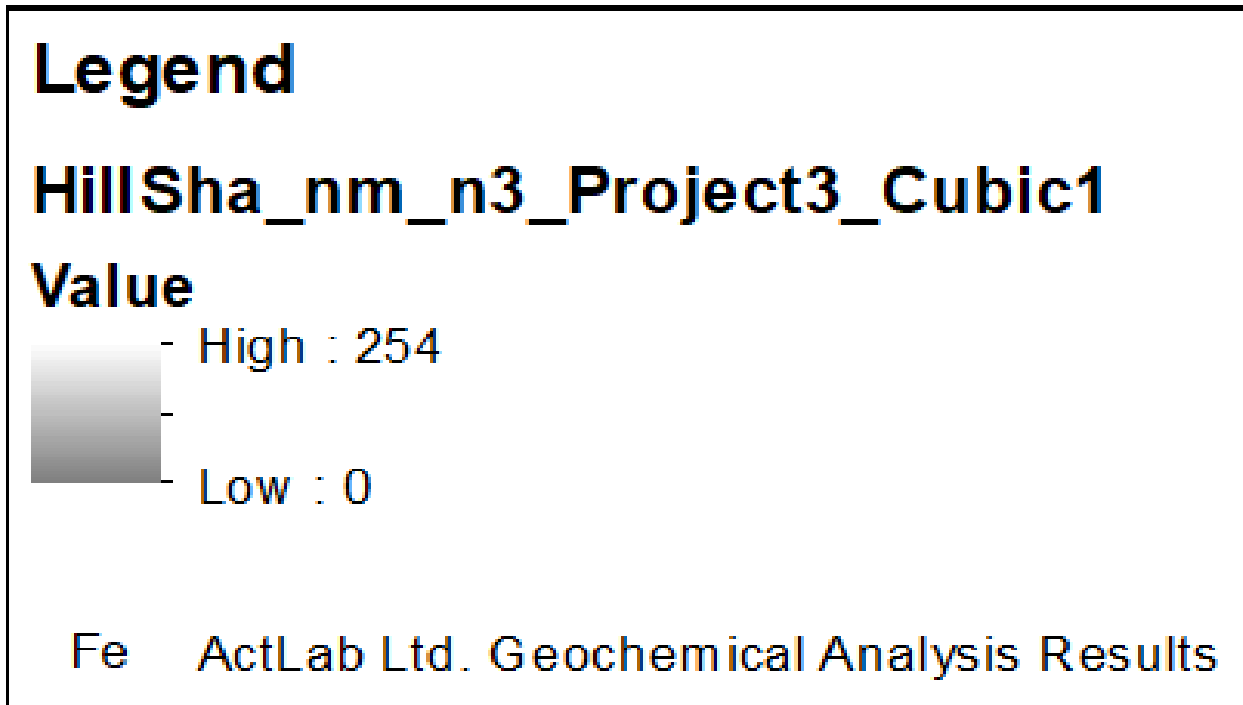


Figure 39: Actlabs geochemical result georeferenced on an ArcGIS platform at the Apache Hills.

Table 7: Actlabs Geochemical Analysis results from ArcGIS table report.

ActLabs Geochemical Analysis Results (Fe)				
Sample #	Apache Hills Mines	Lat DD	Long DD	Fe
AH-001	Apache	31.844444	-108.305556	10
AH-002	Apache	31.843611	-108.305833	9.22
AH-003	Unknown Name	31.836111	-108.282778	1.91
AH-004	Chapo	31.828611	-108.2725	4.85
AH-005	Mairland	31.826667	-108.268611	2.11
AH-006	Last Chance	31.821944	-108.285278	0.89
AH-007	Last Chance	31.822222	-108.285278	2.09
AH-008	Last Chance	31.822222	-108.285278	1.96
AH-009	Quartz Prospect	31.822222	-108.285556	1.62
AH-010	Quartz Prospect	31.822222	-108.285556	25.1

5.3 Metadata: Landsat 8 (OLI)

A cloud-free, level1 Tier1 (Table 4) and terrain are radiometric corrected Landsat-8 (OLI) raster image (bands 1-7) LC08_L1TP_034038_20140107_20170306_01_T1(Path/Row 038/034) (Figure 28) obtained through the U.S. Geological Survey (USGS) Earth Resources Observation and Science Center (EROS) (<http://earthexplorer.usgs.gov>), shows consistent maps of minerals and hydrothermal alteration proficiently. They comprise a generalized region to a more localized area of the Apache Hill, Hidalgo County, New Mexico using Landsat 8 (OLI/TIRS) data.

The Landsat product identifier tag on all downloads carries important attribute value information. This data set (Table 4) includes the acquisition date (Blue), generated date (Red), path (Green), row (Orange), collection category (Purple), sun elevation/azimuth (Gold for radiometric correction purposes), and sensor identifiers (Brown). The identifier tag (Table 4) is color-coded to show that the product identifier label recognizes different data set attributes in an all-in-one tagline when downloaded from the USGS website (e.g., Landsat Product Identifier Attribute Value (Table 4)).

Some data set features collected and downloaded, such as UTM zone, datum, and map projection, are necessary attribute value information for applicable GIS platforms. The spatial digital data files derived from the Landsat 8 (OLI)

satellite must be uploaded and projected accurately to match the layer properties of a GIS platform such as ArcMap 10.8. After processing and filtering the data, the results render accurate geographical maps. The datasets (Table-3, bands 1-11) will launch on the GIS platform as black and white raster images with the appropriate latitude and longitude coordinate location on ArcMap 10.8. Moisture and precipitation from cloud cover can affect the result images created on an image platform, rendering a misleading data raster image and inadvertently leading to an improper interpretation of the mineral identification results.

Table 4: Dataset attribute and values, Landsat 8 OLI bands 1-11, for Raster images on ArcMap (<https://earthexplorer.usgs.gov>).

Data set Attributes	AttributeValues
Landsat Product Identifier	LC08_L1TP_034038_20140107_20170306_01_T1
Acquisition Date	2014/01/07
Date L-1 Generated	2017/03/06
Target WRS Path	038
Target WRS Row	034
Collection Category	T1
Land Cloud Cover	0.96
Sun Elevation L1	31.59619305 (Radiometric Correction)
Sun Azimuth L1	154.77537844 (Radiometric Correction)
Sensor Identifier	OLI_TIRS
Map Projection Level-1	UTM
UTM Zone	12
Datum	WGS84
Center Latitude	31°44'32.60 "N
Center Longitude	108°18'12.64"W
Grid Cell Size Reflective	30.00
Grid Cell Size Thermal	30.00
Grid Cell Size Panchromatic	15.00

5.4 Integrating Remote Sensing Spatial Data & GIS Platform (ArcGIS-ENVI)

Figures (35, 40, 43, 46, 49, 52, and 55) show the result of integrating remote sensing spatial data on a GIS platform. The figures are created using different band indices ratio combinations using Table 5a. The figures are accompanied by a legend identifying the concentrations of ferric and ferrous iron minerals distribution in the Apache Hills and Sierra Rica Hidalgo County, New Mexico. The legends place the classification statistics as count, minimum, maximum, sum, mean, standard deviation, and break values. The processing figures (Appendix-2) illustrate the Jenks natural break classification algorithm (ArcGIS 10.8) used to classify the resulting figures into 3, 4, 5, and 32 classes. The Jenks natural breaks are a data clustering method designed to determine the best configuration of values into different classes. The process seeks to reduce the variance within classes and maximize the variance between classes (Jenks). Jenks's natural break algorithm is a dependent classification method. It does not require ground points as input for the training with natural breaks classification (Jenks) classes based on inherent natural groupings in the data. Class breaks are created to best group similar values and maximize class differences. The features are divided into categories whose boundaries are set where the data values have relatively significant differences. (Lamqadem, 2018).

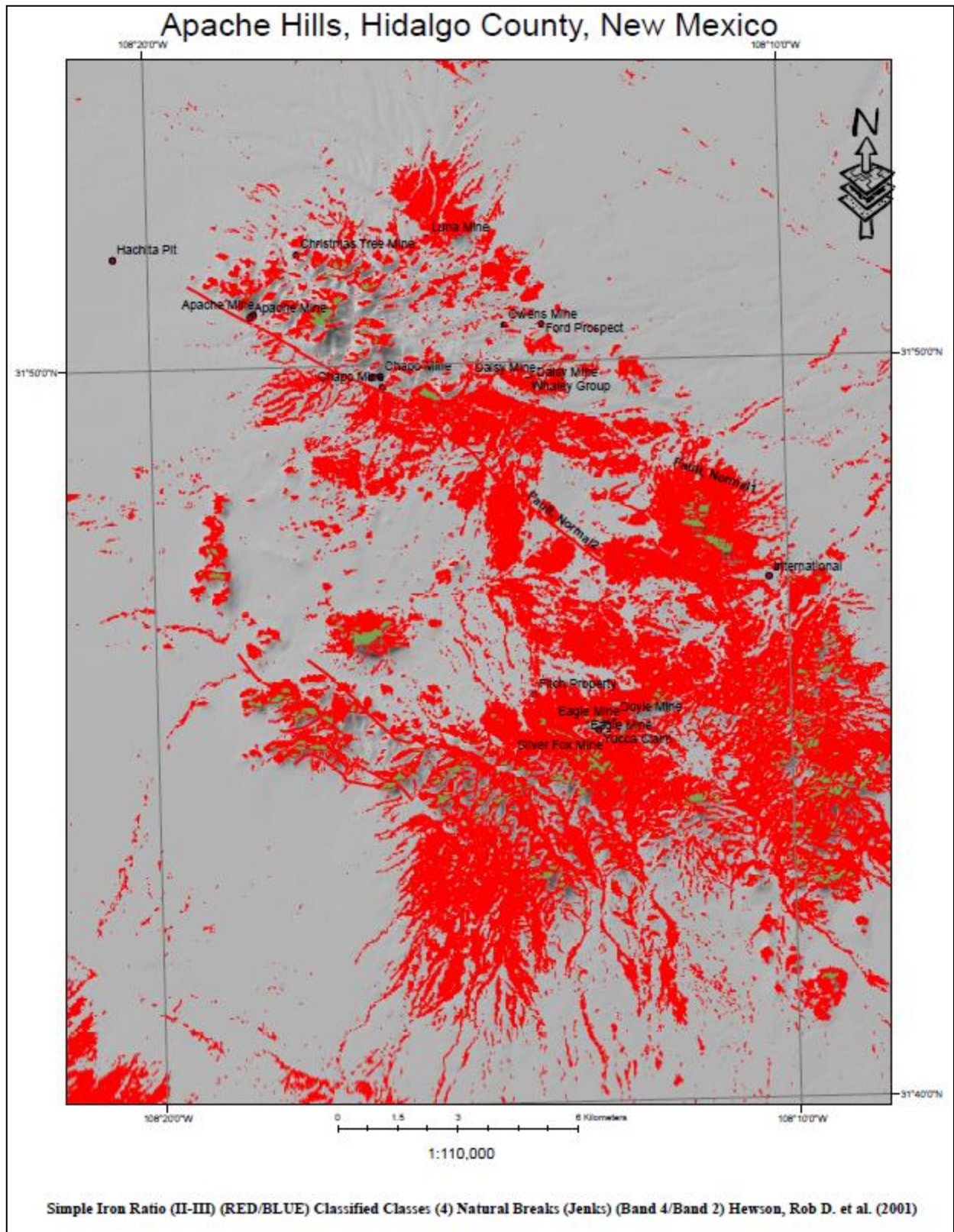


Figure 40a: Remote sensing band ratio results integrated on an ArcMap 10.8 GIS platform for Simple Iron Ratio (RED/BLUE) Classified (4) Natural Breaks (Jenks) (B4/B2) Hewson, Rob D. et al. (2001) Table 5b reference index 78.

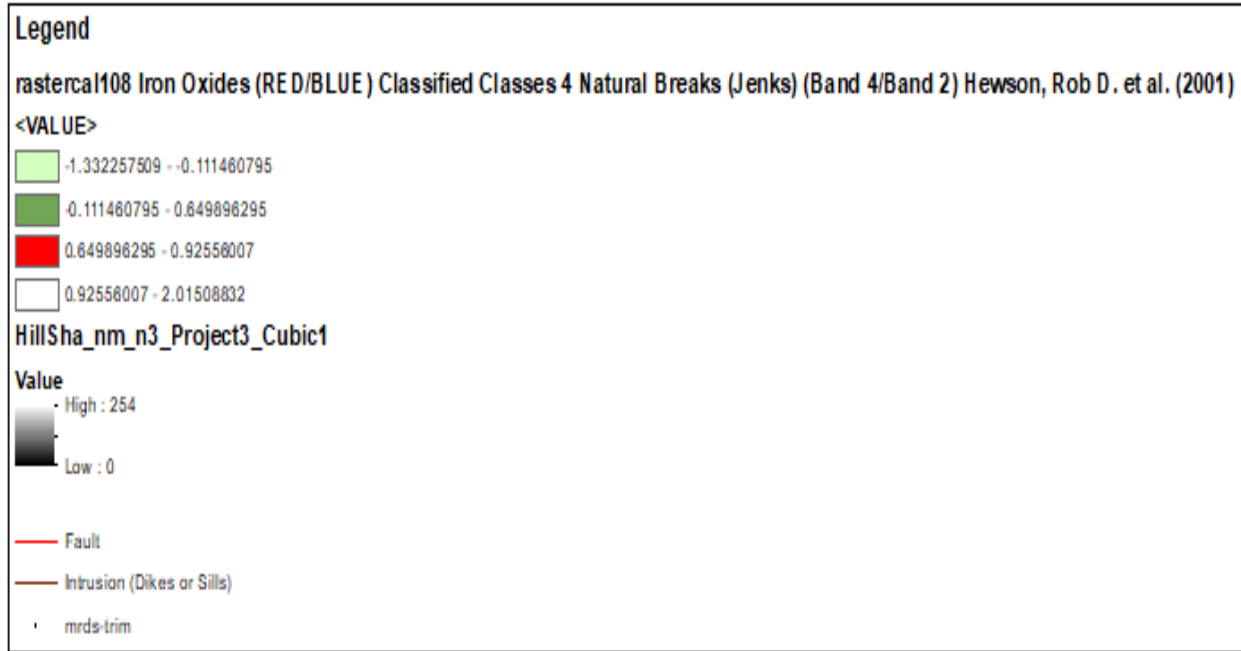


Figure 40b: Simple Iron mineral ratio (SWIR1/RED) Classified (4) Natural Breaks (Jenks) (B4/B2) on a Hillshade background Volesky, J.C. et al., (2003). Table 5b reference index 78.

Figures 40a, 40b, and 40c (Appendix-2) demonstrate the alteration, classification, and distribution of simple iron minerals (red) surrounding the Apache Hills and Sierra Rica, New Mexico. The numbers (e.g., 14, 15, and 21) describe lithology (Figures 10-11), but only the contact boundary outlines are shown in these figures. The Apache fault is prominent across the Apache Hills from the Apache mine to Mexico as a linear band of iron-rich alteration (e.g., Figures 40a and 40d). Other faults are visible as linear alteration bands, as in the Sierra Rica Mountains. The indices band ratio used was Band 4/Band2 or SWIR1/Red from Table 5b, reference 78.

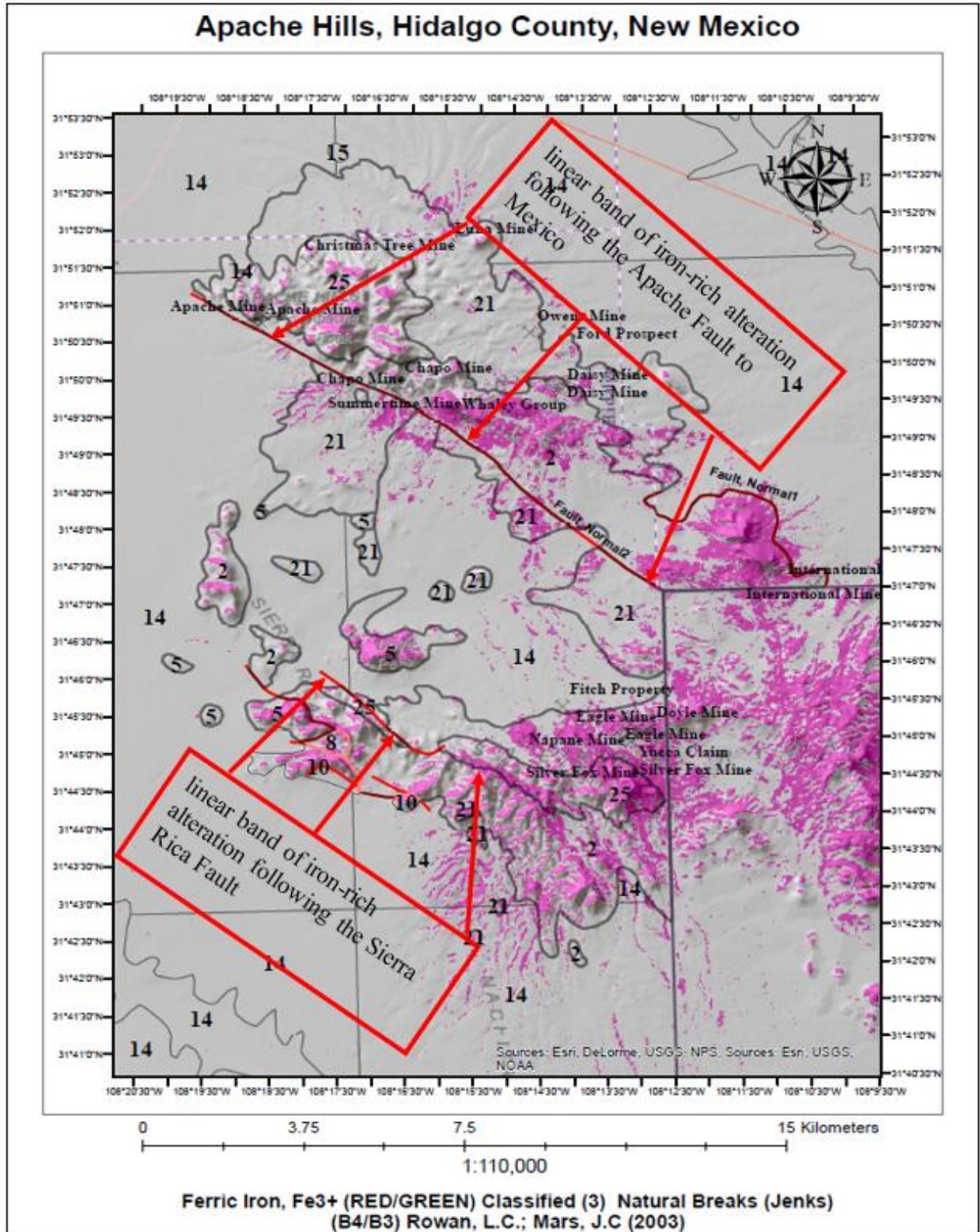


Figure 40d: Remote sensing band ratio results integrated on an ArcMap 10.8 GIS platform for Ferric Iron Fe₃⁺, (RED/GREEN) Classified (3) Natural Breaks (Jenks) (B4/B3) Rowan, L.C.; Mars, J.C (2003)-Table 5b reference index 20.

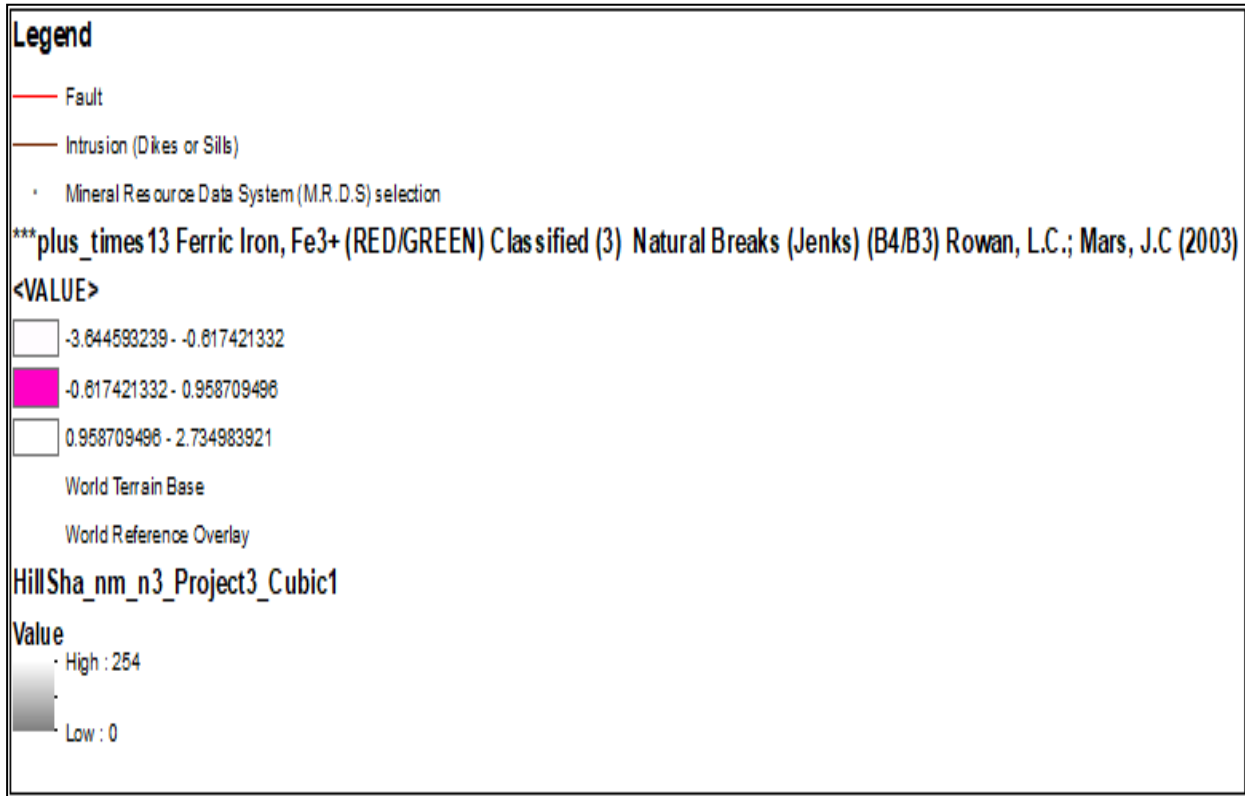


Figure 41: Legend Ferric Iron, Fe³⁺ (RED/GREEN) Classified (3) Natural Breaks (Jenks) on a Hillshade background and a World reference overlay. (B4/B3). Concentration values in Magenta. Rowan, L.C.; Mars, J.C (2003). Table 5b reference index 20.

Figures 40d, 41, and 42 (Appendix 2) demonstrate the alteration, classification, and distribution of Fe³⁺ (magenta) surrounding the Apache Hills and Sierra Rica, New Mexico. The indices band ratio used was Band 4/Band 3 or Green/Red from Table 5b indices reference 20. The numbers (e.g., 14, 15, and 21) describe lithology (Figures 10-11), but only the contact boundary outlines are shown in these figures. The Apache faults again are visible across The Apache Hills from the Apache mine to Mexico as linear bands of iron concentrations. Other faults are visible in the Sierra Rica Mountains (Figures 40d and 43).

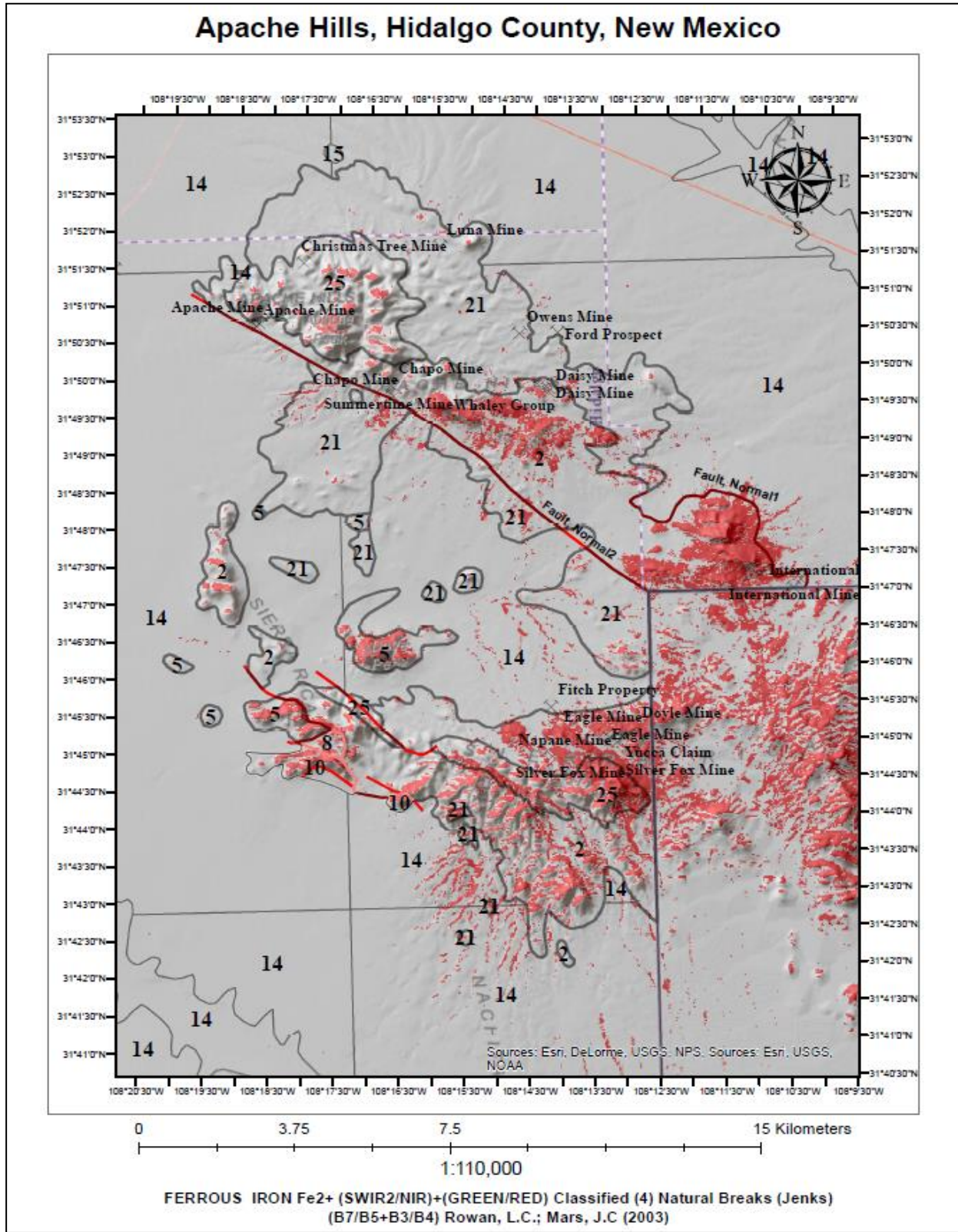


Figure 43: Remote sensing band ratio results integrated on an ArcMap 10.8 GIS platform for Ferrous Iron Fe₂₊ (SWIR2/NIR) + (Green/Red) Classified (4) Natural Breaks (Jenks) (B7/B5+B3/B4) Rowan, L.C.; Mars, J.C (2003). Table 5b reference index 19.

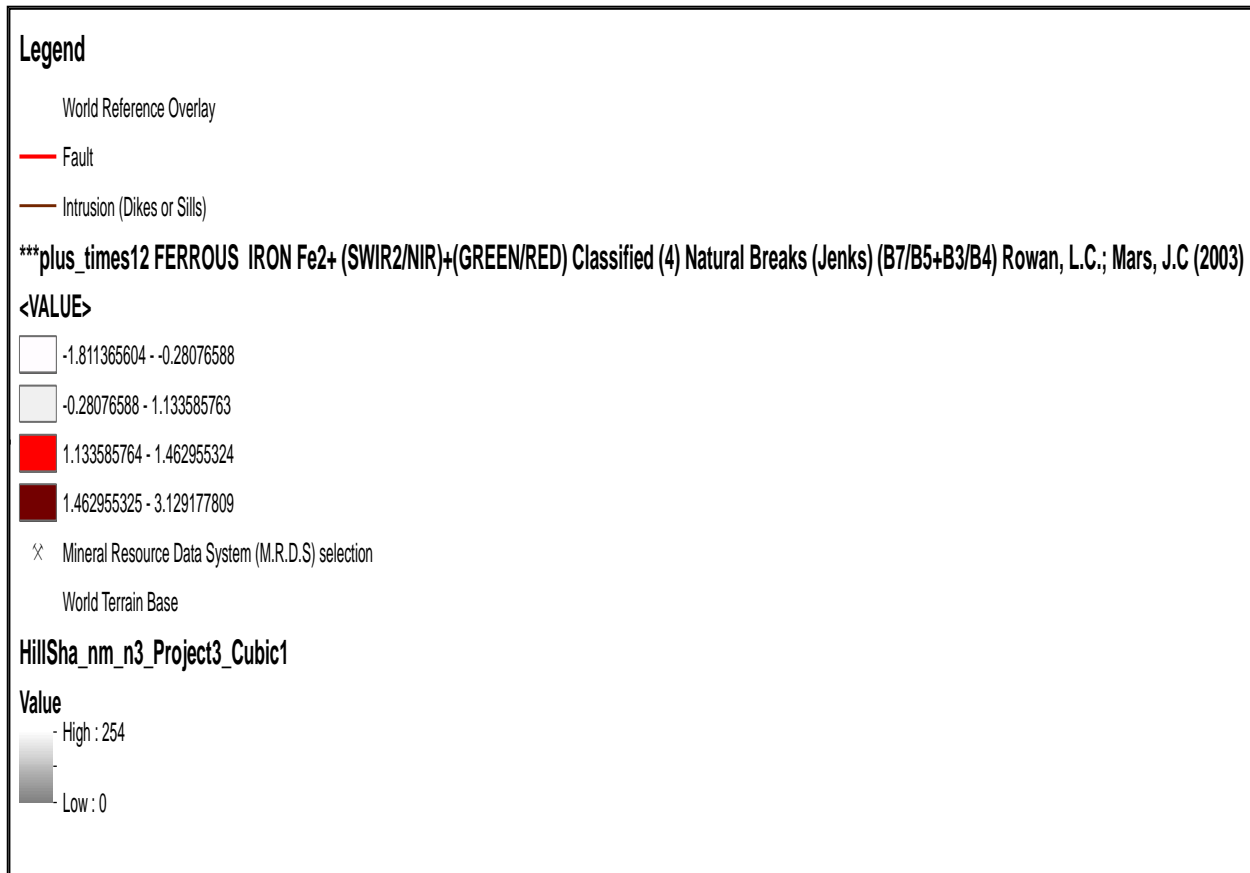


Figure 44: Legend: Ferrous Iron Fe²⁺) on a Hillshade background and a World reference overlay. Concentrated Ferrous Irons values are in Red. Rowan, L.C.; Mars, J.C (2003).

Figures 43, 44, and 45 (Appendix-2) demonstrate the distribution and classification pattern of ferrous iron Fe²⁺ throughout the Apache Hills and Sierra Rica, New Mexico. The Fe²⁺ alterations are visible in dark brown and red on a Hillshade background. The band indices used to visualize Fe²⁺ (SWIR2/NIR) + (Green/Red) Classified (4) Natural Breaks (Jenks) (B7/B5+B3/B4) and a reference index 19 Table 5b. The numbers (e.g., 14, 15, and 21) describe lithology (Figures 10-11), but only the contact boundary outlines are shown in these figures.

Apache Hills, Hidalgo County, New Mexico

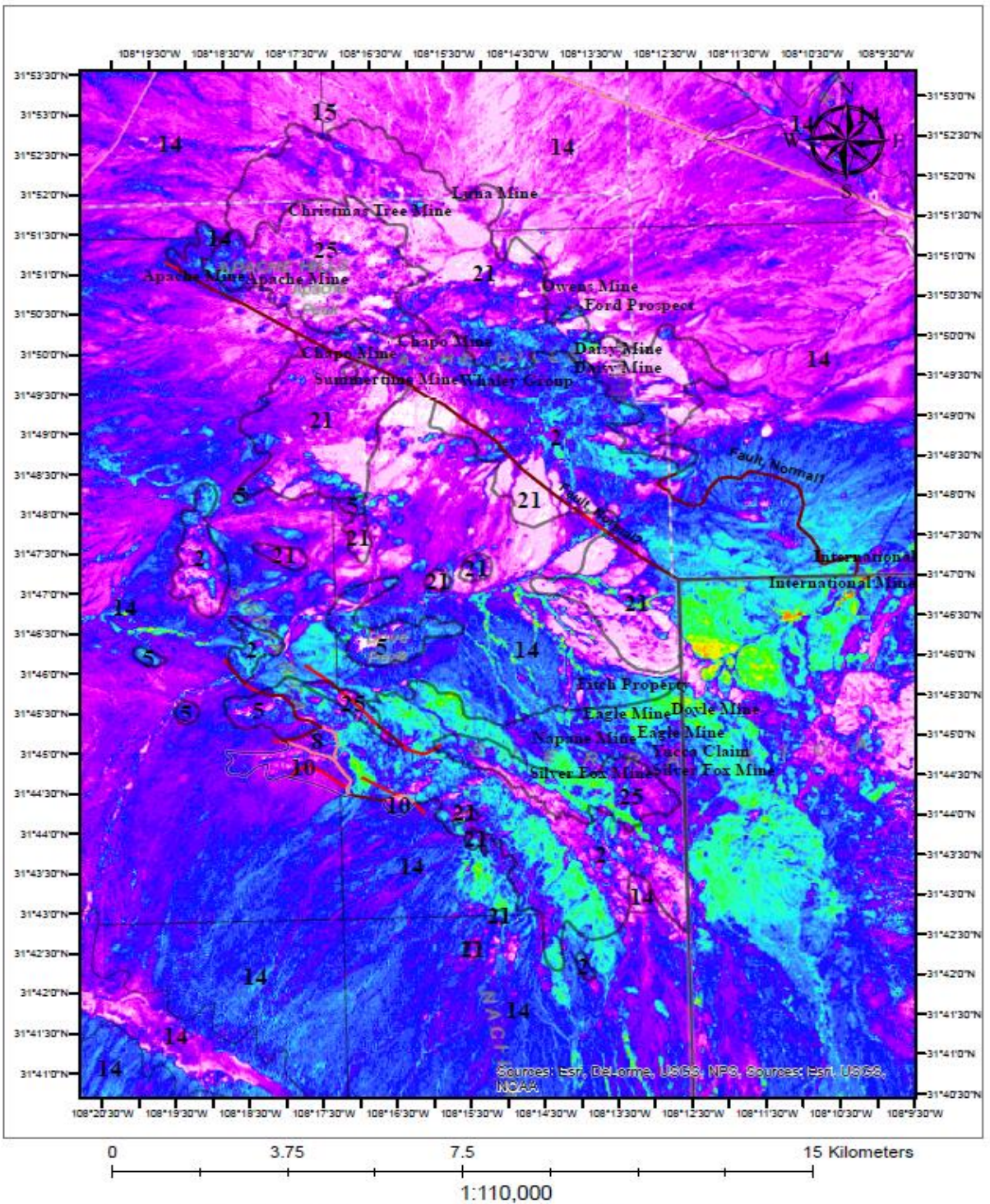


Figure 46: Remote sensing band ratio results integrated on an ArcMap 10.8 GIS platform for Ferric Oxides (SWIR1/NIR) Classified (32) Quantile (B6/B5) Henrich, V. et al., (2011). Including lithologic contact boundaries. Table 5a reference index 21.

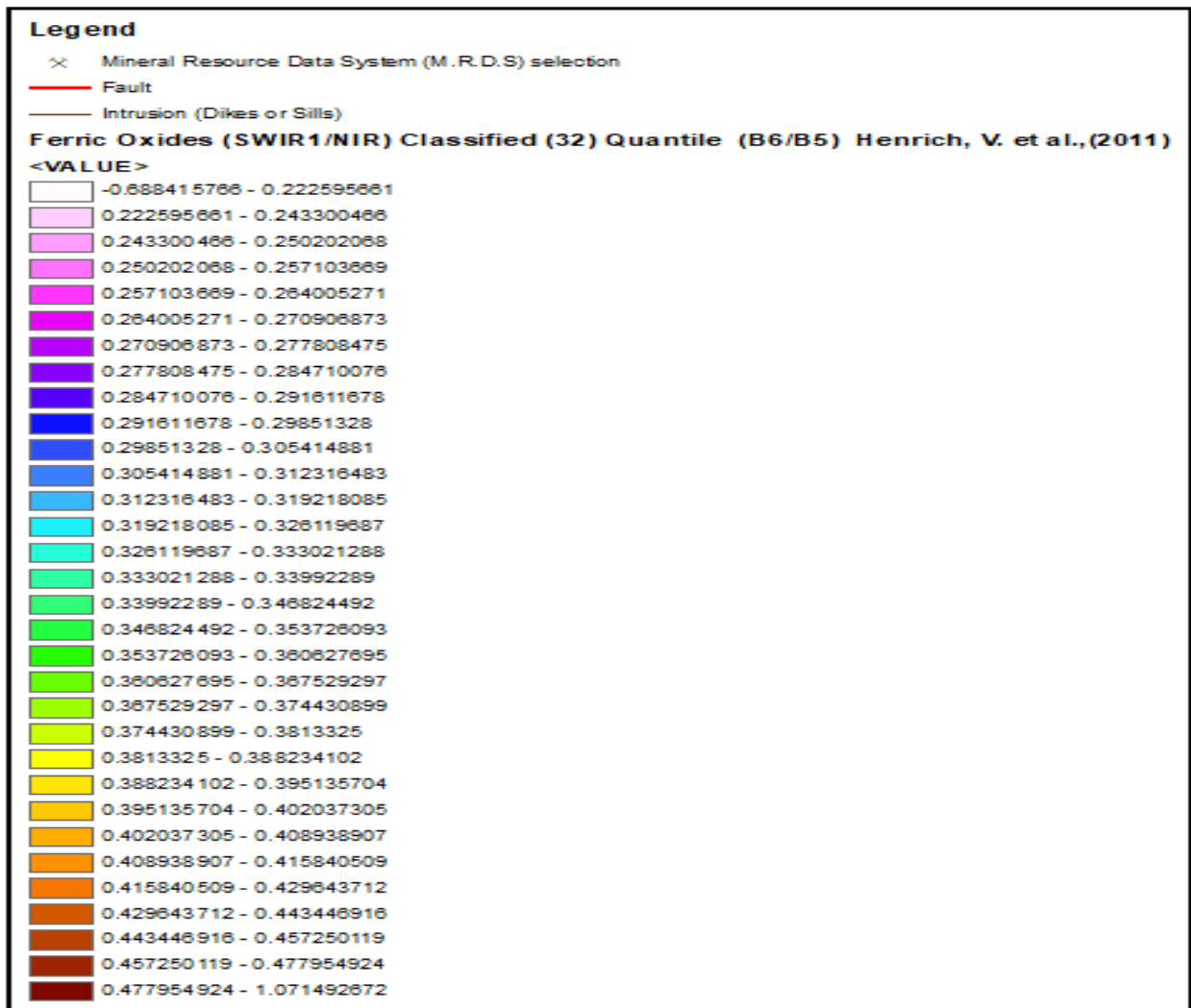
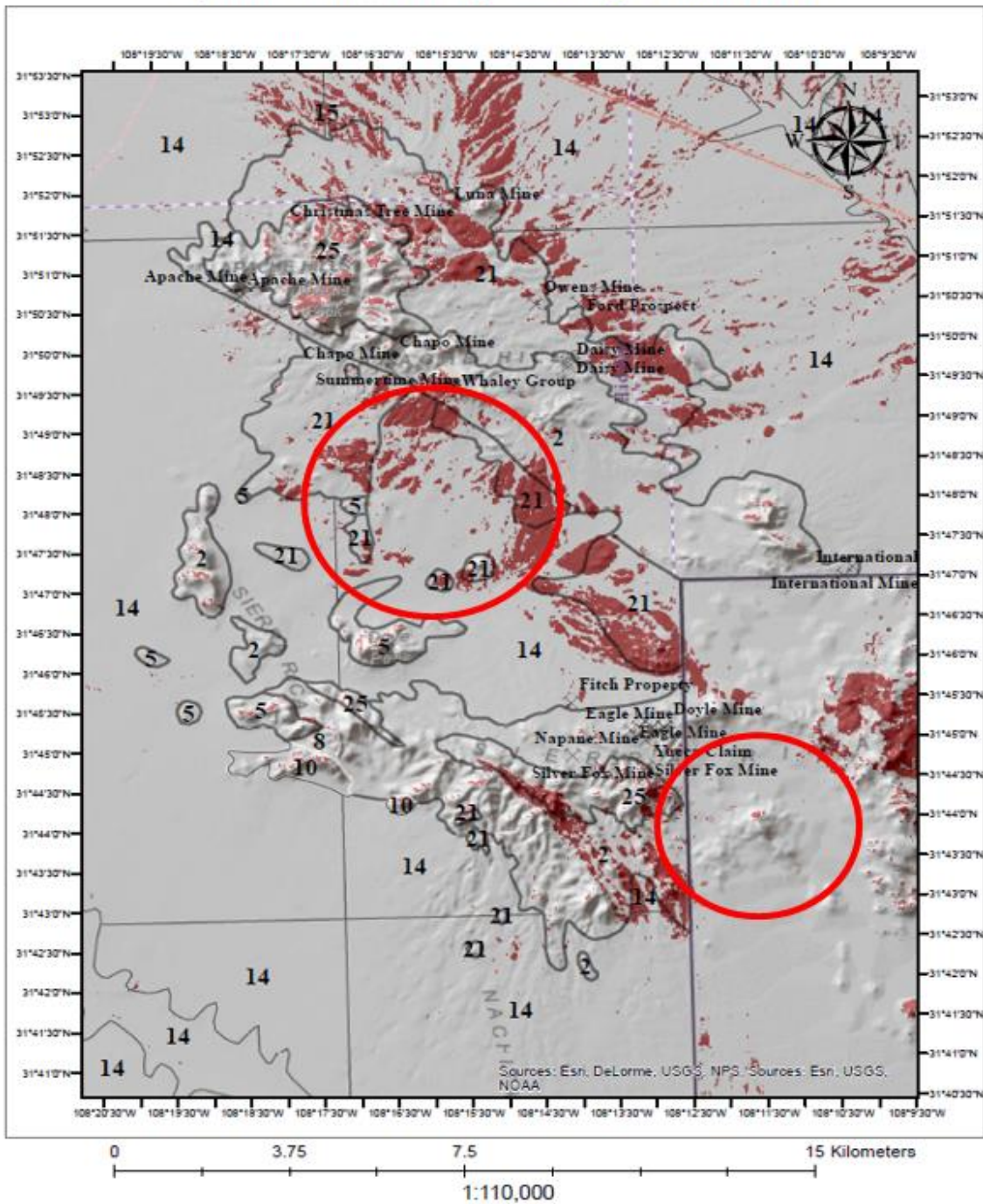


Figure 47: Legend: Concentrated Ferric Oxide values in Magenta and white (Henrich, V. et al., (2011).

The concentrations and distribution of ferric oxides alteration using band indices (SWIR1/NIR) Classified (32) Quantile (B6/B5) are represented in figures 46, 47, and 48 (Appendix-2). The numbers (e.g., 14, 15, and 21) describe the contact lithology (Figures 10-11). The dissemination of the iron oxide alterations is visible North of the Apache Hills and South of Sierra Rita.

Apache Hills, Hidalgo County, New Mexico



Gossan (SWIR1/RED) Classified (3) Natural Breaks (Jenks) (B6/B4) Volesky, J.C. et. al., (2003)

Figure 49: Remote sensing band ratio results integrated on an ArcMap 10.8 GIS platform for Gossan (SWIR1/RED) Classified (3) Natural Breaks (Jenks) (B6/B4) on a Hillshade background Volesky, J.C. et al., (2003) Table 5a reference index 26. Red circled areas may be of future interest for the possibility of a hidden porphyry Elston, (1976).



Figure 50: Gossan (SWIR1/RED) Classified (3) Natural Breaks (Jenks) (B6/B4) in a Hillshade background Volesky, J.C. et al., (2003) Red Circles Area of Future Interest.

Figures 49, 50, and 51 (Appendix 2) use bands (B6/B4) or (SWIR1/RED) reference indices 26 from Table 5a and Classified (3) Natural Break (Jenks). Gossan is observable throughout the Apache Hills-Sierra Rica Mountains, New Mexico, particularly in faulted areas. The Gossan is noticeable as the dark red-brown stain-like pattern on a Hillshade background. The numbers (e.g., 14, 15, and 21) describe lithology (Figures 10-11), but only the contact boundary outlines are shown in these figures. The copper concentration is higher than other levels in the surrounding area, and other alterations (e.g., phyllic, argillic Figures 105 and 106) are present in these areas. There are areas of interest for future work and discovery.

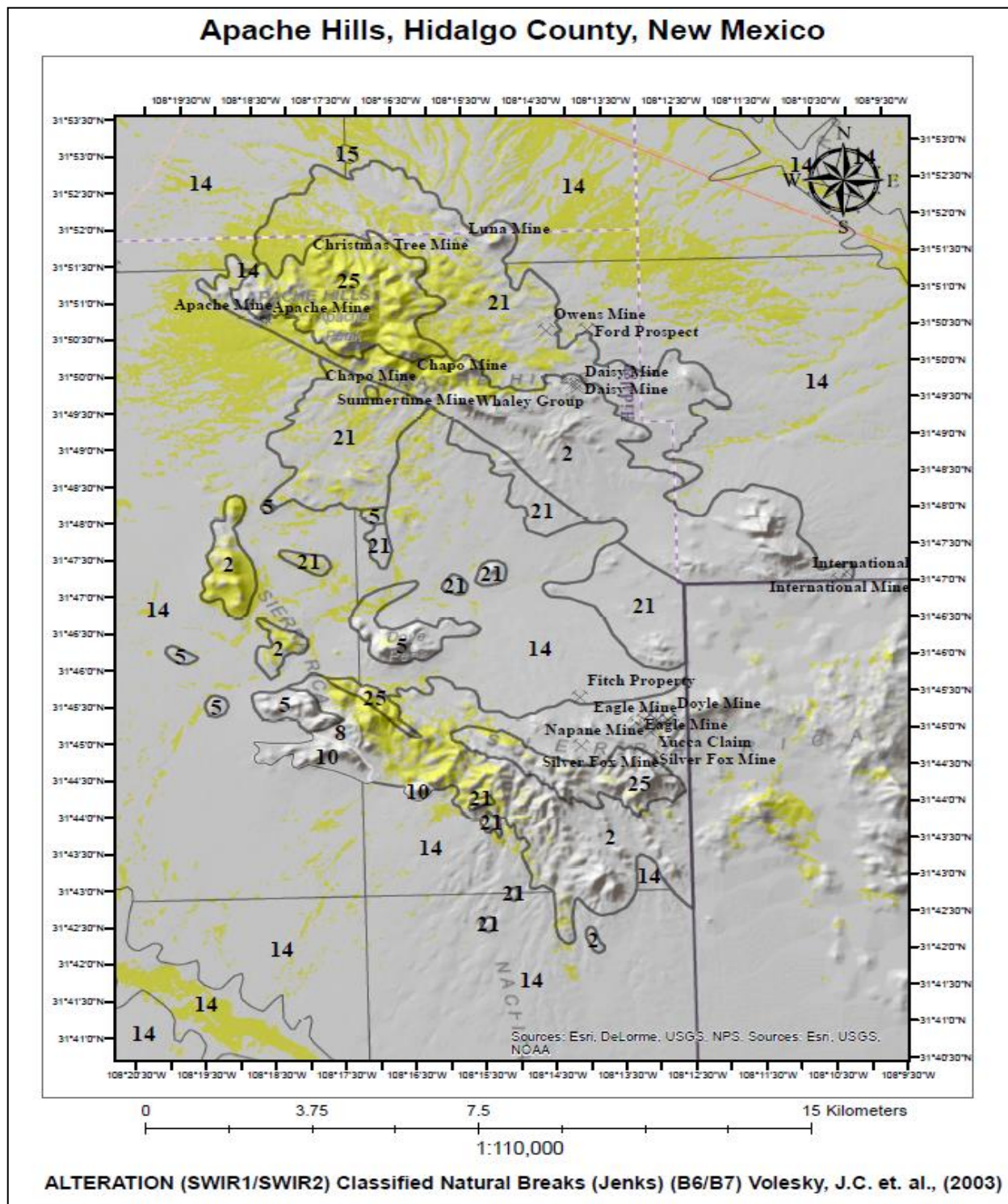


Figure 52: Remote sensing band ratio results integrated on an ArcMap 10.8 GIS platform for Alteration (SWIR1/SWIR2) Classified Natural Breaks (Jenks) (B6/B7) Volesky, J.C. et al., (2003). Table 5a references 3 and 39. Note: Both references are the same band ratios but different reference sources 3 is referenced as an alteration, and 39 is referenced as a Laterite, which is a form of a profound alteration exposed on the surface by a form of erosional weathering and fluvial transport.

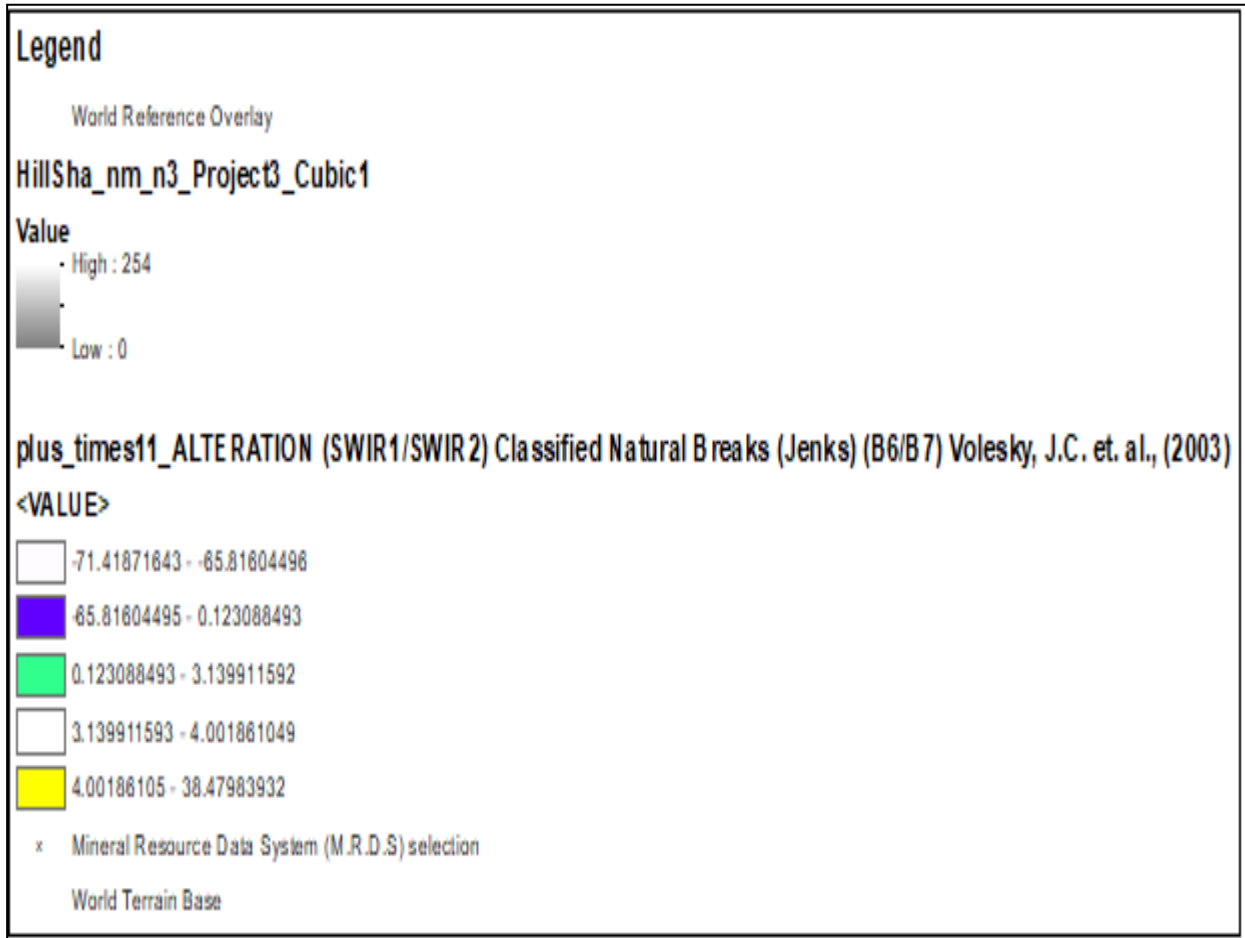


Figure 53: Classified Natural Breaks (Jenks) (B6/B7) on a Hillshade background Volesky, J.C. et al., (2003). Table 5a references 3 and 39.

Figures 52, 53, and 54 (Appendix-2) display remote sensing band ratio (B6/B7) or (SWIR1/SWIR2) results on an ArcMap 10.8 GIS platform for alteration Classified (5) Natural Breaks (Jenks). Referenced indices band ratio is from Table 5a 3 and 39. Note: Both references in Table 5a are the same band ratios but different reference sources. Number three is referenced as an alteration, and number 39 is referenced as a Laterite, a form of a profound alteration exposed on the surface.

The image from Figure 55a is created using ENVI 5.3 and is processed with this software to render a final band combination RGB much like the ArcGIS processed RGB (Figure 55b). A significant color quality difference exposes specific topographical and mineral alterations. These geological features encompass the local lithology (igneous intrusion-Red Box), (fluvial transport-Yellow Box), and ferric oxide and hydroxyls (Figure 55e) alterations surrounding Doyle Peak (Purple Box).

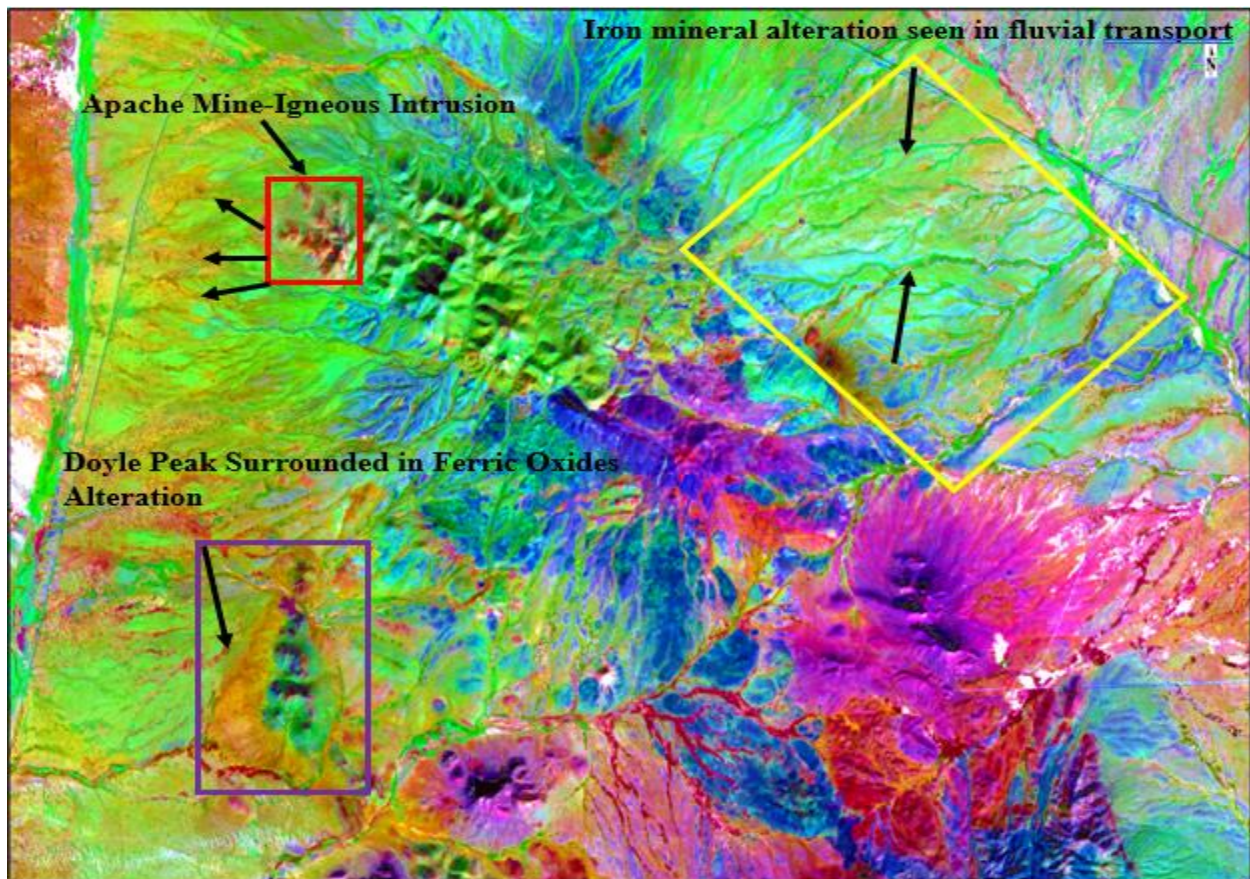


Figure 55a: ENVI 5.3 image of the Apache Hills in RGB Combination showing Iron Oxides Alterations surrounding Doyle Peak (Purple-Box, Black Arrow), the Apache Mine (Red Box, Black Arrows), and Northeast of the Apache Hills (Yellow-Box, Black Arrows).

Figures 55b, 55c, 55d, 55e, 55f, and 55g are RGB composite (7,4,2) bands that discriminate the lithology and alteration of the study area. Figures 55h, 55i, and 55j (Appendix-2) are the processed spatial data classification and statistics. Figures 55c, 55d, 55e, and 55g are RGB band combinations that include band ratio combinations that expose iron oxides and hydroxyls. Figure 55g consists of the Copper values from the Actlab analysis from AH-001-AH010. All of these figures have been integrated with ArcGIS and ENVI software. Figures 55c (Ferric Iron), 55d Ferrous Iron, 55e (hydroxyls), 55f (Gossans), and 55g (Compilation) are add-on shapefile of band ratio indices processed on ENVI and transferred to ArcGIS.

Figure 55i (Appendix 2) shows the classification values for the RGB composite image of band ratios 7,4,2 (Figure 55b). Figure 55j (Appendix-2) displays the Histogram Equalize for the RGB Composite bands 7,4,2. The statistics minimum is -5.06, and the maximum of 2.99, with a standard deviation of 5.30. The ArcGIS image (Figure 55b) is like the ENVI 5.3 image (figure 55a). Both software-derived colored ortho-images share the same composite band 7,4,2 but differ in the color quality of each image. The ENVI (Figure 55a) colors stand out more with darker colors than the ArcGIS image.

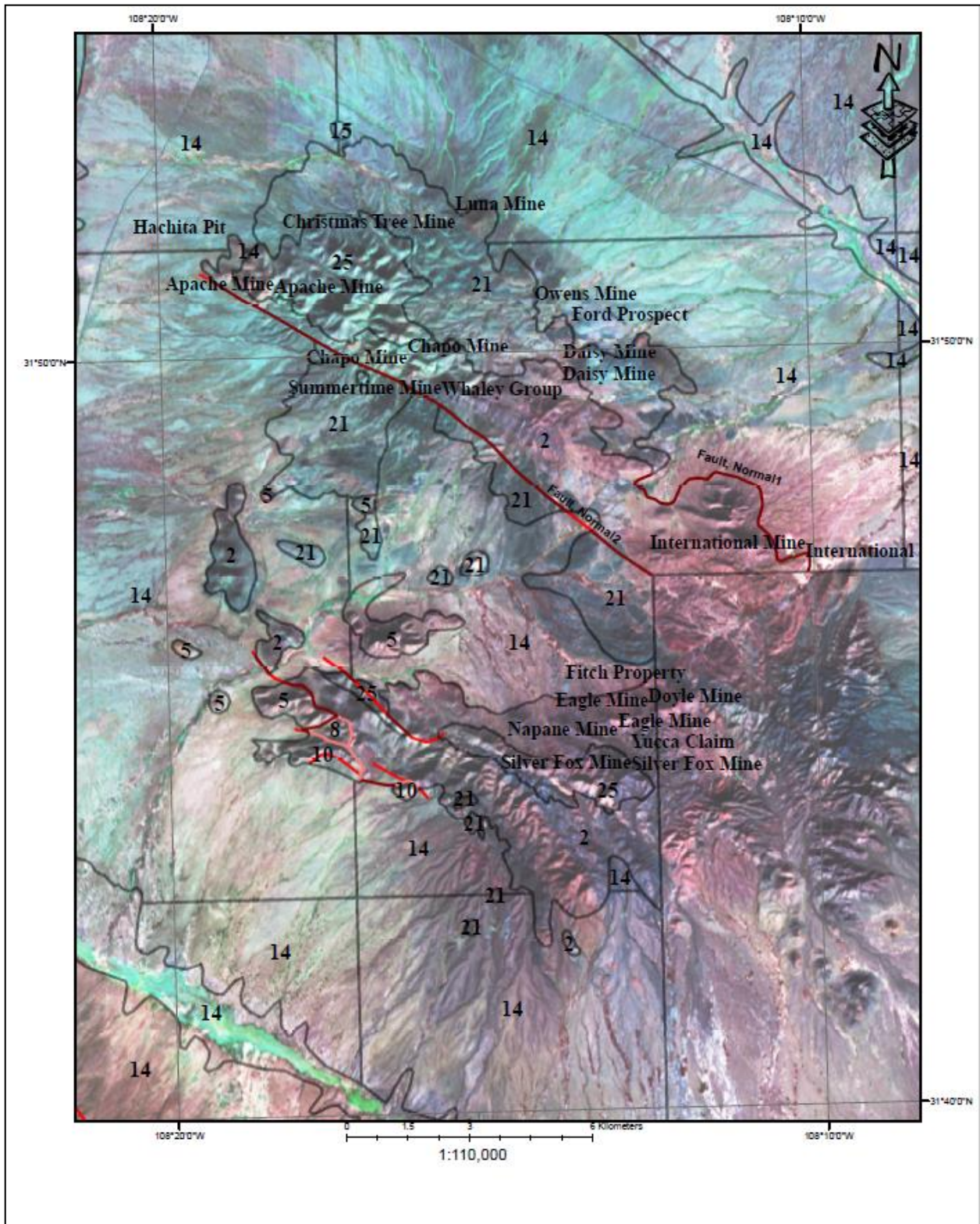


Figure 55b: ArcGIS image of the Apache Hills in RGB (7,4,2) with contact boundaries for general lithological mapping (Imbroane, 2007).

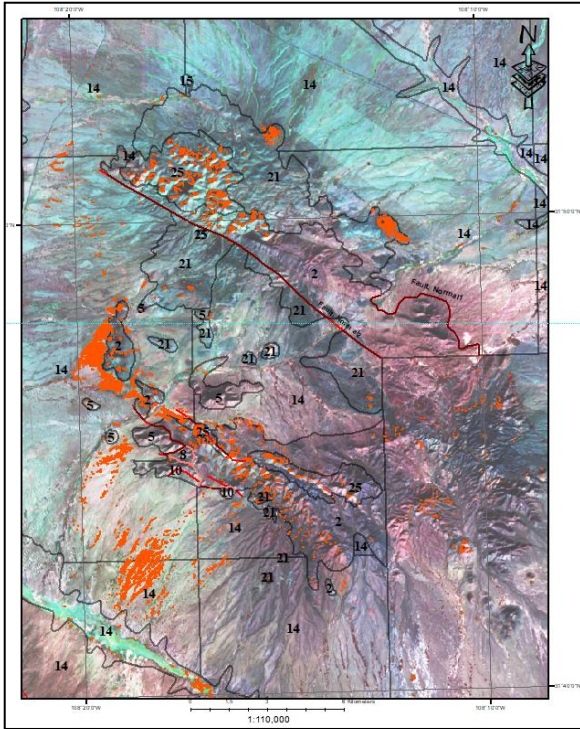


Figure 55c: Created on ENVI 5.3 (Ferric Iron-Orange) and added to ArcGIS as a shapefile.

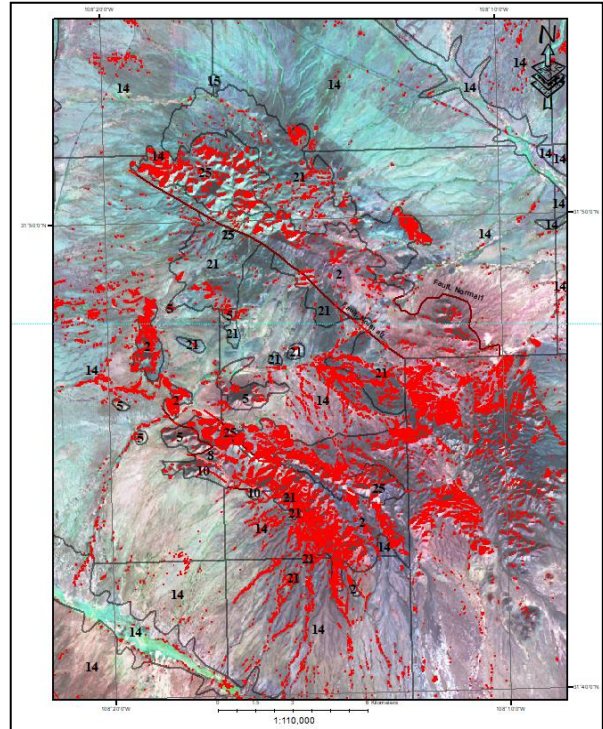


Figure 55d: Created on ENVI 5.3 (Ferrous Iron-Red) and added to ArcGIS as a shapefile.

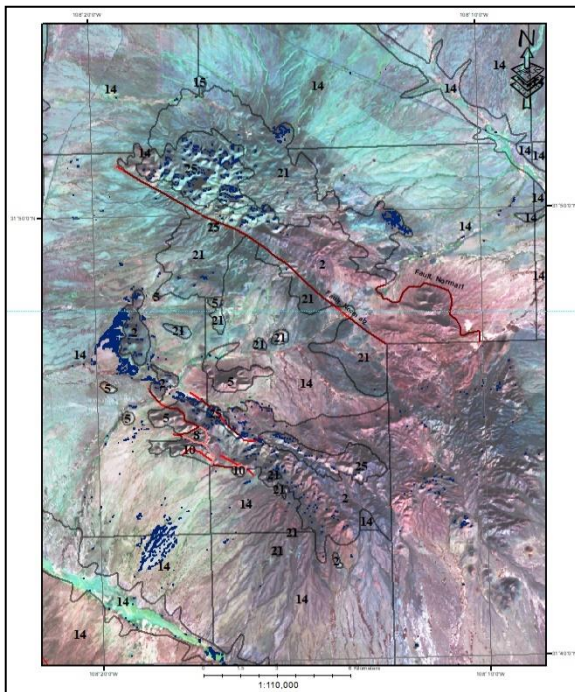


Figure 55e: Created on ENVI 5.3 (Hydroxyls) and added to ArcGIS as a shapefile.

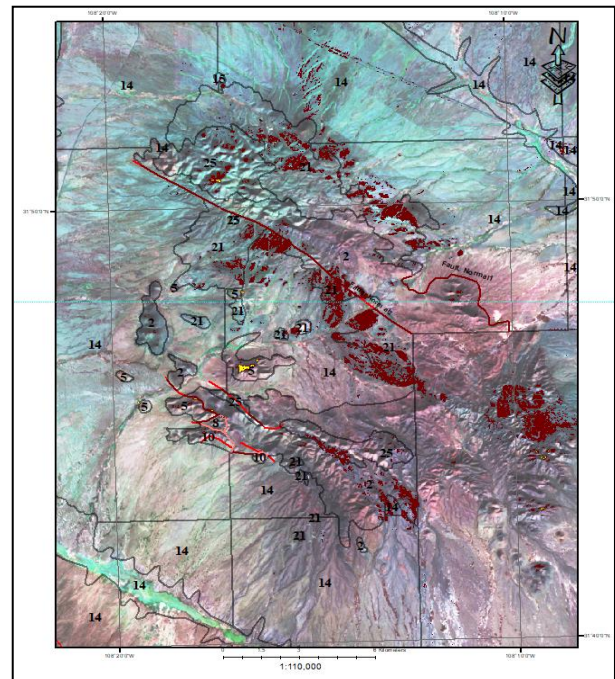


Figure 55f: Gossan (SWIR1/RED) 1 Classified Classes 5 (Band 6/Band 4) Volesky, J.C.; Stern, R.J. et al., (2003).

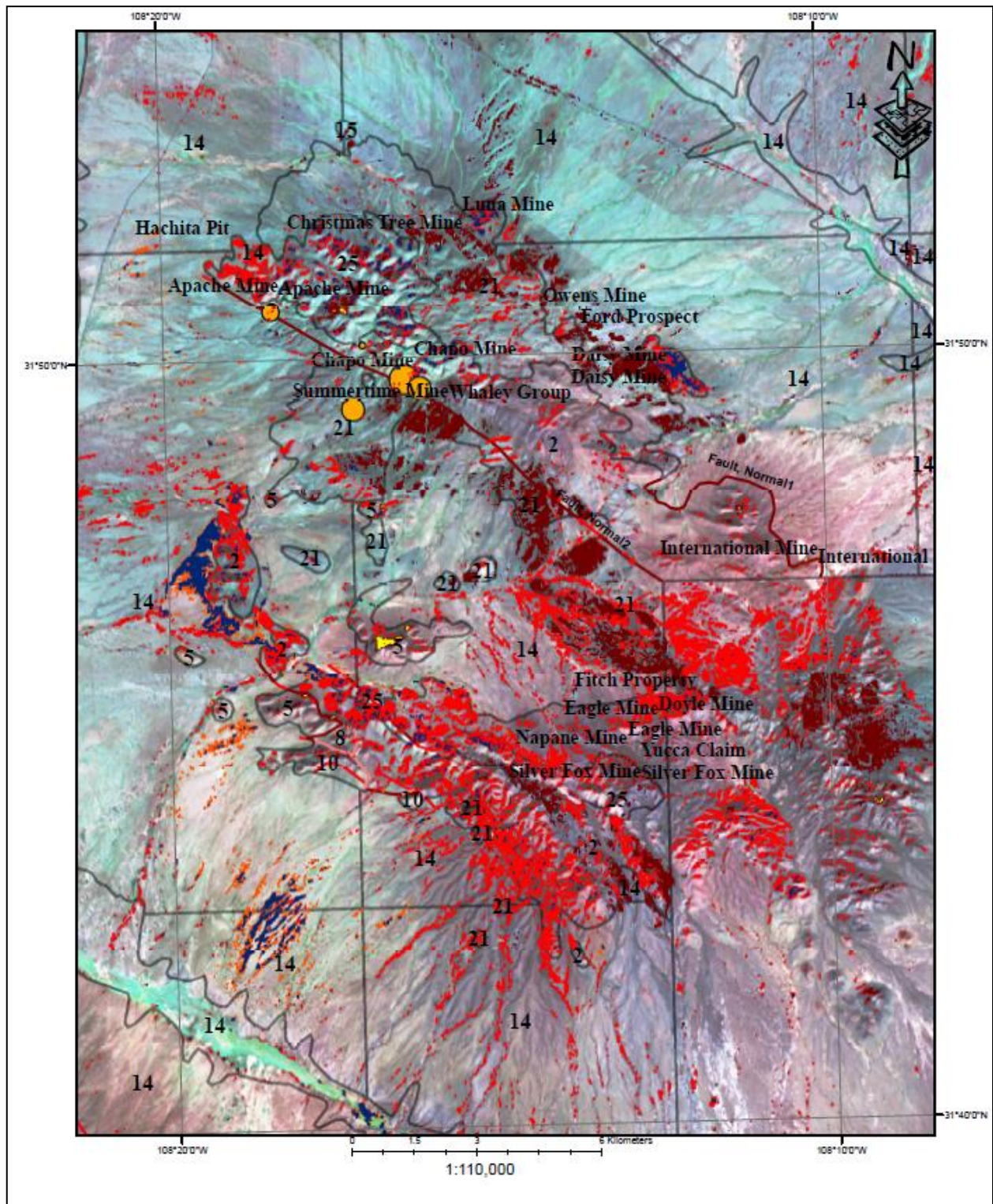


Figure 55g: ArcGIS image of the Apache Hills in RGB (7,4,2) with contact boundaries for general lithological mapping (Imbroane, 2007). A compilation of several band ratios (Figures 55c, 55d, 55 e, and 55f) and Actlab analysis results for copper are included.

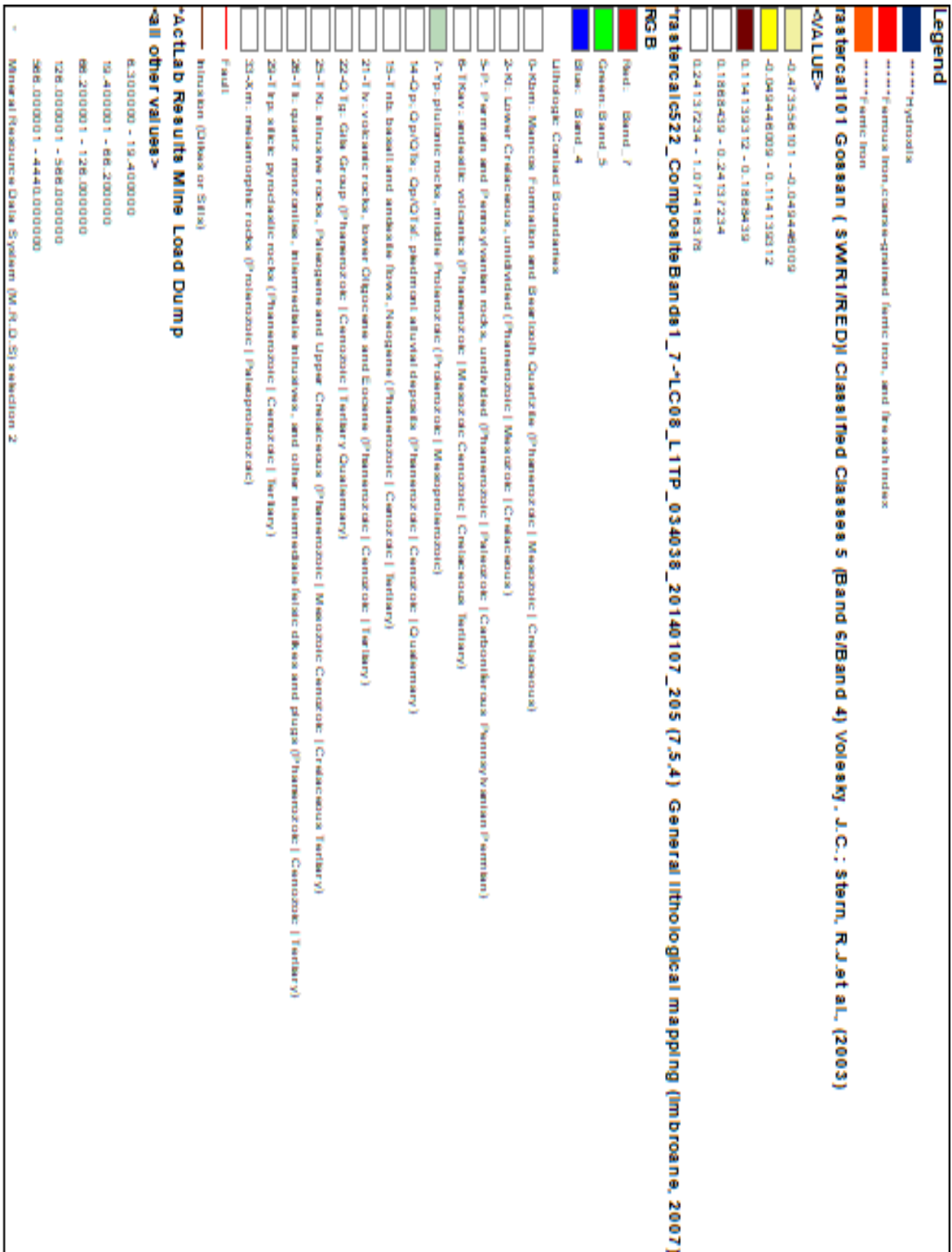


Figure 55h: Legend that describes all the band combinations (Figure 55g) lithology, faults, MRDS mine data, and Actlabs analysis results for copper.

5.5 Spectral Wavelength Signatures (USGS-PRISM, GER3700 & TSG 8 Data Image-Results)

The spectral wavelength signature results incorporate several method techniques that use (1) USGS-PRISM add-on data file of the spectral wavelength signatures incorporating ENVI 4.8 software. (2) The 100-micron meshed sample (AH-001-AH-010) was analyzed with the spectroradiometer (GER3700) for wavelengths signature results, which are compared to the Spectral Library 2006a as a validation source for mineral accuracy. (3) The Spectral Geologist 8 software reinforces the GER 3700 and USGS-PRISM results that support the same or similar wavelength spectral signature of the mineral (e.g., Hematite and Goethite) known to be present in the study area.

5.5.1 USGS-PRISM

The library consists of different spectrometer types used to measure the spectra within the spectral library. The Beckman™ 5270 (480) encompasses the spectral Range of (0.2 to 3 μm) (Kokaly, R.F., 2011) and is the spectrometer type used (Figure 56) from the Spectral Library 2006a digital data (PRISM). The data is uploaded to ENVI 4.8 software.

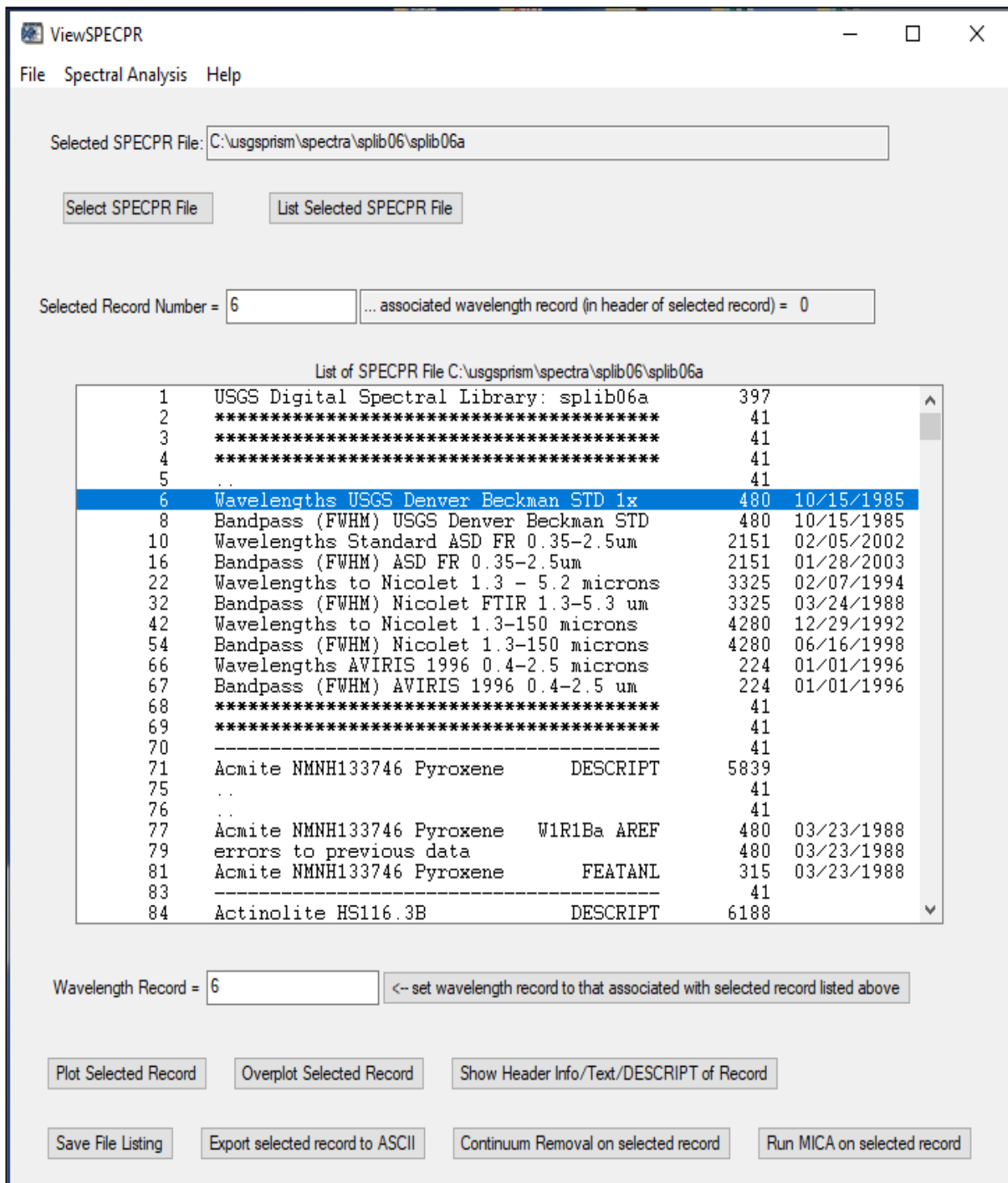


Figure 56: USGS spectral Library 2006a digital data (PRISM) add-on for ENVI 4.8 software. Spectrometer type: Beckman™ 5270 measures spectra in the library covering the spectral range 0.2 to 3 μm (Kokaly, R.F., 2011).

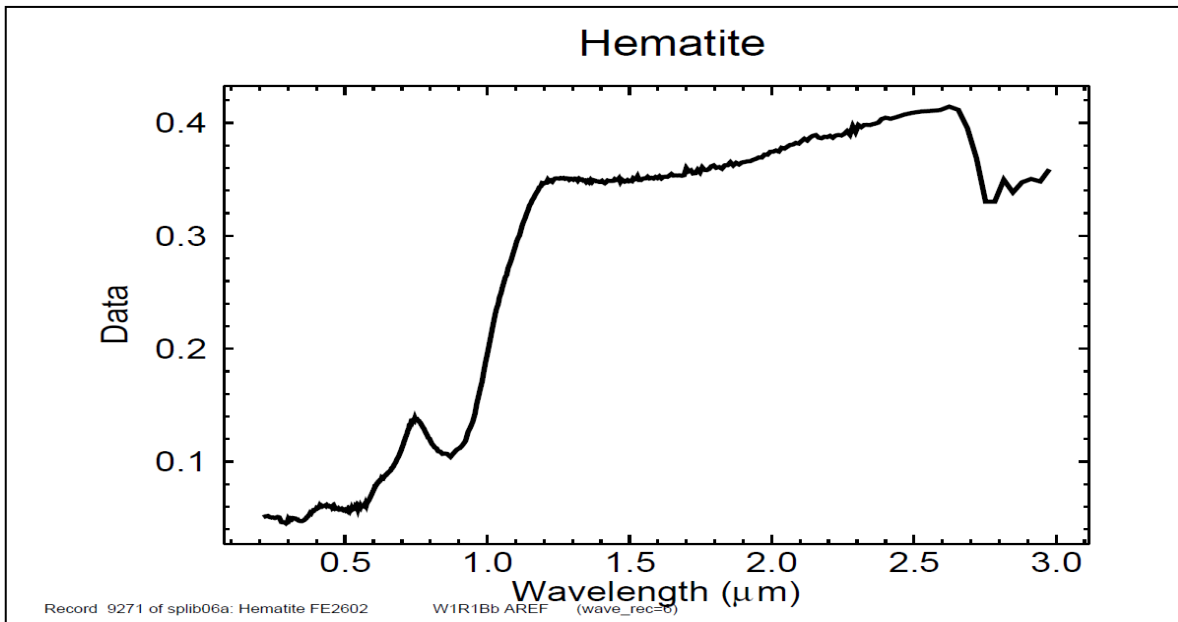


Figure 57: Wavelength spectral signature record (9271) of Hematite courtesy of the USGS Spectral Library 2006. For wavelength comparison and validation purposes, the data results from the GER 3700 and the Spectral Geologist 8.

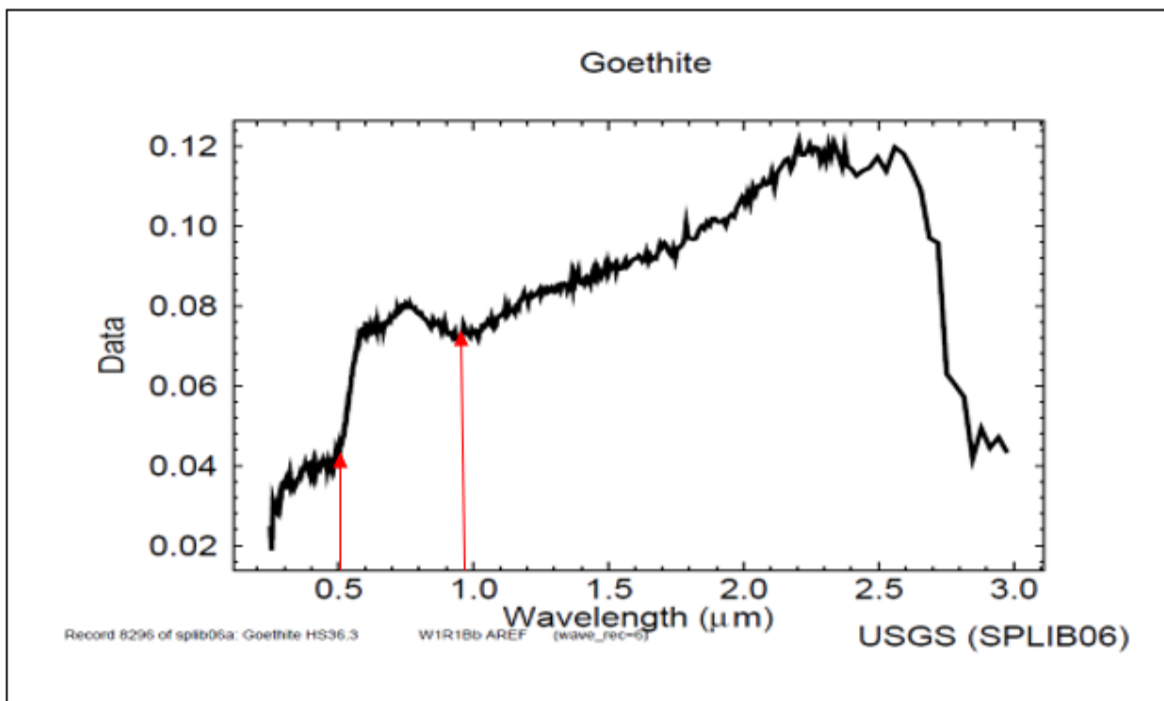


Figure 58: Wavelength spectral signature record (8296) of Goethite courtesy of the USGS Spectral Library 2006. For wavelength comparison and validation purposes, the data results from the GER 3700 and the Spectral Geologist 8.

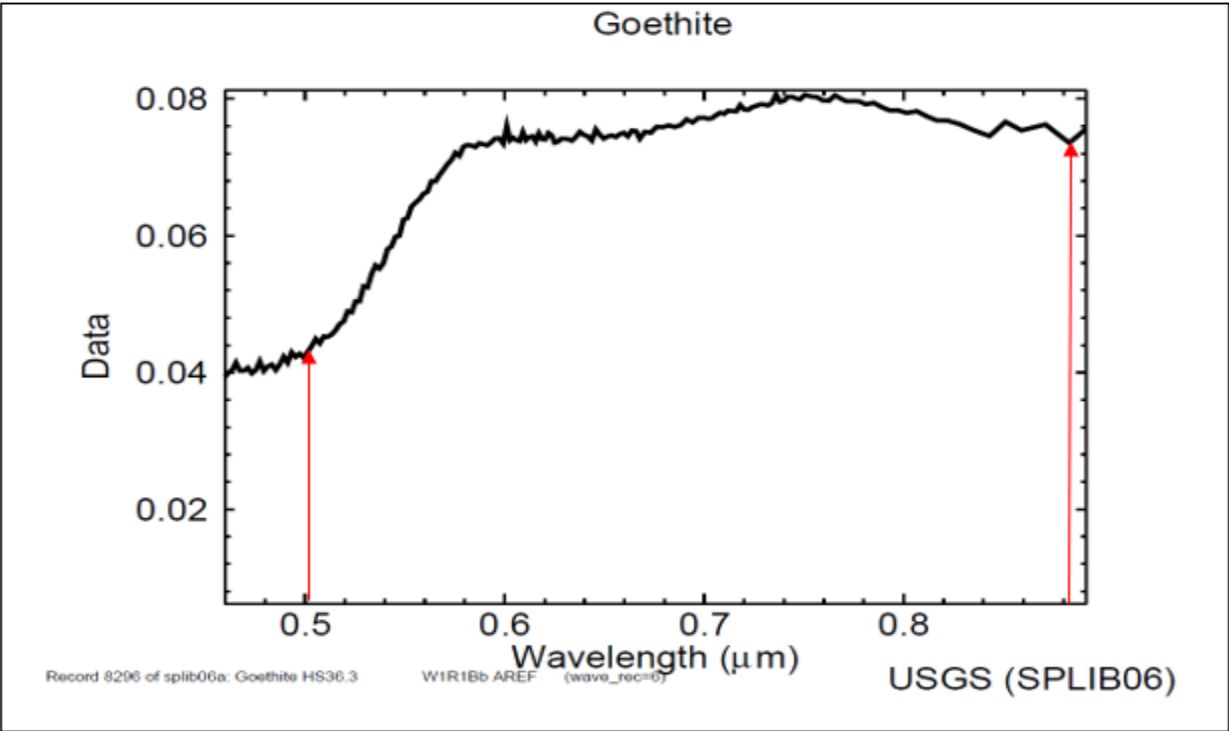


Figure 59: Wavelength spectral signature record (8296) closeup of image (0.5-0.9um) of Goethite courtesy of the USGS Spectral Library 2006. For wavelength and validation comparison purposes to the data results from the GER 3700 and The Spectral Geologist 8.

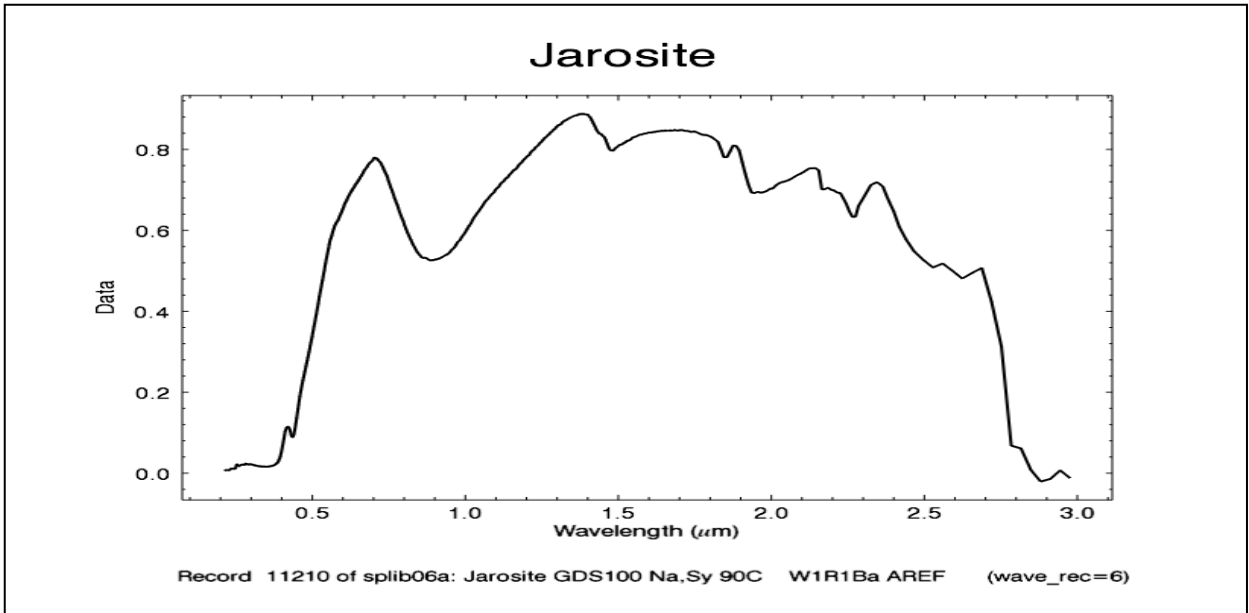
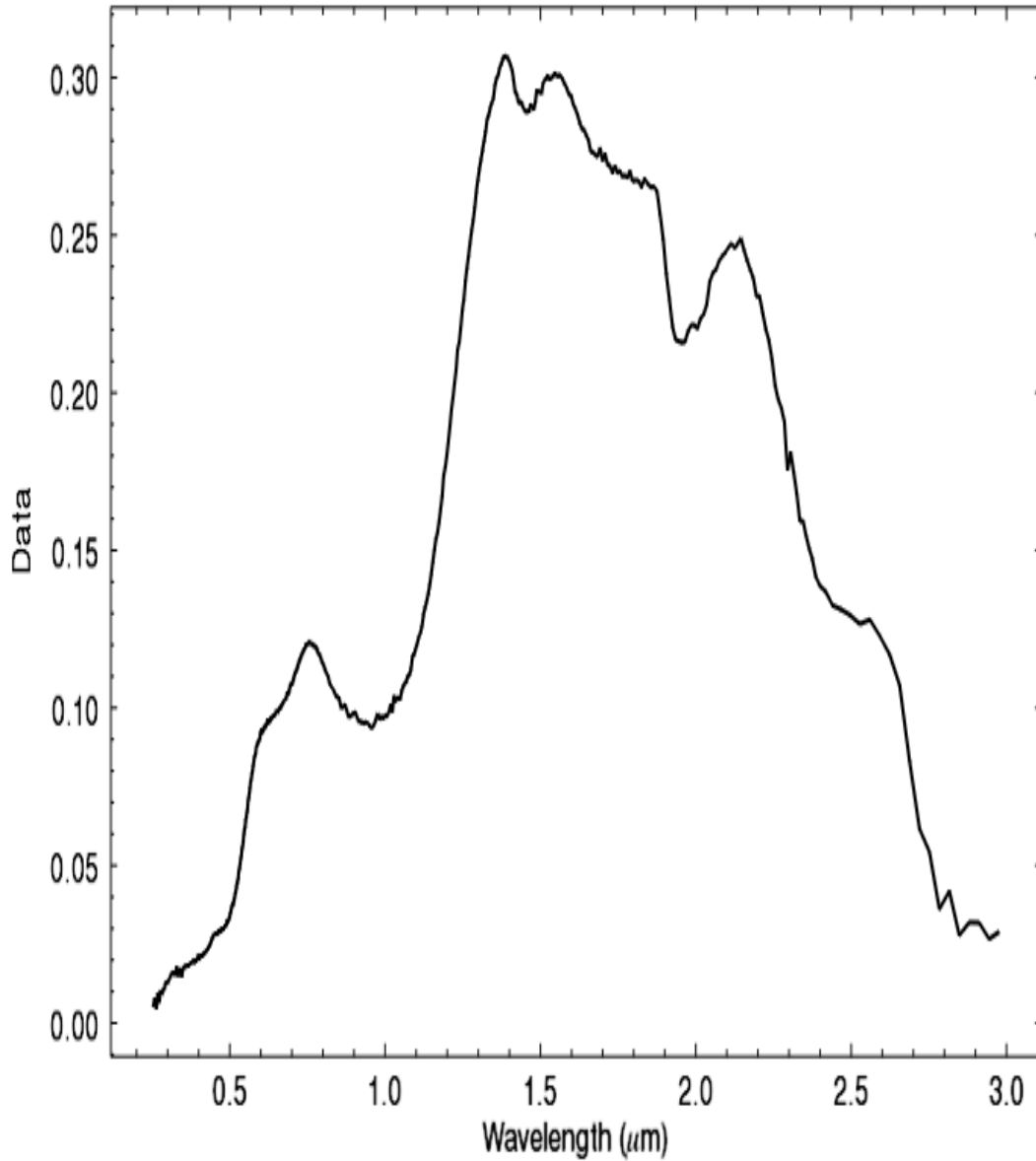


Figure-60: Wavelength spectral signature record (11210) of Jarosite courtesy of the USGS Spectral Library 2006a. For wavelength comparison and validation purposes, the data results from the GER 3700 and the Spectral Geologist 8. Jarosite is not a result of the Spectral Geologist 8 from the samples collected but shares a similar absorption feature of 0.925 (μm) as Goethite and should be recognized. The spectral wavelength signature, however, differentiates from that of Goethite.

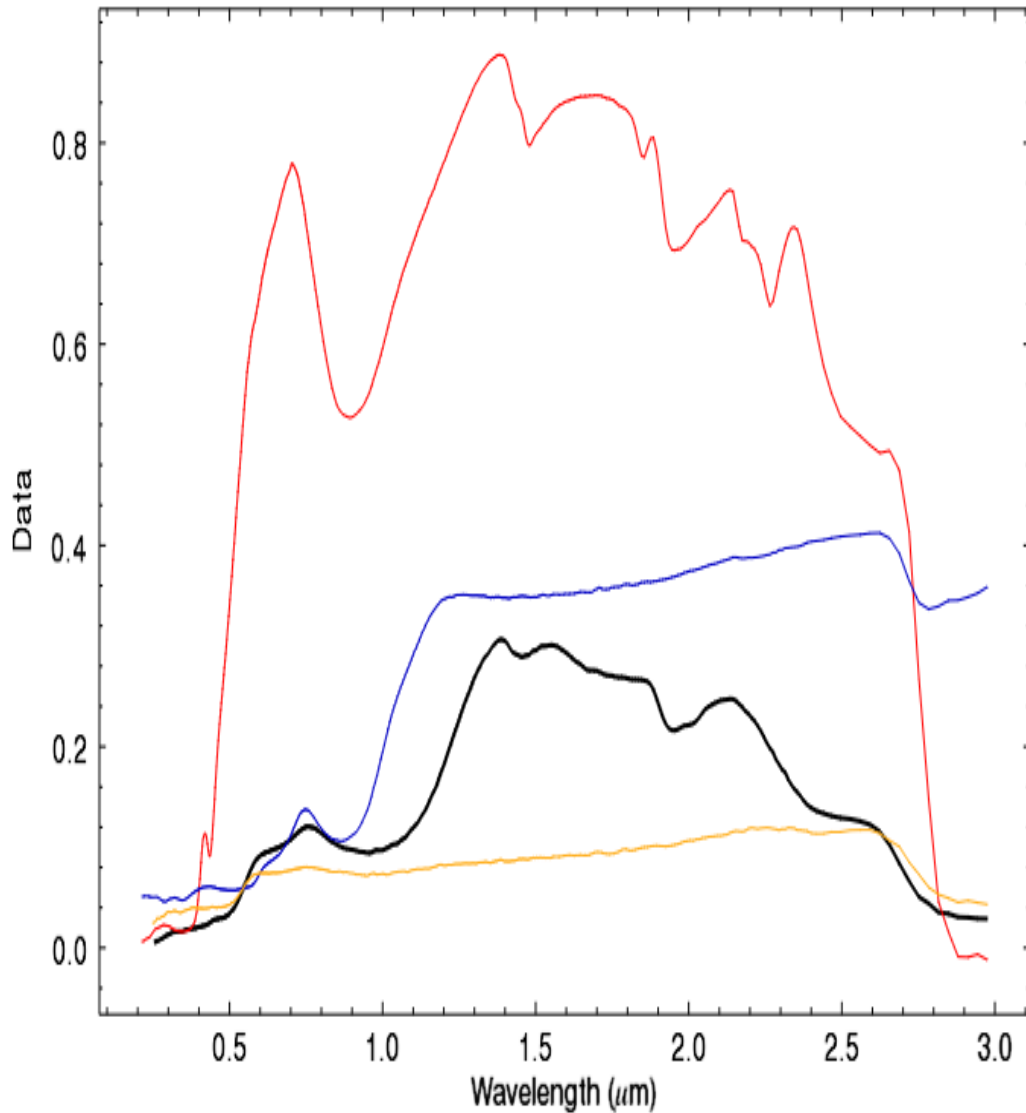
Limonite



Record 12886 of splib06a: Limonite HS41.3 WIR1BbAREF (wave_rec=6)

Figure 61: Wavelength spectral signature record (12886) of Limonite courtesy of the USGS Spectral Library 2006a. For wavelength comparison and validation purposes, the data results from the GER 3700 and the Spectral Geologist 8.

Wavelength Overplot Comparison



IPLLOT: splib06a

Record 12886 of splib06a: Limonite HS41.3	W1R1Bb AREF	(wave_rec=6)
Record 11210 of splib06a: Jarosite GDS100 Na,Sy 90C	W1R1Ba AREF	(wave_rec=6)
Record 9271 of splib06a: Hematite FE2602	W1R1Bb AREF	(wave_rec=6)
Record 8296 of splib06a: Goethite HS36.3	W1R1Bb AREF	(wave_rec=6)

Figure 62: Wavelength spectral signature records of (9271) Hematite, (8296) Goethite, (12886), Limonite, and Jarosite (11210) courtesy of the USGS Spectral library 2006a. For wavelength comparison and validation purposes, too, the data results from the GER 3700 and the Spectral Geologist 8.

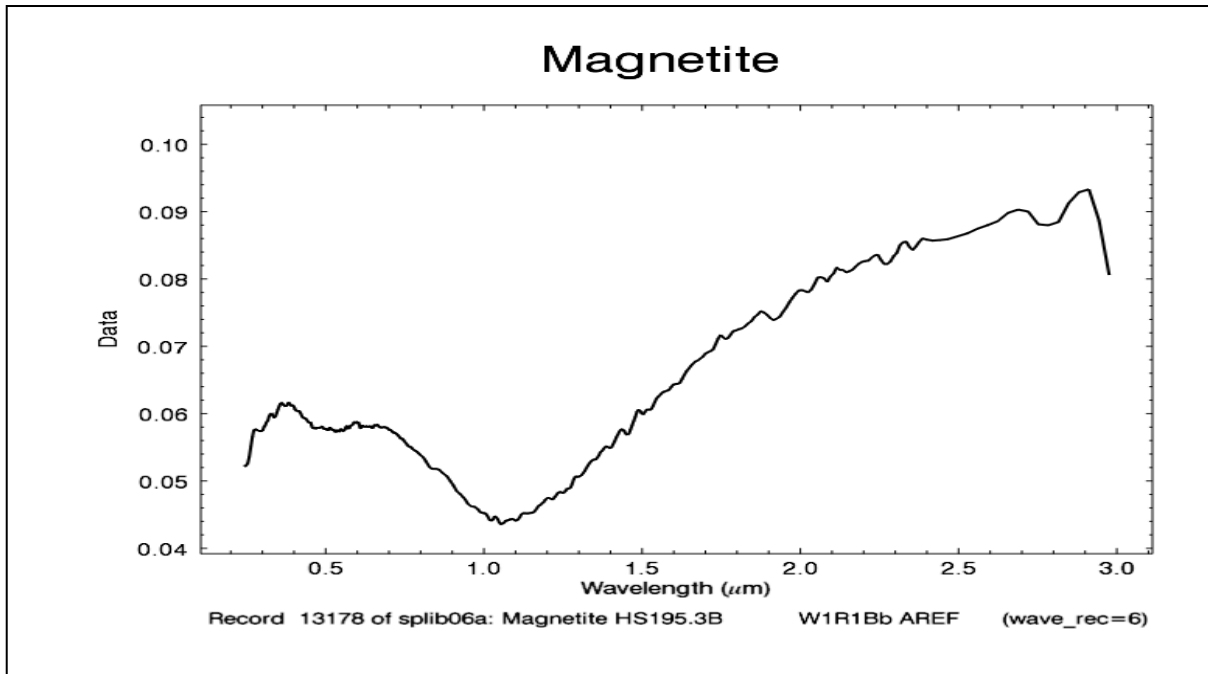


Figure 64: Wavelength spectral signature of Magnetite. Field surveys and previous research (Strongin, 1957) indicate the presence of this mineral.

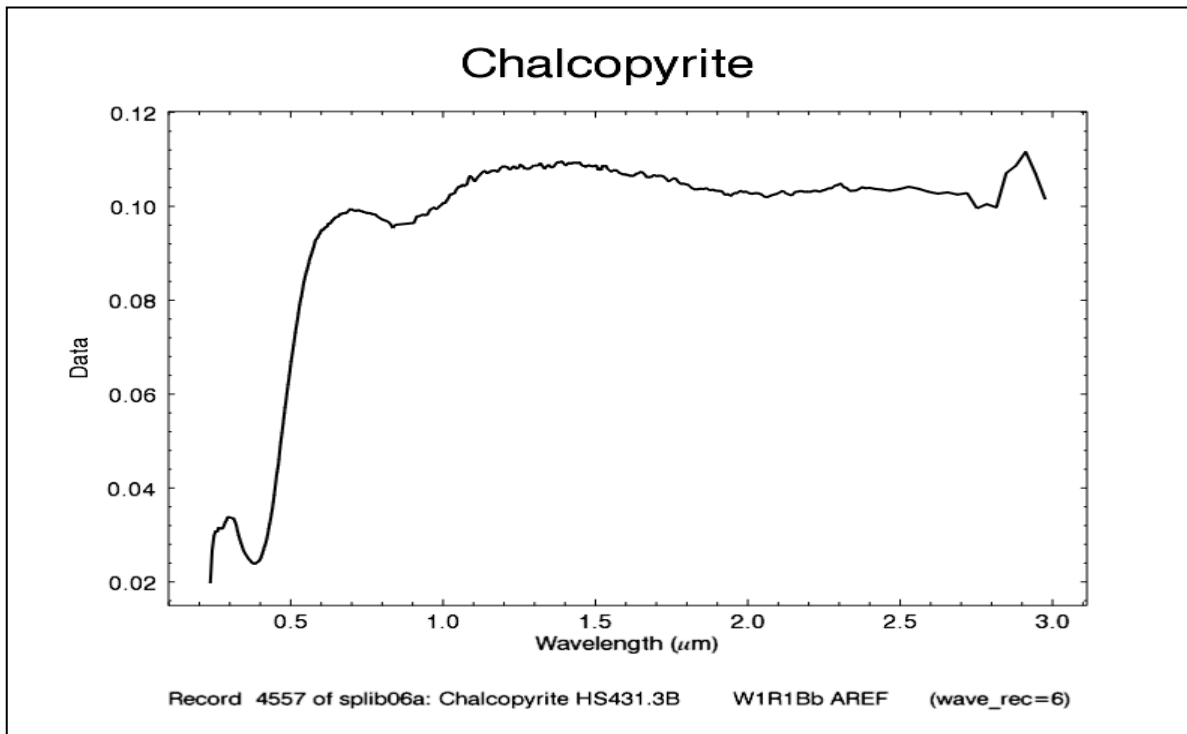


Figure 65: Wavelength spectral signature of Chalcopyrite. Field reconnaissance, and previous research (Strongin, 1957), indicates the presence of this mineral.

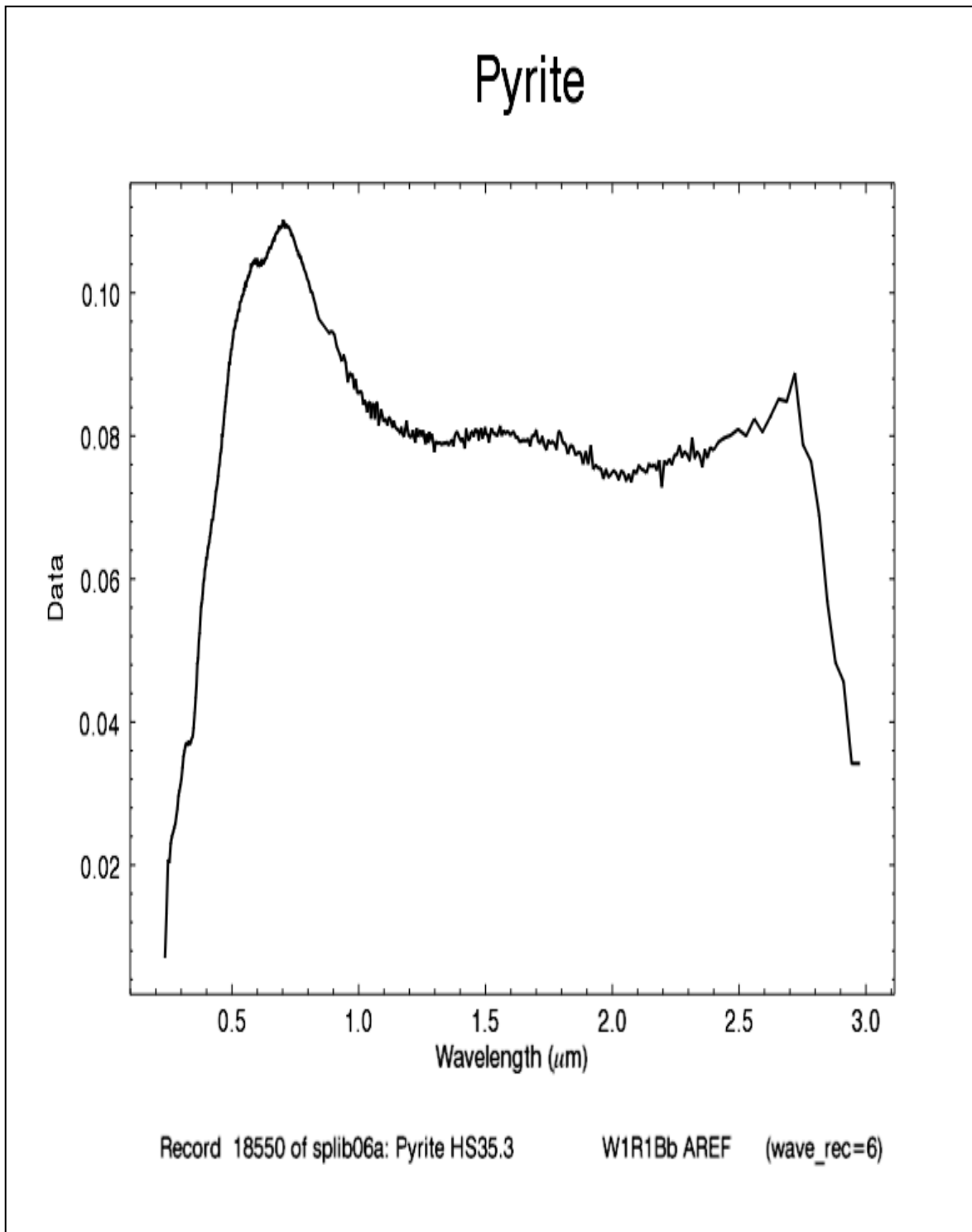


Figure 66: Wavelength spectral signature of Pyrite. Field reconnaissance, and previous research (Strongin, 1957) indicate the presence of this mineral.

5.5.2 The Spectral Geologist 8 (TSG 8) & GER3700 (Spectroradiometer)

A combination of the Spectral Geologist 8 (TSG 8) and the GER 3700 (Spectroradiometer) is used to identify and validate the presence of iron alteration minerals in the samples collected from Apache Hill, Hidalgo, County, New Mexico. The spectral wavelength results from the GER 3700 configuration setup (Figure 27) reveal the spectral wavelength of the ten samples provided, sieved at 100 mesh. The numerical data is further processed, and an Excel spreadsheet is generated. The results are input into The Spectral Geologist 8 for signature wavelength comparison. The TSG 8 has a consortium of examples within the software to cross-reference with the data provided by the GER3700. It should be noted (disclaimer) that unreliable results, as seen in Figures 67,71, 73, 79, 82, 85, 91, and 94, are interpreted by the TSG 8 as spectral unmixing. The TSG 8 has not found a perfect fit; hence, the results are just the best estimate of the TSG 8 (Huntington, 1997; Berman, 1999). A smooth line is the wavelength signature from the TSG 8 reference library. The rough (e.g., squiggly) line is the wavelength that results from the GER3700. Figures 76 and 88, however, display as reliable. The wavelength and reflectance data input results from the GER 3700 are viewed through the Short-wave infrared (SWIR) (e.g., Figures 67, 70, 75, 78, 81, 84, 87, 90, and 93) and visible near-infrared (VNIR) (e.g., Figures 67,71, 73, 76, 88, 79, 82, 85, 91, and 94) spectral feature option of The Spectral Geologist 8 software.

It is a reminder that even TSA 8, a state-of-the-art automated spectral unmixing algorithm, is imperfect. A human should authenticate TSA results - ideally, an expert. The results should be checked against reference spectra provided in the TSG Reference library to ensure consistency (Berman 1999).

For VNIR spectra, the Not in Library (NIL) statistic is a non-negative number. When used with the default value of the regularization parameter, $\lambda = 0.9$, good quality spectra which are mixtures of (at most) two materials in the VNIR library, should have a NIL value threshold less than 60 (Berman 1999). VNIR spectra with a NIL value above this threshold should be cautiously treated (Berman 1999). Figures 67, 71, 73, 79, 82, 85, and 91 all had values higher than 60, but Figures 76 and 88 had values below the threshold. The spectral wavelength results from TSG 8 were cross-referenced with the USGS-PRISM spectral reference library 2006a [add-on] to ENVI 4.8 (e.g., Figures 57, 58, and 59) as a preliminary precaution for approximate identification. The spectral wavelength signatures from the TSG 8 and PRISM were a match. The candidate results (*) from the spectral analyst (TSG 8) identified Figures 69, 72, 74, 76, 77, 88, 89 as Goethite and Figures 80, 83, 86, 91, and 95 as Hematite. These mineral alterations are profoundly noticeable from the remote sensing results and have been documented in prior research for the Apache Hills.

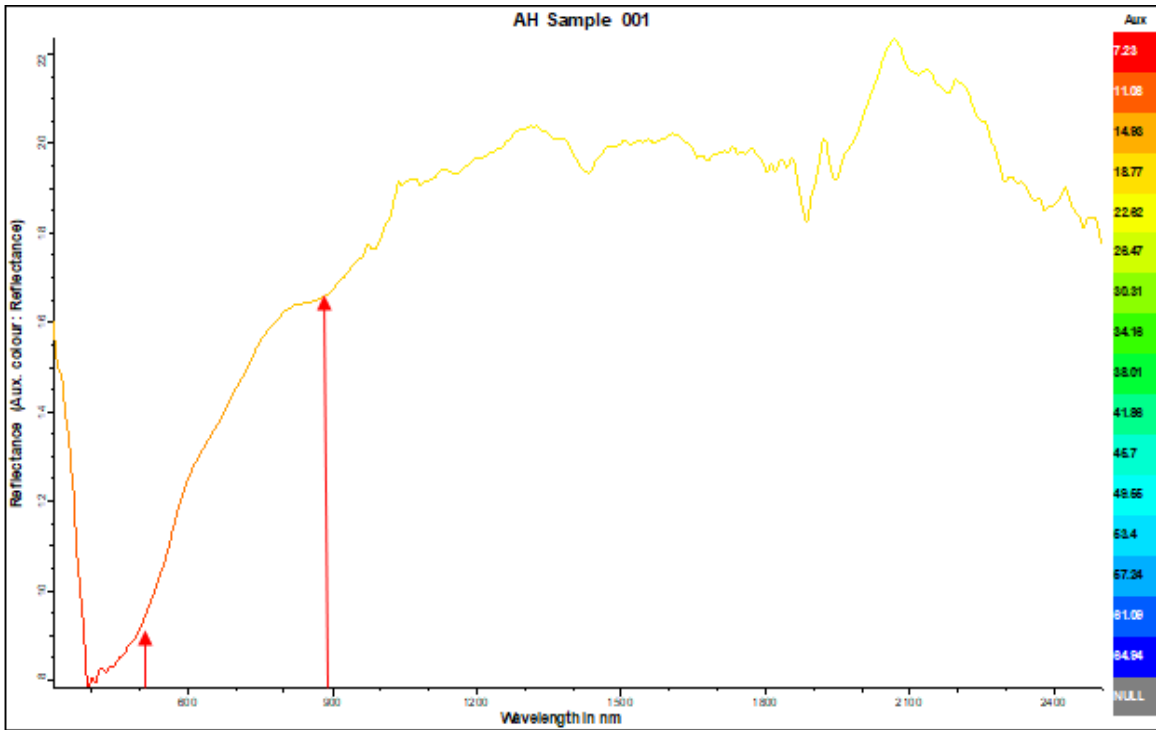


Figure 67: Apache Hills Sample 001 (Apache Mine) wavelength and reflectance data input results from the GER 3700 viewed through a combination of SWIR and VNIR from The Spectral Geologist 8 software platform.

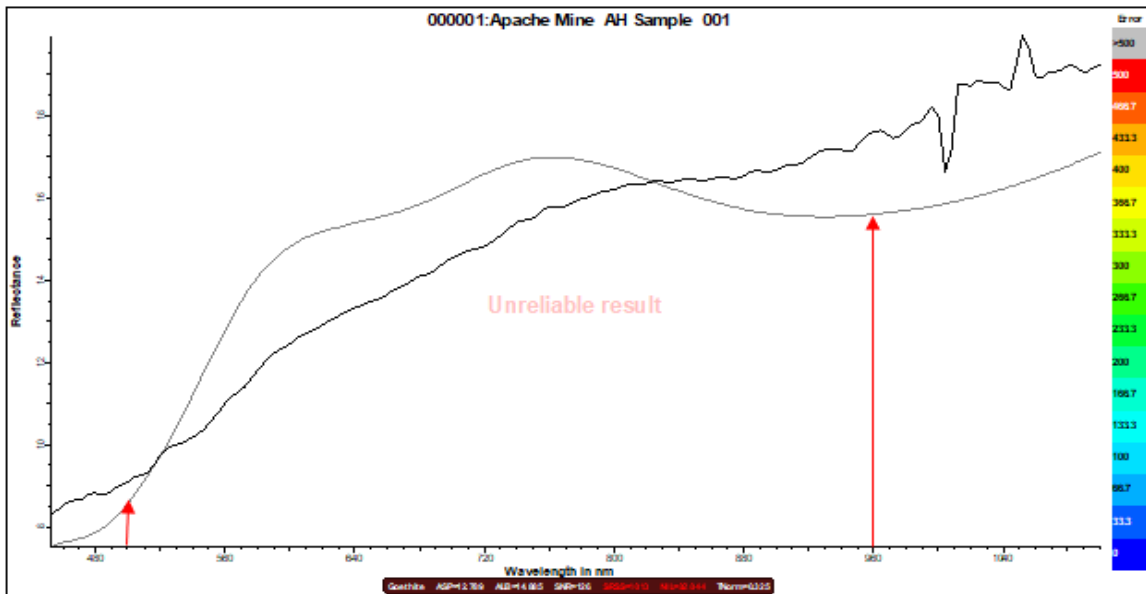


Figure 68: Apache Hills Sample 001 close-up of the image indicated by the red arrows (Apache Mine) wavelength and reflectance data input results from the GER 3700 viewed through the visible near-infrared (VNIR) spectral feature option of The Spectral Geologist 8 software platform. A smooth line is the wavelength signature for Goethite according to the Spectral Geologist 8 spectral library. The rough line is the wavelength results from the GER3700.

Candidate TSA results	
*Goethite	[1013]
Hematite	[1027]
Goethite	[2413]
Vegetation-Green	[3619]
55% Hematite + 45% Goethite	[538]
86% Hematite + 14% Vegetation-Green	[669]
74% Hematite + 26% Goethite	[811]
87% Goethite + 13% Vegetation-Green	[831]
78% Goethite + 22% Vegetation-Green	[1818]

Figure 69: Sample 001 candidate results from The Spectral Analyst Astrid (*) indicate a possible spectral signature match according to The Spectral Geologist 8 data library.

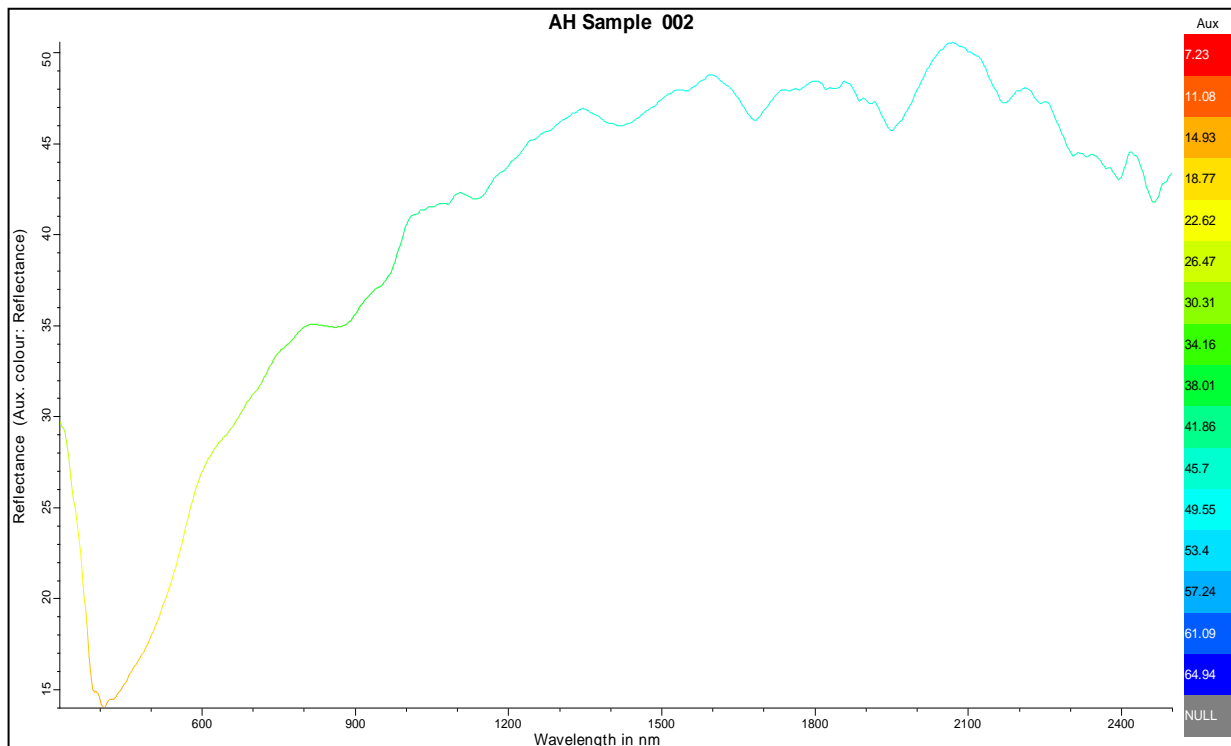


Figure 70: Apache Hills Sample 002 (Apache Mine) wavelength and reflectance data input results from the GER 3700 viewed through a combination of SWIR and VNIR from The Spectral Geologist 8 software platform.

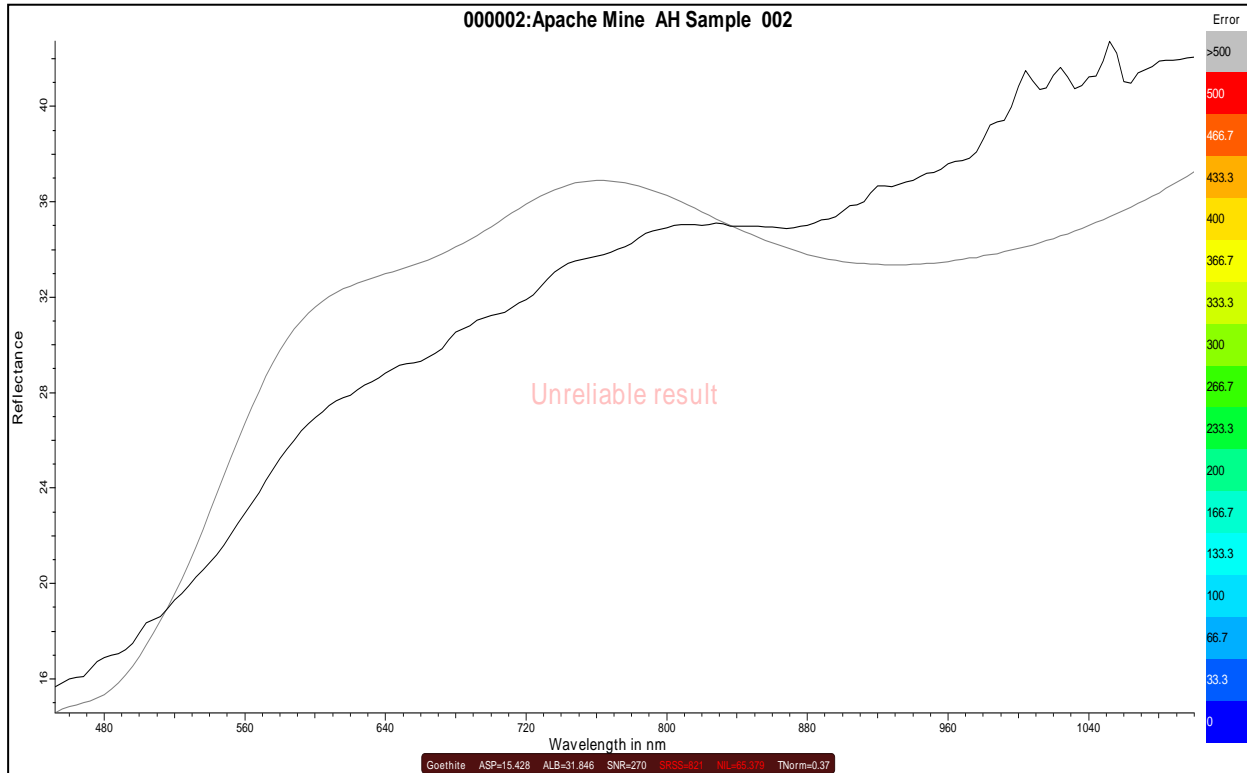


Figure 71: Apache Hills Sample 002 close-up of image (Apache Mine) wavelength and reflectance data input results from the GER 3700 viewed through the visible near-infrared (VNIR) spectral feature option of The Spectral Geologist 8 software platform. A smooth line is the wavelength signature for Goethite according to the Spectral Geologist 8 spectral library. The rough line is the wavelength results from the GER3700.

Candidate TSA results
*Goethite [821]
Hematite [1028]
Goethite [2148]
Vegetation-Green [3907]
50%Hematite + 50%Goethite [445]
92%Goethite + 8%Vegetation-Green [742]
69%Hematite + 31%Goethite [744]
88%Hematite + 12%Vegetation-Green [780]
83%Goethite + 17%Vegetation-Green [1768]

Figure 72: Sample 002 candidate results from The Spectral Analyst Astrid (*) indicate a possible spectral signature match according to The Spectral Geologist 8 data library.

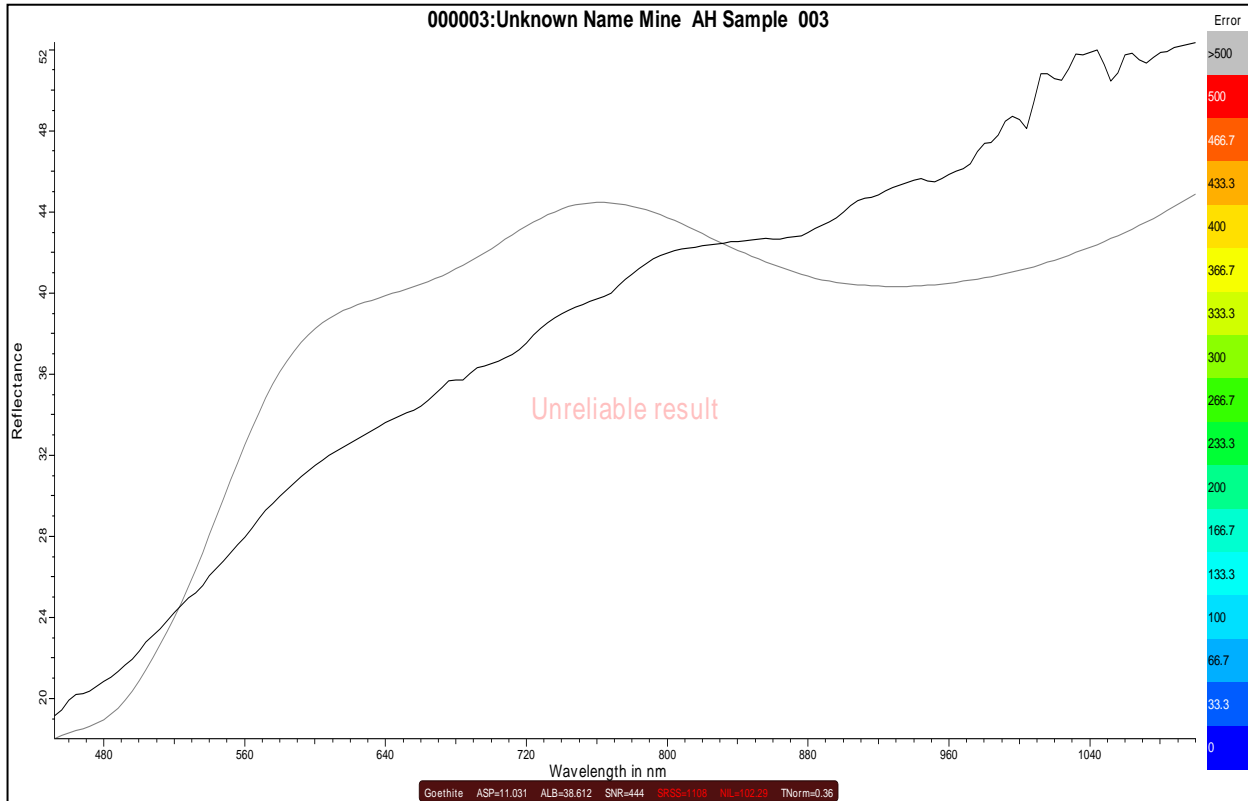


Figure 73: Apache Hills Sample 003 (unknown Mine-Adjacent to Chapo Mine) wavelength and reflectance data input close-up results from the GER 3700 viewed through visible near-infrared (VNIR) spectral feature option of The Spectral Geologist 8 software platform. A smooth line is the wavelength signature for Goethite according to the Spectral Geologist 8 spectral library. The rough line is the wavelength results from the GER3700.

Candidate TSA results
*Goethite [1108]
Hematite [1203]
Goethite [2482]
Vegetation-Green [3549]
53%Hematite + 47%Goethite [708]
86%Hematite + 14%Vegetation-Green [858]
87%Goethite + 13%Vegetation-Green [943]
74%Hematite + 26%Goethite [1004]
78%Goethite + 22%Vegetation-Green [1913]

Figure 74: Sample 003 candidate results from The Spectral Analyst feature denotes an Astrid (*) indicating a possible spectral signature match according to The Spectral Geologist 8 data library.

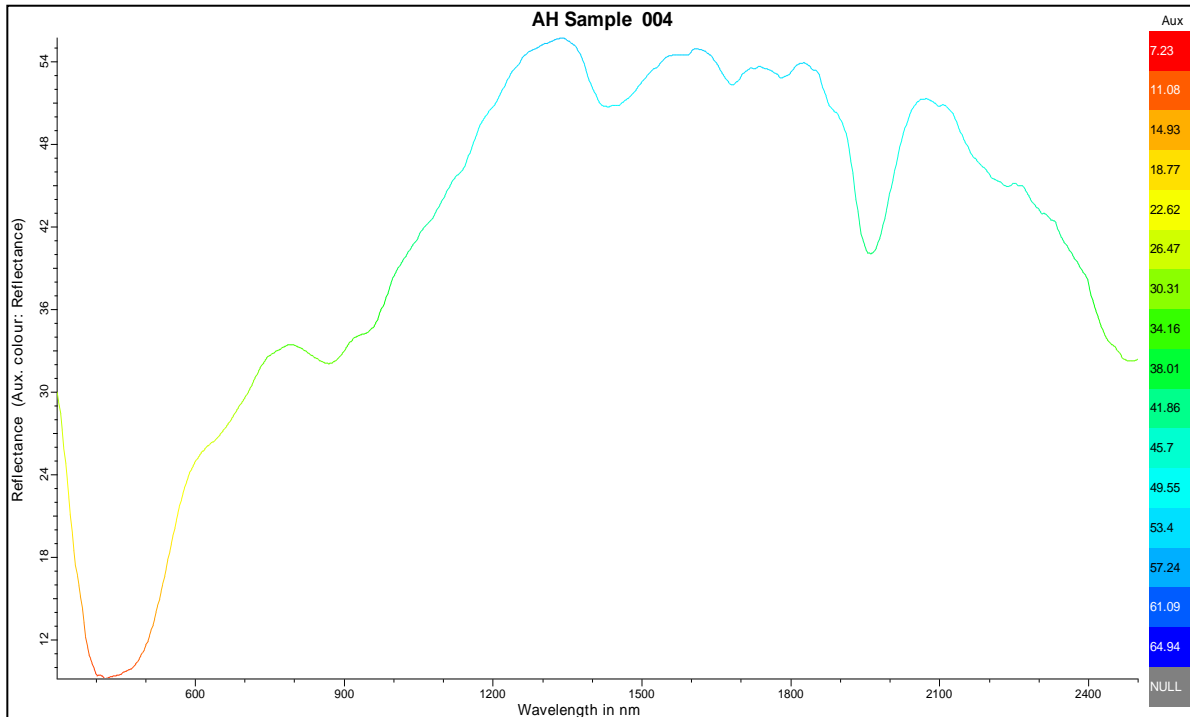


Figure 75: Apache Hills Sample 004 (Chapo Mine) wavelength and reflectance data input results from the GER 3700 viewed through a combination of SWIR and VNIR from The Spectral Geologist 8. software platform.

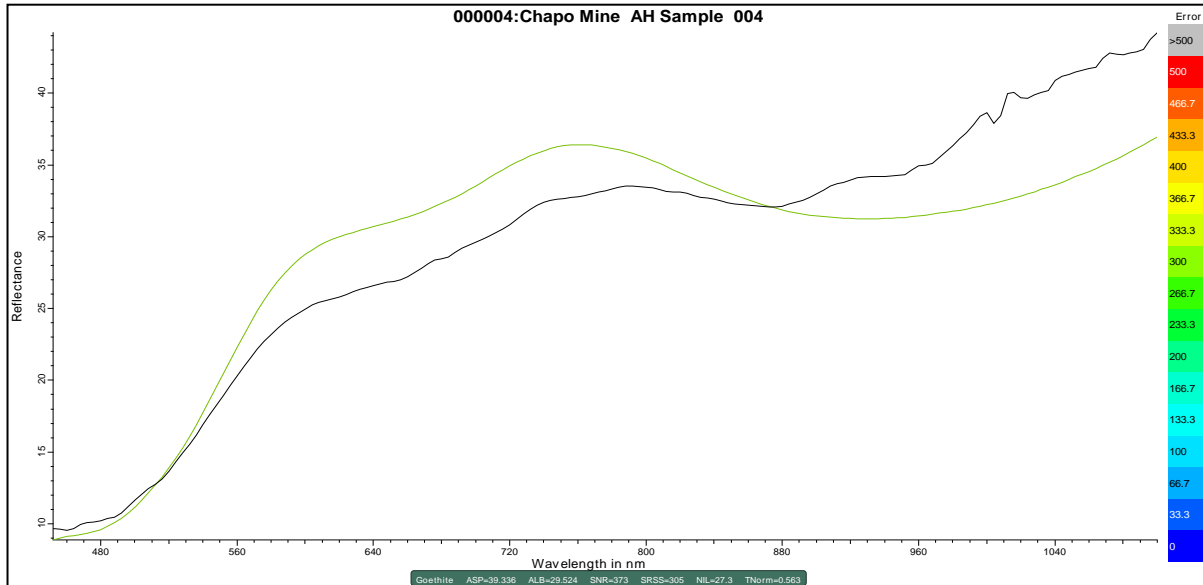


Figure 76: Apache Hills Sample 004 (Chapo Mine) wavelength and reflectance data input close-up results from the GER 3700 viewed through the visible near-infrared (VNIR) spectral feature option of The Spectral Geologist 8 software platform. A smooth line is the wavelength signature for Goethite according to the Spectral Geologist 8 spectral library. The rough line is the wavelength results from the GER3700.

Candidate TSA results
*Goethite [305]
Goethite [1107]
Hematite [1202]
Vegetation-Green [3795]
70%Goethite + 30%Hematite [189]
96%Goethite + 4%Vegetation-Green [283]
71%Goethite + 29%ODZincalume [298]
51%Goethite + 49%Hematite [430]
88%Hematite + 12%Vegetation-Green [949]
90%Goethite + 10%Vegetation-Green [959]

Figure 77: Sample 004 candidate results from The Spectral Analyst feature denotes an Astrid (*) indicating a possible spectral signature match according to The Spectral Geologist 8 data library.

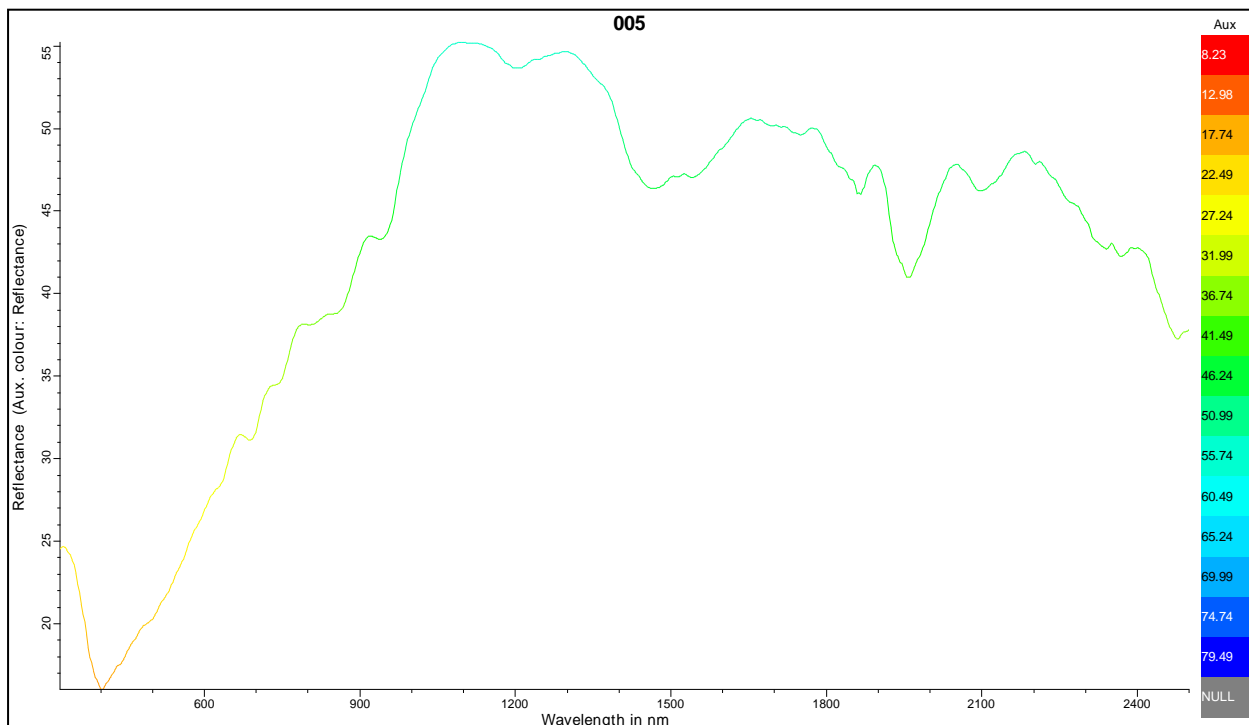


Figure 78: Apache Hills Sample 005 (Mairland Mine) wavelength and reflectance data input results from the GER 3700 viewed through a combination of SWIR and VNIR from The Spectral Geologist 8 software platform.

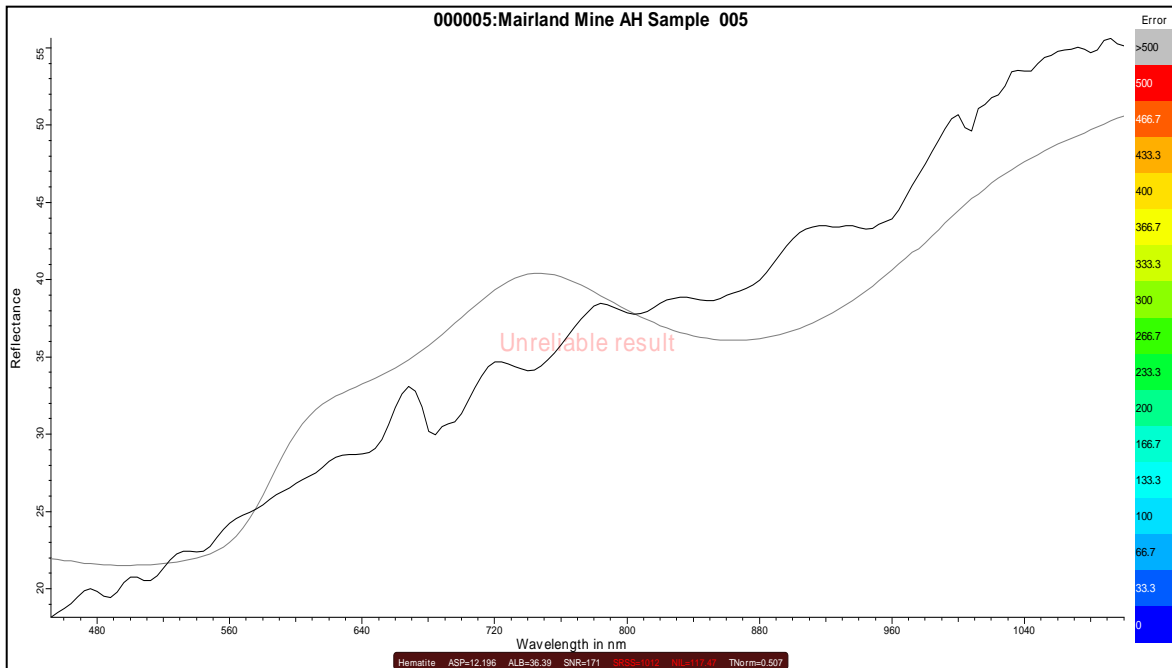


Figure 79: Apache Hills Sample 005 (Mairland Mine) wavelength and reflectance data input close-up results from the GER 3700 viewed through the visible near-infrared (VNIR) spectral feature option of The Spectral Geologist 8 software platform. A smooth line is the wavelength signature for Hematite according to the Spectral Geologist 8 spectral library. The rough line is the wavelength results from the GER3700.

Candidate TSA results	
*Hematite [1012]	
Goethite [1752]	
Goethite [3153]	
Vegetation-Green [3992]	
90%Hematite + 10%Vegetation-Green [815]	
75%Hematite + 25%Goethite [863]	
89%Hematite + 11%Goethite [981]	
86%Goethite + 14%Vegetation-Green [1573]	
59%Goethite + 41%ODZincalume [1734]	
76%Goethite + 24%Vegetation-Green [2543]	
78%Vegetation-Green + 22%ODZincalume [3991]	

Figure 80: Sample 005 candidate results from The Spectral Analyst feature denotes an Astrid (*) indicating a possible spectral signature match according to The Spectral Geologist 8 data library.

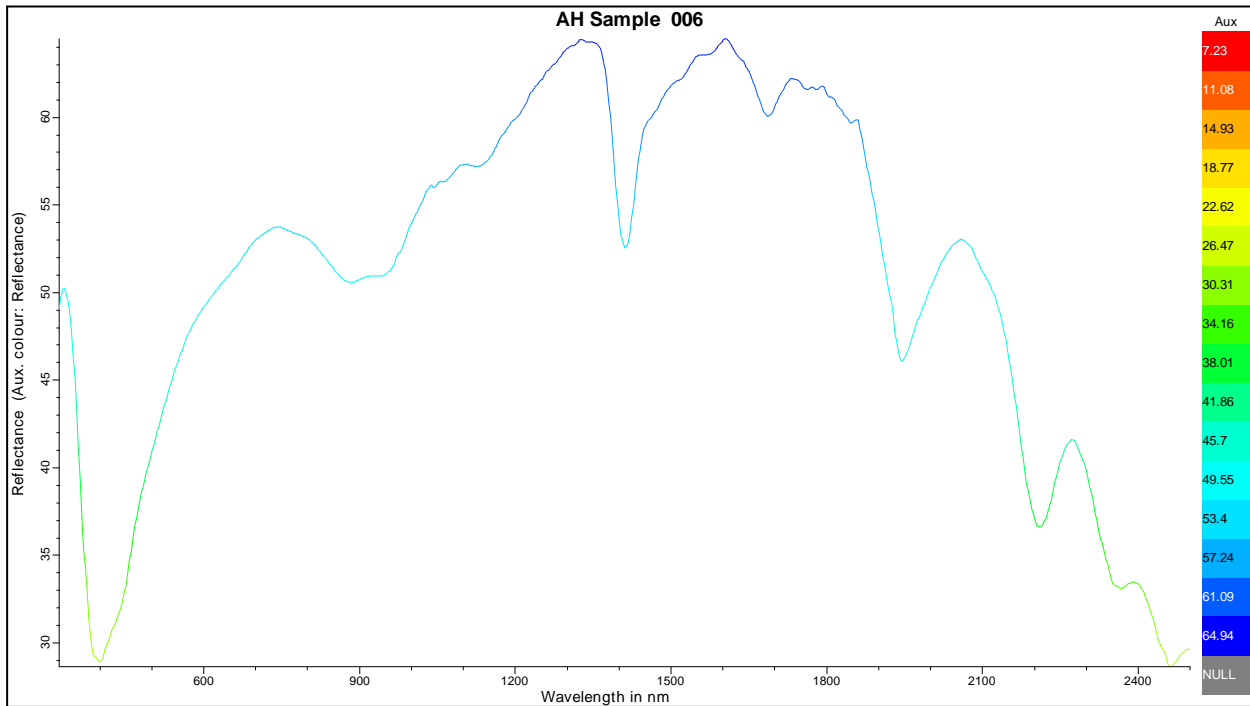


Figure 81: Apache Hills Sample 006 (Last Chance Mine) wavelength and reflectance data input results from the GER 3700 viewed through a combination of SWIR and VNIR from The Spectral Geologist 8 software platform.

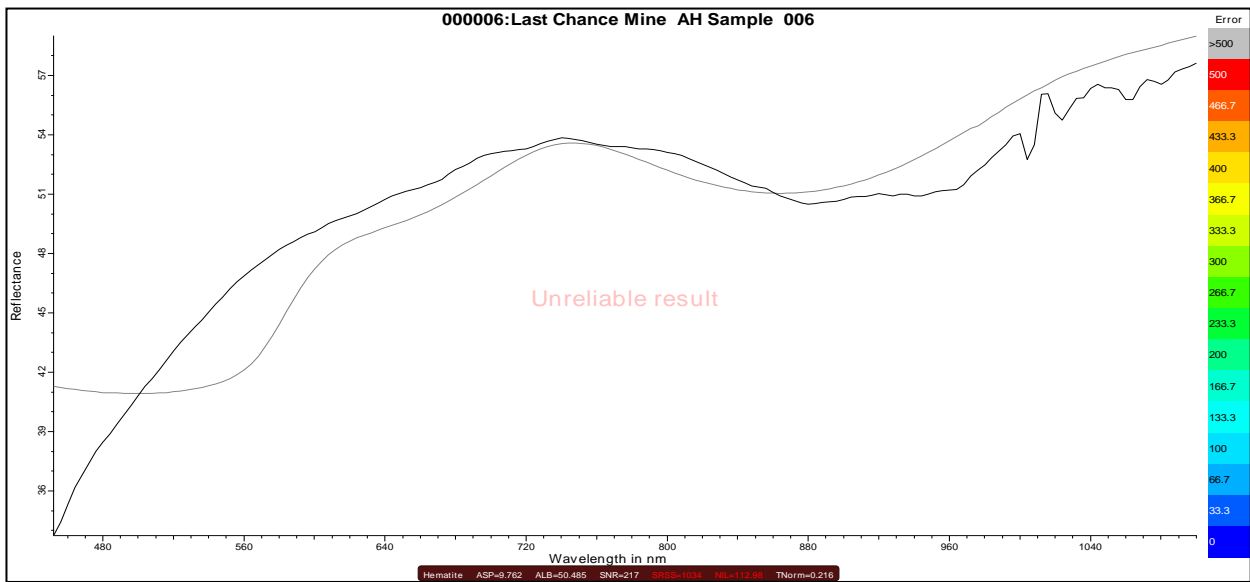


Figure 82: Apache Hills Sample 006 (Last Chance Mine) wavelength and reflectance data input close-up results from the GER 3700 viewed through the visible near-infrared (VNIR) spectral feature option of The Spectral Geologist 8 software platform. A smooth line is the wavelength signature for Hematite according to the Spectral Geologist 8 spectral library. The rough line is the wavelength results from the GER3700.

Candidate TSA results	
*Hematite	[1034]
Goethite	[1238]
Goethite	[2041]
Vegetation-Green	[3910]
62%Hematite + 38%Goethite	[767]
73%Hematite + 27%Goethite	[857]
75%ODZincalume + 25%Goethite	[886]
94%Hematite + 6%Vegetation-Green	[975]
65%Hematite + 35%GalvanisedIron	[978]
96%Goethite + 4%Vegetation-Green	[1223]
97%Goethite + 3%GalvanisedIron	[1238]
89%Goethite + 11%Vegetation-Green	[1905]
50%ODZincalume + 50%Goethite	[1989]
81%ODZincalume + 19%Vegetation-Green	[3751]

Figure 83: Sample 006 candidate results from The Spectral Analyst feature denotes an Astrid (*) indicating a possible spectral signature match according to The Spectral Geologist 8 data library.

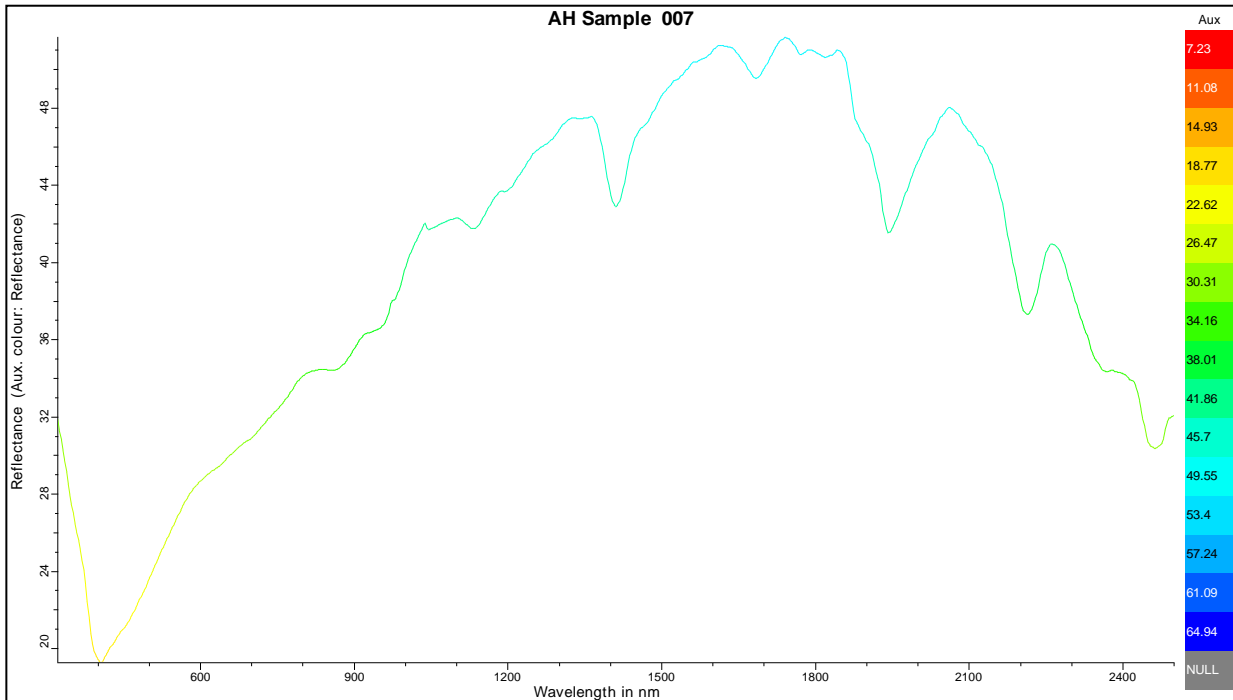


Figure 84: Apache Hills Sample 007 (Last Chance Mine) wavelength and reflectance data input results from the GER 3700 viewed through a combination of SWIR and VNIR from The Spectral Geologist 8 software platform.

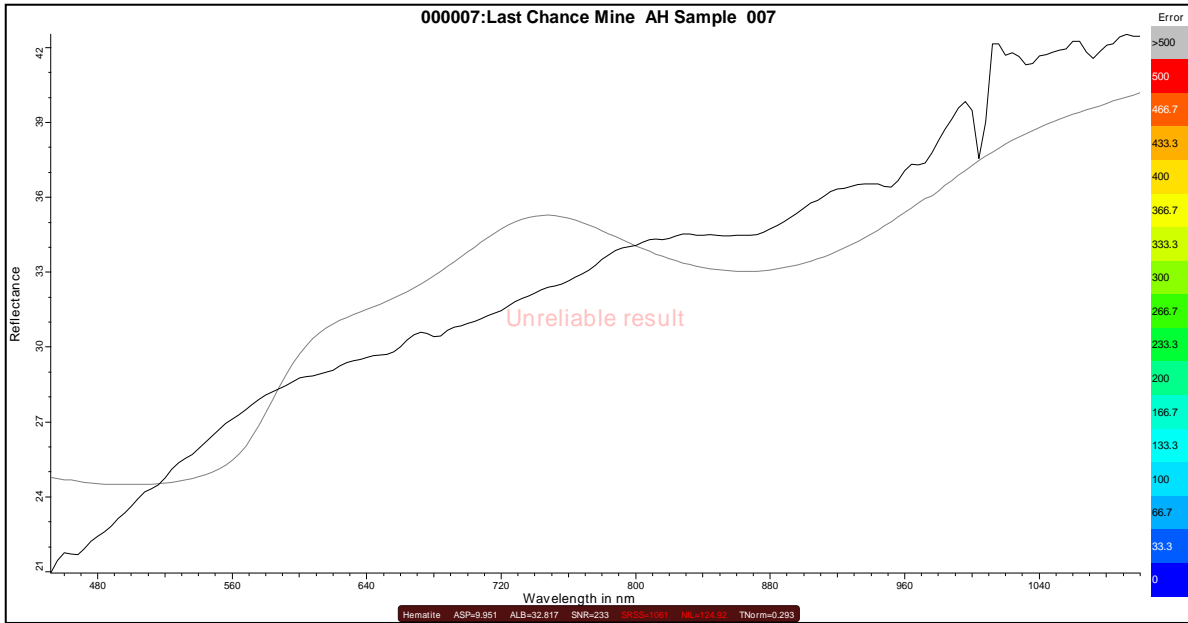


Figure 85: Apache Hills Sample 007 (Last Chance Mine) wavelength and reflectance data input close-up results from the GER 3700 viewed through the visible near-infrared (VNIR) spectral feature option of The Spectral Geologist 8 software platform. A smooth line is the wavelength signature for Hematite according to the Spectral Geologist 8 spectral library. The rough line is the wavelength results from the GER3700.

Candidate TSA results
*Hematite [1061]
Goethite [1403]
Goethite [2519]
Vegetation-Green [3346]
67%Hematite + 33%Goethite [836]
88%Hematite + 12%Vegetation-Green [841]
82%Hematite + 18%Goethite [979]
86%Goethite + 14%Vegetation-Green [1250]
52%ODZincalume + 48%Goethite [1362]
77%Goethite + 23%Vegetation-Green [2026]
53%ODZincalume + 47%Vegetation-Green [3335]

Figure 86: Sample 007 candidate results from The Spectral Analyst feature denotes an Astrid (*) indicating a possible spectral signature match according to The Spectral Geologist 8 data library.

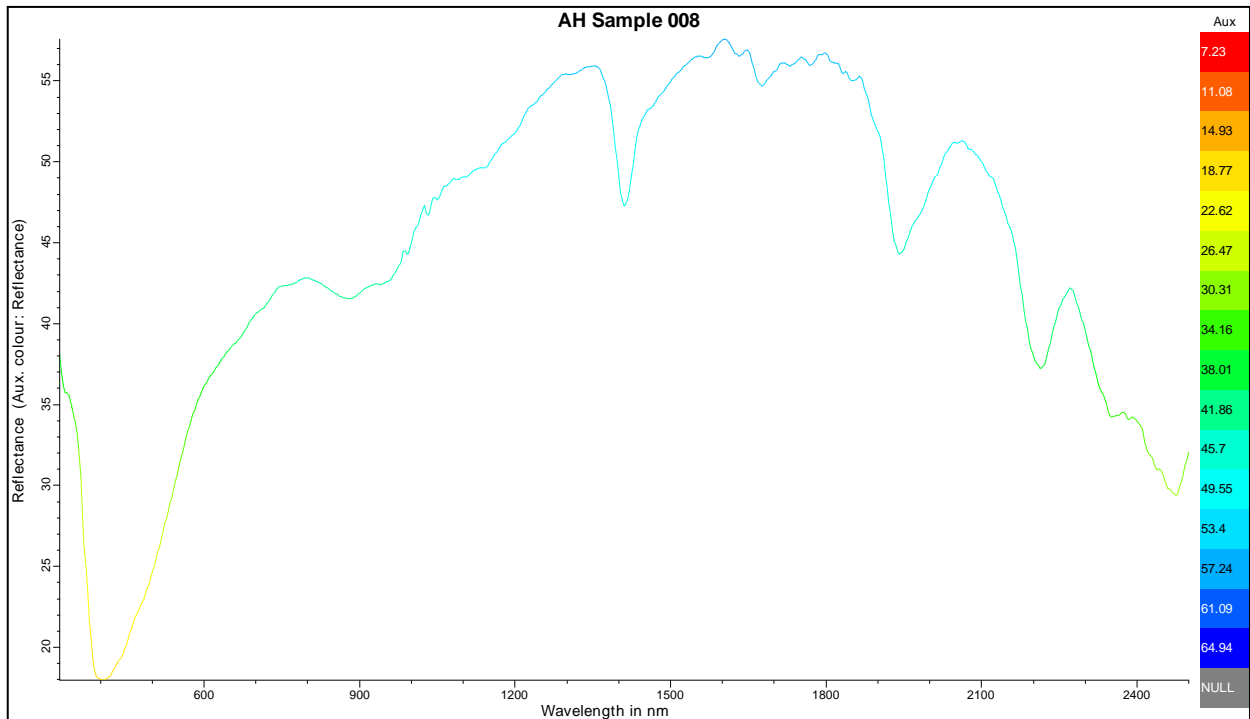


Figure 87: Apache Hills Sample 008 (Last Chance Mine) wavelength, and reflectance data input results from the GER 3700 viewed through a combination of SWIR and VNIR from The Spectral Geologist 8 software platform.

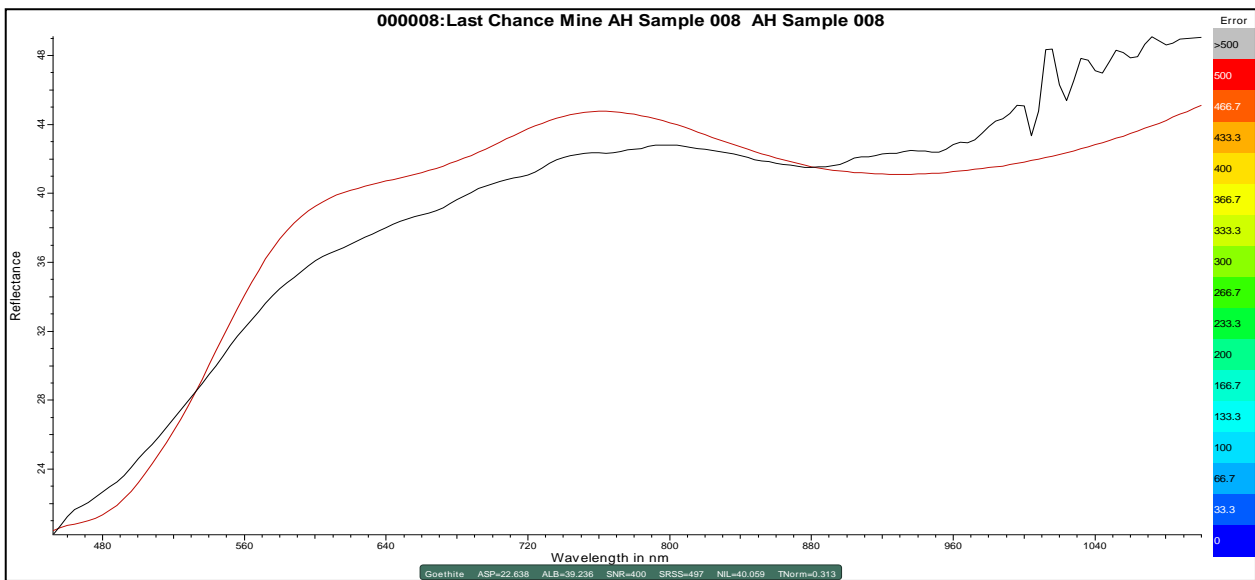


Figure 88: Apache Hills Sample 008 (Last Chance Mine) wavelength, and reflectance data input close-up results from the GER 3700 viewed through the visible near-infrared (VNIR) spectral feature option of The Spectral Geologist 8 software platform. A smooth line is the wavelength signature for Goethite according to the Spectral Geologist 8 spectral library. The rough line is the wavelength results from the GER3700.

Candidate TSA results
*Goethite [497]
Hematite [884]
Goethite [1468]
Vegetation-Green [3604]
56%Goethite + 44%Hematite [242]
51%Goethite + 49%ODZincalume [458]
95%Goethite + 5%Vegetation-Green [467]
61%Hematite + 39%Goethite [472]
90%Hematite + 10%Vegetation-Green [702]
88%Goethite + 12%Vegetation-Green [1268]

Figure 89: Sample 008 candidate results from The Spectral Analyst feature denotes an Astrid (*) indicating a possible spectral signature match according to The Spectral Geologist 8 data library.

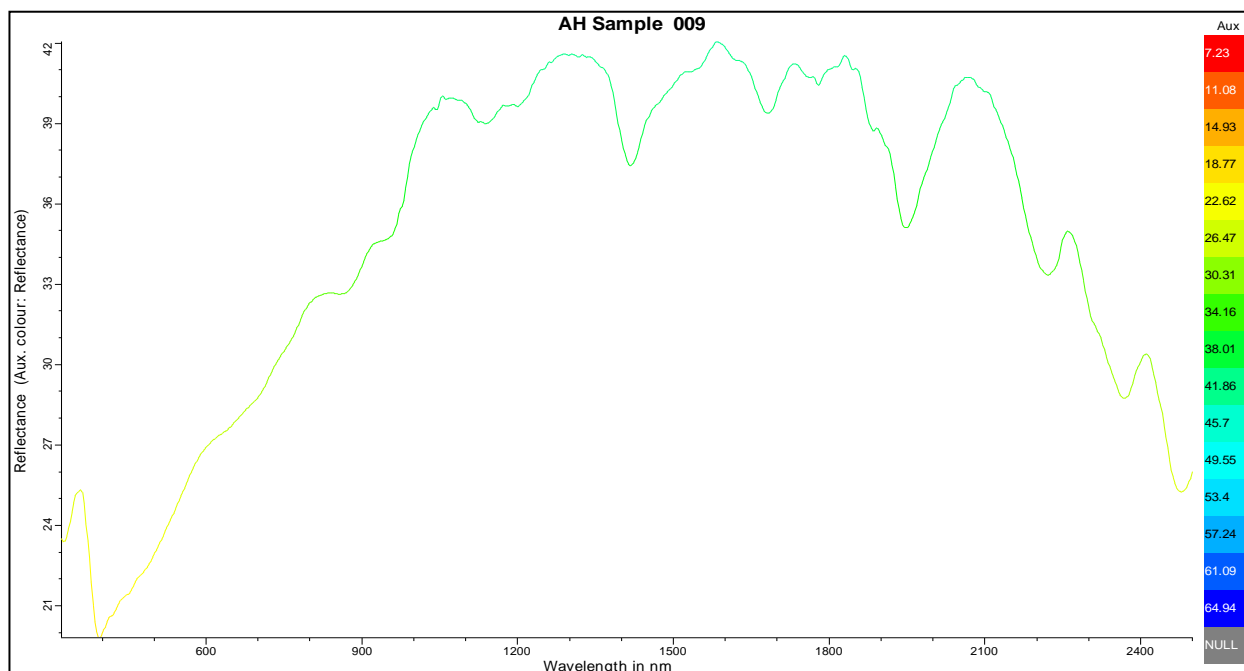


Figure 90: Apache Hills Sample 009 (Quartz Mine) wavelength and reflectance data input results from the GER 3700 viewed through a combination of SWIR and VNIR from The Spectral Geologist 8 software platform.

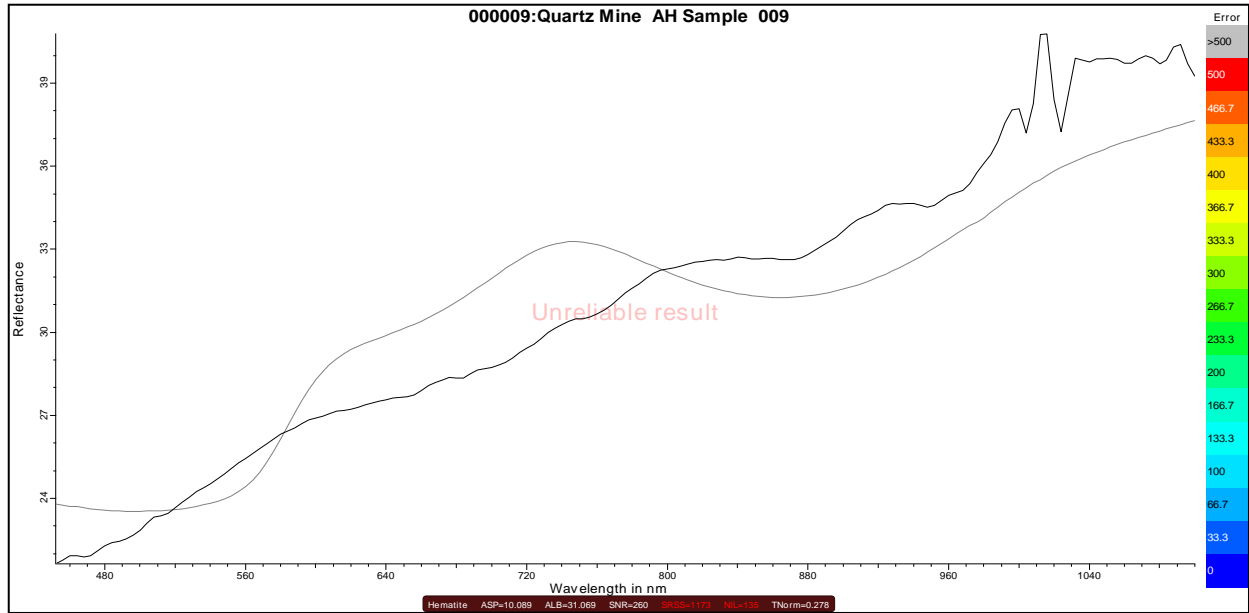


Figure 91: Apache Hills Sample 009 (Quartz Mine) wavelength and reflectance data input close-up results from the GER 3700 viewed through the visible near-infrared (VNIR) spectral feature option of The Spectral Geologist 8 software platform. A smooth line is the wavelength signature for Hematite according to the Spectral Geologist 8 spectral library. The rough line is the wavelength results from the GER3700.

Candidate TSA results
*Hematite [1173]
Goethite [1756]
Goethite [2919]
Vegetation-Green [3523]
86% Hematite + 14% Vegetation-Green [863]
72% Hematite + 28% Goethite [995]
84% Hematite + 16% Goethite [1102]
82% Goethite + 18% Vegetation-Green [1483]
52% ODZincalume + 48% Goethite [1710]
74% Goethite + 26% Vegetation-Green [2229]
61% ODZincalume + 39% Vegetation-Green [3499]

Figure 92: Sample 009 candidate results from The Spectral Analyst feature denotes an Astrid (*) indicating a possible spectral signature match according to The Spectral Geologist 8 data library.

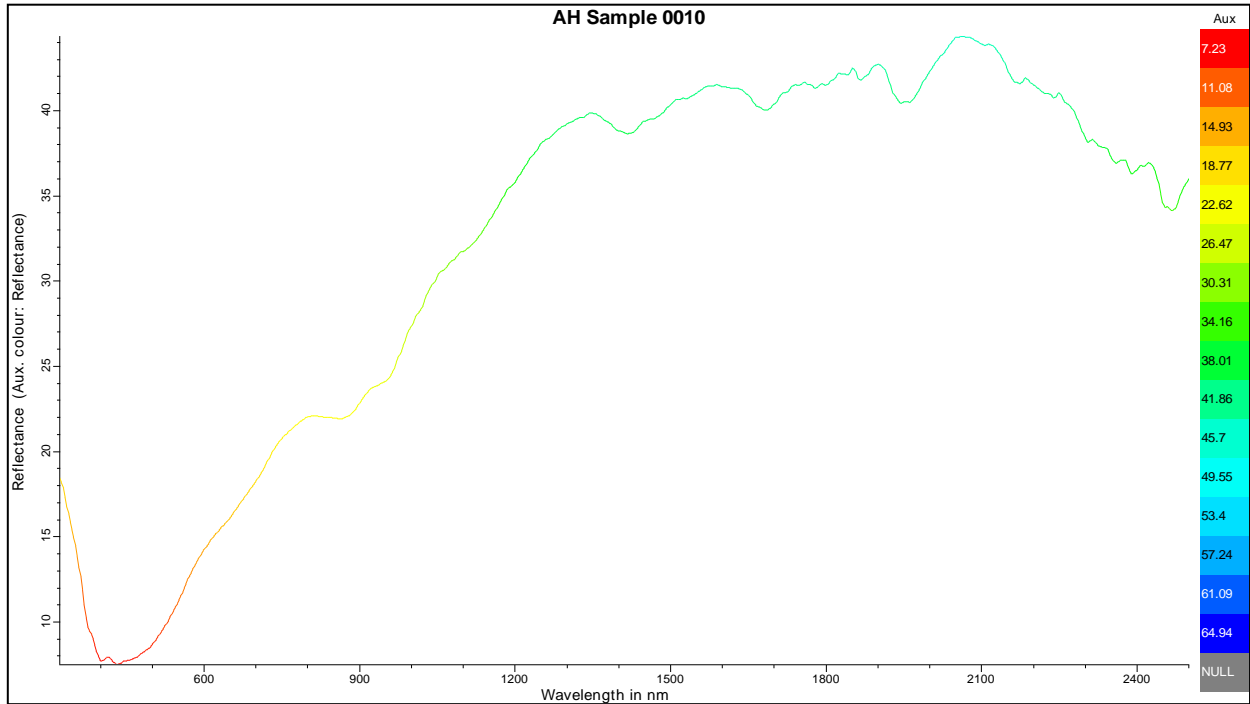


Figure 93: Apache Hills Sample 0010 (Occidental Mine) wavelength and reflectance data input results from the GER 3700 viewed through a combination of SWIR and VNIR from The Spectral Geologist 8 software platform.

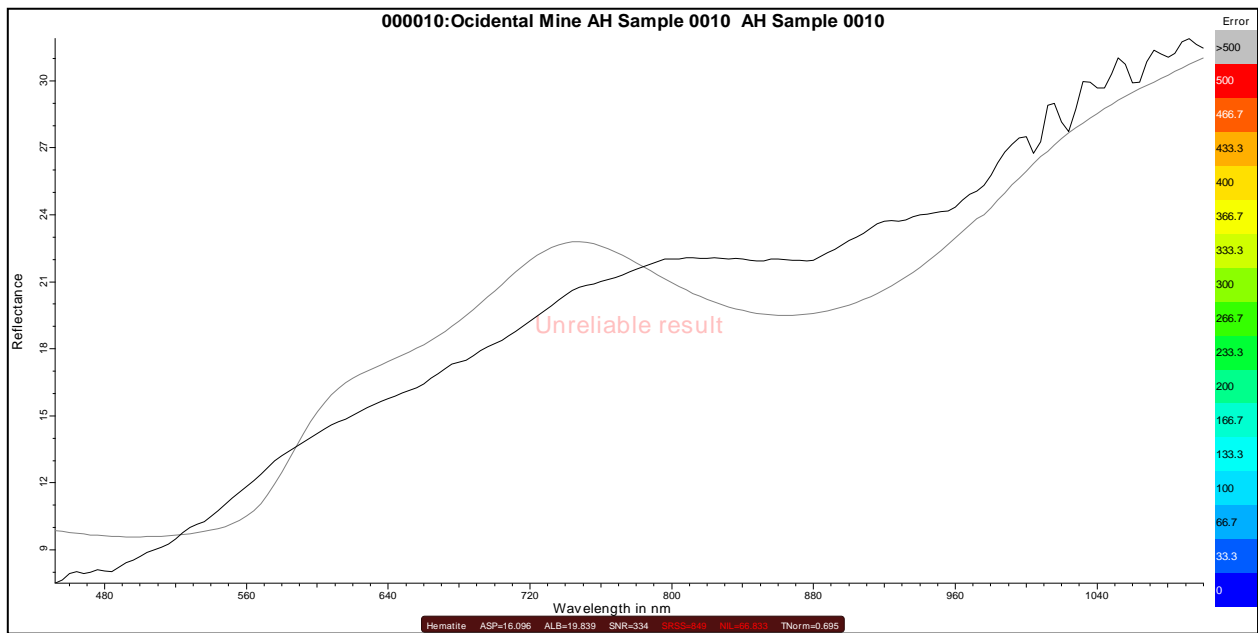


Figure 94: Apache Hills Sample 0010 (Occidental Mine) wavelength and reflectance data input close-up results from the GER 3700 viewed through the visible near-infrared (VNIR) spectral feature option of The Spectral Geologist 8 software platform. A smooth line is the wavelength signature for Hematite according to the Spectral Geologist 8 spectral library. The rough line is the wavelength results from the GER3700.

Candidate TSA results
*Hematite [849]
Goethite [1093]
Goethite [2387]
Vegetation-Green [3876]
61% Hematite + 39% Goethite [452]
88% Hematite + 12% Vegetation-Green [536]
74% Hematite + 26% Goethite [631]
87% Goethite + 13% Vegetation-Green [911]
63% Goethite + 37% ODZincalume [1077]
80% Goethite + 20% Vegetation-Green [1832]

Figure 95: Sample 0010 candidate results from The Spectral Analyst feature denotes an Astrid (*) indicating a possible spectral signature match according to The Spectral Geologist 8 data library.

6. Discussion

A beneficial steppingstone before exploration and discovery begins with extensive research. Identifying surface mineralogical composition using remote sensing presents an opportunity for exploration geologists seeking refined vectors to potential ore-bearing hydrothermal systems (Huntington,1996). Research is one of the most prevalent parts of any exploration project to combine with any applicable scientific method which would contribute to interpretive results. A suitable solution to overcome certain limitations for exploration is, to start with, simple techniques already practical in the field of economic geology investigation.

The research presented for the thesis combines and models several methods for further validation and mapping the presence of Ferric and Ferrous irons of a porphyry copper system. Remote sensing applications by capturing airborne digital images and spectral analysis contributed several dimensions to modern exploration (Swapan et al., 2018). Spectral Geology is a method used for exploration and interpretation, where spectral variation results from different components, the degree of ordering, mixtures, and the size of the grain from various rocks and minerals (Huntington, 1996). Mapping techniques can identify individual species of iron minerals, providing detailed information about hydrothermal mineralization and alteration zones (Thomas and Walter, 2002).

Gossans are the specific end products of oxidation and leaching of iron-bearing sulfide deposits exposed to the surface environment by erosion. They are the signposts that aim at what lies under the surface and are the outcome of oxidation by weathering and leaching sulfide mineralization (Kelly, 1981). Iron alterations such as gossans provide many indications of the character of ore once present now at the topographic surface and, therefore, aid in exploring deposits concealed at depth (Kelly, 1981). The colors significantly depend on the mineralogical composition of iron hydroxides and oxides phases and vary between red (hematite) and yellow jarosite (Swapan et al., 2018).

Iron oxides and a hydrothermal altered porphyry system are significant because one is distinctively correlated to the other; some of the best quantitative mineralogic descriptions of porphyry copper rocks are from the formation of Goethite and Jarosite during the weathering process of sulfide-bearing felsic rocks of the Goethite, Hematite, and Jarosite is in the leached capping. Goethite is usually the first mineral containing ferric iron that forms during weathering of iron sulfide minerals. Jarosite precipitates later than Goethite in weathering environments that originally included significant iron sulfide minerals and potassium concentrations. The near-surface environment and chemical reactions between pyrite, chalcopyrite, and oxygenated groundwater produce Goethite, Hematite, and Jarosite (Locke,1926; Tunell,1980; Blahd, 1983). Mass abundances

of these three minerals in weathered outcrops, such as in the Apache Hills, have been used to infer the identity and relative abundance of sulfide minerals in unseen fresh rock. This procedure has been used to evaluate the economic potential of porphyry copper prospects. However, the ubiquitous distribution of pyrite and chalcopyrite in other lithologies makes the oxidation reactions of general interest. All the ore extracted from the Apache orebody is oxidized. The veins are significantly altered and consist mainly of iron oxide, limonite, or hematite. Gossans are characterized by using iron oxide mineralogy and spectral reflectance as a possible aid to mineral exploration using remote sensing data (Accame et al., 1983). Some Gossan samples produced by the weathering of lead-zinc replacement deposits are composed of Goethite.

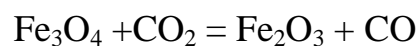
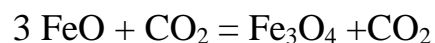
In contrast, other Gossan samples produced by pyrite weathering in the local country rock are composited primarily of Jarosite. The iron oxide assemblages, whereby Goethite precipitated early, are followed by Jarosite and Hematite (Accame et al., 1983). All the ore extracted from the Apache orebody is oxidized. The veins are significantly altered and consist mainly of iron oxide, limonite, or hematite.

Mineral resource and geo-environmental assessments require efficient and accurate mapping to characterize mineral exposures correlated to mined and unmined hydrothermally modified rocks and mine waste (Rockwell, 2013).

Ongoing U.S. Geological Survey (USGS) mineral resource and geo-environmental assessments have utilized mineral maps derived from spectral analysis of remote sensing data to identify and characterize hydrothermally altered rocks and other surfaces with acid-producing or neutralizing potential (Day et al., 2016; Rockwell et al., 2021). Ratio development is necessary to identify mineral groups based on diagnostic absorptions of pure and mixed mineral species in laboratory reference spectra convolved to spectral resolution (Rockwell, 2013). Some methodology presented involves using band combination (RGB) and band ratio indices to identify areas where several specific spectral absorption features are visible through remote sensing. In addition, geochemical analysis, source rock samples, spectrometry, several mineral reference spectral libraries (e.g., spectral library 6a and The Spectral Geologist 8), and previous research validate the presence of the Iron oxides (II) (III). in association with hydrothermal alteration in the study area. This analysis demonstrates the existence of these minerals in the study area and their association with a hydrothermal alteration porphyry system.

The near-surface environments and chemical reactions between pyrite, chalcopyrite, and oxygenated groundwater produce Goethite, Hematite, and Jarosite. Mass abundances of these three minerals in weathered outcrops, such as in the Apache Hills, have been used to infer the identity and relative abundance of sulfide minerals in unseen fresh rock. This procedure has been used to evaluate the

economic potential of porphyry copper. However, the ubiquitous distribution of pyrite and chalcopyrite in other lithologies makes the oxidation reactions of general interest (Locke, 1926; Blanchard, 1968; Bladh, 1982). Copper minerals, mostly chalcopyrite (CuFeS₂), occur in the lower levels and are associated with tactite minerals in zones that have been moderately metasomatized (Strongin, 1957). Almost invariably, chalcopyrite accompanies andradite-epidote veins. It also occurs with other sulfides in veins cutting metamorphosed sediments, particularly at the Apache mine (Strongin, 1957). All the ore extracted from the Apache orebody has been the product of enrichment during surficial oxidation with no economic development of deeper-level host rocks. The mineralized veins are significantly altered in the oxidized zone and consist mainly of iron oxide, either limonite or hematite (Strongin, 1957). The ferric-ferrous ratio was believed by Butler (1923) to be due to the oxidation of original ferrous iron in solution to ferric iron by carbon dioxide released upon recrystallization of limestone according to the formulae:



Given sufficient carbon dioxide concentrations, the first formula is considered appropriate. Lasky (1934), however, believes that the second reaction will not occur because there is not enough CO₂ in the system. Lasky (1934) concluded that reducing CO₂ to CO probably accounts for the oxidation of Fe₃O₄

to Fe_2O_3 . The presence of Fe_2O_3 must be accounted for by the greater volatility of FeCl_3 than FeCl_2 . Therefore, all the Fe_2O_3 in contact deposits must have been transported in the form of FeCl_3 and must have been precipitated directly from chloride and hematite. The ferric-ferrous ratio ranges widely in rock differentiates. The ratio is high in diuretic solution, which commonly produces magnetite, and is high in the solution that forms hypothermal deposits. (Lasky 1934). Presumably, it is insignificant in those that form lower-temperature sulphide deposits. Reasonably, the variation in the ferric-ferrous ratio would seem to be that some of the iron content of magmas and magmatic differentiates exist and migrate in the ferric state and in a ratio to the ferrous iron controlled by whatever oxidation equilibrium conditions exist at the time (Lasky 1934). The high ferric-ferrous ratio in contact deposits seems to be due to a combination of two independent processes: (1) Migration, in the ore-depositing, differentiates part of the iron in the ferric state, but not necessarily all together in the form of ferric chloride; and (2) Oxidation of some of the ferrous iron in this differentiate by carbon dioxide and to a lesser extent by steam (Lasky, 1934).

The band ratio indices (Table 5a) are limited and, therefore, sensitive to Ferric Iron even in low concentrations. Jarosite will generally have deeper absorption than Goethite (Figure 63), but both minerals are common in weathered pyritic rocks (Rockwell, 2013). The band ratio index (Table 5a) specific formula

SWIR2/Near Infrared Green/Red identifies Fe (II). Peterson's (1976) geochemical results confirm the presence of hematite (Fe_2O_3) bearing oxidized basalts in a young (Tertiary) volcanic field (Figures 30-33). Coarse-grained Goethite, having deep and broad crystal-field absorptions near 1.0 micrometers (Figure 63), is present in rock sample spectrometry analysis (GER3700 and TSG 8) (Figures 68, 69, 71, 72, 73, 74, 76, 77, 88, and 89). and the spectral wavelength captured by remote sensing instruments (Landsat 8 OLI) (Figure 24). The GIS-generated raster band indices images depict these areas in more detail. Doing so allows for a more accurate delineation of a hydrothermal alteration characterized by specific geological alteration zonation distribution patterns related to the Iron Oxide (II) (III) occurrence. The Landsat 8-derived map permits users to focus more rapidly on smaller areas when identifying alteration zones (e.g., pyritic or iron oxidation) in hydrothermally altered rocks, mine waste, or mill tailings. (Rockwell, 2021). The presence and mineralogy of altered rocks are essential factors in determining the occurrence potential of concealed mineral deposits. The presence and type of alteration can provide critical information for mineral resource investigations (Rockwell, 2013). Hydrolytic alteration commonly occurs along faults and fractures that are conduits for potentially metal-bearing fluids. This pattern is visible in the study area as linear bands of iron-rich material, as seen in Figures 40d and 43. In addition, the region of Little Hatchet, Apache Hills, Sierra Rica, and

south-southeastern New Mexico/Mexico indicate anomalous zones of prospective porphyry-type mineralization where alterations are generally more identifiable and more likely to host near-surface deposits. Exploration programs for porphyry Cu deposits rely on many techniques. Mineral discoveries are typically tangible on surface studies. Remote sensing applications that capture airborne digital images and spectral analysis contributed several dimensions to modern exploration (Swapan et al., 2018).

Nonetheless, from a geologist's perspective, whole rock litho-geochemical and shortwave (SWIR) and visible near-infrared (VNIR) spectrometry have become standard tools in addition to the hammer and hand lens (Halley et al., 2015). Strongin's (1957) research paper presents information including geology, structure, faults (Figure 17), mineralization (Table 20), and background mining history (Table 1-2). Modern research papers present hypothetical models (Figures 1 and 8) of the regional area's geologic history and geographic changes (Lawton, 2020). The distribution of iron throughout the Apache Hills supports a watershed transport mechanism for disseminating iron minerals, as seen on the map (Figure 35), where stream flow patterns are apparent as Fe-rich streaks along drainages heading in altered zones. Thus, these stream patterns themselves point upstream to potential mineral deposits, in line with long-established geochemical sampling techniques. Rockwell (2013) suggests that deposits surrounding watersheds reveal

the importance of sulfide-bearing altered rocks and mine waste as diffuse sources of acidic solutions that can transport metals into the hydrologic system.

Gossan is severely oxidized, weathered, or decomposed rock, usually the upper and exposed part of an ore deposit or mineral vein. In the classic gossan or iron cap, all that remains is iron oxides and quartz, often in the form of box works (quartz-lined cavities holding the shape of the dissolved ore minerals). In other cases, quartz and iron oxides, limonite, goethite, and jarosite, exist as pseudomorphs, replacing the pyrite and primary ore minerals (Guilbert, 1986). Gossans may also be called iron cap because it denotes a concentration of iron hydroxides on the top of sulphide mineral veins, where it reaches the surface. It forms during the supergene sulphide ore enrichment when weakly acid surface water percolates through the mineral deposit. Many sulphide ores are oxidized in this process and brought into solution (red box) (Figure 96) (Asmus 2013). Ferric iron sulfate minerals, including Jarosite and Goethite, are produced during the weathering process of Pyrite. Furthermore, large concentrations of undifferentiated ferrous and ferric iron oxide and sulfate minerals are identifiable using the analysis methodology from Landsat 8 data (Rockwell, 2021).

6.1 Summary of Key Results

Gossans provide many indications of ore's character once present in the plane of the topographic surface (Figure 96). They are the specific end products of

oxidation and leaching of iron-bearing sulfide deposits exposed to the surface environment by erosion. Gossans are the signposts that aim at what lies under the surface and the outcome of oxidation by weathering and leaching sulfide mineralization (Kelly, 1981). Peterson (1976) describes the presence of Limonite Gossans at the Apache and Daisy mine, which is visible with remote sensing in Figure 103. Quartzite Ridge (Figure 104) combines remote sensing with a magnetic anomaly, where Peterson (1976) suggests that mineralization is associated with a magnetic anomaly centered on the southern end of the Quartzite Ridge. The copper value metadata table (Tables 9 and 10) created on ArcGIS explains the geochemical collection analysis results by Leonard Resources AH-11 (1974) geochemical collection analysis results by Leonard Resources AH-11 (1974), and AH-14 (1975) presented by Peterson (1976).

Furthermore, Peterson (1976) states that Figures 98 and 99 are areas of good exploration of the host rock. Two methods integrated into this Figure (98 & 99) include 1) Remote Sensing (Ferrous Iron 3+ Band ratio (RED/GREEN)); the red boxes show the 2) Geochemical assay results of copper values determined by the legend (Figures 98 and 99). Other figures 102-103 show copper value results from other geochemical result sources applied to GIS. The highest copper values (Orange-Circles) extend from the Apache, Daisy, Summertime, and Mairland mine well into Doyle Peak Township 29S and Range 15W in sections 12 and 13 (Red

Box) (Figure 99). Two methods are integrated into Figure 99 and 100, 1) remote sensing using band ratio (RED/GREEN) to expose the mineral alteration of Ferrous Iron 3+, and 2) Geochemical assay copper values determined by the legend figure 100.

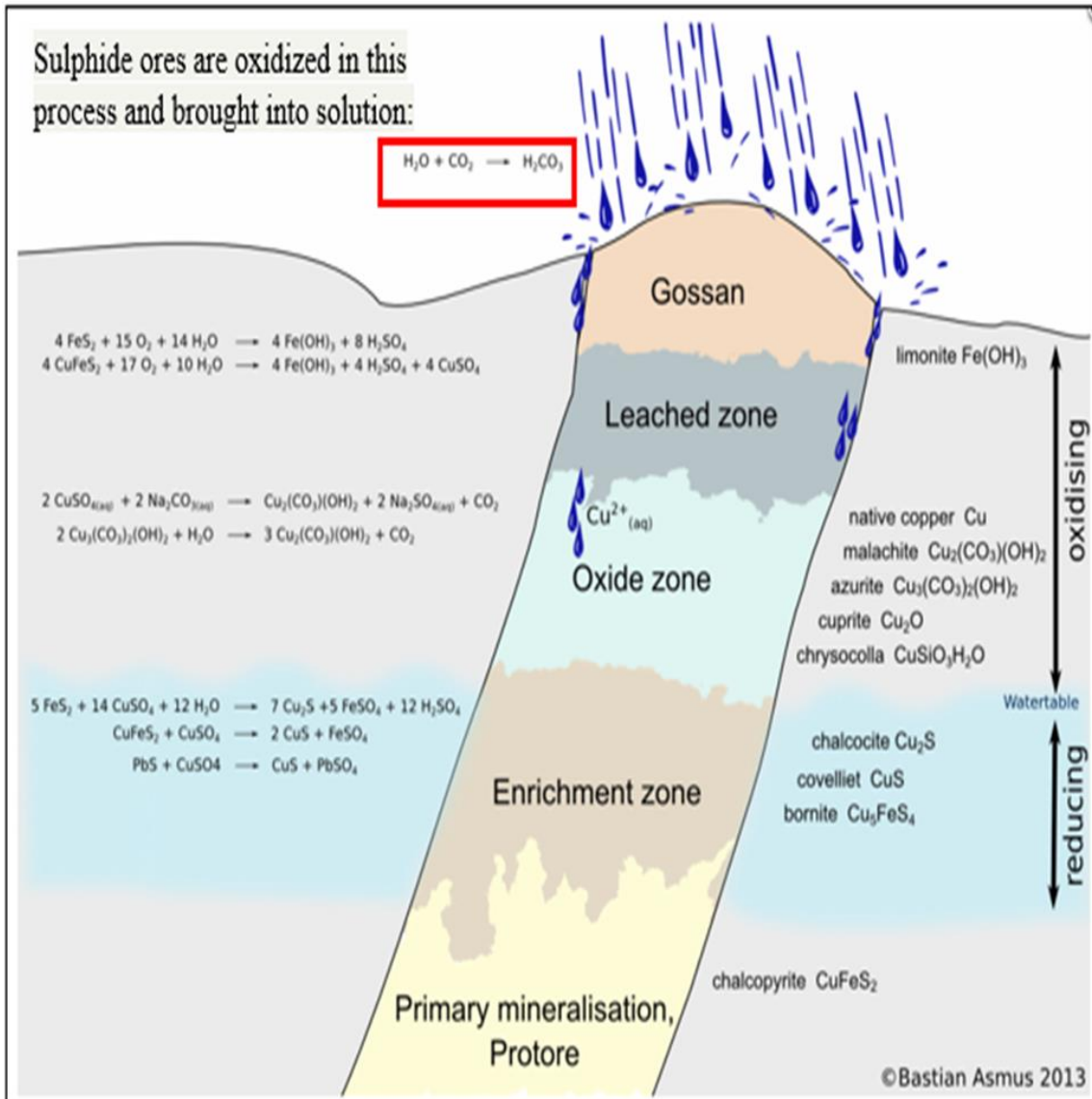


Figure 96: Schematic view of a sulphide vein. With a clear outlook of the oxidation zone, consisting of the gossan, the leached zone, and the oxidized zone. The reducing zone consists of the enrichment zone and the area of primary mineralization. (Modified from Asmus 2013) <http://en.archaeometallurgie.de/gossan-iron-cap/>.

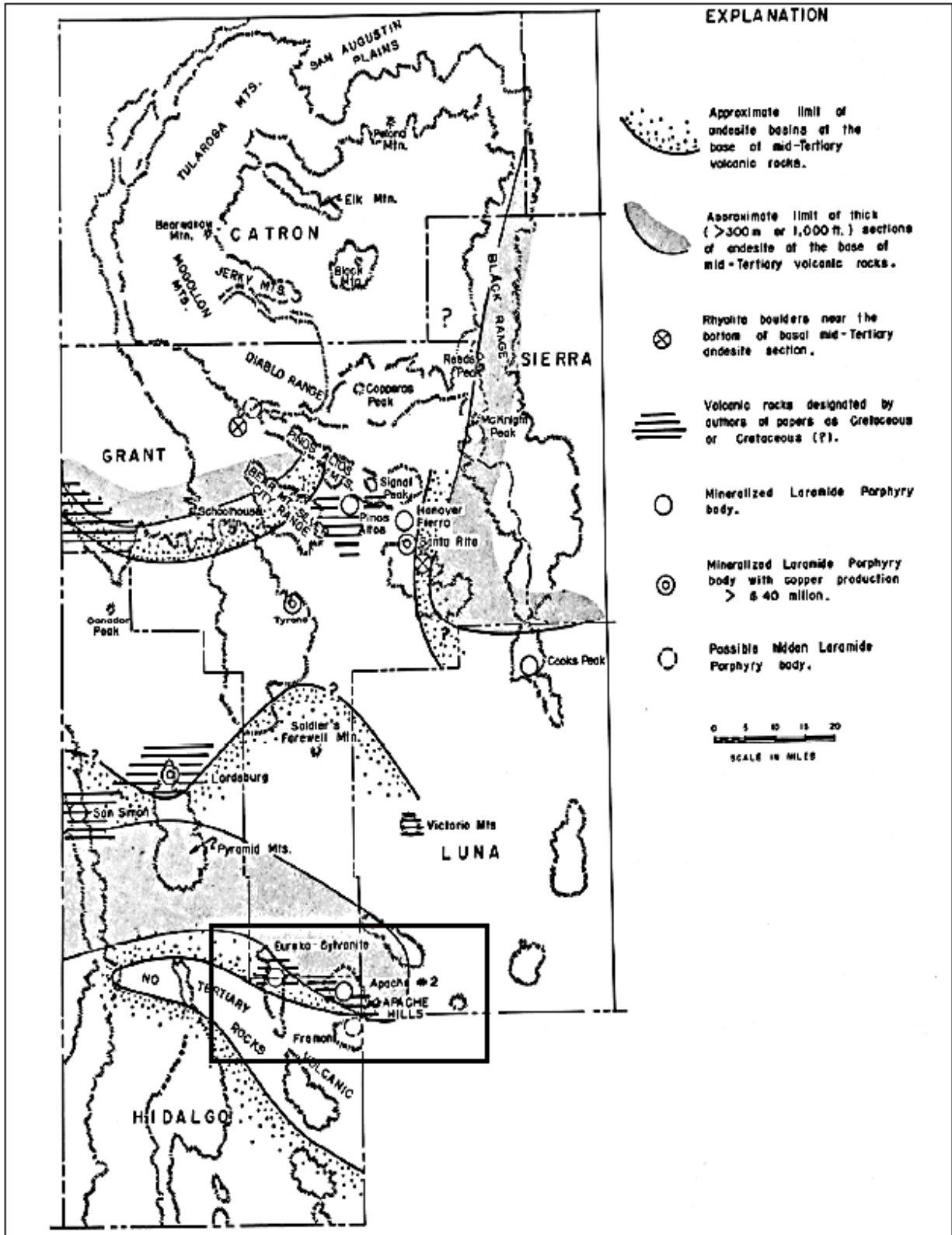


Figure 96a: Relationship of Laramide porphyry bodies to Cretaceous and basal mid-Tertiary andesites modified (From Elston, 1970, Figure 4, p. 152).

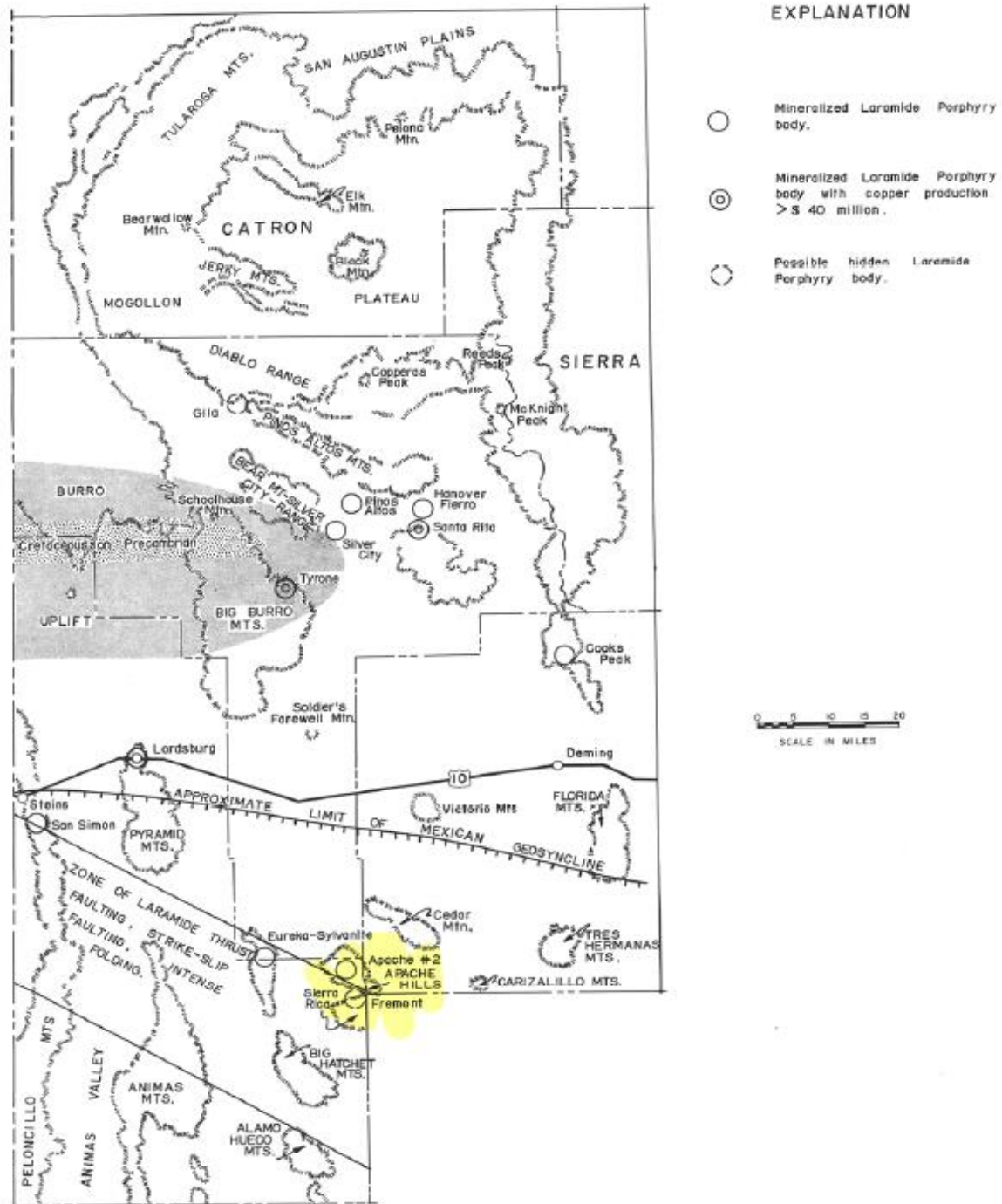


FIGURE 1.
Major tectonic provinces of southwestern New Mexico.

Figure 97: Major Tectonic provinces of southwestern New Mexico highlighted in yellow is a possible hidden Laramide porphyry body modified (From Elston, 1970 Figure 1, p.

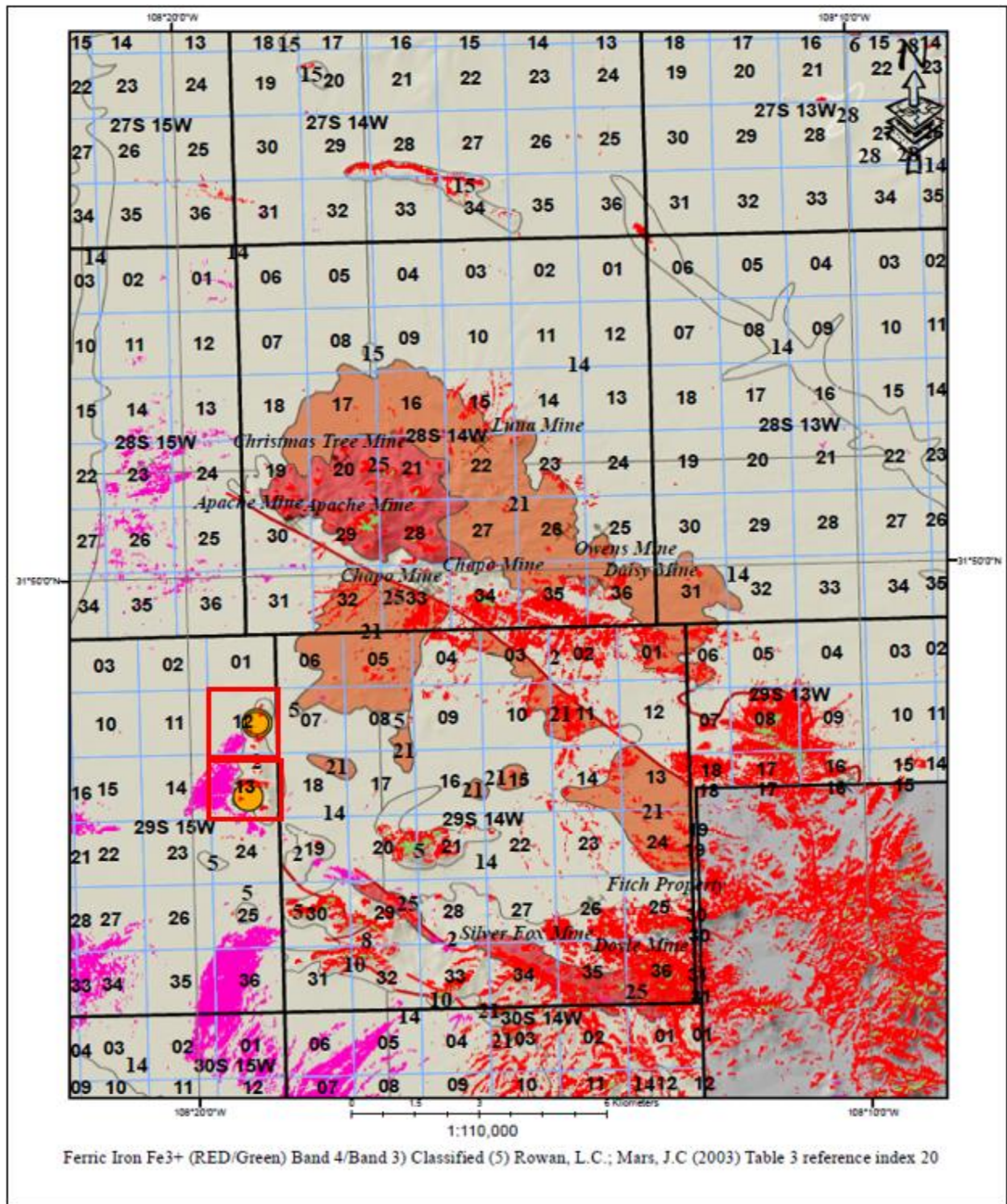


Figure 98: Ferrous Iron 3+ (RED/GREEN) Band 4/Band 3) Classified (5) Rowan, L.C.; Mars J.C (2003) Table 5a reference index 20. Including the Copper assay result samples from *Leonard Resources AH-14 Assay Township 29S and Range 15W in sections 12 and 13 (Red Box) (1974-1975) georeferenced on a GIS platform from Peterson (1976) for future exploration.

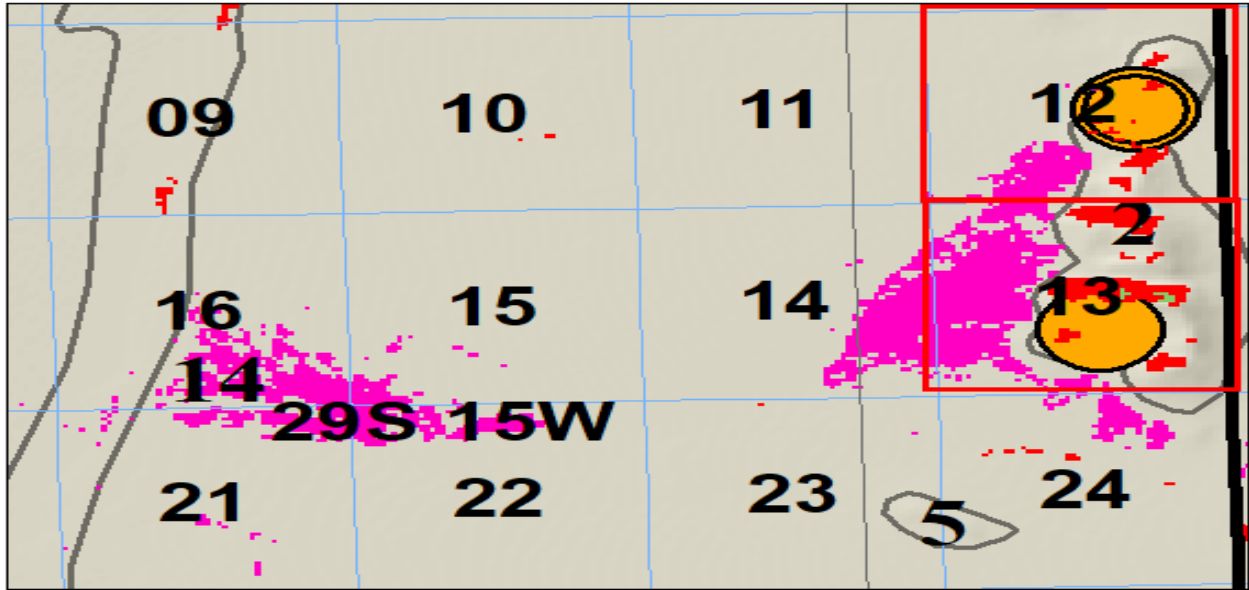


Figure 99: Township 29S and Range 15W Sections 12 and 13 visualize the section area through ArcGIS Peterson describes as an area of favorable exploration of the host rock. Two methods are integrated into this figure, Remote Sensing Ferrous Iron 3+ Band ration (RED/GREEN) and the red boxes showing the Geochemical assay results from the copper values determined by the legend (Figure 100).

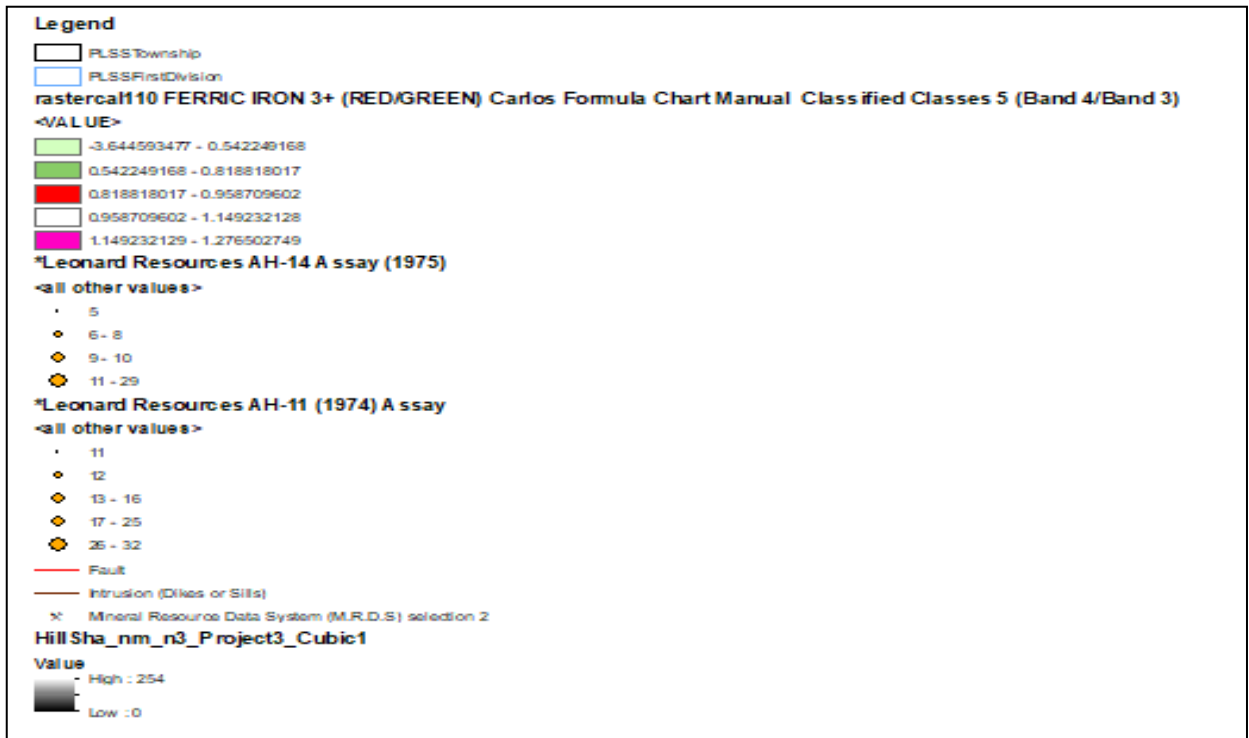


Figure 100: Legend results from Figure 98 depicting Ferrous Iron 3+ Band ration (RED/GREEN) and the Geochemical Assay Results from Leonard Resources (1975). Sourced from Peterson (1976 with the Township and Range added on an ArcGIS platform).

Table 9: Leonard Resources AH-14 Assay (1975) results of copper. These results are captured on Figure in section 13 Township 29S Range 15W for visualization and interpretation that would integrate Remote Sensing band indices combination for future interpretations.

***Leonard Resources AH-14 Assay (1975)**

Depth:	Lat DD	Long DD	Cu
300-350	31.784043	-108.319333	10
350-400	31.784043	-108.319333	10
400-450	31.784043	-108.319333	5
450-500	31.784043	-108.319333	10
500-550	31.784043	-108.319333	10
550-600	31.784043	-108.319333	8
600-650	31.784043	-108.319333	5
650-700	31.784043	-108.319333	5
700-750	31.784043	-108.319333	5
750-800	31.784043	-108.319333	5
800-850	31.784043	-108.319333	5
850-900	31.784043	-108.319333	5
900-950	31.784043	-108.319333	10
930-950	31.784043	-108.319333	29

Table 10: Leonard Resources AH-11 Assay (1974) results of copper. These results are captured on Figure in section 12 Township 29S Range 15W for visualization and interpretation that would integrate Remote Sensing band indices combination for future interpretations.

***Leonard Resources AH-11 (1974) Assay**

Depth:	Lat DD	Long DD	Cu ppm
20-70	31.800597	-108.316732	11
70-120	31.800597	-108.316732	12
120-170	31.800597	-108.316732	16
170-200	31.800597	-108.316732	25
200-250	31.800597	-108.316732	32
250-300	31.800597	-108.316732	21

Table 11: Assay data of mines in the Apache No. 2 mining District, Hidalgo County, New Mexico (modified from Peterson 1976, Table 4 p.61). Red lines describe Limonite Chalcopyrite & Gossans in the Summertime, Daisy, and Apache Mine.

SAMPLE LOCATION	Cu	Mo	Pb	Zn	Ag	DESCRIPTION OF SAMPLE
1. <u>Summertime mine</u> sec.33, T28S, R14W	1.1%	66	200	100	---	<u>andradite skarn with chalcopyrite</u>
2. Last Chance mine sec. 32, T28S, R14W	182	126	3.8%	300	---	quartz vein in quartz latite host rock
3. Luna mine sec. 22, T28S, R14W	2.0%	224	5.2%	2.8%	---	quartz vein in a rhyolite dike
4. Christmas mine sec. 20, T28S, R14W	0.5%	37	1.6%	0.1%	---	quartz vein in a rhyolite dike
5. Queen's Taste mine sec. 23, T28S, R14W	0.4%	3	1.2%	0.3%	---	quartz vein in andesite host rock
6. <u>Daisy mine</u> sec. 36, T28S, R14W	0.4%	22	850	625	2.1 oz.	<u>limonite gossan</u> sampled over a 50 ft. traverse
7. Apache mine	18	77	800	48	0.2 oz.	drill core at 778 feet dark mottled marble
8. Apache mine	18	77	480	52	0.2 oz.	drill core at 795 feet dark mottled marble
9. Apache mine	26	66	720	42	0.2 oz.	drill core at 926 feet dark gray marble
10. Apache mine	35	11	500	42	0.1 oz.	drill core at 1109 feet calcareous hornfels
11. Apache mine	14	800	90	15	0.1 oz.	drill core at 762 feet dark-gray marble
12. Apache mine	1.3%	96	6.0%	0.1%	5.1 oz.	<u>limonite gossan</u> sampled over a 100 foot traverse
13. Apache mine south prospect pit	0.6%	3	320	0.2%	---	6 foot channel sample
14. Apache mine	120	17	220	200	0.25 oz.	100 foot sample traverse over main waste dump
15. <u>Apache mine</u> north prospect pit	---	---	0.7%	---	2.0 oz.	<u>limonite gossan</u> along rhyolite-marble contact.

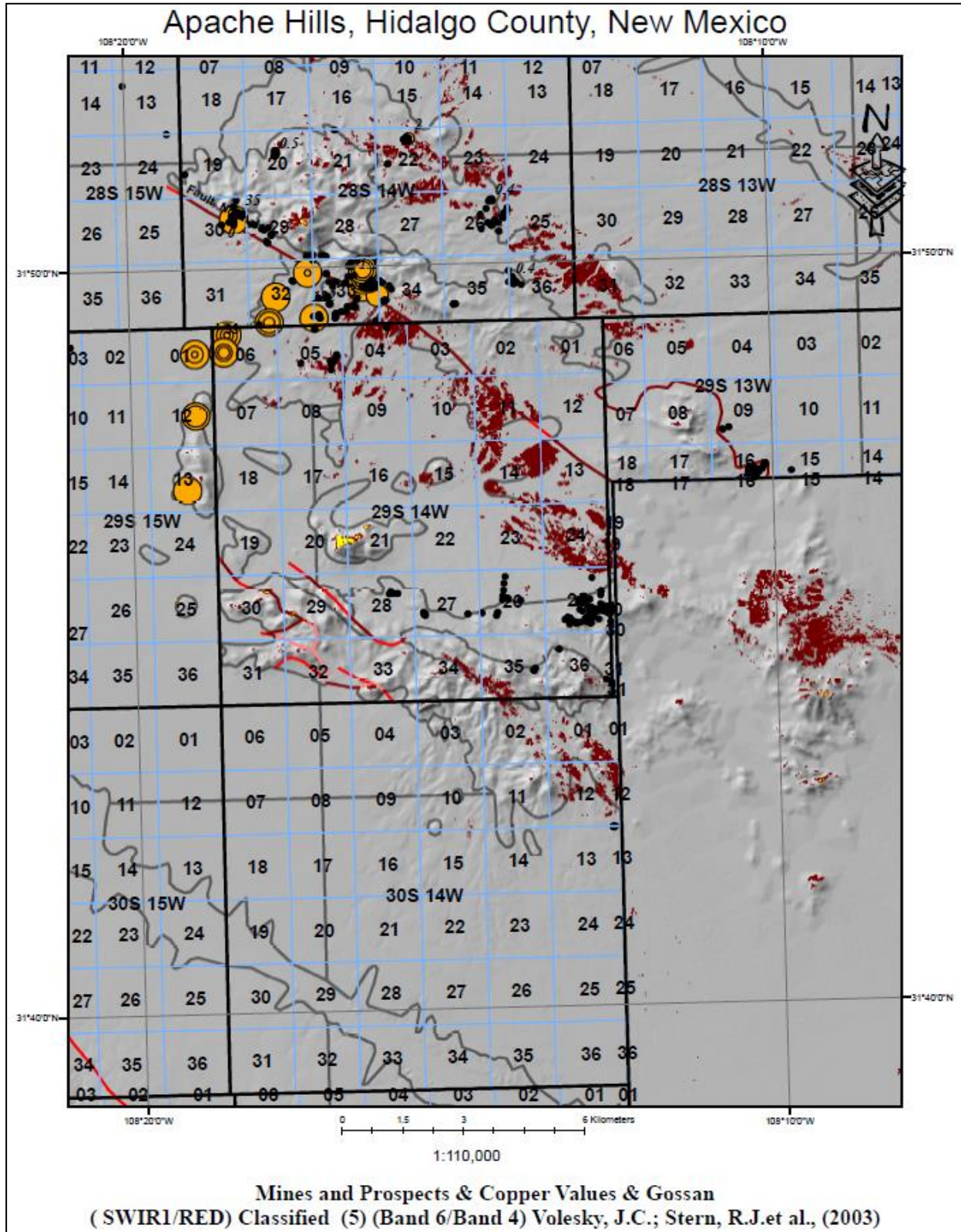


Figure 102: Gossan (Band 6/ Band 4) Section 33 & 36 Township 29S, and Range 14W, including mines with Copper values in Hillshade.

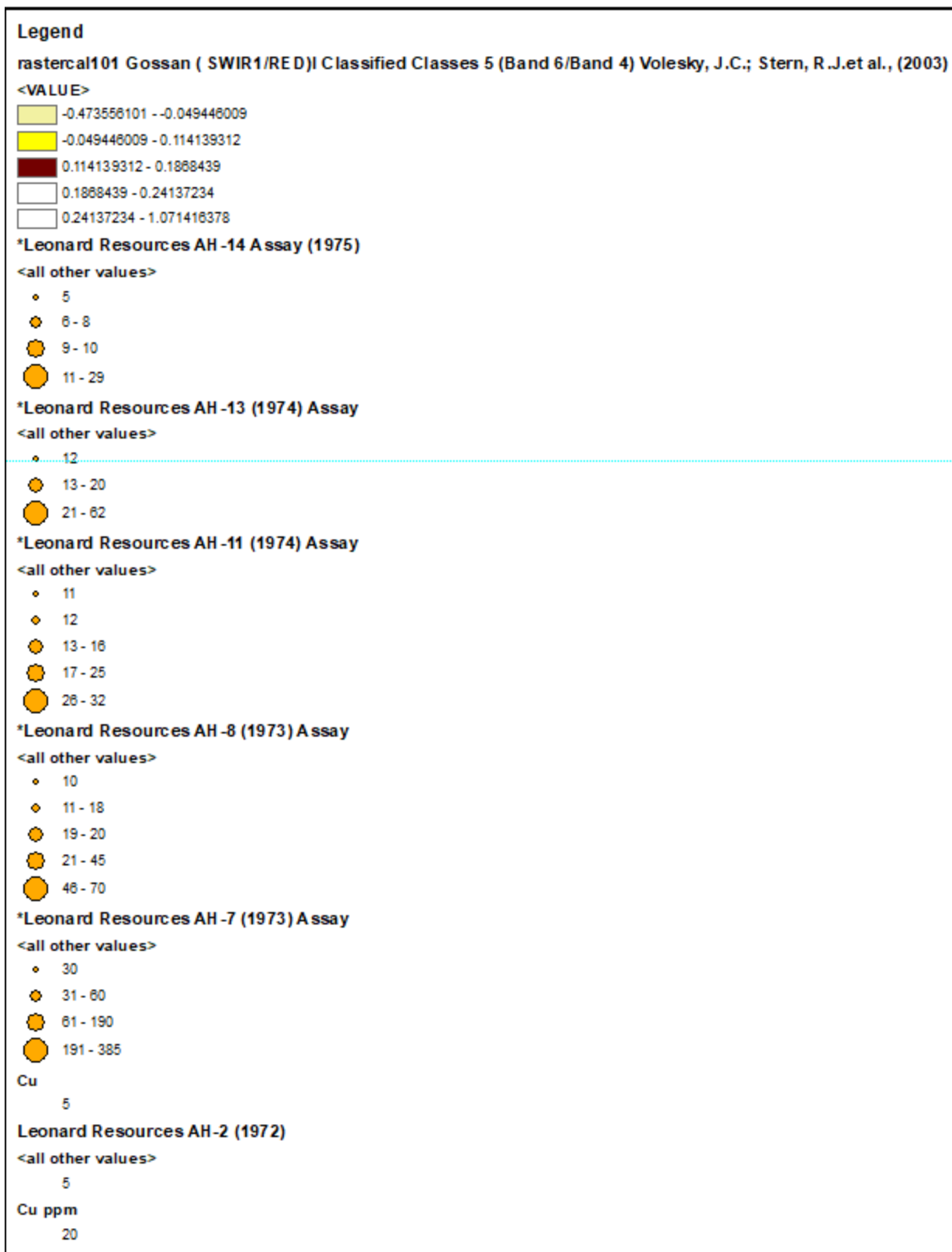


Figure 102a: Gossans (SWIR1/RED) and Copper values from Leonard Resources (1972-1975) reported by Peterson (1976).

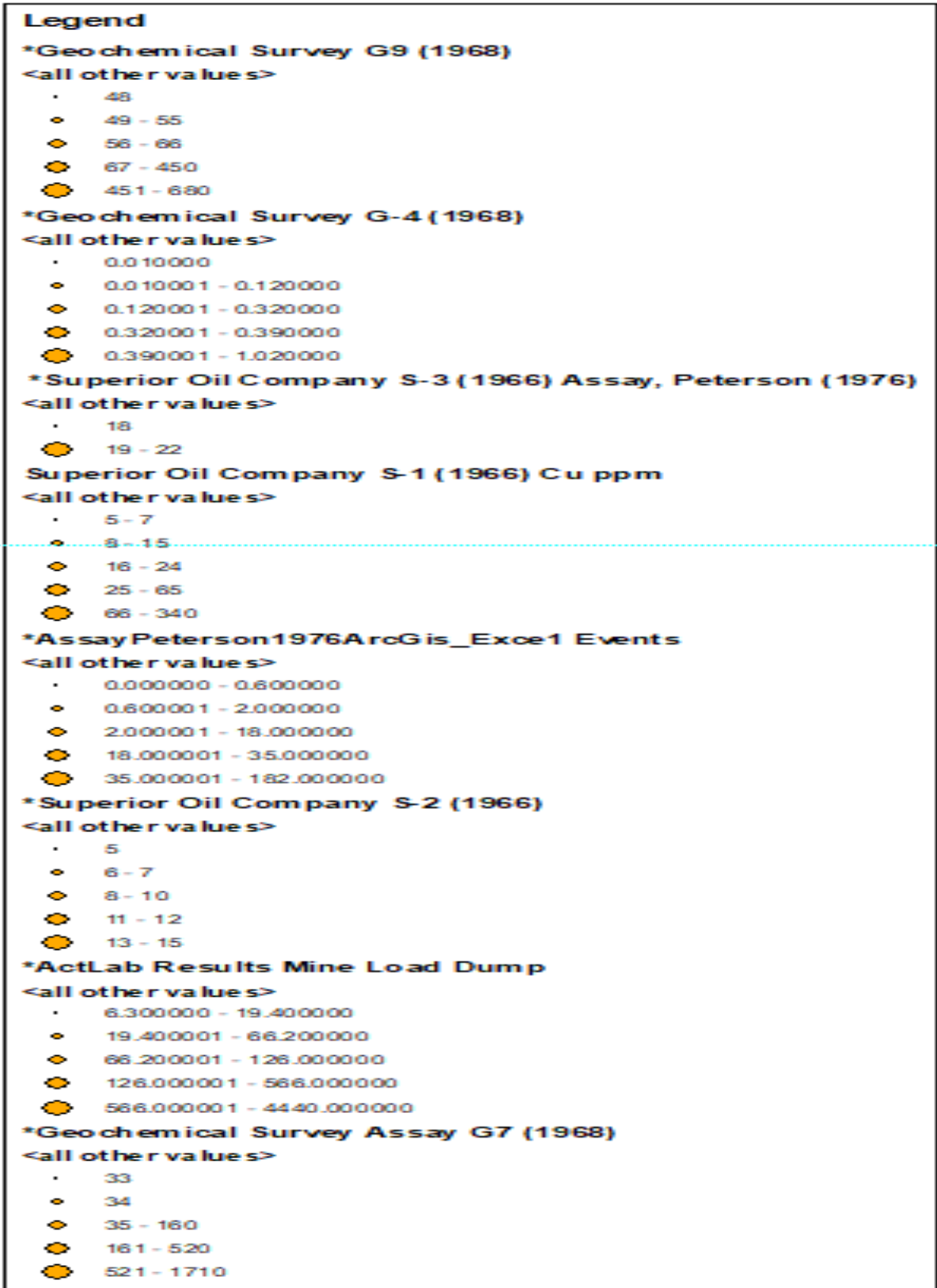


Figure 102b: Copper values reported by Geochemical Survey (1968), Superior Oil (1966) Peterson (1976), and Actlabs (2018).

Peterson (1976) describes the presence of Chalcopyrite and Gossans from the assay data Table 11 mines and in the sample locations Summertime, Apache, and Daisy mines Section 30,33 and 36 in Township 28S and Range 14W. Integrating remote sensing spatial data validates the existence of Gossan (dark brown) in the section areas. Copper values are included in Figure 103 and are explained further in Figures 102a and 102b.

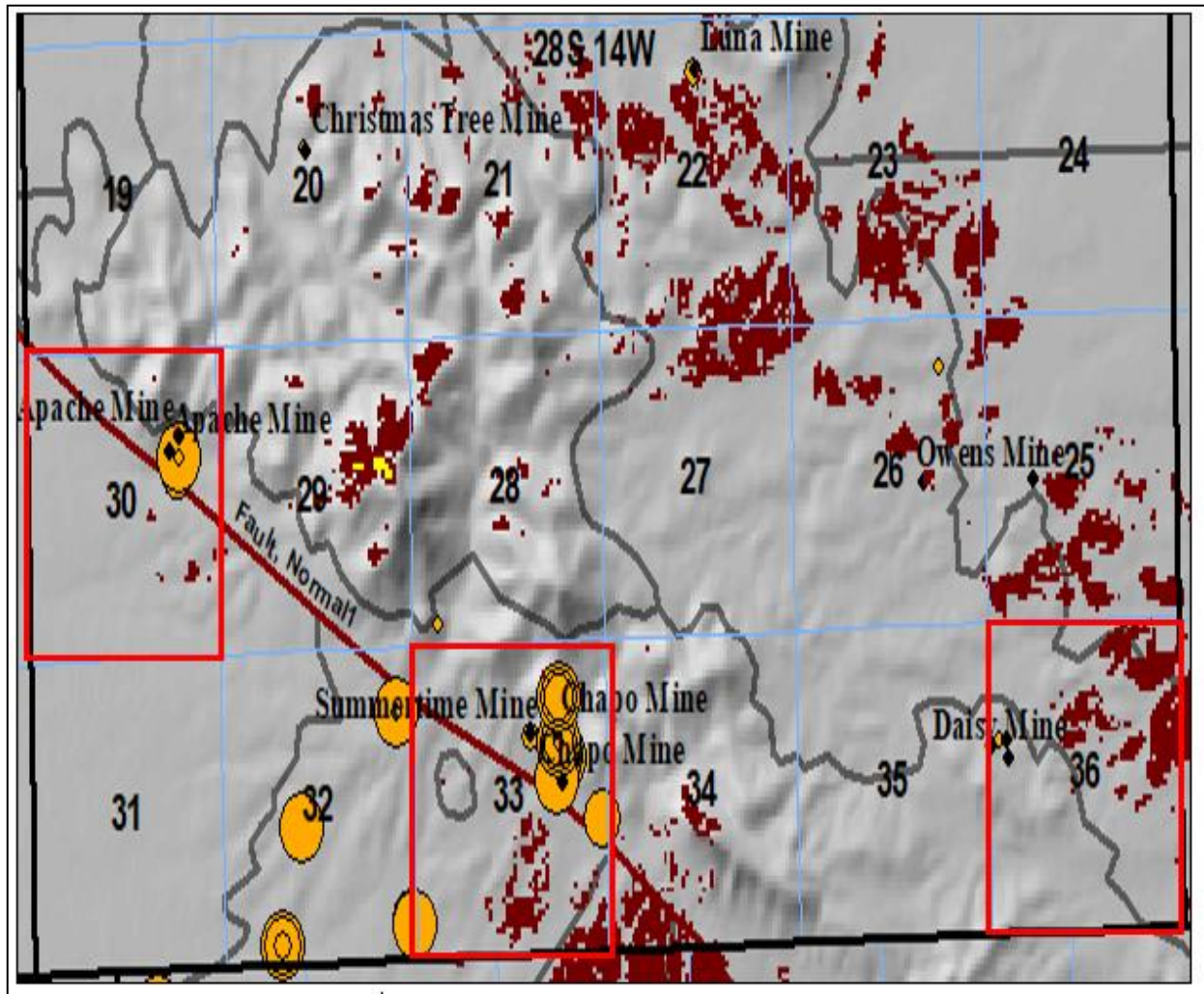


Figure 103: Township 28S and Range 14W Sections 30,33, and 36 illustrating the presence of Gossan (Dark Red) as described by Peterson (1976) Table 11

The mineral deposits of the Apache No. 2 mining District occur in Oligocene rocks except for possible mineralization related to a magnetic anomaly (Figure 104) in the lower Cretaceous Mojado Formation (Figure 7) (Peterson, 1976). Considerable hydrothermal alteration is present where copper ore has been mined. Several areas show some promise for further mineral exploration. They are associated with a magnetic anomaly centered on the southern end of the Quartzite Ridge in Section 12 & 13 Township 29S and Range 14W (Figure 104) (Peterson, 1976).

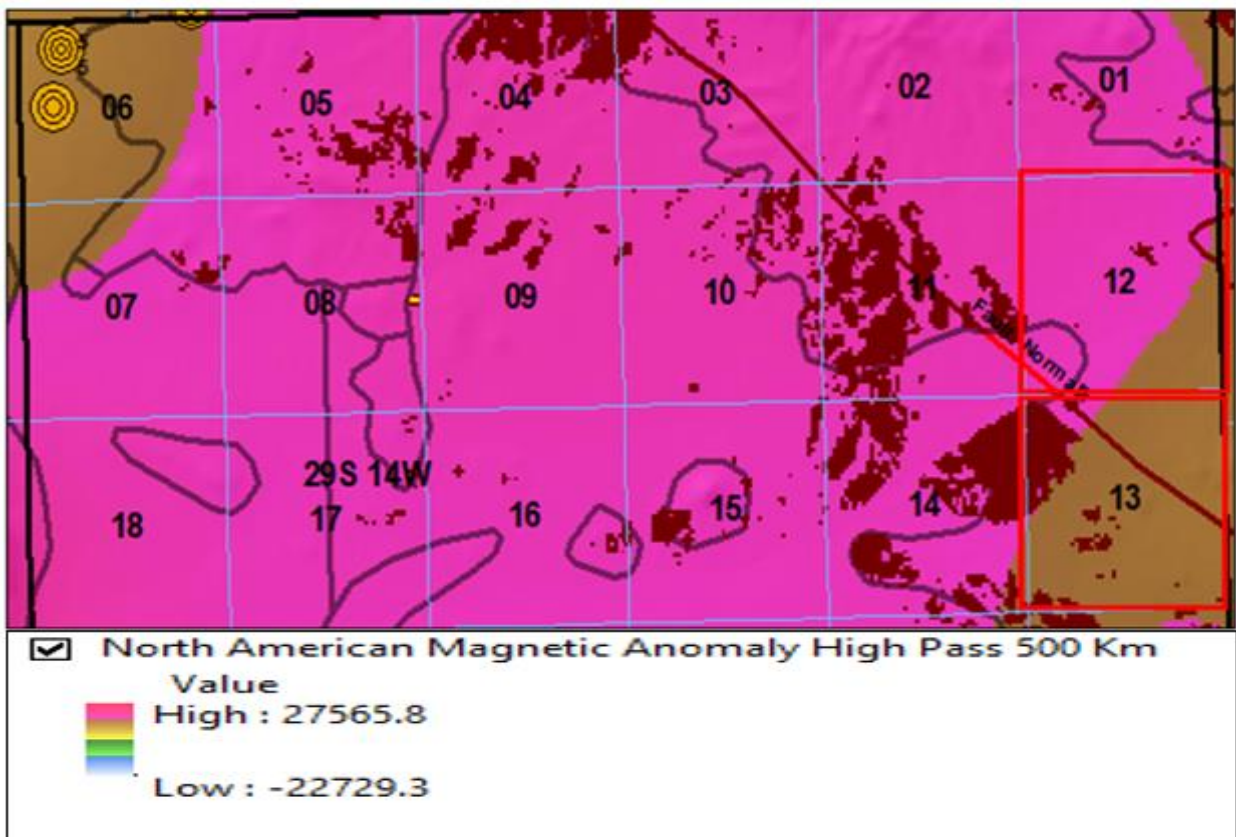


Figure 104: Township 29S and Range 14W Sections 12 and 13 illustrating the presence of Gossan (Dark Red) and a magnetic anomaly as described by Peterson (1976) Table 11.

7. Conclusion

A beneficial steppingstone before exploration and discovery begins with extensive research. Identifying surface mineralogical composition using remote sensing presents an opportunity for exploration geologists seeking refined vectors to potential ore-bearing hydrothermal systems (Huntington,1996).

In line with Strongin's (1957) and McLemore's (1960) conclusions, undiscovered ore bodies exist. Still, the favorable area for exploration would be intersections of the marbleized limestone in the Indian and McKinley-Chapo faults and other north or northeast-trending faults (Figure 17). Mclemore et al. (1996) say that major north-trending structures controlled the mineralization. The most prominent of these structures is the McKinley fault, which hosts the Apache deposits on its southeast side (McLemore et al.,1996).

It has been demonstrated in this thesis that remote sensing is a powerful tool for geological mapping of Ferric and Ferrous iron alterations in the Apache Hills and Sierra Rica Mountains, Hidalgo County, New Mexico. Research and exploration outline the iron alteration visible in fluvial sediment environments and structural features. The iron alterations (Figures 55a and 55b) follow a fluvial stream pattern (Figure 35) and faults (Figure 40d) as linear alteration bands. The geochemical sample, laboratory spectrometry, and remote sensing unequivocally validate the presence of iron alteration (e.g., Hematite, Limonite, Goethite). In

comparison, prior research from Strongin (1957) and Peterson highlights the occurrence of Hematite, Pyrite, Chalcopyrite, Magnetite Jarosite, and Limonite.

8. Future Work

Mineral deposits of the Apache No. 2 mining District occur in Oligocene rocks except for possible mineralization related to a magnetic anomaly (Figure 104) in the lower Cretaceous Mojado Formation (Figure 7) (Peterson, 1976). The Apache Hills' intrusive volcanic rocks are identified in Figure 6 as number 6 (black box). Deal (1978) illustrates the regional area surrounding the Apache Hills, which outlines the approximate location of the inner margins of calderas flow, constituting various flow-tuff calderas (Figure 6). Peterson (1976) describes the area as a good host rock; the host rocks are near the Chapo, Summertime, and Apache mines. He suggests a hidden Laramide porphyry body within volcanic rocks. Peterson (1976) says drilling has not intersected an ore horizon with any continuity.

Ferric iron sulfate minerals, including Jarosite and Goethite, are produced during the weathering process of Pyrite. Peterson (1976) proposes that future exploration for skarn mineralization should be directed toward finding an area with pre-ore ground preparation by faulting and fracturing to permit the ingress of mineralizing fluids and where the host rock is favorable for the formation of replacement ores. McLemore (1996) says three types of deposits occurred in the

district (Figure 15). 1) Skarns, 2) Carbonate-hosted Pb-Zn polymetallic replacement vein oxidized skarns, and 3) Carbonate-hosted lead-zinc deposits with copper sulfides replacing strata of Cretaceous U-Bar Limestone at the contact with the Quartz Monzonite. The deposit extends into the Sierra Rica Mountains of Mexico, where little exploration has been done in the district (McLemore, 1996). Rockwell (2013) indicates that deposits surrounding watersheds (Figure 35) reveal the importance of sulfide-bearing altered rocks and mine waste as diffuse sources of acidic solutions that can transport metals into the hydrologic system.

Hydrothermal magnetite is common in skarns, and other hydrothermal mineralization may be the origin of the significant magnetic anomalies associated with the Gossens documented here, a hypothesis that requires further testing. Additionally, magnetization analysis may determine if the ore deposit has been subject to the tectonic rotation of disrupted blocks or constrain the age of discrete hydrothermal pulses (Taylor 2000; Astudillo et al. 2008; Astudillo 2010; Riveros 2013). Geophysical methodologies should include an in-depth examination of the magnetic anomalies (Figure 112), incorporating a systematic scalar analysis on a GIS platform, encompassing the lower portion of the Basin and Range Province (Figure 18) surrounding Apache Hill and the Sierra Rica Mountains. A method necessary to understand and quantify the anomaly's magnetic effects on surface oxidation developed in the Apache Hills and Sierra Rica. The mineralization

associated with the magnetic anomaly is centered over Gossans on the southern end of the Quartzite Ridge in Section 12 & 13 Township 29S and Range 14W (Figure 104) (Peterson, 1976). Areas where prominent magnetic anomalies are present and more intense should be areas of potential interest for future mineral exploration (Figures 49, 96a, and 97).

Remote sensing techniques demonstrate considerable hydrothermal alteration in the Apache Hills, where copper ore has already been mined (Tables 1 and 2). The Mars and Rowen's (2013) hydrothermal alteration (Table 12) Interactive Data Language (IDL) logical operator algorithms, in conjunction with Advanced Spaceborne Thermal Emission and Reflection (ASTER) Radiometer data, expose mineral alteration to map hydrothermally altered rocks in the central and southern parts of the Basin and Range province of the Apache Hills. Within un-metamorphosed volcanic rocks and most mine waste, the presence of alteration and (or) supergene weathering of Pyrite can be inferred if both ferric iron groups and the clay-sulfate-mica-marble mineral groups are present, especially in the same pixel (Rockwell, 2021).

Future studies of the spatial data band combination results reveal hydrothermal alterations (e.g., Phyllic, Argillic, Propylitic, and Hydrothermal) (Figures 104-111) present in the Apache Hills and Sierra Rica. The porphyry model (Figure 113) Halley et al. (2015) vertical and lateral distribution illustrates a hydrothermal alteration system's trace element and alteration footprints. Halley et al. (2015) trace element vertical distribution thresholds (Figure 113) may be applied in the Apache Hills area and compared with the geochemical data results (Figure 114) collected from Peterson (1976) and Actlabs samples. The graph illustrates the trace element abundance according to the location where the samples were collected in the study area. The trace element abundance from the geochemical data results (Figure 114) meets or exceeds the minimum trace element footprint for a porphyry system (Figure 113). Geochemical analyses from previous, current, and future research (e.g., copper values) exploration illustrated in figures 104-111 should continue to extend further into the southwest portion of the Basin, Range Province, surrounding the Apache Hills, Sierra Rica, and Mexico.

Integrating new methods with previous techniques (e.g., ASTER data algorithm, Landsat 8, Spectroscopy, Geochemical analysis, Geophysics, and GIS platforms) may reveal the hidden porphyry body or bodies projected to be present by Elston (1976) in the Apache Hills and Sierra Rica. Figures 104-111 depict black dots that are either spread out or collectively constricted to specific areas. Those

dots represent USGS Mineral Resource Data System (MRDS) mines. Any future work should take into consideration where mining has been done and what was extracted.

Table 12: Interactive Data Language (IDL) logical operator algorithms used with Advanced Spaceborne Thermal Emission and Reflection (ASTER) Radiometer data to map hydrothermally altered rocks in the central and southern parts of the Basin and Range province of the United States. Algorithm notations follow the usage of Mars and Rowan (2006). b, band; float, floating point; le, less than or equal to; lt, less than; ge, greater than or equal to; gt, greater than (Mars and Rowen 2006; Mars and Rowen 2013, Table 1 p.3).

Hydrothermally altered rock	Algorithm
Hydrothermal silica-rich (hydrous silica, chalcedony, opal)	$((\text{float}(b3)/b2) \leq 1.55) \text{ and } (b4 \text{ gt } 2400) \text{ and } ((\text{float}(b4)/b7) \geq 1.413) \text{ and } ((\text{float}(b13)/b12) \geq 1.025) \text{ and } ((\text{float}(b12)/b11) \text{ lt } 1.02)$
Propylitic (carbonate)	$((\text{float}(b3)/b2) \leq 1.55) \text{ and } b4 \text{ gt } 2600 \text{ and } (\text{float}(b6) / b8 \text{ gt } 1.162) \text{ and } (b5 \text{ gt } b6) \text{ and } (b7 \text{ gt } b8) \text{ and } (b9 \text{ gt } b8) \text{ and } ((\text{float}(b13) / b14) \text{ gt } 1.005)$
Propylitic (epidote-chlorite)	$((\text{float}(b3)/b2) \leq 1.55) \text{ and } b4 \text{ gt } 2600 \text{ and } (\text{float}(b6) / b8 \text{ gt } 1.162) \text{ and } (\text{float}(b5) / (\text{float}(b4)+b6) \text{ gt } 0.456) \text{ and } (b5 \text{ gt } b6) \text{ and } (b6 \text{ gt } b7) \text{ and } (b7 \text{ gt } b8) \text{ and } (b9 \text{ gt } b8) \text{ and } ((\text{float}(b13) / b14) \leq 0.999)$
Argillic (alunite, kaolinite)	$((\text{float}(b3)/b2) \leq 1.55) \text{ and } (b4 \text{ gt } 2600) \text{ and } ((\text{float}(b4)/b6) \text{ gt } 1.492) \text{ and } ((\text{float}(b5)/b6) \leq 1.105) \text{ and } ((\text{float}(b7)/b6) \geq 1.03)$
Phyllic (sericite-muscovite)	$((\text{float}(b3)/b2) \leq 1.55) \text{ and } (b4 \text{ gt } 2600) \text{ and } ((\text{float}(b4)/b6) \text{ gt } 1.492) \text{ and } ((\text{float}(b5)/b6) \text{ gt } 1.105) \text{ and } ((\text{float}(b7)/b6) \geq 1.03)$

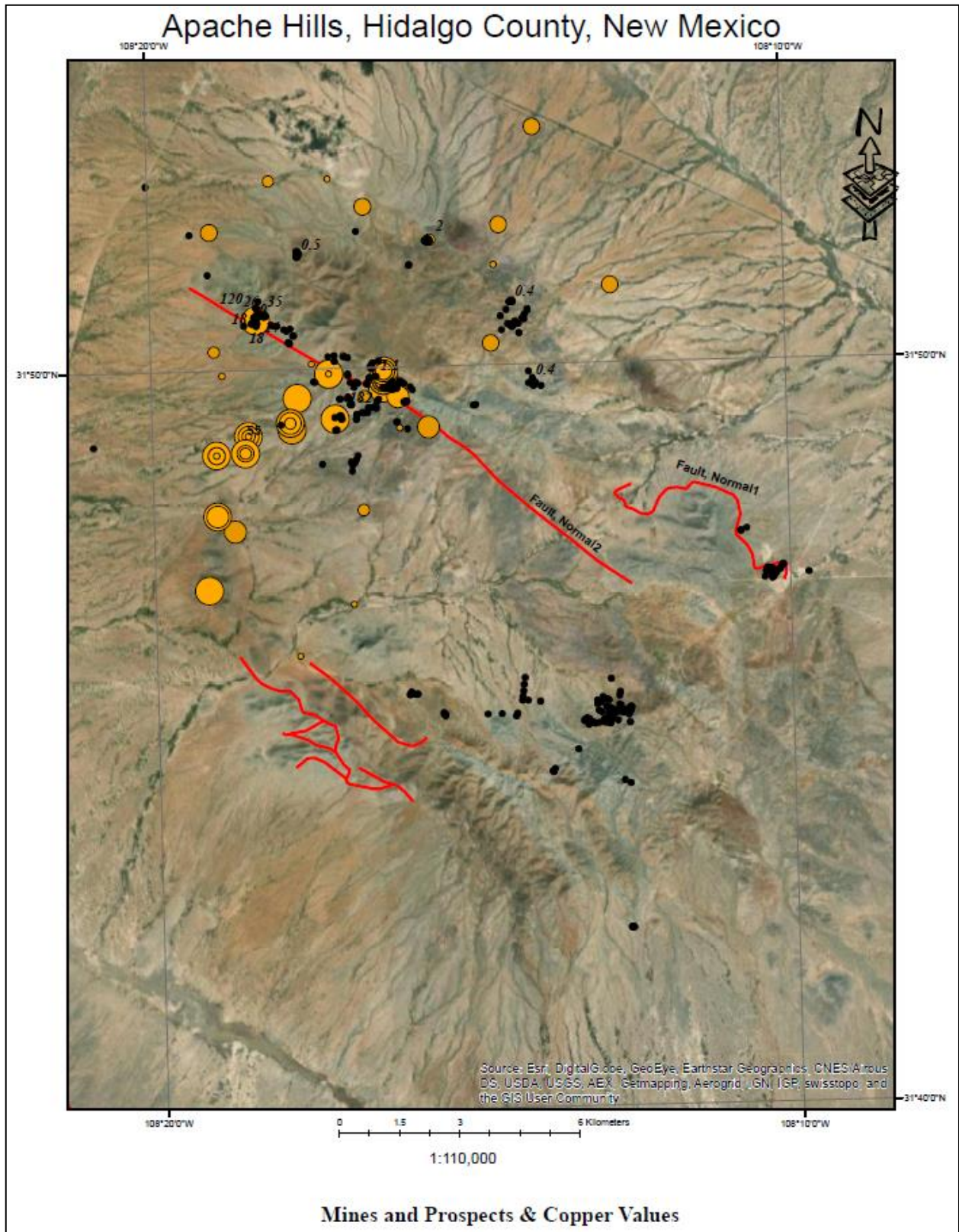


Figure 104a: Mines (black dots) with copper values and faults covering the Apache Hills and Sierra Rica.

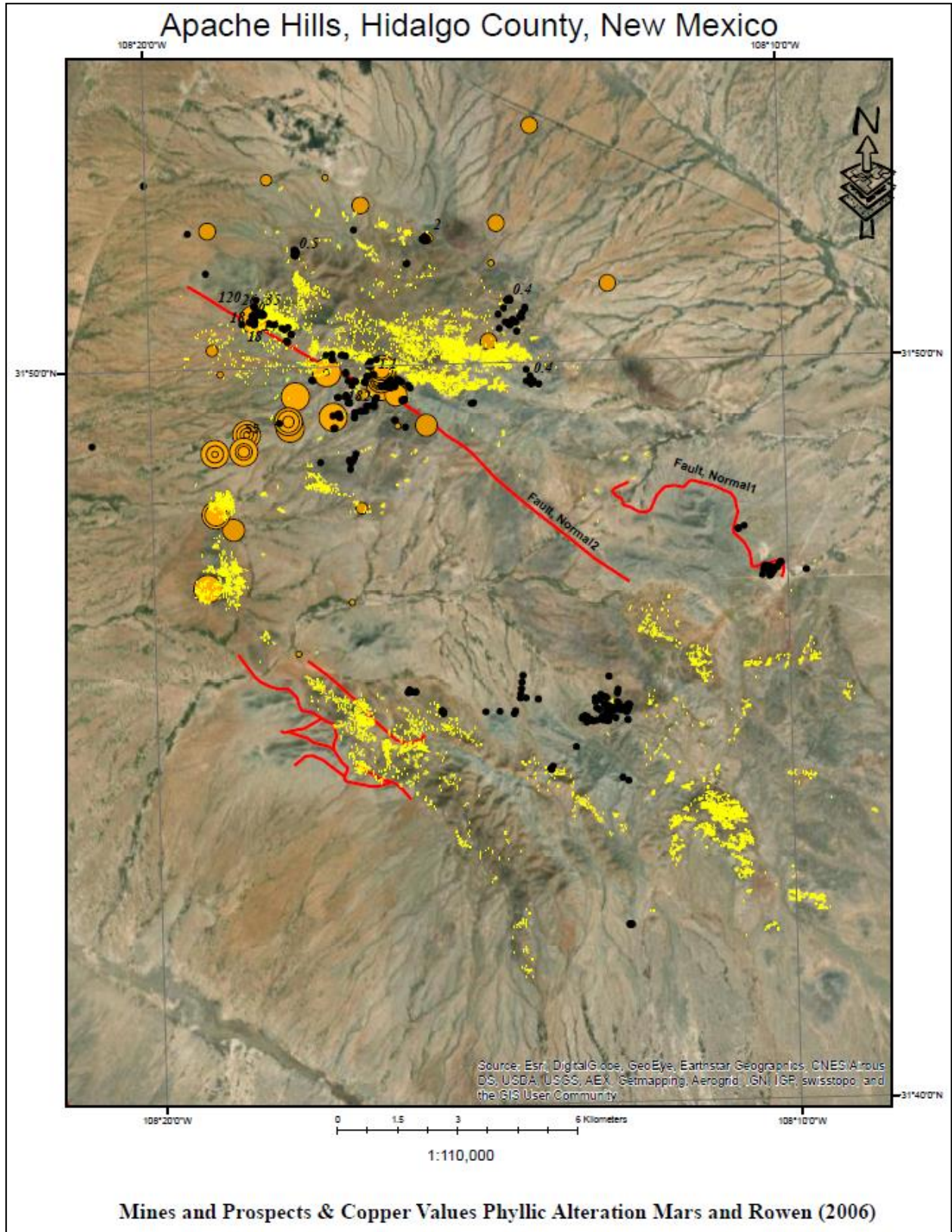


Figure 105: Mines (black dots) with Phyllic Alteration Mars and Rowen algorithm (2006).

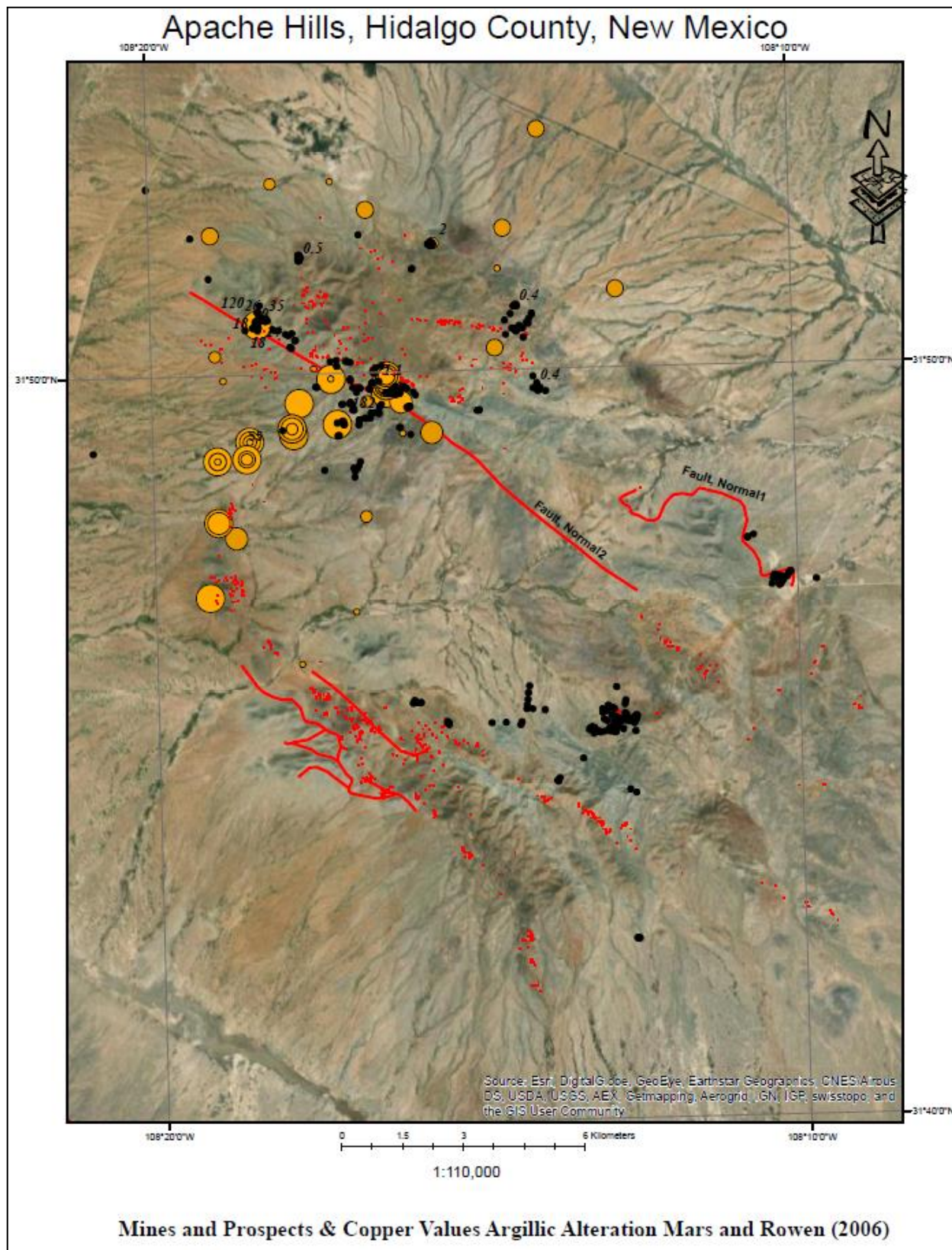


Figure 106: Mines (black dots), copper values, and Argillic Alterations Mars and Rowen (2006).

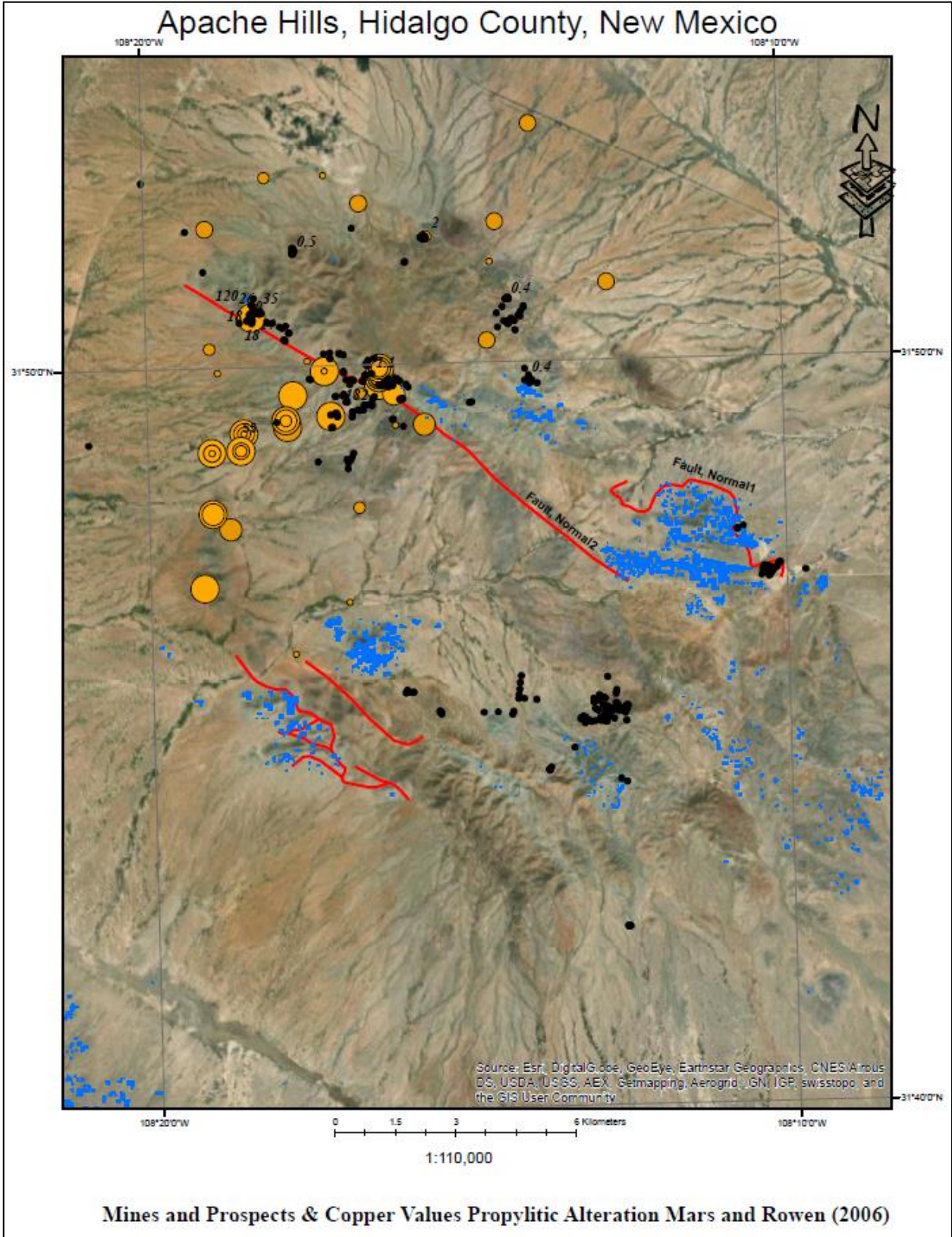


Figure 107: Mines (black dots), copper values, and Propylitic Alterations Mars and Rowen (2006).

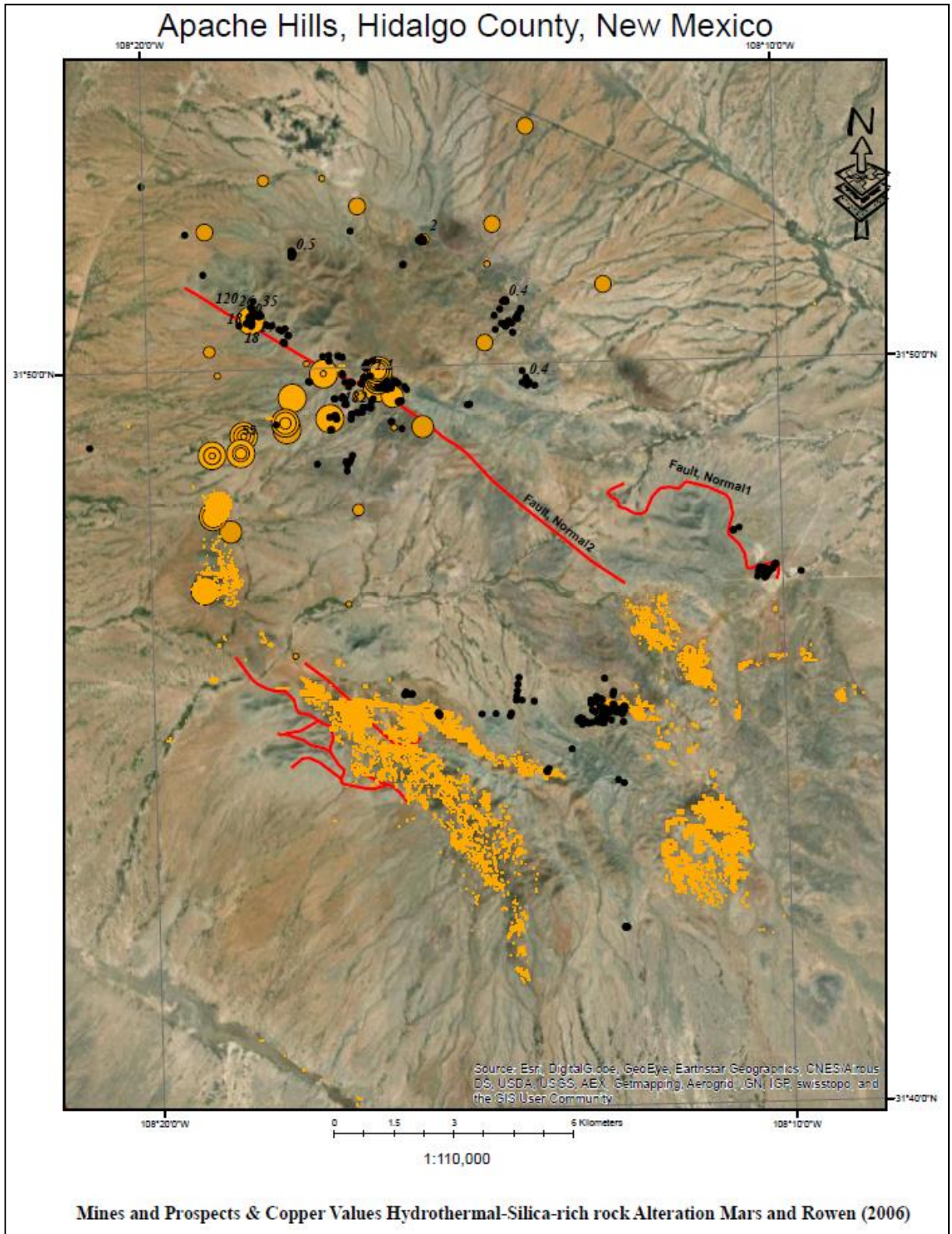


Figure 108: Mines (black dots), copper values, and Hydrothermal-Silica-rich rock Alterations Mars and Rowen (2006).

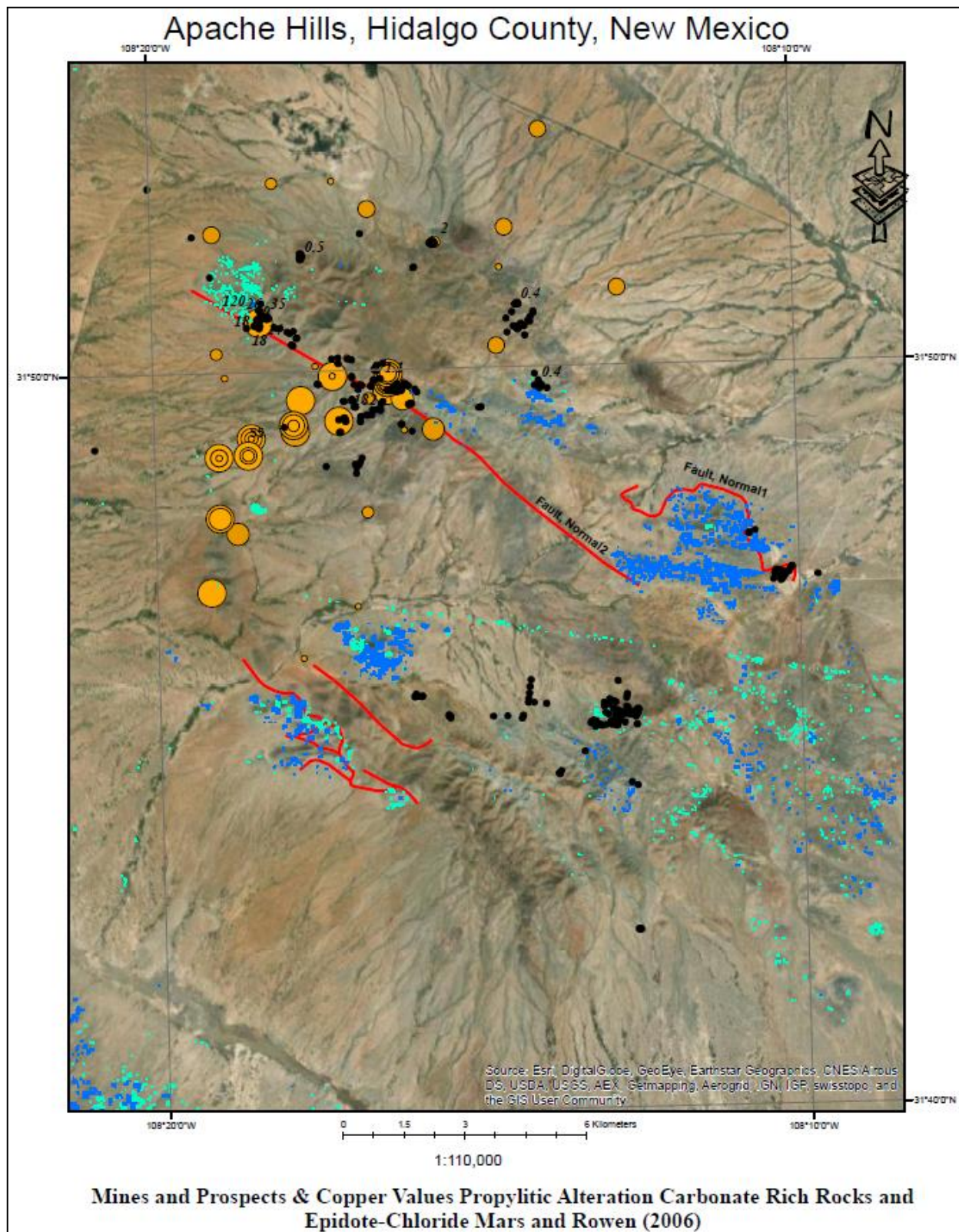


Figure 109: Mines (black dots), copper values, and Propylitic Alterations Carbonate rich rocks and Epidote-Chloride Mars and Rowen (2006).

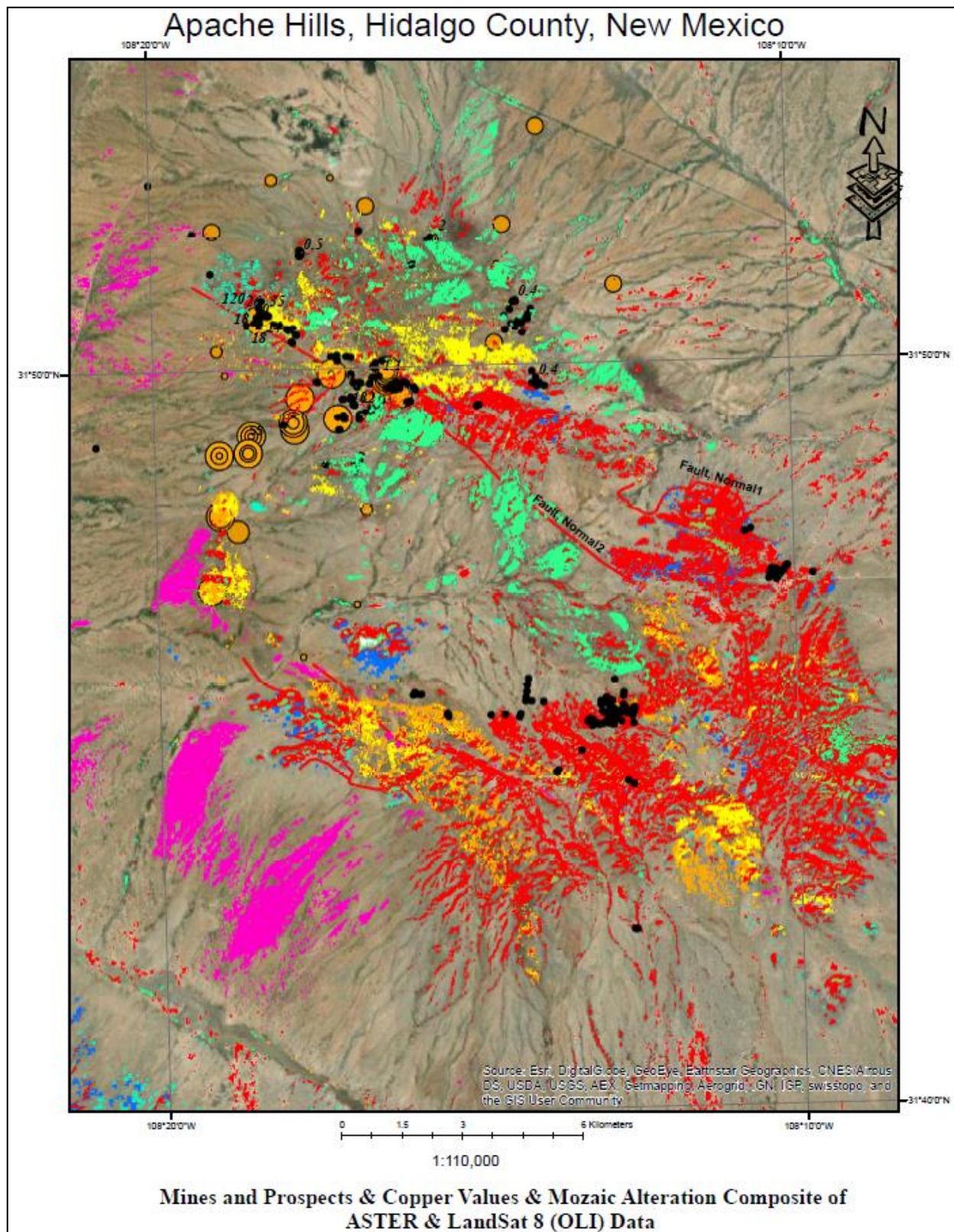


Figure 110: Mines (black dots), copper values, and a Mozaic Composite Landsat 8 (OLI) and ASTER from Mars and Rowen Algorithm (2006).

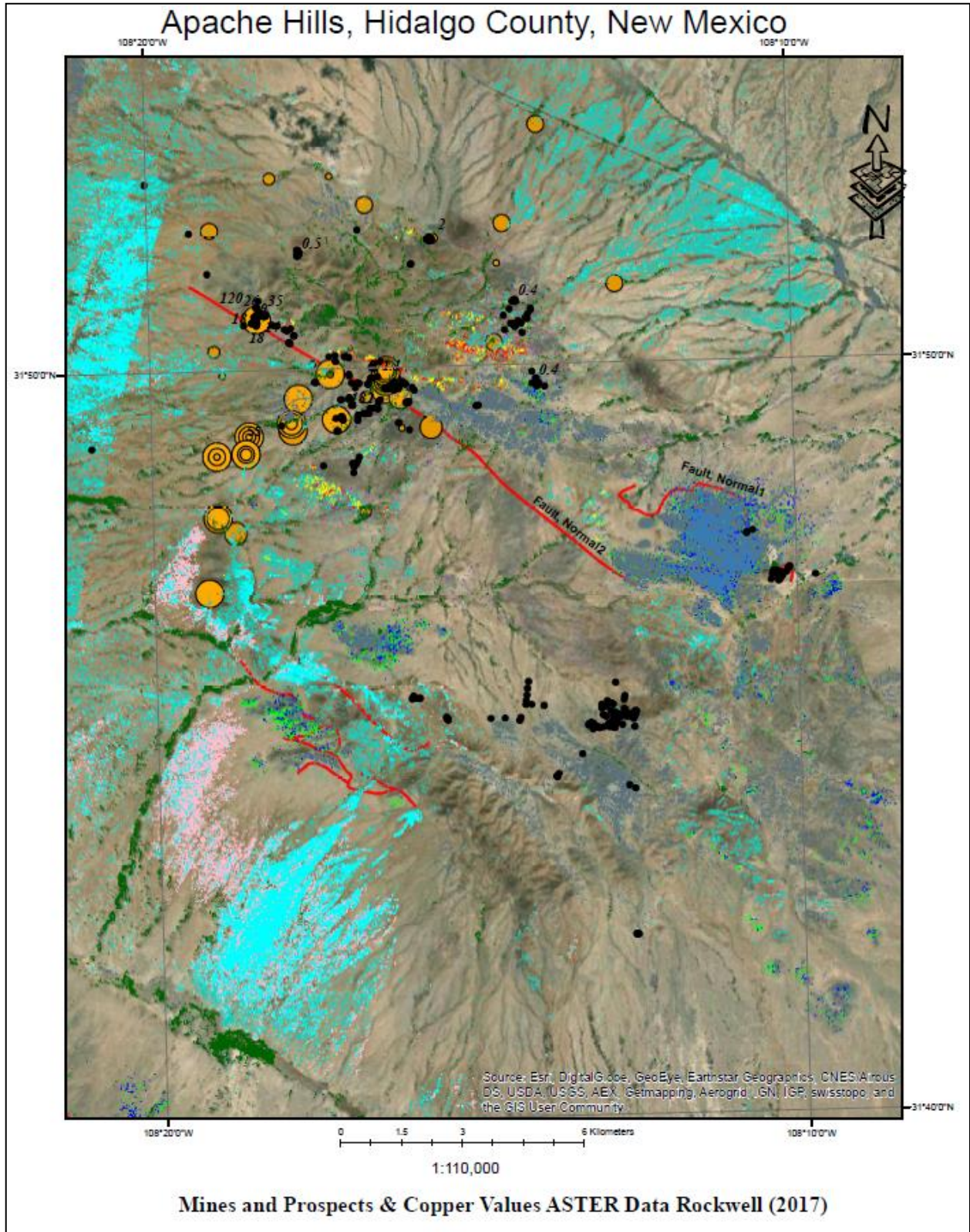


Figure 111: Mines (black dots), copper values, and ASTER data from Rockwell (2017).

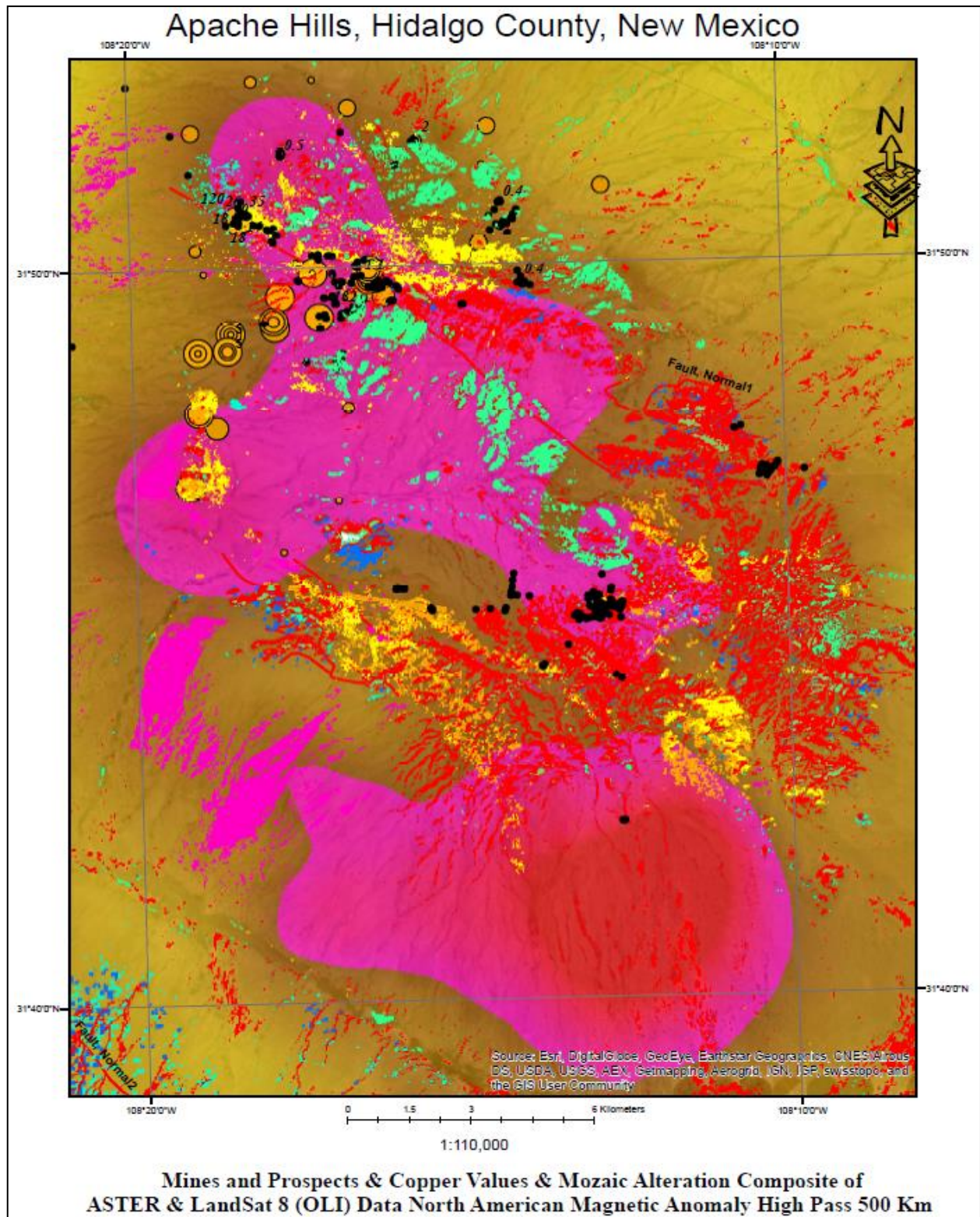


Figure 112: Mines (black dots) and Copper values a Mozaic alteration composite of ASTER & Landsat 8 (OLI) Data. Including the North American Magnetic Anomaly High Pass 500 km.

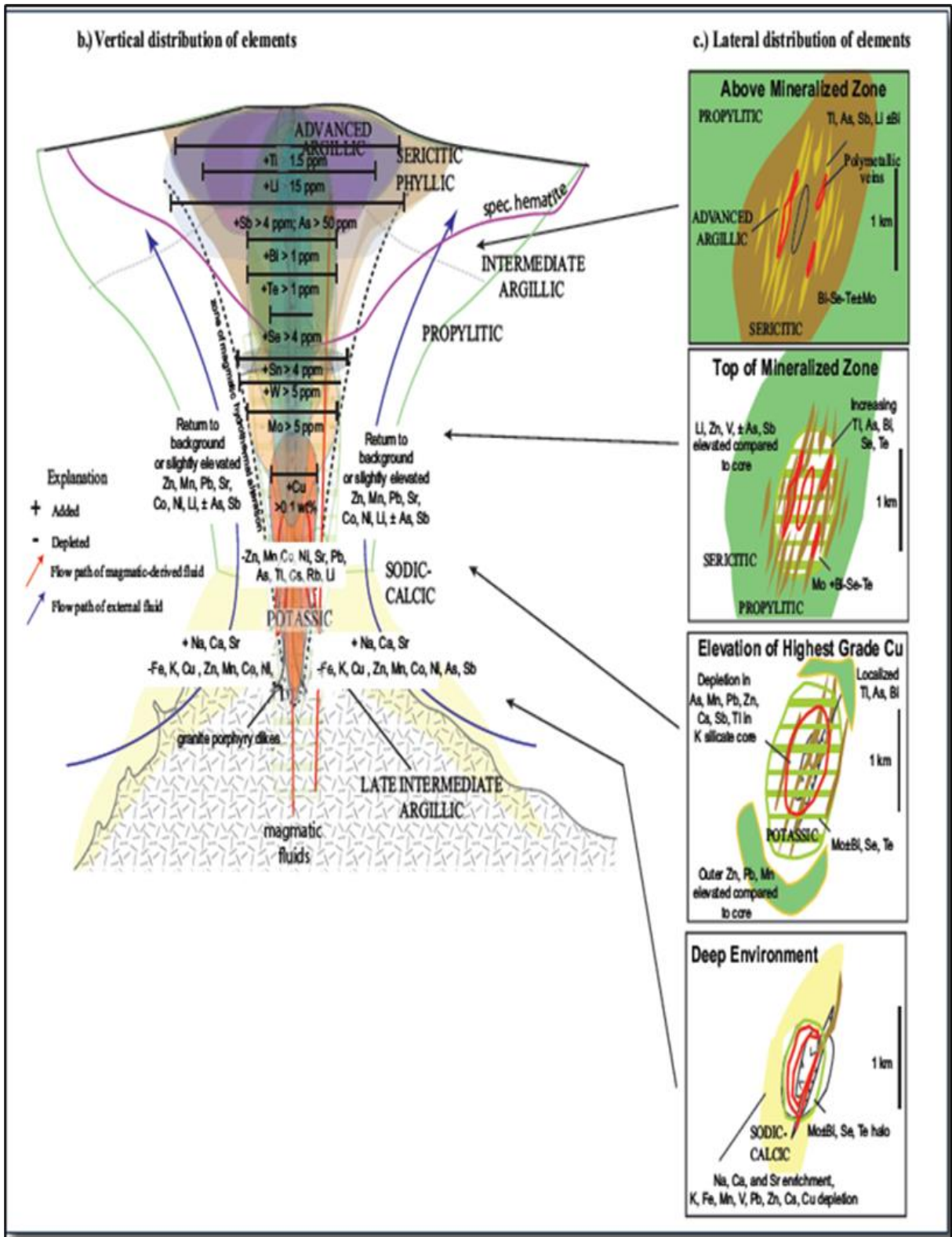
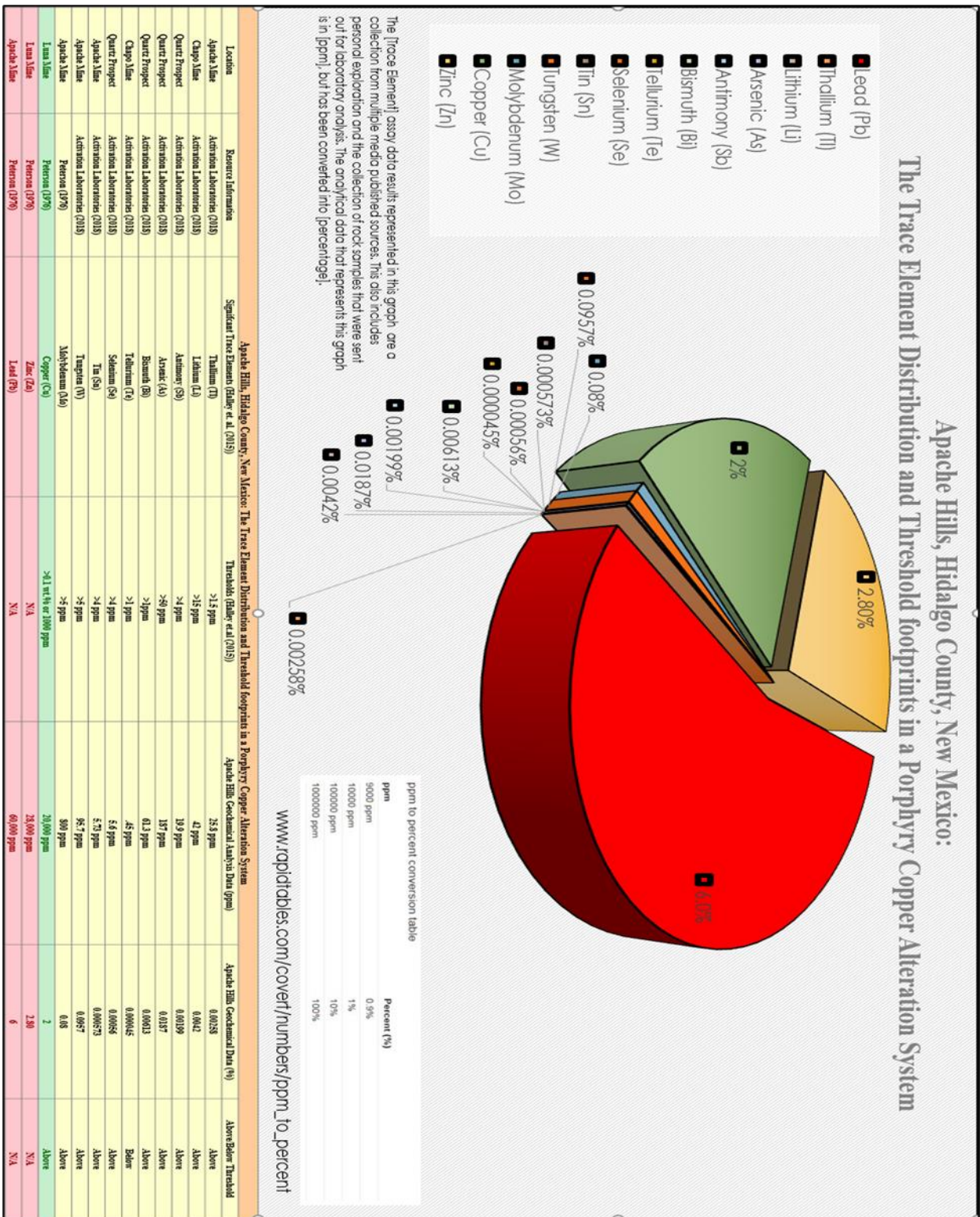


Figure 113: Vertical variations in trace elements in a porphyry Cu system. c.) Schematic changes in hydrothermal alteration assemblages and trace elements through a porphyry Cu system viewed as a series of map views through a vertical system. Figure 1, p. 12



Location	Resource Information	Significant Trace Elements (Haley et al. (2015))	Thresholds (Haley et al. (2015))	Apache Hills Geochemical Analysis Data (ppm)	Apache Hills Geochemical Data (%)	Above/Below Threshold
Apache Mine	Actlabs Laboratories (2018)	Talium (Tl)	>1.5 ppm	26.3 ppm	0.0026	Above
Chapo Mine	Actlabs Laboratories (2018)	Lithium (Li)	>15 ppm	41 ppm	0.0042	Above
Quartz Prospect	Actlabs Laboratories (2018)	Antimony (Sb)	>4 ppm	10.9 ppm	0.00109	Above
Quartz Prospect	Actlabs Laboratories (2018)	Arsenic (As)	>8 ppm	167 ppm	0.0167	Above
Quartz Prospect	Actlabs Laboratories (2018)	Bismuth (Bi)	>1 ppm	61.3 ppm	0.00613	Above
Chapo Mine	Actlabs Laboratories (2018)	Tellurium (Te)	>1 ppm	45 ppm	0.0045	Above
Quartz Prospect	Actlabs Laboratories (2018)	Selenium (Se)	>4 ppm	5.8 ppm	0.00058	Above
Apache Mine	Actlabs Laboratories (2018)	Tin (Sn)	>4 ppm	5.73 ppm	0.000573	Above
Apache Mine	Actlabs Laboratories (2018)	Tungsten (W)	>5 ppm	95.7 ppm	0.00957	Above
Apache Mine	Peterson (1976)	Molybdenum (Mo)	>5 ppm	809 ppm	0.0809	Above
Apache Mine	Peterson (1976)	Copper (Cu)	>4.1 wt% or 1000 ppm	20,000 ppm	2	Above
Apache Mine	Peterson (1976)	Zinc (Zn)	N/A	28,000 ppm	2.80	Above
Apache Mine	Peterson (1976)	Lead (Pb)	N/A	60,000 ppm	6	Above

Figure 114: Trace element distribution and threshold footprints in a porphyry copper alteration system. Combination sample results from Actlabs and Peterson (1976).

References

- Advances in Spectral Geology and Remote Sensing:2008-2017 “Proceedings of Exploration 17: Sixth Decennial International Conference on Mineral Exploration” edited by V. T Schirhart and M.D. Thomas, 2017, Geosciences Australia (2014).
- Accame, G.; Robinson, B.; and Biehl, L., "Iron Oxide Genesis and Its Influence on the Spectral Reflectance Properties of Gossans" (1983). LARS Technical Reports. Paper 68. <http://docs.lib.purdue.edu/larstech/68>
- Arunachalam, M., Joshua, R.M., Kochuparampil, A.J. *et al.* ArcOLITIRS: A Toolbox for Radiometric Calibration and Surface Temperature Estimation from Landsat 8 Products in ArcGIS Environment. *J Indian Soc Remote Sens* (2022). <https://doi.org/10.1007/s12524-022-01636-2>
- Armstrong, R. L. 1972. Low-angle (denudational) faults, hinterland of the Sevier orogenic belt, eastern Nevada, and western Utah. *Bull. Geol. Soc. Am.* 83, 1729-54.
- Aronoff S. *Remote Sensing for GIS Managers*. 1st ed. Redlands Cal: ESRI Press; 2005.
- Asmus, B. 2013. Gossan or the iron cap. *Archaeometallurgy*. en.archaeometallurgie.de/gossan-iron-cap/
- Astudillo N (2008) Mineralogía magnética y paleomagnetismo en los

megayacimientos tipo pórfido cuprífero Chuquicamata y El Teniente, Chile. Unpublished Ph.D. thesis, Universidad de Chile, p 306

Astudillo N, Roperch P, Townley B, Arriagada C, Makshev V (2008) Importance of small block rotations in damage zones along Transcurrent faults. Evidence from the Chuquicamata open pit, Northern Chile. *Tectonophysics* 450:1–20. doi 10.1016/j.tecto.2007.12.008

Astudillo N, Roperch P, Townley B, Arriagada C, Chauvin A (2010) Magnetic polarity zonation within El Teniente copper-molybdenum Porphyry deposit, central Chile. *Miner Deposita* 45:23–41. doi:10.1007/s00126-009-0256-0

Banerjee SK (1991) Magnetic properties of Fe–Ti oxides. In: Lindsley DH (ed), *Oxide minerals: petrologic and magnetic significance*. *Rev Mineral* 25: 107-128

Banerjee, Krishnendu & Jain, Manish & Panda, Surajit & Jeyaseelan, Ayyemperumal. (2019). Landsat 8 OLI Data for Identification of Hydrothermal Alteration Zone in Singhbhum Shear Zone using Successive Band Depth Difference Technique—A New Image Processing Approach. *Current science*. 116. 1639-1647. 10.18520/cs/v116/i10/1639-1647. May 2019

Bladh, K.W., 1982, The formation of goethite, jarosite, and alunite during the weathering of sulfide-bearing felsic rocks: *Economic Geology*, v. 77, no. 1, p. 176-184.

Burchfiel, B. C., and Davis, G. A., 1971, Clark Mountain thrust complex in the Cordillera of southeastern California: Geologic summary and field trip guide, in Elders, W. A., ed. *Geological excursions in southern California: University of Riverside, Campus Museum Contribution 1*, p. 1-29. 1972, Structural framework and evolution of the southern part of the Cordilleran orogen, western United States: *American Journal of Science*, v. 272, p. 97-118. 1975, Nature and controls of Cordilleran orogenesis, western United States: Extensions of an earlier synthesis: *American Journal of Science*, v. 275-A, p. 363-396. 1977, Geology of Sagamore Canyon-Slaughterhouse Spring area, New York Mountains, California: *Geological Society of America Bulletin*, v. 88, p. 1623-1640.

- C.J. Busby, T.L. Pavlis, S.M. Roeske, B. Tikoff, 2023. "The North American Cordillera during the Mesozoic to Paleogene: Selected questions and controversies," *Laurentia: Turning Points in the Evolution of a Continent*, Steven J. Whitmeyer, Michael L. Williams, Dawn A. Kellett, Basil Tikoff
- Bert Sylvenus Butler; A suggested explanation of the high ferric oxide content of limestone contact zones. *Economic Geology* 1923; 18 (4): 398–404.
doi: <https://doi.org/10.2113/gsecongeo.18.4.398>
- William X. Chavez; Supergene Oxidation of Copper Deposits: Zoning and Distribution of Copper Oxide Minerals. *SEG Discovery* 2000; (41): 1–21.
doi: <https://doi.org/10.5382/SEGnews.2000-41.fea>
- Clark, R.N., Swayze, G.A., Wise, R., Livo, E., Hoefen, T., Kokaly, R., Sutley, S.J. 2007. USGS digital spectral library splib06a. U.S. Geological Survey, Digital Data Series, 231. Available at <http://speclab.cr.usgs.gov/spectral.lib06>
- Clinkscales, Chris & Lawton, Timothy. (2017). Mesozoic–Paleogene structural evolution of the southern U.S. Cordillera as revealed in the Little and Big Hatchet Mountains, southwest New Mexico, USA. *Geosphere*. 14. 10.1130/GES01539.1.
- Coney, P.J. & Reynolds, S.J. 1977. Cordilleran Benioff zones. *Nature*, 270,4036

Coney, P. J. 1980. Cordilleran metamorphic core complexes: an overview. In: CRRTENDEN, M.L., Coney P, J.& Davis, G.H. (eds.) Cordilleran Metamorphic Core Complexes. *Mem. Geol. Soc. Am.* 153.7-34.

Coney, P. J. January 1987. The regional tectonic setting and possible causes of Cenozoic extension in the North America Cordillera; *Geological Society, London, Special Publications.* 28. 177-186.
10.1144/GSL.SP.1987.028.01.13.

Cross Reference: Data Credit: The Land Process (LP) Distributed Active Archive Center (DAAC), Japan's Ministry of Economy, Trade, and Industry (METI), Japan's Earth Remote Sensing Data Analysis Center, and NASA.

De Smith MJ Goodchild MF Longley P. *Geospatial Analysis: A Comprehensive Guide to Principles Techniques and Software Tools.* 6th ed. United States: Place of publication not identified; 2018.

Deal, E.G., Elston, W.E., Erb, E.E., Peterson, S.L., Reiter, D.E., Damon, P.E., and Shafiqullah, M., 1978, Cenozoic volcanic geology of the Basin and Range province in Hidalgo County, southwestern New Mexico, in Callender, J.F., and others, eds., Land of Cochise, southeastern Arizona: New Mexico Geological Society 29th Field Conference Guidebook, p. 219-229.

- William R. Dickinson, Timothy F. Lawton; Carboniferous to Cretaceous assembly and fragmentation of Mexico. *GSA Bulletin* 2001;13 (9): 1142–1160.
doi: [https://doi.org/10.1130/0016-7606\(2001\)113<1142:CTCAAF>2.0.CO;2](https://doi.org/10.1130/0016-7606(2001)113<1142:CTCAAF>2.0.CO;2)
- William R Dickinson, Timothy F Lawton; Tectonic setting and sandstone Petrofacies of the Bisbee basin (USA–Mexico), *Journal of South American Earth Sciences*, Volume 14, Issue 5, 2001, Pages 475-504, ISSN 0895-9811,
[https://doi.org/10.1016/S0895-9811\(01\)00046-3](https://doi.org/10.1016/S0895-9811(01)00046-3).
- Dickinson, W. R., 1976, Sedimentary basins developed during the evolution of Mesozoic-Cenozoic arc-trench system in western North America: *Canadian Journal of Earth Sciences*, v. 13, p. 1268-1287.
- Dickinson, W. R. 1981. Plate tectonic evolution of the southern Cordillera. In: Dickinson, W.R. & Payne, W.D. (eds.) Relations of Tectonics to Ore Deposits in the Southern Cordillera. *Digest Ariz. Geol. Soc.* 14, 113-35.
- Dickinson, W. R., Klute, M. A., and Swift, P. N., 1986a, The Bisbee basin and its bearing on late Mesozoic paleo-geographic and paleo-tectonic relations between the Cordilleran and Caribbean regions, in Abbott, P. L., ed., Cretaceous stratigraphy of western North America: *Society of Economic Paleontologists and Mineralogists, Pacific Section*, p. 51-62.
- Drewes, H., 1978, The Cordilleran orogenic belt between Nevada and Chihuahua: *Geological Society of America Bulletin*, v. 89, p. 641-657

Wolfgang E. Elston 1965, pp. 210-214. <https://doi.org/10.56577/FFC-16.210> in:
Southwestern New Mexico II, Fitzsimmons, J. P.; Balk, C. L.; [eds.], New
Mexico Geological Society 16th Annual Fall Field Conference Guidebook,
244 p. <https://doi.org/10.56577/FFC-16>

Wolfgang E. Elston 1970, pp. 147-153. <https://doi.org/10.56577/FFC-21.147> in:
Tyrone, Big Hatchet Mountain, Florida Mountains Region, Woodward, L.
A.; [ed.], New Mexico Geological Society 21st Annual Fall Field
Conference Guidebook, 176 p. <https://doi.org/10.56577/FFC-21>

Elston, W.E. 1976. Tectonic significance of mid-Tertiary volcanism in the Basin
and Range province: a critical review with special reference to New Mexico.
In: Elston, W.E. & Northrup, S.A. (eds.) *Cenozoic Volcanism in
Southwestern New Mexico. Special Publication New Mexico Geol. Society*
5, 93-151.

Green, G.N., and Jones, G.E., 1997, Digital geologic map of New Mexico in
Arc/Info export format: *U.S. Geological Survey Open-File Report OF-97-*
52, scale 1: 500,000. USGS <https://pubs.er.usgs.gov/publication/ofr9752>.
Geologic Names lexicon found at <http://ngmdb.usgs.gov/Geolex/>
<https://ngmdb.usgs.gov/Geolex/search>

- Green, G.N., and Jones, G.E., 1997, Digital geologic map of New Mexico in Arc/Info export format: *U.S. Geological Survey Open-File Report OF-97-52*, scale 1: 500,000. USGS <https://pubs.er.usgs.gov/publication/ofr9752>.
Geologic Names lexicon found at <http://ngmdb.usgs.gov/Geolex/>
<https://ngmdb.usgs.gov/Geolex/search>
- Guilbert, John M. and Charles F. Park Jr (1986) *The Geology of Ore Deposits*, W. H. Freeman, pp 799–830, ISBN 0-7167-1456-6
- Scott Halley, John H. Dilles, Richard M. Tosdal; *Footprints: Hydrothermal Alteration and Geochemical Dispersion Around Porphyry Copper Deposits. SEG-Discovery* 2015;(100):1–17.
doi: <https://doi.org/10.5382/SEGnews.2015-100.fea>
- Hamilton, W., 1982, Structural evolution of the Big Maria Mountains, northeastern Riverside County, southeastern California, in Frost, E. G., and Martin, D. L., eds., *Mesozoic Cenozoic tectonic evolution of the Colorado River region, California, Arizona, and Nevada: San Diego, California, Cordilleran Publishers*, p. 1-27.
- Horton, J.D., 2017, The State Geologic Map Compilation (SGMC) geodatabase of the conterminous United States (ver. 1.1, August 2017): U.S. Geological Survey data release, <https://doi.org/10.5066/F7WH2N65>.

Horton, J.D., San Juan, C.A., and Stoesser, D.B., 2017, The State Geologic Map Compilation (SGMC) geodatabase of the conterminous United States (ver. 1.1, August 2017): *U.S. Geological Survey Data Series 1052*, 46 p., <https://doi.org/10.3133/ds1052>.

Huntington, JF 1996, 'The role of remote sensing in finding hydrothermal mineral deposits on Earth.' In: *Evolution of Hydrothermal Ecosystems on Earth (and Mars?)*, *Ciba Foundation Symposium 202*, edited by Bock GR and Goode JA, John Wiley & Sons, Chichester, UK, pp. 214-235.

Huntington JF. The role of remote sensing in finding hydrothermal mineral deposits on Earth. *Ciba Found Symp.* 1996; 202:214-31; discussion 231-5. doi: 10.1002/9780470514986.ch12. PMID: 9243018.

Imbroane, M.A., Melenti, C. & Gorgan, D., 2007, Mineral Explorations by Landsat Image Ratios. In *Proceedings of the Ninth International Symposium on Symbolic and Numeric Algorithms for Scientific Computing*, September 26-29, Timisoara, Romania, IEEE computer society, pp. 335-340.

Jenks, George F. 1967. "The Data Model Concept in Statistical Mapping," *International Yearbook of Cartography* 7: 186–190.

George F. Jenks (1963). Generalization in Statistical Mapping, *Annals of the Association of American Geographers*, 53:1, 15-26, DOI: [10.1111/j.1467-8306.1963.tb00429.x](https://doi.org/10.1111/j.1467-8306.1963.tb00429.x)

- Jones, F. A. (1904). *New Mexico Mines and Minerals Being an Epitome of the Early Mining History and Resources of New Mexican Mines, in the Various Districts, down to the Present Time United States: New Mexican Printing Company.*
- Kelly, W.C. (1981). Gossan. In: *Mineralogy. Encyclopedia of Earth Science.* Springer, Boston, MA. https://doi.org/10.1007/0-387-30720-6_55
- R. F. Kokaly and T. Bahr, "The USGS PRISM system for spectral analysis — An ENVI/IDL-based software," *2014 6th Workshop on Hyperspectral Image and Signal Processing: Evolution in Remote Sensing (WHISPERS)*, 2014, pp. 1-4, doi: 10.1109/WHISPERS.2014.8077552.
- Kokaly, R.F., Clark, R.N., Swayze, G.A., Livo, K.E., Hoefen, T.M., Pearson, N.C., Wise, R.A., Benzel, W.M., Lowers, H.A., Driscoll, R.L., and Klein, A.J., 2017, USGS Spectral Library Version 7 Data: U.S. Geological Survey data release, <https://dx.doi.org/10.5066/F7RR1WDJ>.
- Kokaly, R.F., Clark, R.N., Swayze, G.A., Livo, K.E., Hoefen, T.M., Pearson, N.C., Wise, R.A., Benzel, W.M., Lowers, H.A., Driscoll, R.L., and Klein, A.J., 2017, USGS Spectral Library Version 7: U.S. Geological Survey Data Series 1035, 61 p., <https://doi.org/10.3133/ds1035>.
- Kruse, FA 1994, Imaging spectrometer data analysis-a tutorial. *Proc. Int. Symp. Spectral Sensing Res.* 1, 44-50.

- Lamqadem AA, Saber H, Pradhan B. Quantitative Assessment of Desertification in an Arid Oasis Using Remote Sensing Data and Spectral Index Techniques. *Remote Sensing*. 2018; 10(12):1862. <https://doi.org/10.3390/rs10121862>
- Lasky, Grossman Samuel; Ferric-ferrous ratio in contact-metamorphic deposits; discussion. *Economic Geology* 1934; 29 (2): 203–206. doi: <https://doi.org/10.2113/gsecongeo.29.2.203>
- S.G. Lasky 1947; Geology and ore deposits of the Little Hatchet Mountains, Hidalgo and Grant Counties, New Mexico DOI10.3133/pp208, Publication Type Report, Publication Subtype USGS Numbered Series, *Professional Paper, Series Number 208, pp208, Source USGS Publications Warehouse*.
- Timothy F. Lawton, Jeffrey M. Amato, Sarah E.K. Machin, John C. Gilbert, Spencer G. Lucas; Transition from Late Jurassic rifting to middle Cretaceous dynamic foreland, southwestern U.S., and northwestern Mexico. *GSA Bulletin* 2020; 132 (11-12): 24892516. doi: <https://doi.org/10.1130/B35433.1>
- Lipman, P.W., Protska, H. J. & Christiansen, R. L. 1971. Evolving subduction zones in the western United States as interpreted from igneous rocks. *Science*, 174, 821-5.

Mack H. Greg. May 1987 Mid-Cretaceous (late Albian) change from rift to a retro-arc foreland basin in southwestern New Mexico. *GSA Bulletin* 1987; 98 (5): 507514. doi: [https://doi.org/10.1130/00167606\(1987\)98<507:MLACFR>2.0.CO;2](https://doi.org/10.1130/00167606(1987)98<507:MLACFR>2.0.CO;2)

Mars, J.C., 2013, Hydrothermal alteration maps of the central and southern Basin and Range province of the United States compiled from Advanced Spaceborne Thermal Emission and Reflection Radiometer (ASTER) data (ver1.1, April 8, 2014: U.S. Geological Survey Open-File Report 2013–1139, 6 p., 13 plates, scale 1:1,300,000, <http://dx.doi.org/10.3133/ofr20131139>

McLemore, V.T., Sutphin, D.M., Hack, D.R., and Pease, T.C., 1996, Mining history and mineral resources of the Mimbres Resource Area, Dona, Ana, Luna, Hidalgo, and Grant Counties, New Mexico: New Mexico Bureau of Mines and Mineral Resources Open-File Report OF-424, 251 p.

V.T. McLemore, New Mexico Bureau of Mines and Geology, written communication, 2007.

McGookey, D. P., Haun, J. D., Hale, L. A., Goodell, H. G., McCubbin, D. G., Weimer, R. J., and Wulf, G. R., 1972, Cretaceous System, in Mallory, W. W., ed., Geologic atlas of Rocky Mountain region: *Rocky Mountain Association of Geologists*, p. 190-228.

Mishra N, Haque MO, Leigh L, Aaron D, Helder D, Markham B. Radiometric Cross Calibration of Landsat 8 Operational Land Imager (OLI) and Landsat 7 Enhanced Thematic Mapper Plus (ETM+). *Remote Sensing*. 2014; 6(12):12619-12638. <https://doi.org/10.3390/rs61212619>

New Mexico Bureau of Geology and Mineral Resources, 2003, Geologic map of New Mexico: New Mexico Bureau of Geology and Mineral Resources, scale 1:500,000, accessed August 2011 at <https://geoinfo.nmt.edu/publications/maps/geologic/state/home.cfml>.

NGMDB—Available at https://ngmdb.usgs.gov/Prodesc/proddesc_59219.htm.

<http://earthexplorer.usgs.gov>, U.S. Geological Survey (USGS) publish date 2015/04/15; *U.S. Geological Survey (USGS) Earth Resources Observation and Science (EROS) Center*, Sioux Falls, SD, NASA ASTER Level 1T.

NGMDB—Available at https://ngmdb.usgs.gov/Prodesc/proddesc_22974.htm.

Peterson, Stephen L. "Geology of the Apache No. 2 Mining District Hidalgo County, New Mexico." (1976) https://digitalrepository.unm.edu/eps_etds/186

Pour, A.B., & Hashim, M. (2014). The application of Landsat-8 OLI/TIRS data for geological mapping: A case study from SE Iran.

PIGMD—Available at <https://pubs.usgs.gov/of/2005/1351/#NM>.

- Rangin, C., 1978, Speculative model of Mesozoic geodynamics, central Baja California to northeastern Sonora (Mexico), in Howell, D. G., and McDougall, K. A., eds., Mesozoic paleogeography of western United States-. *Society of Economic Paleontologists and Mineralogists, Pacific Section, Pacific Coast Paleogeography Symposium, 2nd*, p. 85-106.
- Reynolds, S. J., Keith, S. B., and Coney, P. J., 1980, Stacked overthrusts of Precambrian crystalline basement and inverted Paleozoic sections emplaced over Mesozoic strata, west-central Arizona: *Arizona Geological Society Digest*, v. 12, p. 45-51.
- Riveros Jensen, Karl & Veloso, Eugenio & Campos, Eduardo & Menzies, Andrew & Véliz, W. (2014). Magnetic properties related to hydrothermal alteration processes at the Escondida porphyry copper deposit, northern Chile. *Mineralium Deposita*. 49. 10.1007/s00126-014-0514-7.
- Rockwell, B.W., 2012, Description and validation of an automated methodology for mapping mineralogy, vegetation, and hydrothermal alteration type from ASTER satellite imagery with examples from the San Juan Mountains, Colorado: U.S. Geological Survey Scientific Investigations Map 3190, 35 p. pamphlet, 5 map sheets, scale 1:100,000.

Rockwell, B.W., 2013, Automated mapping of mineral groups and green vegetation from Landsat Thematic Mapper imagery with an example from the San Juan Mountains, Colorado: U.S. Geological Survey Scientific Investigations Map 3252, 25p. pamphlet, 1 map sheet, scale 1:325,000, <https://pubs.usgs.gov/sim/3252/>

Rockwell, B.W., and Bonham, L.C., 2017, Digital maps of hydrothermal alteration type, key mineral groups, and green vegetation of the western United States derived from automated analysis of ASTER satellite data: U.S. Geological Survey data release, <https://doi.org/10.5066/F7CR5RK7>.

Rockwell, B.W., Gnesda, W.R., and Hofstra, A.H., 2021, Improved automated identification and mapping of iron sulfate minerals, other mineral groups, and vegetation using Landsat 8 Operational Land Imager data, San Juan Mountains, Colorado, and Four Corners Region: U.S. Geological Survey Scientific Investigations Map 3466, 1 sheet, scale 1:325,000, 37-p. pamphlet, <https://doi.org/10.3133/sim3466>.

Schaepman, M. and S. Dangel, "Solid laboratory calibration of a non-imaging spectroradiometer," *Appl. Opt.* 39, 3754-3764 (2000).

- Stewart, J.H. 1978. Basin and Range Structure in Western North America: a review. In: Smith, R.B. Eaton, G.L. (eds.) *Cenozoic Tectonics and Regional Geophysics of the Western Cordillera. Mem. Geol. Soc. Am.* 152, 1-31.
- Strongin, Oscar, 1957, *Geology and ore deposits of Apache Hills and northern Sierra Rica, Hidalgo County, New Mexico: Columbia Univ. unpublished Ph.D. dissertation, 221 p.*
- Swapam Kumar Haldar, Chapter 3 - Photogeology, Remote Sensing, and Geographic Information System in Mineral Exploration, Editor(s): Swapam Kumar Haldar, *Mineral Exploration (Second Edition)*, Elsevier, 2018, Pages 47-68, ISBN-9780128140222, <https://doi.org/10.1016/B978-0-12-814022-2.000034>. (<https://www.sciencedirect.com/science/article/pii/B9780128140222000034>).
- Thomas, M. 2012. National ASTER Map AIOH group composition. Geoscience Australia, Canberra. <http://pid.geoscience.gov.au/dataset/ga/74356>
- Trauger, Frederick D. 1965, pp. 184-187, *Geologic structure pattern of Grant County, New Mexico* <https://doi.org/10.56577/FFC-16.184> in *Southwestern New Mexico II*, Fitzsimmons, J. P.; Balk, C. L.; [eds.], New Mexico Geological Society 16th Annual Fall Field Conference Guidebook, 244 p. <https://doi.org/10.56577/FFC-16>

Thomas M, Walter MR., Application of hyperspectral infrared analysis of hydrothermal alteration on Earth and Mars. *Astrobiology*. 2002 Fall;2(3):335-51. doi: 10.1089/153110702762027916. PMID: 12530243.

U.S. Geological Survey (USGS) Earth Resources Observation and Science (EROS) Center Publication date: 2006/05/10. Landsat 8 OLI/TIRS Collection 1 Tier 1; Remote-Sensing Image; U.S. Geological Survey (USGS) *Earth Resources Observation and Science (EROS) Center*, Sioux Falls, South Dakota, USA.
<https://earthexplorer.usgs.gov>

Index Data Base Band References (Table 5b):

Henrich, V., Jung, A., Götze, C., Sandow, C., Thürkow, D., Gläßer, C. (2009): Development of an online indices database: Motivation, concept, and implementation. 6th EARSel Imaging Spectroscopy SIG Workshop Innovative Tool for Scientific and Commercial Environment Applications Tel Aviv, Israel, March 16-18, 2009.

Henrich, V. and Krauss, G. and Götze, C. and Sandow, C. *The Index Database 2011*. <https://www.indexdatabase.de/db/i-single.php?id=22>,

Henrich, V., Krauss, G., Götze, C., Sandow, C. (2012): IDB - www.indexdatabase.de, Entwicklung einer Datenbank für Fernerkundungsindizes. AK Fernerkundung, Bochum, 4.-5. 10. 2012.

Hewson, Rob D.; Cudahy, T. J.; Huntington, J. F. Geologic and alteration mapping at Mt Fitton, South Australia, using ASTER satellite-borne data. *Journal Geoscience and Remote Sensing Symposium*, 2001. Volume 2, Pages 724-726.IGARSS'01.IEEE2001International.DOI:10.1109/igarss.2001.976615https://www.indexdatabase.de/db/isingle.php?id=78

Kalinowski, Aleks; Oliver, Simon. ASTER Mineral Index Processing Manual *Journal Remote Sensing Applications 2004, Geosciences Australia* https://www.indexdatabase.de/db/i-single.php?id=39

Rowan, L.C.; Mars, J.C.; Lithologic mapping in the Mountain Pass, California area using Advanced Spaceborne Thermal Emission and Reflection Radiometer (ASTER) data. *Journal Remote Sensing of Environment* 2003; Volume 84; Pages 350- 366.

Volesky, J.C.; Stern, R.J.; Johnson, P.R...Geological control of massive sulfide mineralization in the Neoproterozoic Wadi Bidah shear zone, southwestern Saudi Arabia, inferences from orbital remote sensing and field studies. *Journal Precambrian Research* 2003; Volume123; Issue 2-4, Pages 235-247.

GER 3700 Reference Information

Geophysical and Environmental Research Corporation, “GER3700: highest resolution, photodiode & photo conductor array-based spectroradiometer,” product data sheet Geophysical and Environmental Research Corporation, Millbrook, N.Y., 1993, pp. 1–2.

K. Staenz, R. P. Gauthier, D. P. Witz, M. E. Schaepman, and K. I. Itten, “GER 3700—a new array-based instrument for field spectroscopy in the VNIR SWIR wavelength regions,” in *Proceeding of the International Symposium on Spectral Sensing Research* Topographic Engineering Center, U.S. Army Corps of Engineers, Alexandria, Va., 1995.

The Spectral Geologist 8 References

Berman, Mark, Leanne Bischof, and Jon Huntington. ‘Algorithms and Software for the Automated Identification of Minerals Using Field Spectra or Hyperspectral Imagery.’ In *Proceedings of the 13th International Conference on Applied Geologic Remote Sensing, Vancouver*, 1:222–32. Environmental Research Institute of Michigan Ann Arbor, 1999.

Huntington, Jon, Peter Mason, and Mark Berman. ‘Geological Evaluation of The Spectral Assistant (TSA) for Mineralogical Identification.’ *Commonwealth Scientific and Industrial Research Organization, Australia, Exploration and Mining Report 417* (1997): 74.

Appendix (Research Data Acquisition & Processed Data)

This section consists of previous research data retrieval information relevant to the depicted figure it corresponds to. The Mine Resource Data System (*M.R.D.S*) (*Table 8*) is mine-name information from the Apache Hills (red box) and the productivity of certain mines. The wavelength and absorption spectra of Limonite, Jarosite, Hematite, and Goethite are represented in Figure 63. The figure has been modified to illustrate the absorption features of iron minerals.

The classification method (Appendix 2 Figures) identified the cut-off points between categories using the Jenks optimization algorithm; this algorithm groups data according to the inherent breaks in the data, which means that this classification does not require training data as input. It needs only to identify the number of classes. The points where the difference is maximized are identified and used as the thresholds for each natural category (Lamqadem, 2018).

Appendix 1 Research Data Acquisition

Table 8: USGS Mineral Resource Data System (MRDS) of the mines surrounding the Apache Hills, Hidalgo County, New Mexico.

Mineral Resource Data System (M.R.D.S)		
SITE_NAME	DEV_STAT	CODE_LIST
Apache Mine	Past Producer	CU AG PB ZN AU BI W
Eagle Mine	Past Producer	PB AG CU AU BI
International Mine	Past Producer	PB AG CU AU ZN
Fitch Property	Past Producer	PB AG
Barnett Property	Past Producer	CU AG AU
Doyle Property	Past Producer	PB ZN AG
Daisy Mine	Past Producer	CU AG AU
American Mine	Occurrence	CU AG
Chapo Mine	Past Producer	CU PB AG AU
Silver Fox Mine	Past Producer	PB AG
Napane Mine	Past Producer	CU
Christmas Tree Mine	Past Producer	CU PB AG
Nutshell Mine	Prospect	CU AG
Luna Mine	Past Producer	PB ZN
Yucca Claim	Past Producer	CU AU AG
Silver Fox Mine	Prospect	PB AG
Hachita Pit	Occurrence	SDG
Chapo Mine	Past Producer	CU PB
Owens Mine	Unknown	CU PB
Summertime Mine	Past Producer	CU
Whaley Group	Past Producer	CU AG
Daisy Mine	Past Producer	CU PB AG
Eagle Mine	Past Producer	PB AG BI
Occidental Mine	Prospect	PB ZN
American Mine	Past Producer	CU AG
International	Past Producer	PB AG CU AU ZN
Doyle Mine	Prospect	PB ZN AG
Apache Mine	Past Producer	CU AG BI PB W
Barnett Mine	Prospect	CU AU AG
Ford Prospect	Occurrence	PB

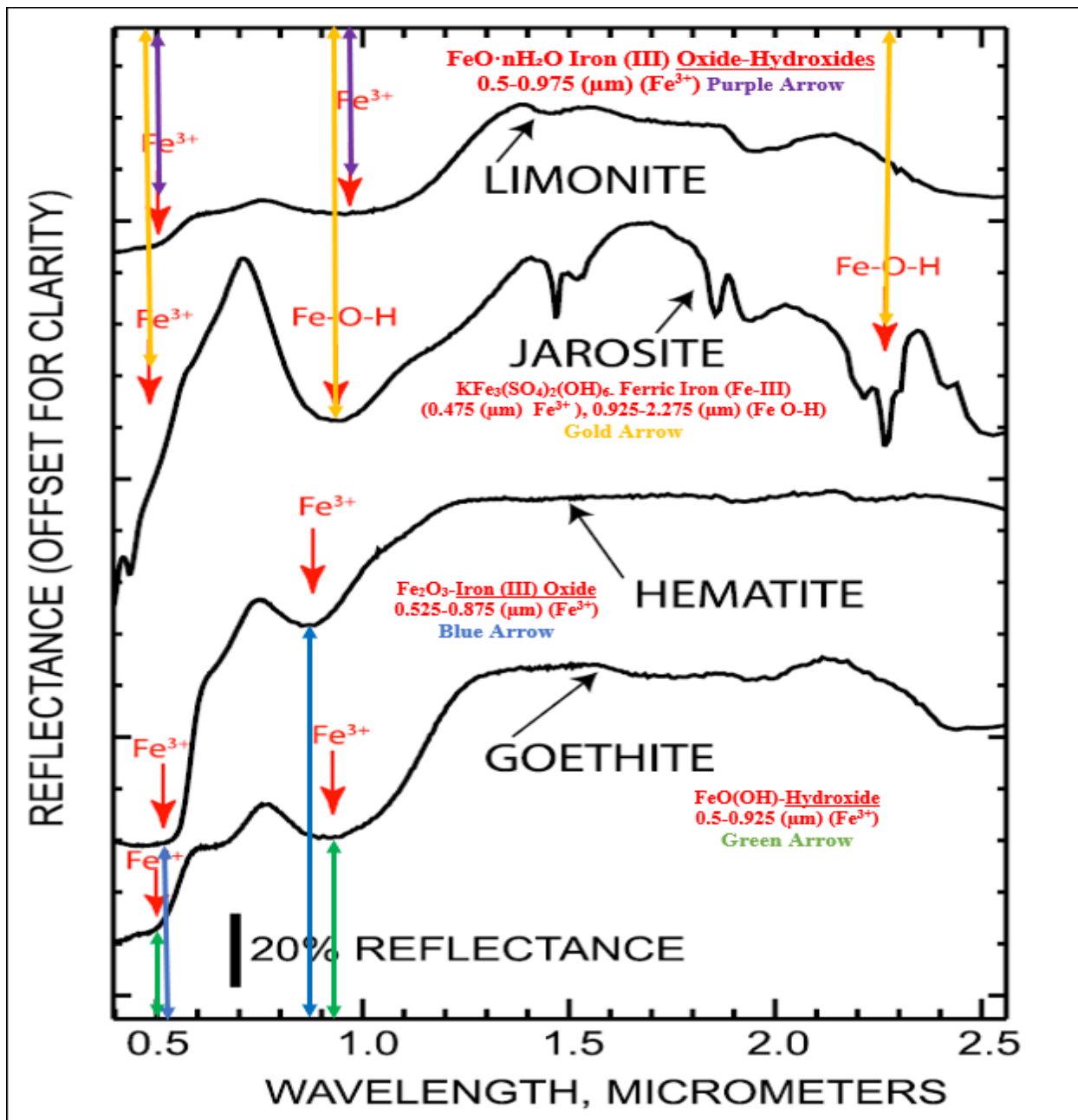


Figure 63: Laboratory spectra of Limonite, Jarosite, Hematite, and Goethite. Limonite, Hematite, and Goethite have strong Fe³⁺ absorption features at 0.97–0.83 and 0.48-micrometer. Jarosite has Fe-O-H absorption features at 0.94 and 2.27 micrometers. Red arrows and labels identify and point to absorption features of Limonite FeO·nH₂O Iron(III) Oxide-Hydroxides 0.5-0.975 (μm) (Fe³⁺) Purple Arrows, Jarosite KFe₃(SO₄)₂(OH)₆ Ferric Iron (Fe-III) (0.475 (μm) Fe³⁺), 0.925-2.275 (μm) (Fe O-H) Gold Arrow, Hematite Fe₂O₃-Iron (III) Oxide 0.525-0.875 (μm) (Fe³⁺), Blue Arrow, Goethite FeO(OH) Hydroxide 0.5-0.925 (μm) (Fe³⁺) Green Arrow. The generic formula is frequently written as FeO(OH)·nH₂O. However, the ratio of oxide to hydroxide compositions can vary quite widely (modified from R.A. Ayuso (2010) and Mars and Rowan (2006)).

Appendix 2 Processed Data (ArcGIS-Figures Classification Method)

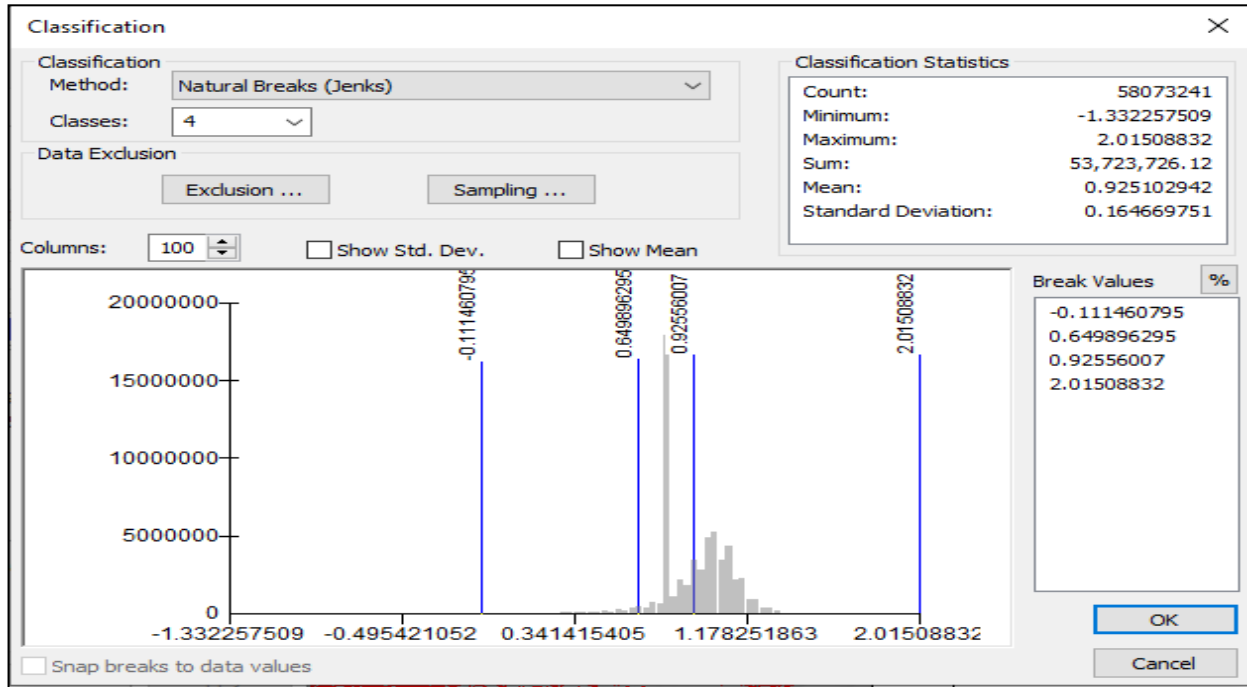


Figure 40c: Classification method type Natural Breaks (Jenks) Classes 4 including mean-maximum statistics and standard deviation.

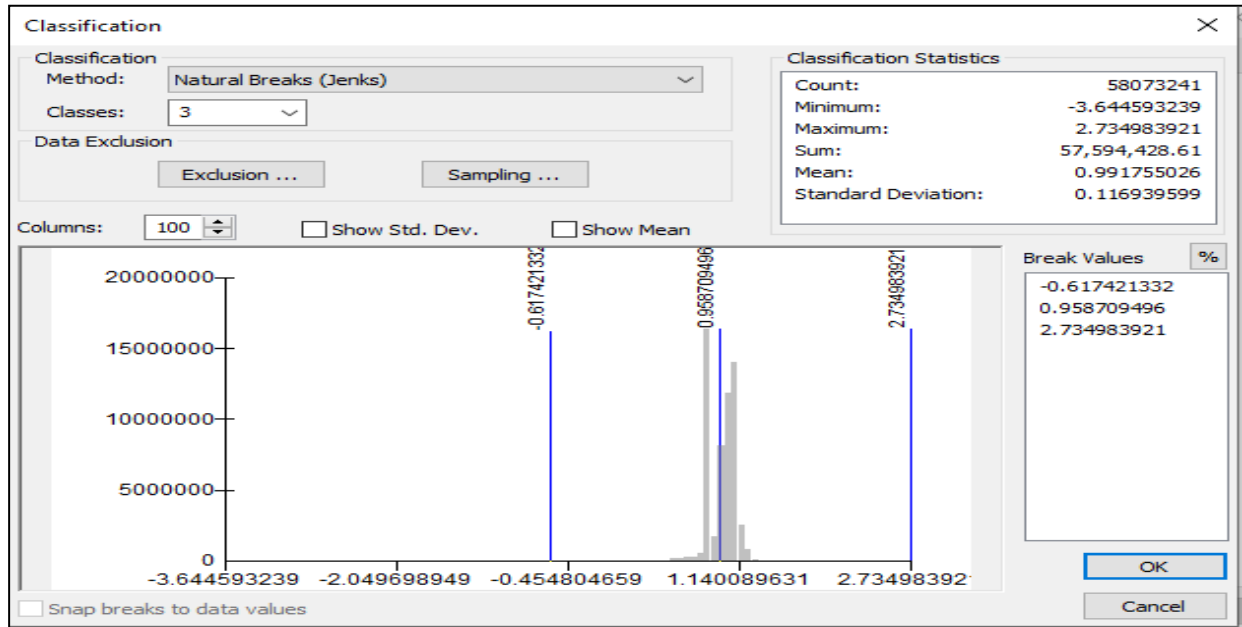


Figure 42: Classification method type Natural Breaks (Jenks) Classes 3 including mean-maximum statistics and standard deviation.

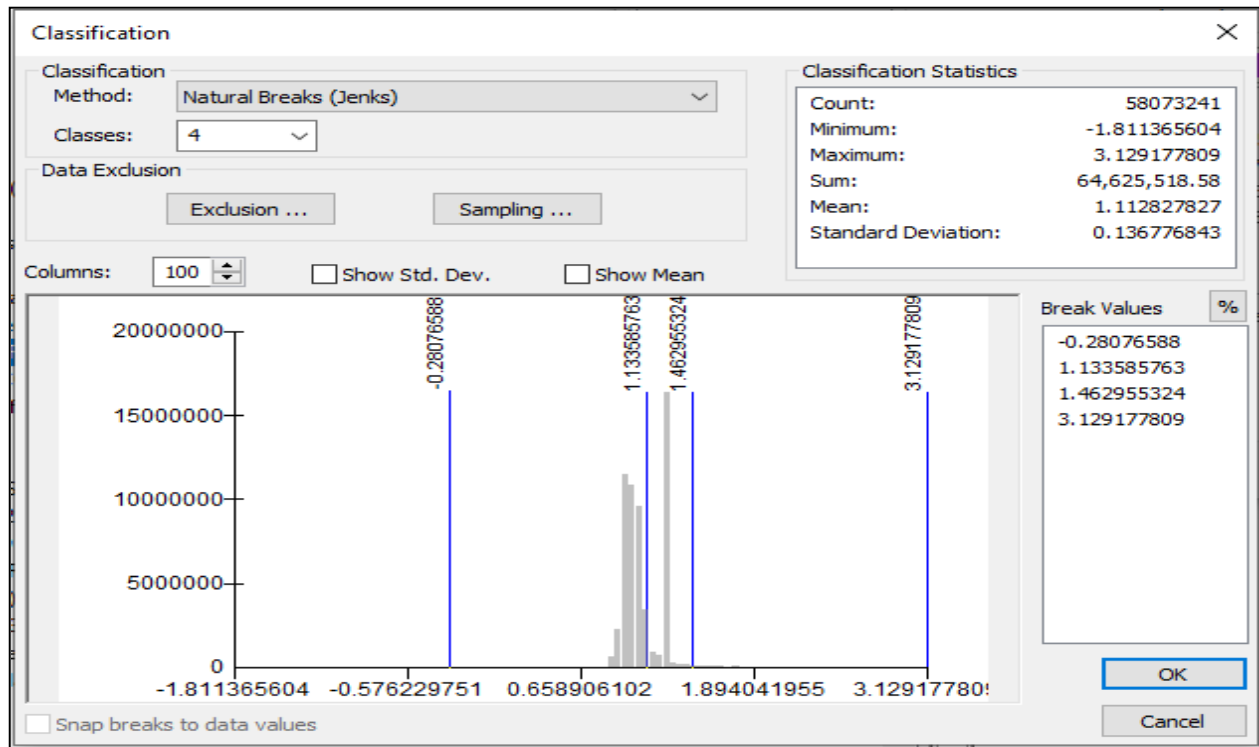


Figure 45: Classification method type Natural Breaks (Jenks) Classes 4 including mean-maximum statistics and standard deviation.

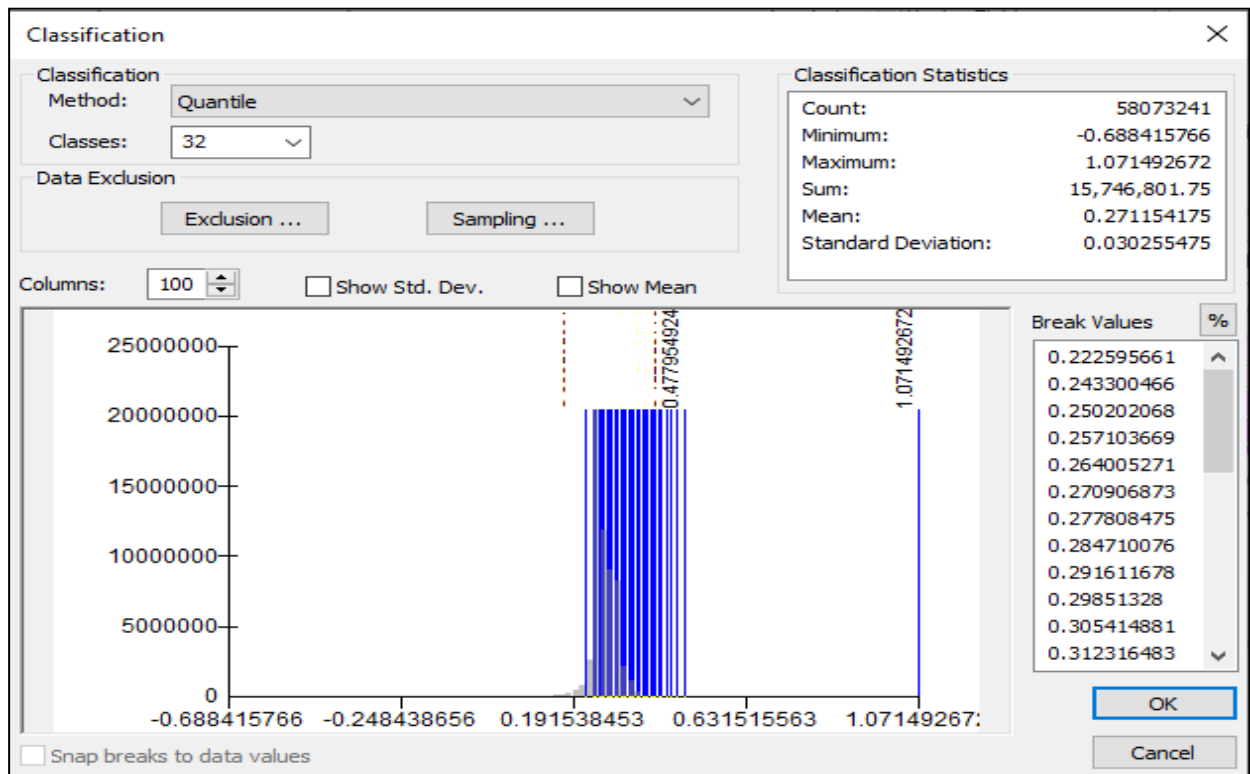


Figure 48: Classification method type Quantile Classes 32 including mean-maximum statistics and standard deviation.

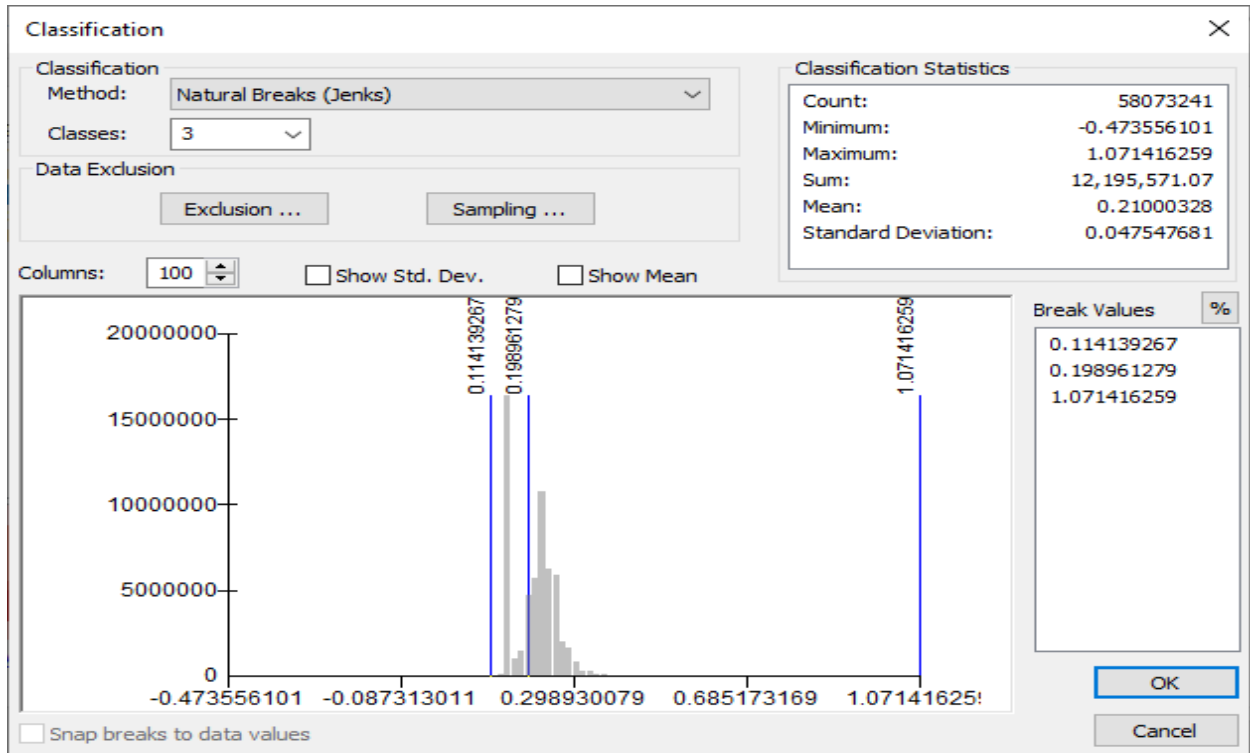


Figure 51: Classification method type Classified (3) Natural Breaks (Jenks) including mean-maximum statistics and standard deviation.

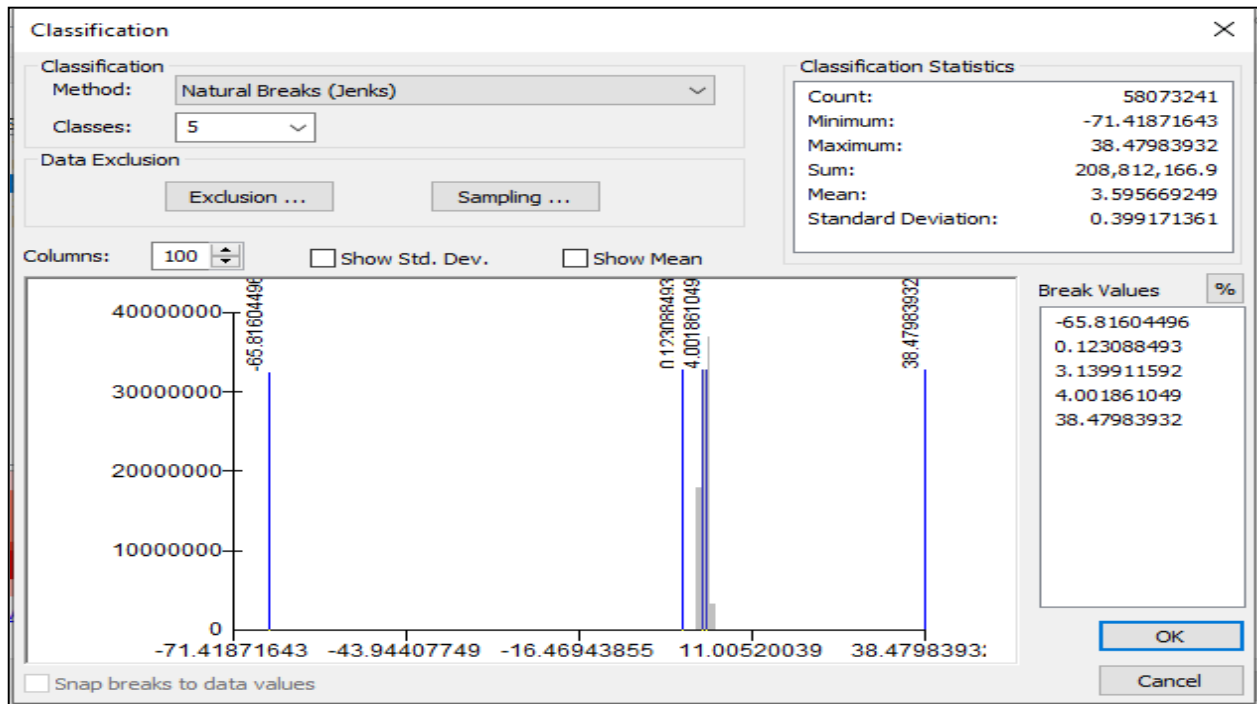


Figure 54: Classification method type Classified (5) Natural Breaks (Jenks) including mean-maximum statistics and standard deviation.

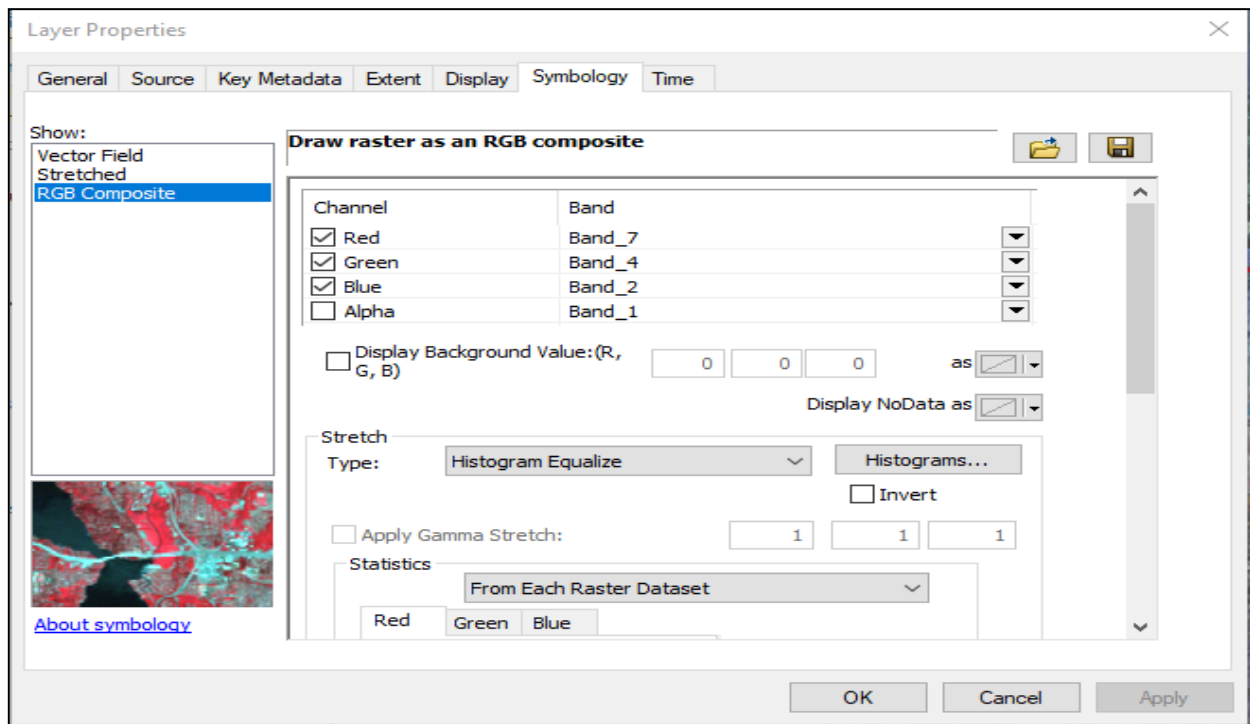


Figure 55i: Classification RGB (7,4,2) Composite Stretch Type Histogram Equalize)

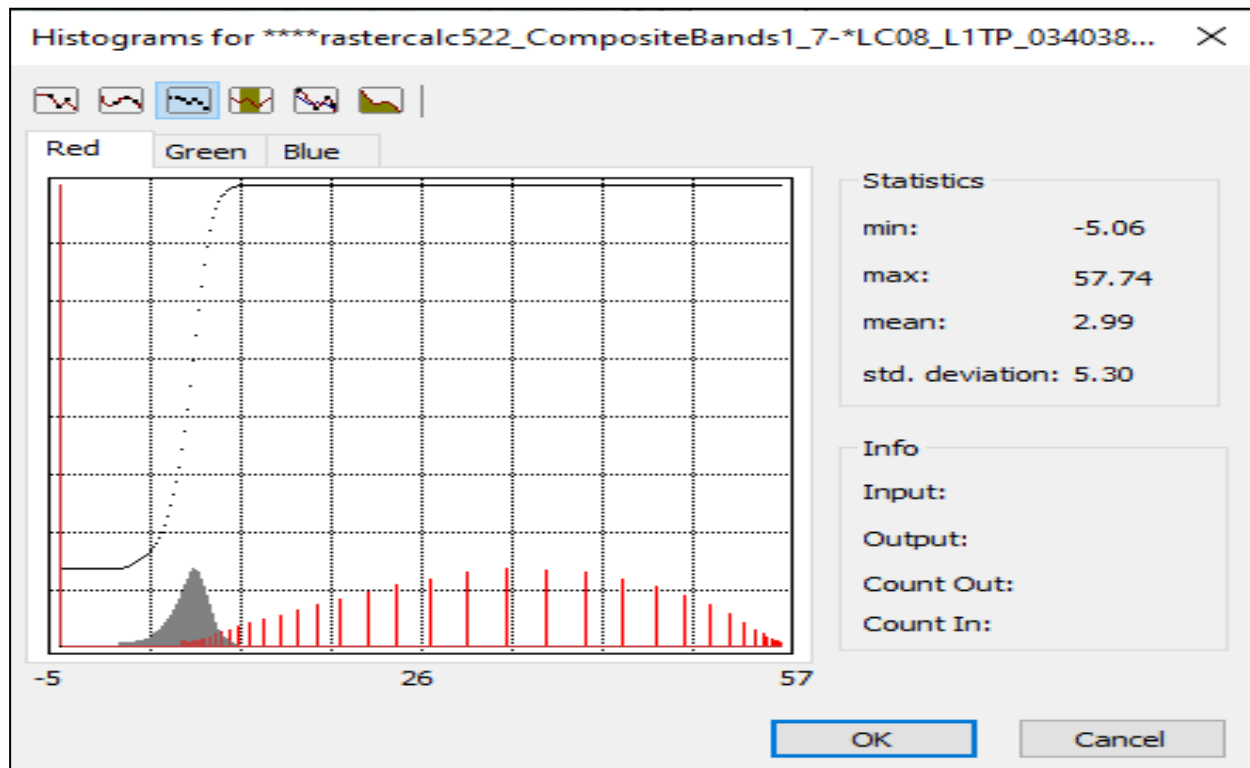



Figure 55j: Histogram Equalize for RGB Composite bands 7,4,2. The statistics minimum is -5.06, and the maximum of 2.99, with a standard deviation of 5.30.

Appendix-3 Actlabs Certificate of Analysis

Quality Analysis ...		Innovative Technologies
----------------------	---	-------------------------

UNIVERSITY OF TEXAS AT EL PASO DEPT. GEOLOGICAL SCIENCES 500 W. UNIVERSITY AVE. EL PASO TX 79968 United States	Date Submitted: 14-Nov-18 Invoice No.: A18-17520 Invoice Date: 23-Nov-18 Your Reference: AH-NM
---	---

ATTN: SERGIO G MACIAS


CERTIFICATE OF ANALYSIS

10 Crushed Rock samples were submitted for analysis.
The following analytical package(s) were requested: Code UT-1-0.5g Aqua Regia ICP/MS

REPORT A18-17520

This report may be reproduced without our consent. If only selected portions of the report are reproduced, permission must be obtained. If no instructions were given at time of sample submittal regarding excess material, it will be discarded within 90 days of this report. Our liability is limited solely to the analytical cost of these analyses. Test results are representative only of material submitted for analysis.

Notes:
Assays are recommended for values above the upper limit. The Au from AR-MS is only semi-quantitative. For accurate Au data, fire assay is recommended.

CERTIFIED BY:

Emmanuel Esemé, Ph.D.
Quality Control

ACTIVATION LABORATORIES LTD.
41 Bittern Street, Ancaster, Ontario, Canada, L9G 4V5
TELEPHONE +905 648-9611 or +1.888.228.5227 FAX +1.905.648.9613
E-MAIL Ancaster@actlabs.com ACTLABS GROUP WEBSITE www.actlabs.com

Page 1/7

Figure 101: Actlabs Ltd. Certificate of Analysis November 14, 2018.

Vita

Sergio G. Macias was born and raised in El Paso, Texas. He completed his Associate's degree in Geological Sciences at El Paso Community College in May 2010, his Bachelor's degree in Geological Sciences at the University of Texas at El Paso in May 2015, where he was nominated for the Student Achievement Award and his Master's degree in Geological Sciences at the University of Texas at El Paso May 2023

Sergio's research focused on Economic Geology and applying remote sensing and Geographic Information Systems for mapping, exploration, and discovery. As a graduate student, Sergio started his thesis research project in Economic Geology with Dr. Philip C. Goodell and Dr. Terry L. Pavlis as his primary consulting advisors. He participated in two internships at Freeport-McMoRan as a field geologist in Morenci, Arizona Summer of 2018, and the Sierrita Mine south of Tucson, Arizona Summer of 2019 while continuing his educational studies.

Sergio was employed by El Paso Community College from 2006-2008 as a Lab Assistant at the Prep Lab for entry-level Jr. College students and as a Teacher's Assistant in the Geology Department from 2008-2010.

jerrymacias2000@yahoo.com